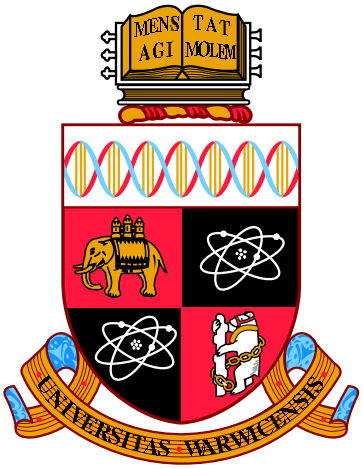

Advancing Diffusion Tensor Image Analysis and Interpretation for Clinical Application

by

Surya Rajan

Thesis

Submitted to the University of Warwick

for the degree of

Doctor of Philosophy

School of Engineering

February 2021

Contents

List of Figures

List of Tables

Acknowledgments

I would like to thank Joanna Collingwood, my supervisor, for being a mentor to me both professionally and personally. Her unwavering passion for science that keeps strong even in the midst of struggles is simply amazing. Without her support and belief in my capabilities, I would not have been able to design and carry out this research.

I would also like to thank Julia Brettschneider for bringing a fresh perspective to my often misbehaving data. Her support has been crucial in revealing some of the important results described in this thesis. I also thank Christopher James and Natasha Khovanova, my thesis committee members, for their support over the past three years. Thanks also to Keith White at the University of Florida, for his kind guidance at the start of the course on diffusion imaging, and continued support throughout.

Two friends deserve my heartfelt thanks - Ahmad Mannan and Jierong Luo. Without their support and insight, I would not have been able to finish the chapter on modelling. Ahmad kindly guided me through the world of numerical simulation, with our break-room chats often turning into crash-courses, while Jierong and her text books' worth of MRI knowledge imparted over several lunch hours, along with some excellent baking tips, have helped me through designing the MRI experiment. I would also like to thank Saad Jbabdi, for catalysing some of the novel contributions within the modelling chapter, especially the part addressing the effects of transverse relaxation time on diffusion tensor images.

I would also like to thank the School of Engineering for funding my degree, and to the Alzheimer's Disease Neuroimaging Initiative for providing me with data

for my research. Thanks also to the Scientific Computing Research Technology Platform for providing me access to their computing facilities, and to David Quigley for allowing access to his group's dedicated computing nodes when I needed it.

I dedicate this thesis to my parents, whose unfaltering faith in me has played no small part in getting me where I am today. My family has been a constant source of encouragement, support, and good food that happened to appear out of nowhere. Thanks also to my friends, those far and near, for some great laughs that kept me sane. Thanks to my group members for their support - Frederik Lermyte, Jake Brooks, Jane Donnelly, Zeido Solomon, and Kharmen Billimoria.

My husband Vishnu is entitled to a special mention for putting up with me over the last few months. His persistent attempts to cheer me up on stressful days have been extremely annoying. But without his support and encouragement, as well as his keen eye on the modelling work, this thesis would not have finished in time.

Finally, many thanks to those amazing people with Alzheimer's disease and dementia, whose selfless contributions to clinical studies have made progress in research possible. I sincerely hope that one day we succeed in finding a cure to Alzheimer's disease.

Declarations

I hereby declare that the work presented in this thesis is my own work except where stated otherwise, and was carried out entirely at the School of Engineering, University of Warwick, from February 2017 to December 2020, under the supervision of Dr Joanna Collingwood with collaborative support from Dr Julia Brettschneider, Department of Statistics. The research described here has not been submitted, either wholly or in part, in this or any other academic institution. Data used in this thesis were obtained with permission from the Alzheimer's Disease Neuroimaging Initiative database (www.adni.loni.usc.edu).

Surya Rajan
February 2021

Abstract

The white matter of the brain is increasingly understood to play a crucial role in neurodegenerative diseases including mild cognitive impairment (MCI) and Alzheimer's disease (AD). Diffusion tensor imaging (DTI) has been developed to image the white matter *in vivo*, and several parameters such as fractional anisotropy (FA), mean diffusivity (MD), radial diffusivity (RD) and axial diffusivity (AxD) may be computed from the acquired signal to infer the integrity of the tissue microstructure. The studies carried out in this thesis aim to improve DTI analysis for clinical applications and investigate the association of DTI signal with the underlying white matter physiology. Imaging data and neurophysiological assessments used in this thesis were obtained from the Alzheimer's Disease Neuroimaging Initiative (ADNI).

A qualitative comparison between three different segmentation strategies of the corpus callosum emphasised the need for a consistent analysis protocol across DTI studies. It was demonstrated that the median of pixel values in a manually delineated ROI may provide more accurate measurements compared to the more widely used atlas-based ROI. A study of corpus callosum sub-regions using this segmentation strategy revealed statistically significant ($p<0.05$) alterations in DTI parameters in specific regions projecting to motor-related areas of the brain in MCI and AD, compared with healthy ageing. This involvement of the corpus callosum was supported by neurophysiological assessments of subjects that showed increased motor deficits in MCI patients such as tremors and gait imbalance.

Further evidence to support these results was obtained from tractography-based analysis of the corpus callosum of these subjects where similar alterations were

found in DTI parameters in motor-related regions ($p < 0.003$). Results obtained from NODDI-DTI (an adaptation of Neurite Orientation and Dispersion Density Imaging (NODDI) for clinically acquired images) analysis of the healthy ADNI cohort indicated a decrease in neurite density in the corpus callosum with ageing that correlated with changes in FA. Adaptation of advanced methods to clinically acquired images was thus demonstrated to provide more specific information about the white matter changes, extending what was achieved in the conventional DTI analysis.

In the final section of the thesis, numerical models of healthy white matter, acute and chronic demyelination, and neuroinflammation were simulated to investigate the associations of FA, MD, RD, and AxD with underlying physiological mechanisms. The results indicated that acute demyelination generated a larger decrease in FA and larger increases in MD, RD, and AxD compared to other disease models - the pattern that is most seen in clinical studies. The study also investigated the dependence of these metrics on the transverse relaxation time (T_2) of the white matter and its compartments. The results suggested that separating out the effects of relaxation and diffusion on the acquired signal provided a more accurate estimation of DTI metrics, achievable for the white matter as a whole at typical clinical scan settings, and for its compartments at more advanced scan settings.

Data collected in this thesis using DTI, tractography, and NODDI-DTI suggested that a reduction in fibre packing density was a major factor contributing to the decrease in FA and increases in MD, RD, and AxD, as widely reported in ageing, MCI, and AD. These results were demonstrated in the corpus callosum, but are likely to hold in other white matter tracts as well. The results from white matter modelling supported these findings, where acute demyelination (modelled as a decrease in fibre packing density) was found to cause the largest alterations in FA, MD, RD, and AxD, compared to other disease cases modelled.

In summary, the collected work in this thesis presents an analysis framework enabling application of research developments in clinical DTI, supported by improved specificity gained from modelling.

Abbreviations

Aβ	Amyloid Beta
AD	Alzheimer's Disease
ADC	Apparent Diffusion Coefficient
ADNI	Alzheimer's Disease Neuroimaging Initiative
AFNI	Analysis of Functional Neuroimages
ANCOVA	Analysis of Covariance
APOE	Apolipoprotein E
AxD	Axial Diffusivity
cdf	Cumulative Distribution Function
CHARMED	Composite Hindered and Restricted Model of Diffusion
CT	Computed Tomography
CSD	Constrained Spherical Deconvolution
CSF	Cerebro-spinal Fluid
DMS	Diffusion Microscopist Simulator
DTI	Diffusion Tensor Imaging
DW-MRI	Diffusion Weighted Magnetic Resonance Imaging
ECS	Extra-cellular Space
FA	Fractional Anisotropy
FCNN	Fully Convolutional Neural Network
FDG	Flurodeoxyglucose
FDT	FMRIB's Diffusion Toolbox

FMRI	Functional MRI
FMRIB	Oxford Centre for Functional MRI of the Brain
FOD	Fibre Orientation Distribution
FSL	FMRIB's Software Library
GUI	Graphical User Interface
HARDI	High Angular Resolution Diffusion Imaging
HC	Healthy Controls
HCP	Human Connectome Project
ImageJ	Image Processing and Analysis in Java
MCI	Mild Cognitive Impairment
MD	Mean Diffusivity
MEDUSA	Microstructure Environment Designer with Unified Sphere Atoms
MNI	Montreal Neurological Institute
MR	Magnetic Resonance
MRI	Magnetic Resonance Imaging
ND	Neurite Density
NMR	Nuclear Magnetic Resonance
NODDI	Neurite Orientation Dispersion and Density Imaging
OD	Orientation Distribution Index
ODF	Orientation Distribution Function
PDF	Probability Distribution Function
PET	Positron Emission Tomography
PiB	Pittsburgh compound B
RA	Relative Anisotropy
RESTORE	Robust Estimation of Tensors by Outlier Rejection
RF	Radio Frequency
ROI	Region of Interest
ROIEditor	Region of Interest Editing Tools

RD	Radial Diffusivity
SMC	Significant Memory Concern
SNR	Signal to Noise Ratio
TBSS	Tract Based Spatial Statistics
TE	Echo Time
TOM	Tract Orientation Mapping
TR	Repetition Time

Chapter 1

Introduction and Background

1.1 Alzheimer's disease and mild cognitive impairment

Dementia is one of the leading health challenges in the world. It describes a set of symptoms including memory loss and impaired mental and cognitive faculties, leading to difficulty carrying out routine tasks in daily life. Alzheimer's disease (AD) is a neurodegenerative disorder characterised by progressive deficits in memory and cognitive function and the most common cause of dementia. The prevalence of AD was estimated to be at about 5% in Europe [Niu et al., 2017] with a huge socio-economic impact in the society. Many risk factors for AD have been identified, including age, gender, smoking, obesity, and diabetes [Li et al., 2016].

The first case of AD was reported in 1906 by Dr. Alois Alzheimer [Hippius and Neundörfer, 2003; Möller and Graeber, 1998]. When examining post-mortem brain tissue of a patient who had presented with symptoms including memory loss, aggression, and confusion, he discovered abnormal histological features such as senile plaques and neurofibrillary tangles. Plaques are extracellular deposits of the protein amyloid beta (Aβ) and neurofibrillary tangles are phosphorylated forms of the protein tau [Brion, 1998; Cras et al., 1991]. Despite extensive research, it is still unclear whether abnormal Aβ and tau deposition are causing the pathological changes leading to AD or their by-products.

When a person exhibits symptoms of cognitive decline greater than what is normally expected with their age but not sufficient to be diagnosed with dementia, they are categorised as a patient with mild cognitive impairment (MCI). Patients with MCI are at a higher risk of progressing to AD and AD dementia [Gauthier et al., 2006].

1.1.1 Symptoms of AD

The symptoms of AD are manifold. Cognitive deficits including impaired functions of memory, awareness, and judgement are recognised as clinical manifestations of AD pathology and have been extensively studied [Bature et al., 2017]. Neuropsychiatric symptoms such as apathy, depression, anxiety, and aggression have been reported in patients with AD, although behavioural and other non-memory related symptoms were found to be more common in younger patients [Zhao et al., 2016; Barnes et al., 2015]. Neuroimaging studies have mapped these symptoms to various regions of the brain network and neurochemical associations have been reported with tau, as well as with acetylcholine and serotonin which are neurotransmitters involved in communication processes in the brain [Boublay et al., 2016; Rosenberg et al., 2015; Bruen et al., 2008].

Sensory and motor impairments have been reported in pre-clinical and very early stages of AD, even when cognitive and neuropsychiatric symptoms have not yet presented. Impairment in olfactory function has been observed to be an early symptom, significantly associated with memory deficits and a reduced volume of hippocampus [Murphy, 2019; Albers et al., 2015]. Visual impairment, due to a loss of retinal ganglion cells and a subsequent reduction in retinal layer thickness, has been observed in patients with AD [Javaid et al., 2016; Bublak et al., 2011]; as well as a deficit in auditory function corresponding to pathology in the brain auditory pathway [Golden et al., 2015]. Reduced motor functions, including tremor, impaired gait, and rigidity of the limbs have also been reported [Albers et al., 2015]. These non-memory related symptoms have been observed to be some of the earliest manifestations in the course of AD pathology.

1.1.2 Age and gender as risk factors for AD

Ageing is the single biggest risk factor for AD. The human body becomes increasingly vulnerable as it ages, often getting pushed into a pre-disease or disease state by dysregulation in various functional networks. The pre-disease state is thought to be potentially reversible and is a major area of focus for research into drug development. Dyshomeostasis of body systems with ageing have been found to be associated with increased risk of incidence of AD [Riedel et al., 2016].

The incidence of AD has also been observed to be greater in women than in men with a relative risk of 1.33 [Li et al., 2016]. Traditionally, this was thought to be due to an average longer lifespan for women than men, but recent evidence has helped establish that some risk factors affect both genders in different ways.

For instance, there are risk factors that may have a stronger effect in women (e.g. the Apolipoprotein E (APOE) genotype), or may be more common in women (e.g. socio-cultural factors such as lower education) or affect only women (e.g. menopause) [Nebel et al., 2018]. Longitudinal rate of cognitive decline in MCI has been reported to be greater in women than in men [Lin et al., 2015]. Clinical trials testing new drugs for treatment of AD have considered these differences in outcomes for both genders while recruiting subjects, but have often neglected them when analysing the effects of drugs on patients. Gender has now been established to be an important risk factor for AD and needs to be given appropriate importance in clinical studies for better advances in diagnosis and individualised treatment development [Mielke, 2018].

In the investigations carried out in this thesis, the effects of age and gender on study outcomes will be accounted for by including them in statistical testing for differences between healthy ageing, MCI, and AD to ensure that individual variations in the impacts of these risk factors are addressed.

1.1.3 Diagnosis criteria for MCI and AD

A set of criteria for clinical diagnosis of MCI have been proposed where MCI was defined as the pre-dementia phase of AD when symptoms have already started to appear [Albert et al., 2011]. Diagnosis of MCI require the expert judgement of a doctor based on the results of clinical and neuropsychological examinations. The currently followed diagnostic criteria have been summarised in box 1.1. Although different imaging biomarkers have been proposed for MCI including Aβ and tau levels in the cerebrospinal fluid (CSF), these require further validation and therefore have been recommended for use in research settings only. Longitudinal follow-ups were strongly advised for patients with MCI to monitor symptoms and track their progression to AD.

Box 1.1: MCI diagnostic criteria

- Evidence of impairment in cognitive domains such as memory, language, or executive functions
- Ability to independently carry out daily tasks despite the problems mentioned above
- Cognitive deficits not being sufficient for a diagnosis of dementia

Currently, there are no means to conclusively diagnose AD until post-mortem. However, a diagnosis of 'probable AD' may be given to the patient while alive. A set of criteria for clinical diagnosis of probable AD has been proposed in 1984 [McKhann et al., 1984]. Clinically presenting symptoms were to be supported by other relevant factors such as family history and evidence of cortical atrophy on computed tomography (CT) scans. With more information on AD gained as a result of extensive research over the years, AD diagnostic criteria have been revised in 2011 as summarised in box 1.2 [McKhann et al., 2011].

Box 1.2: AD diagnosis criteria

- Dementia established through clinical and neuropsychological exams
- Cognitive deficits in multiple functional areas and progressive loss of memory
- Gradual onset of symptoms over a span of months or years
- Patient aged between 40 and 90 years
- Absence of other brain disorders
- Biomarkers of Aβ deposition in the brain:
  - Low levels of Aβ_{42} in CSF samples
  - Positron emission tomography (PET) scans showing amyloid deposition as plaques in the brain
- Biomarkers of neuronal injury:
  - Elevated levels of tau protein in CSF samples
  - Decreased metabolism in the temporo-parietal cortex in PET scans
  - Brain atrophy as imaged using magnetic resonance imaging (MRI)

1.2 The brain

1.2.1 Neuron

A neuron is the basic building block of the human nervous system specialised in conduction of electrical impulses. It has three main components - the cell body, dendrites, and axons. The cell body contains the nucleus and various organelles, and controls the functions of the cell. It projects to axons and dendrites, which

are responsible for communication between neurons; dendrites bring information into the cell body and axons carry information out to the next neuron. Axons are longer projections than dendrites and may be of the order of 1 metre. They have an insulating layer of fatty tissue around them called myelin that enables transmission of electrical nerve impulses efficiently through the nervous system. Periodic gaps in the myelin sheath, called nodes of Ranvier, facilitate rapid saltatory conduction of impulses.

A schematic of the neuron is given in Figure 1.1 along with some of the other cells in the brain. Oligodendrocytes are glial cells responsible for producing myelin. They repeatedly envelop axons with myelin layers forming an insulating sheath. Neighbouring segments of axons may be covered with myelin produced by different oligodendrocytes. Astrocytes are a different type of glial cells responsible for specialised functions such as information transmission and processing in the brain. They release neurotropic factors, aid the development of neurons, are involved in neurotransmitter metabolism, and maintain pH and K^+ levels [Dong and Benveniste, 2001]. Oligodendrocytes and astrocytes are collectively called the macroglia. On the other hand, microglia are cells that remove brain debris and are macrophage cells activated by disturbances to brain homeostasis by events such as infection or trauma [Ginhoux et al., 2013].

Cell bodies, dendrites, and axon terminals collectively make up the grey matter of the brain. It has a light grey appearance in living tissue arising from cell bodies and blood vessels. On the other hand, axons appear white due to the presence of myelin, thus constituting the white matter of the brain. White matter can be

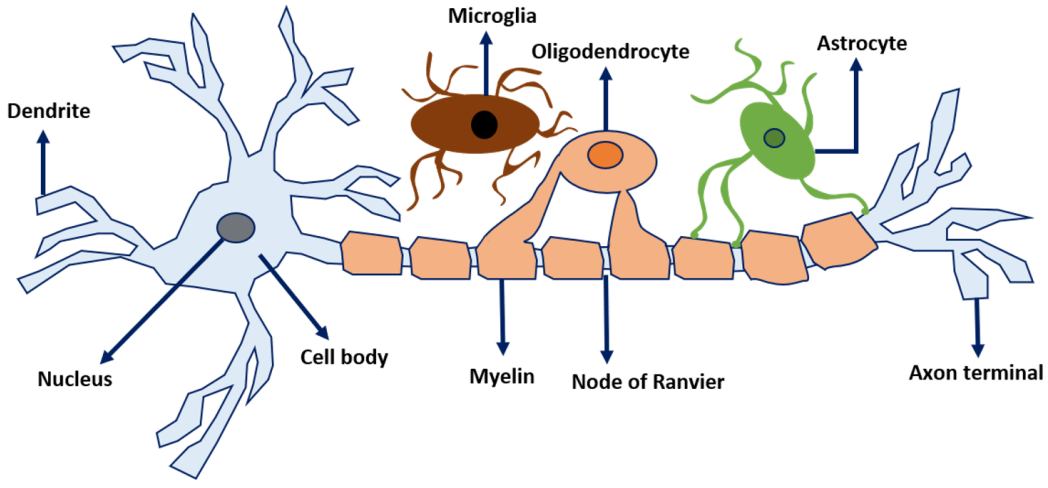

Figure 1.1: A schematic of cells in the white matter.

thought of as communication pathways in the brain connecting different grey matter tissues with each other.

1.2.2 Grey matter in ageing, MCI, and AD

The grey matter of the brain is known to be affected by degenerative processes, whether as part of normal ageing or diseases such as MCI and AD. Global brain atrophy has been reported in ageing brains, but a few studies have suggested that lifestyle factors such as physical activity and balanced diet may preserve grey matter volume [Batouli and Saba, 2017; Aribisala et al., 2013]. Increasing rate of atrophy with age in the medial temporal lobe, which contains grey matter structures such as the hippocampus responsible for memory and other cognitive functions, has been used to predict future cognitive decline in healthy individuals [Ritchie et al., 2015; Rusinek et al., 2003]. On the other hand, a few studies have reported relative preservation of the medial temporal lobe with age but did not compare results with cognitive levels of study subjects [Good et al., 2001]. Prediction of brain age (as opposed to chronological age) based on grey matter changes has been proposed as a means to evaluate degeneration and mortality to support management of clinical care [Cole et al., 2018].

Grey matter atrophy has also been reported in MCI in the medial temporal lobe, specifically in the hippocampus [Yi et al., 2016; Pennanen et al., 2005; Karas et al., 2004]. Similar changes have also been found in the thalamus, amygdala, and putamen [Yi et al., 2016; Balthazar et al., 2009; Karas et al., 2004]. Along with grey matter atrophy, abnormal tau deposition has also been observed in the medial temporal lobe [Cho et al., 2016]. Neuroinflammation has been reported in amyloid-positive MCI patients where brain regions with inflammation and amyloid deposition were found to coincide [Parbo et al., 2017]. Longitudinal tracking of these changes may support prediction of patient conversion from MCI to AD [Yi et al., 2016; Sexton et al., 2010].

Grey matter changes reported in patients with AD are similar to that in MCI, though far more extensive. Global grey matter atrophy has been observed in AD, including in the medial temporal lobe, specifically the hippocampus, and limbic regions [Dicks et al., 2019; Phillips et al., 2019; Yi et al., 2016]. Grey matter atrophy has been associated with cognitive deficits, with an early onset of AD observed to progress faster than a late onset [Agosta et al., 2015]. However, longitudinal tracking of patients has revealed a heterogeneous pattern of degeneration. Therefore, monitoring atrophy in persons with a genetic risk of AD has been proposed to help track symptoms and slow down disease progression during pre-clinical stages of AD

[Reiter et al., 2017]. In addition to atrophy, tau pathology has also been reported in most cortical regions in AD [Cho et al., 2016]. Although neuroinflammation in AD has been detected, it was not found to be associated with tau. Combining this result with the one described previously where inflammation was found to coincide with amyloid deposition, it has been suggested that inflammation may precede tau pathology and may carry a protective role to remove Aβ [Parbo et al., 2018; Suridjan et al., 2015].

1.2.3 White matter in ageing, MCI, and AD

Post-mortem studies of the human brain have found that age-related volume loss in the white matter may exceed that in grey matter [Piguet et al., 2009]. This atrophy has been attributed to a loss of myelinated nerve fibres [Tang et al., 1997]. White matter lesions may often be observed in the ageing brain and have been associated with grey matter atrophy and cognitive decline [Maniega et al., 2015; Aribisala et al., 2013]. Neuroinflammation has also been observed in the white matter, suggested to be more prominent than in the grey matter [Gefen et al., 2019]. Age-related alterations in the white matter microstructure have typically been observed in association (superior and inferior longitudinal fasciculi, inferior fronto-occipital fasciculus, and uncinate fasciculus), thalamic (anterior, posterior and superior thalamic radiations), commissural (forceps major and minor), and limbic (cingulate gyrus, parahippocampal cingulum) tracts [Cox et al., 2016; Cremers et al., 2016].

Alterations in white matter properties have been reported in patients with MCI, even when their grey matter structures were relatively preserved. For instance, the white matter integrity has been found to be damaged in limbic tracts, the corpus callosum, and more generally in the temporal, frontal, and parietal white matter in MCI [Zhuang et al., 2012; Ukmar et al., 2008; Medina et al., 2006]. These pathological changes have been found to be similar to that reported for AD, although not as extensive. They have been associated with grey matter atrophy and cognitive impairment, and reportedly predicted conversion of HC to MCI [Giulietti et al., 2018; Doi et al., 2015; Debette and Markus, 2010]. Neuroinflammation has also been observed in the white matter in MCI [Wang et al., 2016].

More widespread damage to the white matter has been reported in AD. Early impacts of disease mechanisms have been observed in the temporal stem, which is the white matter tract connecting the temporal and frontal lobes [Hanyu et al., 1998]. Although many studies have investigated white matter changes in AD, there is still no consensus on whether these are primary effects of underlying pathological

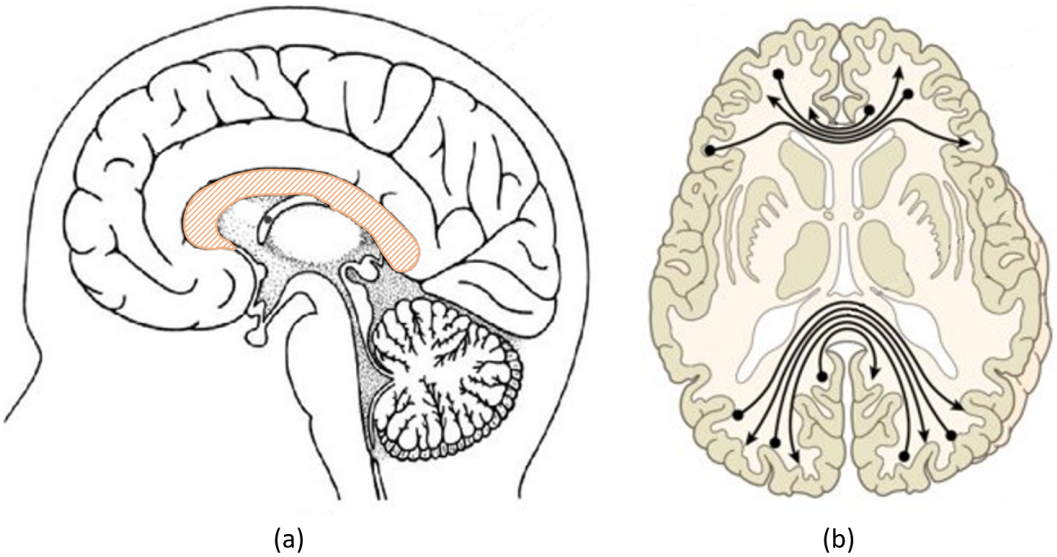

Figure 1.2: (a) The right brain hemisphere as viewed from the left side with the corpus callosum marked in orange (b) Brain as viewed from the top with the corpus callosum fibres shown to be connecting both hemispheres. Images have been adapted with permission from Cover et al. [2018] and *wileyessential.com*.

mechanisms, or occur secondary to grey matter atrophy [Kaskikallio et al., 2019; Caballero et al., 2018; McAleese et al., 2017; Fischer et al., 2015]. Extensive damage has been reported in the global brain white matter, including in the corpus callosum, cingulum, and the association tracts [Mayo et al., 2017]. This has also been found to be influenced by Aβ deposition [Vipin et al., 2019]. Local interactions between various factors as well as the sequence of these events have been reported to affect both grey matter and white matter in different ways [Villain et al., 2010].

1.2.4 Corpus callosum

The corpus callosum is the largest white matter tract in the human brain and consists of a bundle of fibres connecting the left and right hemispheres. It is also the largest of the commissural tracts connecting corresponding regions in the hemispheres. The size of the corpus callosum has been suggested to be influenced by ethnicity, genetic factors, and gender [**?**Woldehawariat et al., 2014; Sullivan et al., 2001], although some studies have reported evidence that suggests the contrary [Bishop and Wahlsten, 1997; Pozzilli et al., 1994]. Schematics of the brain from an axial (top) view and that of a brain hemisphere from a sagittal (side) view are shown in Figure 1.2 with the corpus callosum annotated.

The corpus callosum is known to be a heterogeneous bundle of fibres with

differing diameters [Aboitiz et al., 1992]. It continues to grow in area and mature through childhood into adolescence. Different parts of the corpus callosum have been reported to develop at different rates with the peak maturity of development achieved in mid-life (between 30 and 45 years of age) [Prendergast et al., 2015]. Several studies of the corpus callosum have suggested that anterior regions may be affected by age-related mechanisms earlier than posterior regions [Slater et al., 2019; Prendergast et al., 2015], although a few investigations have reported no significant differences between the effects of age on different regions [Bennett et al., 2017]. Atrophy of the corpus callosum has been associated with cognitive and motor deficits in healthy ageing, MCI, and AD [Qiu et al., 2016; Lee et al., 2016; Wang et al., 2015b; Zhu et al., 2012; Ryberg et al., 2007]. Changes in callosal volume and thickness have been attributed to a variety of reasons including demyelination and axonal damage [Luders et al., 2010].

1.3 Theories of AD pathogenesis

Several potential sequences of events in the brain have been proposed as leading to AD pathogenesis. Although it is not possible within the scope of this thesis to describe them in depth, the primary theories are highlighted here.

1.3.1 Neuroinflammation

Inflammation in the brain has been widely reported as involved in AD pathogenesis, although it is not quite clear whether it plays a protective or harmful role [Steardo et al., 2015; Latta et al., 2015]. It is possible that Aβ accumulation triggers an inflammatory reaction, but environmental risk factors of AD may modify the response of the brain immune system [Heneka et al., 2015]. Molecular characteristics of neuroinflammation may prove to be a critical area of research in future studies of drug development [Van Eldik et al., 2016].

1.3.2 Trace metals and oxidative stress

Oxidative stress has now been established as a significant factor contributing to the pathogenesis of AD. Trace metals in the brain, such as iron, copper, and zinc, may potentially bind to high affinity sites on Aβ, catalysing free radical generation and leading to accumulation of reactive oxygen species and oxygen damage over time [Cheignon et al., 2018; González-Reyes et al., 2017; Huang et al., 2016]. Oxidative stress and abnormal mitotic signalling (required for cell division processes)

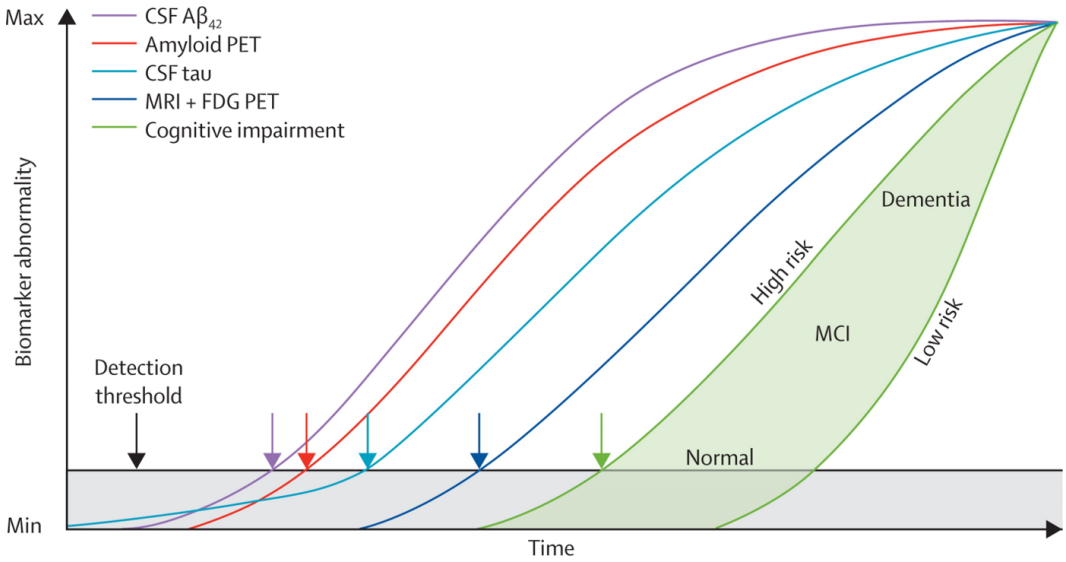

Figure 1.3: A diagram of the amyloid cascade hypothesis. The figure shows the perceived progression of biomarkers over time in AD pathology. Each biomarker needs to be above a threshold level to be detected. Picture obtained with permission from Jack Jr. et al. [2013]

may independently trigger disease mechanisms, despite both being necessary for progression to AD [Zhu et al., 2004]. Although not sufficient to provide a complete picture of AD pathogenesis, oxidative stress has been established to be closely associated with the disease.

1.3.3 Tau hypothesis

This theory proposes a critical role for tau aggregates in triggering AD pathology. While initially formed in only some parts of the brain, they later propagate to other regions and gradually lead to neurodegeneration [Kametani and Hasegawa, 2018; Maccioni et al., 2010]. Tau phosphorylation has been hypothesised to be a neuronal response against degenerative mechanisms such as oxidative stress [Lee et al., 2005]. A possibility of Aβ and tau triggering AD pathogenesis together has also been proposed [Ittner and Götz, 2011; Small and Duff, 2008].

1.3.4 The amyloid cascade hypothesis

The most widely cited theory of AD pathogenesis is arguably the amyloid cascade hypothesis, which consists of the following sequence of events [Jack Jr. et al., 2013]. Tau aggregates start forming in the brain triggering the gradual accumulation of Aβ peptides and leading to inflammation, oxidative stress, and subsequent vascular

and neuronal damage. Aβ deposition accelerates tau pathology resulting in the deposition of neurofibrillary tangles and eventual neuronal death. The last of clinically detectable symptoms to arise are deficits in memory and other executive functions. Although this model of AD remains popular, it has been criticised for an overly simplistic and linear trajectory of aetiology [Herrup, 2015; Reitz, 2012]. A diagrammatic representation of AD progression under the framework of this hypothesis has been given in Figure 1.3. Although the role of amyloid in AD has not been discarded, the amyloid cascade theory by itself has been demonstrated to be incomplete, as inferred from failures in drug trials that targeted amyloid in patients with AD [Reitz, 2012].

1.3.5 Myelin

Even though the amyloid cascade hypothesis is widely accepted, clinical trials that reduced Aβ deposition in the brain have failed to improve cognitive functions in patients with AD, suggesting that the theory may not be sufficient to explain AD pathogenesis [Reitz, 2012]. Instead, AD has been hypothesised to be a disease of the white matter [Bartzokis, 2011]. This theory has been developed based on the results of neuroimaging studies that showed degenerative changes in the white matter occurring years before and independent of grey matter atrophy (see section 1.2.3). It suggests that age-related myelin degeneration may be a trigger for AD-related pathological mechanisms. Processes occurring in the brain to repair myelin have been postulated to lead to the production of Aβ and tau. AD is thus regarded to be a 'homeostatic response' to the breakdown of myelin [Bartzokis, 2011, 2004].

This theory has also looked at AD pathogenesis from an evolutionary point of view. It suggests that myelin is the component in the brain that is the most recently evolved and is therefore vulnerable to damage being the weakest link. Rather than discounting the contributions of Aβ and tau to AD aetiology, this theory attempts to bring a broader perspective to AD by combining several aspects and pathways of the disease. It may require modifications in the future as more information on the molecular, epidemiologic, pathologic, and mechanistic characteristics of myelin and white matter pathways is unravelled [Bartzokis, 2011].

1.4 Imaging in AD

Various imaging modalities may be utilised in different stages of AD to detect and investigate biomarkers, and provide suitable tools to test the validity of hypotheses described in section 1.3. Some of them have been summarised here in the context of

clinical diagnosis of AD.

Aβ is now known to have accumulated in the brain by early and cognitively normal phases of AD. This may be reflected in the abnormal Aβ levels in patient CSF samples. Aβ deposits may also be visualised on PET scans of the brain where a radiotracer called Pittsburgh Compound-B (PiB) is used to image amyloid. Fibrillar Aβ deposits have been observed in PET scans of cognitively normal elderly individuals with a high genetic risk of AD and have been associated with accelerated brain atrophy and cognitive decline [Petersen et al., 2016; Reiman et al., 2009]. Interestingly, Aβ accumulation has also been observed in individuals who preserve their cognitive functions at follow-ups. This has been attributed to a relatively high cognitive reserve in these individuals [Jack Jr. et al., 2014; Ewers et al., 2013].

Subsequent neurodegeneration may be reflected in the abnormal tau levels in CSF samples of the patient. Tau deposition may also be visualised on PET scans using fluorodeoxyglucose (FDG) tracer which tracks glucose consumption. Metabolic rate of glucose in the brain has been reported to decrease several years before clinical symptoms of AD manifest [Landau et al., 2011]. FDG-PET has been validated to be an excellent tool to evaluate and diagnose AD at an early stage when clinical symptoms of the disease may not yet have presented [Cabral et al., 2015; Jagust et al., 2007]. In contrast to amyloid-PET scans, which have not correlated well with cognitive decline in all cases, a negative FDG-PET scan has been found to be a strong predictor of clinical stability [Iaccarino et al., 2019].

By early stages of clinically diagnosable MCI, brain atrophy becomes detectable on structural MRI scans. Results of studies investigating atrophy in MCI have been discussed in section 1.2.2. Cognitive abilities start to decline by a detectable measure in patients with MCI and AD. The imaging biomarkers described above may be detectable in patients prior to manifestation of clinical symptoms; whereas cognitive decline is typically observed in patients at a later stage in the disease course, i.e., diagnosable MCI or probable AD [McKhann et al., 2011].

1.4.1 Imaging the white matter

Diffusion tensor imaging (DTI) is an MRI technique that can map the diffusion of water molecules in the brain, and is capable of acquiring an image with a typical resolution of 1-3 mm. It has evolved to become an important tool in neuroscience. DTI may be used to investigate the properties of brain white matter in healthy ageing and diseases. A brief summary on DTI acquisition and mathematical formulations of different parameters that characterise diffusion in the tissue has been provided in chapter 2. Although white matter alterations have been detected in MCI and AD

compared to healthy ageing, it is not yet clear whether these are secondary effects of grey matter atrophy or a primary cause of disease pathology. There is a need to investigate these changes and explore their scope as potential biomarkers of MCI and AD.

1.5 Motivation and Aims

The importance of imaging biomarkers has been acknowledged in the current diagnosis criteria for MCI and AD (boxes 1.1 and 1.2). Biomarkers also play a big role in monitoring subject progression in drug development trials. However, their accuracy depends on the manner in which they are measured; for instance, qualitative inspection or manual, semi-automated, or automated segmentation of the regions of interest (ROI) may provide different measurements [Frisoni et al., 2013]. Although many biomarkers have been proposed and developed in research settings, a majority of them have not been successfully translated into routine clinical practice [Kilimann et al., 2017]. A standardised protocol of quantitative measurement of imaging biomarkers may help speed this up, and enable comparison across studies.

DTI is an excellent tool to image the brain white matter and investigate its role in disease mechanisms in MCI and AD. Many advances have been made in the field of DTI acquisition and processing, some of which have been covered in chapter 2. Routinely acquired clinical DTI scans are typically not suited for analysis using these advanced methods. The studies carried out in this thesis aim to utilise conventional and advanced analyses to extract detailed and specific information from clinical DTI scans.

Standardisation of analysis protocols for clinical applications is important in the context of future studies investigating the role of white matter in AD pathogenesis. It is likely that biomarkers, and protocols to detect them, may depend on the characteristics of the white matter region itself; therefore, a single white matter tract - the corpus callosum - has been focused upon in this thesis to maintain consistency. Against this context, the aim of this thesis is to investigate the following questions:

Aim 1: Do segmentation strategies impact quantitative measurements of DTI biomarkers in the corpus callosum? The results obtained by investigating this question have the potential to clarify whether segmentation practices currently followed need improvement, and enable standardisation of DTI analysis protocols in the scientific and clinical community. Such a standardisation could be critical in comparing results from multiple DTI studies in that any additional uncertainty introduced by the segmentation strategy used can potentially be eliminated.

Aim 2: Are there detectable changes in DTI biomarkers in the corpus callosum of patients with MCI or early AD, compared to normal ageing? Identifying such changes has scope to enable monitoring and tracking of potential patients from an early stage. While most DTI studies on Alzheimer's disease focus on memory-related impairments, it has been suggested that early manifestations may be observed in other functions, such as motor skills. The results from investigating the corpus callosum and its sub-regions are expected to provide indications of what functions may be affected in MCI, since it is the largest white matter tract connecting several regions of the brain.

Aim 3: Can advanced and more specific methods be applied to clinical DTI images to extract information from the corpus callosum that extends results from a conventional DTI analysis? Although DTI has proved to be an invaluable technique in clinical settings, it is also non-specific, i.e., the variations observed in DTI metrics cannot be associated with a specific underlying mechanism. Several advanced DTI techniques exist, but they cannot be applied to scans taken using typical clinical scan settings without appropriate modifications. Two such advanced methods will be demonstrated for use on clinical DTI scans to investigate their potential to improve the specificity of DTI in clinical settings.

Aim 4: How do the DTI metrics vary in specific pathological scenarios and how are their values dependent on the scan settings used? These are two very important questions investigated in this thesis, aiming to bring specificity and improve accuracy of DTI analysis in clinical practice. Models of healthy white matter tissue as well disease cases (acute/chronic demyelination and neuroinflammation) will be developed and simulated DTI scans acquired to understand how the commonly used DTI metrics vary. The dependence of DTI metrics on a scan-specific parameter called transverse relaxation time (explained in Chapter 2) will be investigated. The results are expected to reveal the impact of transverse relaxation time on the estimation of DTI metrics; this has not yet been demonstrated or adopted as routine practice in the community.

1.6 Organisation of the thesis

The fundamentals of MRI and DTI acquisition are briefly explained in chapter 2. The four main DTI parameters that are extensively used in this thesis - fractional anisotropy (FA), mean diffusivity (MD), radial diffusivity (RD), and axial diffusivity (AxD) - are described, followed by their potential associations with the underlying

biology. The open access database Alzheimer's Disease Neuroimaging Initiative (ADNI) and the breadth of information it carries on healthy controls (HC) and patients with MCI and AD are introduced. The information available from ADNI includes MRI, DTI, and PET imaging data, results of clinical and neurophysiological assessments, as well as genotyping and biospecimen data. Chapter 2 also summarises important findings from prior DTI studies in healthy ageing, MCI, and AD, irrespective of whether images from ADNI were used.

Chapter 3 tackles aim 1 given above (section 1.5). Various factors affecting the estimation of DTI parameters are discussed including scan settings, mathematical methods for tensor estimation, and ROI segmentation strategies. Different software packages available for DTI processing and statistical analysis, that are used in this thesis, are briefly introduced. A protocol for analysis of DTI scans is developed after carrying out comparisons between different segmentation strategies. A feasibility study is carried out in the whole brain white matter using DTI scans from ADNI, aimed at exploring their scope for investigations into alterations in the corpus callosum. Detailed analysis of the corpus callosum is then performed using the developed protocol to study the properties of DTI parameters in MCI and AD compared to HC.

Chapter 4 addresses aims 1 and 2 (section 1.5). Images from ADNI are used to investigate DTI parameters in the whole corpus callosum and its sub-regions, using a scheme that divides it into regions based on the areas of the brain they project to. Changes in DTI parameters in healthy ageing are analysed and compared to changes occurring in MCI. The results of neurophysiological assessments of study participants are collected from ADNI to enable comparison with the results of DTI analysis. This investigation is then extended to a small group of patients with AD.

Chapter 5 tackles aim 3 (section 1.5). Two advanced methods of DTI analysis, NODDI-DTI and tractography, are applied on clinical DTI scans to investigate the scope of extracting information that may extend the results obtained from the conventional DTI analysis described in chapter 4. These methods require the DTI images to be acquired using scan parameters that are not typical in clinical settings. However, modifications have previously been proposed to adapt these methods to clinical DTI scans.

Chapter 6 addresses aim 4 (section 1.5). Models of healthy white matter, acute and chronic demyelination, and neuroinflammation are designed, and simulated DTI scans of these models are acquired. The dependence of FA, MD, RD, and AxD on the underlying physiological factors are investigated with and without accounting for the effects of transverse relaxation time. The results are then used to interpret

the data obtained from studies described in the previous chapters. The thesis is concluded in chapter 7.

Data from both ADNI-2 and ADNI-3 have been used for investigations into ageing, MCI, and AD, depending on availability at the time of conducting the study being described. Scan acquisition parameters of images have been included with the details of each study.

Chapter 2

Diffusion Tensor Imaging

2.1 Fundamentals of MRI physics

MRI has become an integral part of routine clinical practice. In an MRI scan, a single voxel of tissue, represented by a greyscale number, is constructed from the collective signal generated from the protons present in the tissue. This is explained in detail below.

The human body consists of about 70% water molecules that in turn, are made up of hydrogen atoms. Each of these atoms consists of a single positively charged proton that spins on its own axis, creating a tiny magnetic field. These spins are randomly oriented and cancel each other out. But in the presence of an external magnetic field like that of an MRI scanner, these spins or tiny magnets align themselves along the direction of the field and start to precess (Figure 2.1), creating a net magnetisation vector. The frequency of precession is determined by the Larmor equation:

$$F = \frac{\gamma B_0}{2\pi} \tag{2.1}$$

where F is the Larmor precession frequency, γ is the gyromagnetic ratio specific to each nucleus (here, the nuclei being that of hydrogen) and B_0 is the strength of the external field. The net magnetisation vector alone is not sufficient to generate a measurable signal from the tissue being imaged. To achieve this, the precessing spins are excited with a radio frequency (RF) energy pulse of the Larmor frequency. As a result of this excitation, the net magnetisation vector M_z flips 90° from the positive z-axis to the transverse xy plane and rotates around B_0 at Larmor frequency. This rotating magnetic field can now be measured as it induces a current in the receiver coils of the MRI scanner.

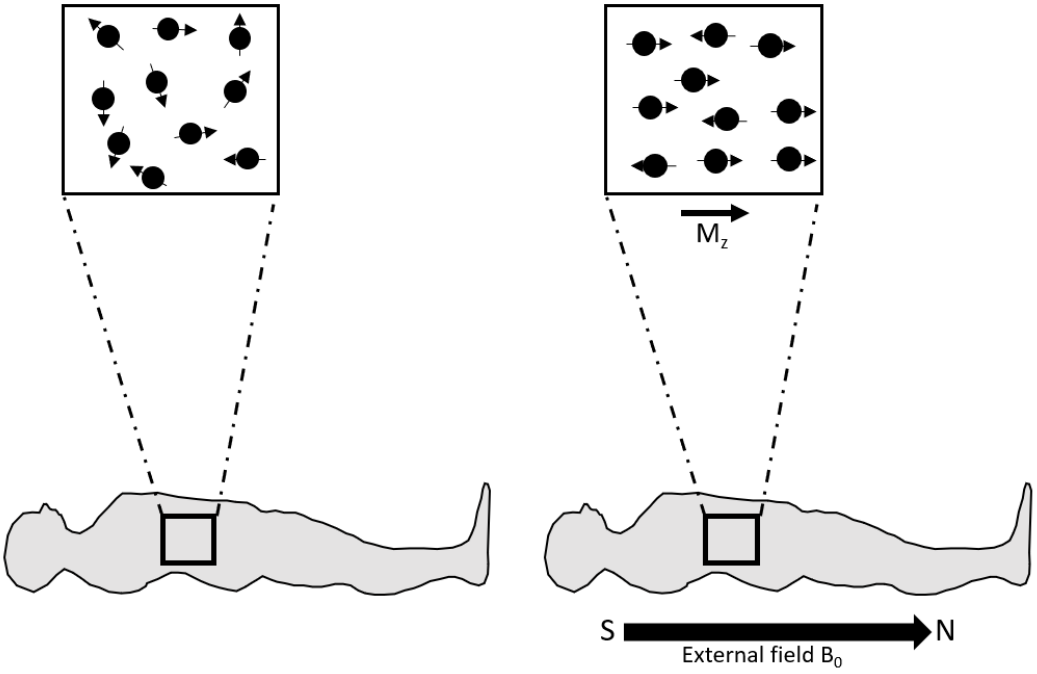

Figure 2.1: In the absence of an external magnetic field, the proton spins are randomly oriented. When an external magnetic field is applied, protons align themselves along its direction; there is a net magnetisation vector M_z parallel to the external field. 'S' and 'N' represent the south and north poles of this magnet respectively.

When the RF pulse is switched off, the protons seek to return to a state of equilibrium or a lower energy state by decay of the net magnetisation over time. This results in a decrease in the strength of the received signal. The process of returning to equilibrium is termed 'relaxation' and the time taken to achieve this is called the 'relaxation time'. There are two types of relaxation - transverse and longitudinal. The process of realignment of spins to the external magnetic field, as they were before the RF pulse was turned on, is called longitudinal relaxation and the corresponding relaxation time is denoted as T_1. It is defined as the time taken for the spins to recover 63% of its equilibrium state. On the other hand, transverse relaxation occurs due to local magnetic field inhomogeneities. Subtle differences are generated in the Larmor frequencies of adjacent spins, resulting in a gradual dephasing of protons. The time taken for this proton dephasing to reduce the signal strength to 37% of its original value is called the transverse relaxation time T_2. T_1 and T_2 may be used in a set of equations to calculate the nuclear magnetisation as a function of time; these are called the Bloch equations [Bloch, 1946].

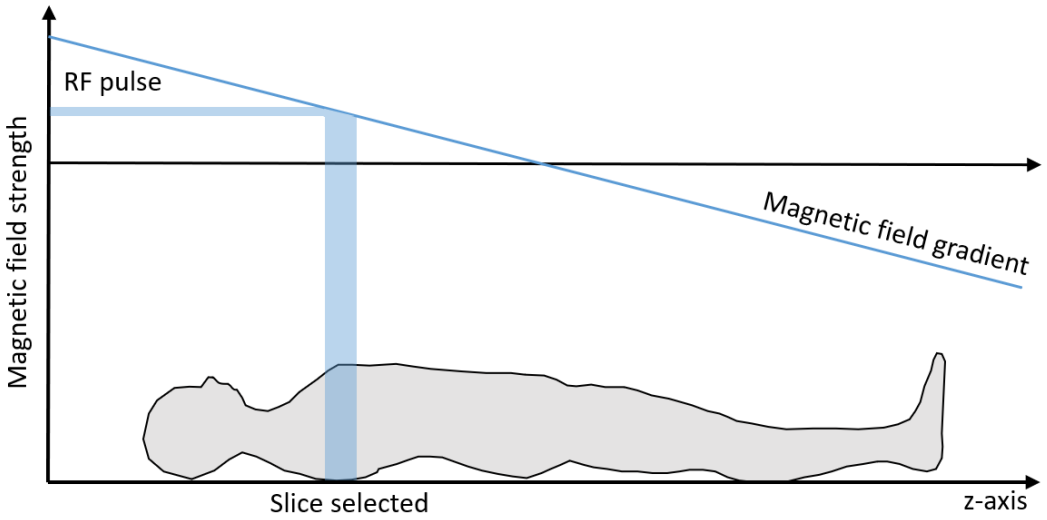

Figure 2.2: Schematic showing slice selection.

A signal is acquired by the MRI scanner in the form of current induced in receiver coils. To reconstruct an image from this signal, it needs to contain information about its point of origin. This is achieved using a technique called slice selection. A small gradient is applied to the main magnetic field (B_0) in order to change the Larmor frequency of protons at different locations by a small amount. Now the RF pulse required to excite the magnetisation vector is different at different locations or 'slices' (Figure 2.2). The pulse frequency is altered to select and image different slices, and the gradient is temporarily applied in the opposite direction to reset the nuclei to their original Larmor frequency before repeating the process to select the next slice.

When a slice is selected, techniques called frequency and phase encoding are used for spatial localisation within the slice. Frequency encoding localises one axis in the xy plane by applying a gradient along the axis in a similar manner as in slice selection. Phase encoding is used to localise the other axis in the slice, by applying a gradient for a short duration and turning it off. This creates a phase shift between protons since they start precessing at different frequencies due to the applied gradient. Data obtained from phase encoding is mapped to the *k-space* frequency domain to preserve location information. Details about these techniques and the k-space are out of scope of this thesis, but may be obtained from several sources including text book chapters [Dietrich, 2007; Brown et al., 2014].

When a gradient is applied to the external magnetic field, it causes spins to precess slower or faster depending on location. Spin frequencies are restored

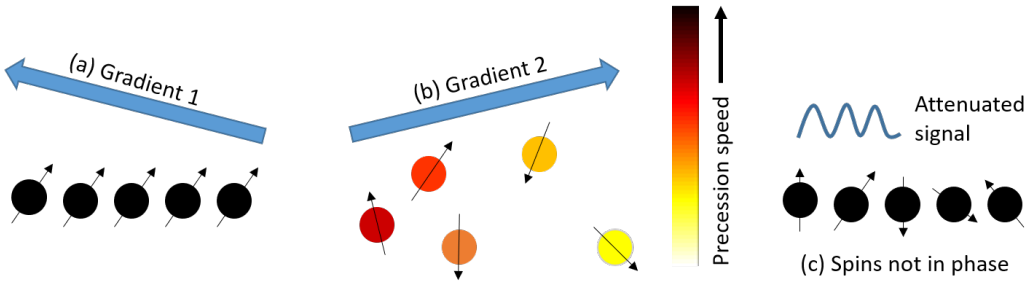

Figure 2.3: (a) A gradient is applied, causing protons to precess faster or slower while also undergoing random diffusion. (b) A gradient of equal magnitude is applied in the opposite direction for the same duration. But the displaced protons do not perceive the gradient strength as equal to that in (a). (c) The spins remain out of phase after turning off the second gradient and the signal is attenuated.

when this gradient is turned off but are now phase-shifted. If a second gradient of equal magnitude is now applied in the opposite direction for the same duration, protons that precessed slower become faster and vice-versa, thus restoring the phase to produce a strong signal. This holds true if the spins are stationary. However, protons (or water molecules) in the human body are constantly diffusing. Because of this displacement, the two gradients applied in opposite directions are received at different magnitudes by a proton. When the second gradient is turned off, protons remain out of phase, and the magnetic resonance (MR) signal is attenuated (Figure 2.3). The attenuation obtained from such a pulse sequence provides information on diffusion of water molecules in the tissue and is the basis for diffusion weighted MRI (DW-MRI).

2.2 History and Mathematical Development of DTI

The development of diffusion nuclear magnetic resonance (NMR) began as early as in 1950, when the effect of diffusion on spin echo signal amplitudes was first recognised [Hahn, 1950]. In a few years, an extended model of Bloch equations was developed to include diffusion terms, thus enabling diffusion NMR [Torrey, 1956]. In 1965, Stejskal and Tanner modified the basic MR spin echo sequence, introducing pulsed diffusion gradients instead of steady state gradients. They observed that the acquired signal was much more sensitive to diffusion when using pulsed gradients and developed the Stejskal-Tanner formula to describe diffusion in terms of signal attenuation [Stejskal and Tanner, 1965]. The simplest case of Gaussian diffusion

may be expressed using this formula as follows:

$$S = S_0 e^{-bD} \tag{2.2}$$

where S is the strength of the signal acquired by applying a pulse sequence with diffusion gradients, S_0 is the signal strength in a pulse sequence with no diffusion sensitisation, and D is the diffusion coefficient of the particles being imaged. The characteristic features of a diffusion weighted pulse sequence have been combined in the following way to obtain a parameter known as the b-value.

$$b = \gamma^2 G^2 \delta^2 (\Delta - \delta/3) \tag{2.3}$$

where G is the strength of the diffusion gradient, δ is the duration of the two diffusion gradients with a delay of Δ between them (Figure 2.4), and γ is the nuclear gyromagnetic ratio. When $\delta << \Delta$, equation 2.3 may be re-written as:

$$b = \gamma^2 G^2 \delta^2 \Delta \tag{2.4}$$

In an MRI or DTI pulse sequence, the duration between the application of two subsequent 90° RF pulses is called the repetition time (TR) and the duration between a 90° RF pulse and subsequent output signal sampling is called the echo time (TE). The 180° RF pulse is usually applied at time TE/2. Depending on the values of T_1, T_2, TE, and TR, different weighting schemes may be generated for an

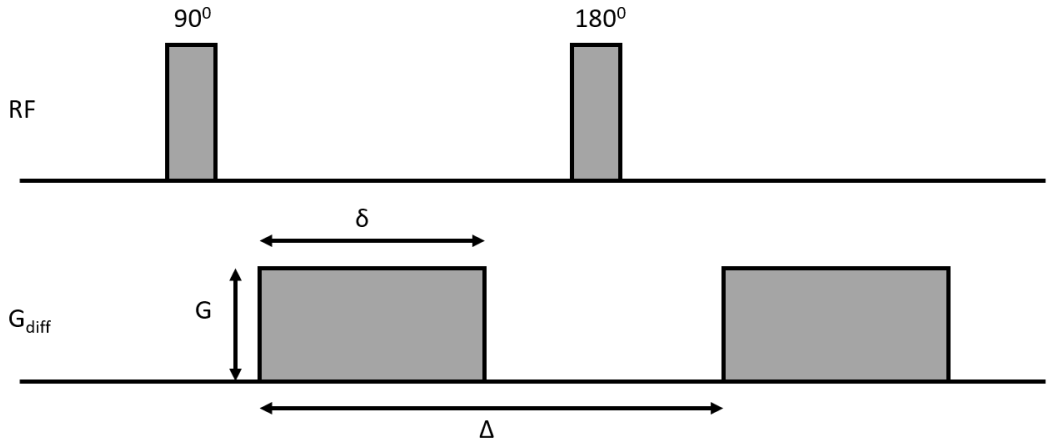

Figure 2.4: A schematic of the Stejskal-Tanner diffusion sensitising pulse sequence. G is the strength of the diffusion gradient, δ is its duration, and Δ is the delay between the two gradients. RF represents radio frequency pulses and G_{diff} represents the axis on which the diffusion sensitisation is carried out.

MR scan sequence. For instance, if TR $\ll T_1$ and TE $\ll T_2$ in a scan a T_1-weighted MRI is acquired, which is an excellent way to visualise anatomy. Keeping TR $\gg T_1$ and TE $\gg T_2$ enables acquisition of a T_2-weighted scan which performs better at identifying pathologies.

By mid-1980s, DW-MRI was conceptualised and developed from diffusion NMR [Le Bihan et al., 1986; Le Bihan and Breton, 1985]. Water diffusion in the body was modelled and the diffusion coefficient estimated using Einstein's equation, assuming Gaussian diffusion:

$$x^2 = 2Dt \tag{2.5}$$

where x is the mean-squared displacement, D is the diffusion coefficient, and t is the time duration. The estimated value D was however, called the 'apparent diffusion coefficient' (ADC) to emphasise its differences from the free diffusion coefficient. The ADC depends on measurement conditions, especially the intensity and time profiles of the gradient pulse. Nevertheless, its development has facilitated several clinical applications of DW-MRI. ADC can be estimated from MR signal using the following equation [Le Bihan et al., 1988]:

$$ADC = \frac{ln\,(S_0/S_1)}{b_1 - b_0} \tag{2.6}$$

where S_0 and S_1 are signal intensities obtained at two b-values, b_0 and b_1.

The development of DTI extended the scope and applications of DW-MRI [Basser et al., 1994a]. While DW-MRI estimated diffusion along a single direction, DTI has enabled three-dimensional measurements. In the presence of directional diffusion, such as that observed in some tissue structures such as the brain white matter, DTI has facilitated full characterisation of diffusion in three dimensions using a mathematical tensor $\mathbf{D}$, whereas DW-MRI provided a partial picture by estimating ADC. A diffusion tensor $\mathbf{D}$ can fully characterise molecular mobility along each of the directions x, y, and z; and correlate mobility in these directions [Le Bihan et al., 2001].

$$\mathbf{D} = \begin{bmatrix} D_{xx} & D_{xy} & D_{xz} \\ D_{yx} & D_{yy} & D_{yz} \\ D_{zx} & D_{zy} & D_{zz} \end{bmatrix} \tag{2.7}$$

The acquired signal (equation 2.2) may be redefined as:

$$S = S_0 e^{-\mathbf{BD}} \tag{2.8}$$

where **B** is the b-matrix, containing the b-values used for imaging along different directions. Since measurements are made in the MRI coordinate system which may not align with the diffusion frame of the tissue being imaged, the above equation is typically expanded as:

$$S = S_0 \exp\left\{-\sum_{i=x,y,z}\sum_{j=x,y,z} b_{ij}D_{ij}\right\} \tag{2.9}$$

where $[x, y, z]$ are coordinates in the MRI scanner coordinate system. In typical clinical scan sequences, the b-value is equal in all directions being imaged. This gives:

$$S = S_0 \exp\left\{-b[D_{xx} + D_{yy} + D_{zz} + 2D_{xy} + 2D_{xz} + 2D_{yz}]\right\} \tag{2.10}$$

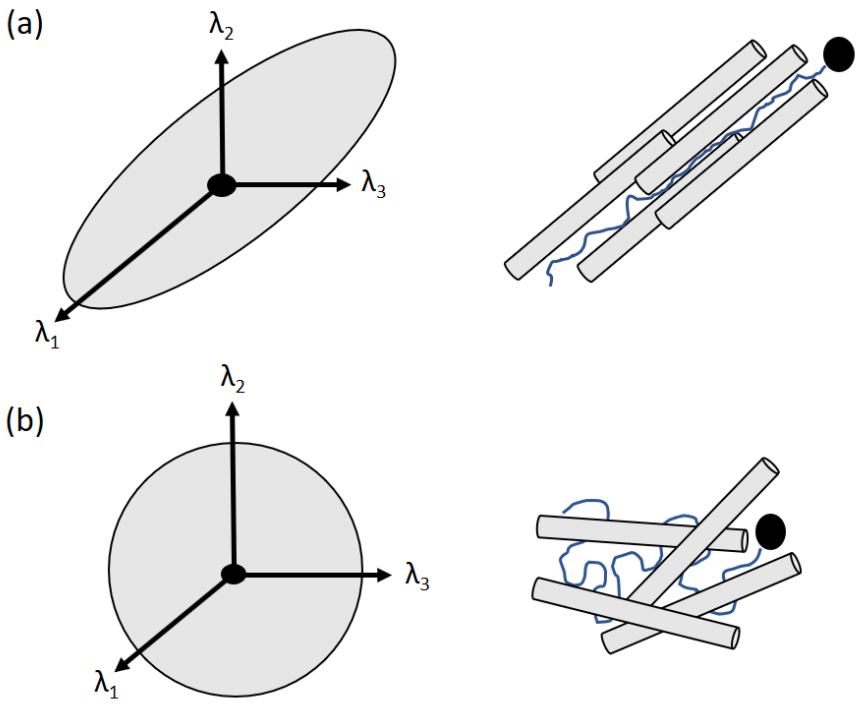

Figure 2.5: A schematic visualisation of diffusion tensor using ellipsoids. (a) shows a case of anisotropic diffusion of a molecule, where the main axis of the ellipsoid indicated by eigen value λ_1 of **D** represents the main direction of diffusion. (b) shows the case of isotropic diffusion, where there is no single dominant direction of diffusion. The figure also shows how water molecules may diffuse in different media, creating trajectories that may then be represented using ellipsoids.

The diffusion tensor **D** is a symmetric matrix. Therefore, a minimum of six images acquired along six diffusion sensitised directions and at least one image acquired without any diffusion weighting are required to estimate **D** by solving equation 2.10. ADC may be expressed in terms of **D** as:

$$ADC = \mathbf{q}^T \mathbf{D} \mathbf{q} \tag{2.11}$$

where,

$$\mathbf{q} = \frac{\gamma \delta G}{2\pi} \tag{2.12}$$

The space of all 3D q-vectors is called the q-space. The acquired signal corresponds to a single q-space point in DW-MRI [Descoteaux, 2008].

Diffusion ellipsoids are often used to visualise **D** [Basser et al., 1994b]. They may be constructed from the eigen values $(\lambda_1, \lambda_2, \lambda_3)$ and eigen vectors of **D** for every voxel in the image. The main axis of the ellipsoid represents the primary direction of diffusion within the voxel and its eccentricity gives a measure of the anisotropy or directionality of diffusion. The length of the ellipsoid in any direction represents the displacement of molecules diffusing in that direction. A schematic of this system of tensor visualisation is shown in Figure 2.5.

Various parameters may be estimated from the eigen values of **D** in order to study the nature of diffusion in the tissue imaged. These parameters have been designed to reveal information about the structure and properties of barriers to the diffusion, thereby indirectly estimating properties of the tissue itself. FA is a commonly used metric used to characterise diffusion anisotropy in the tissue [Basser and Pierpaoli, 1996]. It is a measure of the proportion of diffusion in **D** that can be described as anisotropic. It is calculated as follows [Le Bihan et al., 2001; Basser and Pierpaoli, 1996].

$$FA = \frac{\sqrt{3((\lambda_1 - \lambda)^2 + (\lambda_2 - \lambda)^2 + (\lambda_3 - \lambda)^2)}}{\sqrt{2(\lambda_1^2 + \lambda_2^2 + \lambda_3^2)}} \tag{2.13}$$

where,

$$\lambda = (\lambda_1 + \lambda_2 + \lambda_3)/3 \tag{2.14}$$

The value of FA ranges from 0 to 1, with 0 indicating pure isotropy and 1 indicating pure anisotropy. Other indices such as relative anisotropy (RA), may also be estimated to measure directional diffusion [Basser and Pierpaoli, 1996]. RA is a measure of the ratio of anisotropic part of **D** to its isotropic part, and can vary

between 0 and $\sqrt{2}$, with 0 denoting isotropy and $\sqrt{2}$ denoting infinite anisotropy.

$$RA = \frac{\sqrt{(\lambda_1 - \lambda)^2 + (\lambda_2 - \lambda)^2 + (\lambda_3 - \lambda)^2)}}{\sqrt{3\lambda}} \tag{2.15}$$

Another parameter commonly used in DTI studies is diffusivity. Different types of diffusivity measures have been proposed to represent diffusion in different ways. MD is a measure of the diffusion averaged across all directions. RD is estimated as the diffusion perpendicular to the primary direction, and AxD as the diffusion along it. These parameters may be estimated from the eigen values of $\mathbf{D}$ as follows [Le Bihan et al., 2001].

$$MD = (\lambda_1 + \lambda_2 + \lambda 3)\,/3 \tag{2.16}$$

$$RD = (\lambda_2 + \lambda_3)\,/2 \tag{2.17}$$

$$AxD = \lambda_1 \tag{2.18}$$

2.2.1 Advances: Tractography and Connectomics

The early 21$^{\text{st}}$ century saw major advances to DTI as a response to the need for sophisticated tools to carry out research into the structure and connections in the human brain. Models other than those using the diffusion tensor have been employed to obtain more accurate and specific results, such as cylindrical axon models to estimate axon diameters [Assaf et al., 2008], and multi-compartment diffusion models that enabled association of the MR signal with intra or extra-cellular compartments in the tissue [Jelescu and Budde, 2017].

Tractography is a method developed for DTI images to reconstruct a path of neural connection between two brain regions by starting from one voxel and checking for path continuity in the neighbouring voxels. Continuation of the path in a voxel may be verified using an estimate of the local tract orientation. Tractography algorithms can be classified as either deterministic or probabilistic. Deterministic algorithms typically use the anisotropy estimate from the tensor $\mathbf{D}$ to map connections in the brain. They rely on the hypothesis that the anisotropy calculated in a voxel is representative of the fibre orientation in the voxel. They are generally simple and fast algorithms and label tracked voxels as belonging to a single fibre tract [Alexander et al., 2010].

Probabilistic algorithms generate the probabilities of a tracked voxel belonging

to potential tracts. They provide information about the error in tracking, and thus a measure of confidence in the results. They are typically slower than deterministic algorithms [Parker, 2012]. Path continuity in probabilistic tractography may be verified using orientation distribution functions (ODF) calculated from high angular resolution diffusion imaging (HARDI) data [Tournier et al., 2004]. This has been described in detail in section 2.2.2. Sophisticated techniques have been developed to extract multiple fibre directions in order to accurately estimate fibre orientation in situations such as voxels with crossing fibres [Tournier et al., 2012; Staempfli et al., 2006].

Fibre tracking algorithms are susceptible to inaccuracies in conditions such as low signal to noise ratio (SNR) and low resolution, as well as in cases of tracking near the cortex of the brain [Jeurissen et al., 2019]. Even with these limitations, tractography has proved to be an invaluable tool in neuroscience. For instance, it has been used to develop an atlas of the human brain white matter [Wakana et al., 2004], and comprehensively map neural elements and their interconnections in the brain. The latter has now evolved to be an area of extensive research called connectomics.

2.2.2 Advances: HARDI Imaging

A limitation of DTI is its underlying assumption of Gaussian diffusion that offers a limited number of degrees of freedom for the model. This has been proved to be insufficient to unravel situations such as crossing fibres [Mori and Tournier, 2014]. A higher order model is required to describe a non-Gaussian probability distribution function (PDF) of diffusion. HARDI offers one such model where the true diffusion PDF is reconstructed by sampling the q-space along as many directions and magnitudes as possible [Descoteaux, 2008]. The PDF thus estimated is free of assumptions and can recover the diffusion of water molecules in any scenario including crossing fibres. The HARDI model estimates a 3-dimensional distribution of diffusion as opposed to a scalar metric (ADC) in DW-MRI or a tensor in DTI. However, the image acquisition protocol for HARDI is an extension of DTI, requiring diffusion weighted images in several gradient directions with the same b-value and the directions uniformly spread over a half-sphere [Mori and Tournier, 2014].

Two methods have been proposed to sample the q-space in HARDI [Descoteaux, 2008]. The first is to lay down a grid of points over the q-space and obtain the diffusion PDF by estimating the inverse Fourier transform of the signal at these points. A diffusion ODF is then defined to carry angular information from the diffusion PDF. The second method to sample the q-space is spherical sampling at a

radius r (which is determined by the b-value). This is called single-shell spherical sampling since it involves measuring on a single 'shell' or radius of the q-space. Multi-shell sampling methods have also been developed where measurements are taken at multiple radii.

2.3 Sources of anisotropy in the white matter

Until the development of DTI, microstructural properties of the brain white matter had not been extensively studied *in vivo*. It has now evolved to be an excellent method of investigation of the white matter due to the packed, organised, and oriented structure of fibres. Diffusion has been observed to be mostly isotropic in the grey matter and anisotropic in the white matter, generating a contrast between the two tissue types in an FA image, making it easier to identify the white matter, carry out analyses, and compare properties between two or more subjects.

Extensive investigations have been carried out to determine the sources of diffusion anisotropy in white matter as observed in FA maps. Early studies concluded that the observed anisotropy was a result of diffusion barriers in the white matter presented by myelin sheaths [Thomsen et al., 1987]. Water molecules would preferentially diffuse along the length of the axons and were hindered by myelin if they diffused in a perpendicular direction. This hypothesis, i.e., myelin sheath being the primary source of diffusion anisotropy, remained unproven in the early 1990s, but was still preferred over other theories.

One of the first studies that disproved this hypothesis was an investigation of the normally non-myelinated olfactory nerve of a garfish, which showed anisotropic water diffusion in the absence of myelin [Beaulieu and Allen, 1994a]. This observation has been corroborated by other independent investigations [Seo et al., 1999; Prayer et al., 1997]. However, the presence of myelin was also found to reduce perpendicular diffusivity [Gulani et al., 2001]. It was therefore concluded that myelin was not a requirement for anisotropic diffusion, rather it was a factor that modulated the degree of anisotropy. Myelin and axonal membranes were instead found to be the primary determinant of anisotropy [Beaulieu and Allen, 1994b].

The relationship of DTI with the structure and properties of white matter has enabled its use in investigations of neurological conditions like cerebral infarctions, neurodegenerative diseases like AD, and psychiatric disorders such as schizophrenia. Section 2.4 reviews the results of studies using DTI to investigate the white matter in the context of ageing, MCI, and AD. It summarises how DTI parameters (FA, MD, RD, and AxD) have been interpreted to infer the underlying physiological

mechanisms in white matter. Different patterns of changes in FA, MD, RD, and AxD may imply different processes; five of these have been described by Burzynska et al. in 2010:

1. An increase in both RD and MD may suggest chronic white matter damage. Myelin and axonal membrane degeneration may cause an increase in RD, while cellular debris clearance by microglia may result in a slight increase in longitudinal diffusion and cause an overall increase in MD.

2. An increase in RD accompanied by a reduction in FA may be attributed to loss of myelin.

3. A decrease in FA with no alterations in the other parameters may imply a mixture of subtle differences in RD and AxD. This may likely be due to mild microstructural alterations such as minor fibre loss without gross tissue loss.

4. A decrease in FA and AxD accompanied by an increase in RD and a non-significant difference in MD may be attributed to secondary Wallerian degeneration.

5. A decrease in AxD and MD along with a decrease in FA may suggest acute axonal damage.

Studies in mice have suggested that RD and AxD alterations may be indicators of demyelination and axonal degeneration respectively, although this has been criticised to be a simplistic view of the underlying mechanisms giving rise to anisotropy [Winklewski et al., 2018; Song et al., 2003]. Despite extensive investigations in this area, DTI remains a non-specific technique, i.e., the exact nature of underlying mechanisms causing alterations in DTI parameters is currently not known.

2.4 DTI studies of the white matter

Early applications of DW-MRI in clinical practice were in stroke-related acute brain ischemia [Le Bihan et al., 1992]. The value of ADC was observed to decrease by a significant amount within minutes after an ischemic injury even when conventional MRI appeared normal. The scope of application has been extended with DTI, which offers a means to study white matter structure in healthy ageing and neurological disorders.

2.4.1 Childhood and healthy ageing

Studies investigating brain development in childhood have reported an increase in FA with age and attributed it to myelination of nerve fibres [Lebel et al., 2019; Oyefiade et al., 2018]. The developing myelin sheath was thought to restrict perpendicular diffusion as described in section 2.3. FA has been observed to change with age throughout life. The current consensus is that it increases in childhood, reaches a plateau in mid-life before starting to gradually decline in approximately the fifth decade of life [Sexton et al., 2014]. This trajectory of FA has been attributed to age-related changes in the healthy brain. An increase in FA in early life has been associated with axonal packing or myelination and a decrease in FA in later life with axonal dispersion or demyelination [Geeraert et al., 2019; Branzoli et al., 2016].

Trajectories of diffusivities have also been reported to change with age. An increase in FA has typically been accompanied by a decrease in MD in early life and vice-versa in older life [Lebel et al., 2019; Branzoli et al., 2016]. Both FA and MD have been observed to follow opposite patterns of change with age, i.e. FA increases in childhood and adolescence and decreases in older age, whereas MD decreases in childhood and increases with age. A longitudinal study of 3 years on participants between 20 and 84 years old have reported extensive significant annual decreases in FA and increases in MD, with the rate of annual change also increasing with age [Sexton et al., 2014]. Other diffusivity measures such as RD and AxD have been reported to decrease in childhood and increase in older age similar to the trajectory of MD [Kumar et al., 2012; Burzynska et al., 2010]. Changes in RD and AxD in mice brains have previously been attributed to demyelination and axonal degeneration respectively [Song et al., 2003]. DTI studies in humans have used these findings to attribute changes in RD and AxD to similar processes. However, such an association has been criticised to be a simplistic view of the complex underlying mechanisms [Winklewski et al., 2018].

2.4.1.1 Retrogenesis

One important consequence of DTI studies of the human brain is the emergence of retrogenesis theory. It has stemmed from results of DTI investigations that suggested white matter fibres matured or myelinated at different times and variable rates during brain development. Some were already fully developed by birth or early childhood and others continued to mature through adolescence into early adulthood [Dubois et al., 2014]. Fibres that myelinated earlier in life were thought to be more robust than later-myelinating ones and therefore less susceptible to damage under

ageing and disease-related processes [Stricker et al., 2009]. However, no conclusive evidence has been reported for the retrogenesis theory, with some studies supporting it and a few studies opposing [Brickman et al., 2012; Di Paola et al., 2010; Sexton et al., 2011].

2.4.2 MCI and AD

DTI has been used to study neurodegenerative mechanisms in MCI and AD. It has helped reveal significantly widespread alterations in white matter integrity in AD compared to HC. A decrease in FA has been reported in patients with AD in the temporal, parietal, and frontal lobe regions, cingulum, corpus callosum, fornix, and optic nerves [Nishioka et al., 2015; Agosta et al., 2011; Acosta-Cabronero et al., 2010; Mielke et al., 2009; Zhang et al., 2009, 2007]. Increases in diffusivities have also been observed in the fornix, corpus callosum, cingulum, temporal, parietal, and occipital lobe regions [Hong et al., 2013; Acosta-Cabronero et al., 2012, 2010; Huang and Auchus, 2007]. Similar but less extensive changes in DTI parameters have been reported in MCI in these white matter regions [Gyebnár et al., 2018; Nishioka et al., 2015; Hong et al., 2013; Liu et al., 2013; Agosta et al., 2011].

A meta-analysis of white matter abnormalities reported in MCI and AD has concluded that FA and MD alterations were significant in the fornix, uncinate fasciculus, parahippocampal cingulum, and posterior corona radiata [Yu et al., 2017]. A review of DTI studies in AD has reported similar results and has suggested that changes in AD were dominant in white matter tracts connecting to grey matter structures involved in memory function [Gold et al., 2012]. Very few longitudinal studies have been reported in MCI and AD. In one such investigation, FA has been found to decrease exclusively in the corpus callosum in patients with MCI who later converted to AD [Douaud et al., 2013]. Longitudinal changes have also been reported in the cingulum and the fornix [Nowrangi et al., 2013], uncinate fasciculus, inferior longitudinal fasciculus, and inferior occipitofrontal fasciculus [Kitamura et al., 2013] of patients with MCI and AD. Results of these studies suggest that white matter alterations in MCI and AD differ between individuals, although they may share common features and appear in similar regions.

It has also emerged that FA is the least sensitive DTI measure for picking up group differences. Diffusivity measures have been found to be able to detect more subtle differences than FA in MCI [Yu et al., 2017; Nir et al., 2013]. It has been suggested that brain atrophy may be one of the main reasons of white matter damage observed in disease, although changes independent of atrophy have also been reported in MCI and AD [Amlien and Fjell, 2014; Bosch et al., 2012]. However, DTI

parameters are known for their lack of specificity and a major focus of research in recent years has been to associate physiological processes with parameters measured from DTI.

2.5 Alzheimer's Disease Neuroimaging Initiative

Data and images used in this thesis have been obtained from ADNI, which was launched in 2003 as a public-private partnership, led by principal investigator Michael W. Weiner, MD. The primary goal of ADNI has been to test whether serial MRI, PET, other biological markers, and clinical and neuropsychological assessments can be combined to measure the progression of MCI and early AD.

The first phase of ADNI, called ADNI-1, commenced in October 2004 and collected data from 200 HC, 400 MCI and 200 AD participants. The primary goal of this phase was to develop biomarkers that may be used to measure clinical trial outcomes [Weiner et al., 2013, 2010]. In 2009, ADNI-1 was extended through the ADNI-GO phase, which recruited 200 early MCI participants to the existing cohorts of subjects. This phase focused on investigating biomarkers during early stages of AD and MCI. The second phase of ADNI began in 2011 and was called ADNI-2. In addition to the participants who carried on from ADNI-1/ADNI-GO, 150 HC, 150 AD, 100 early MCI, 150 late MCI and 107 subjects with a self-reported significant memory concern (SMC) were recruited. The primary aim of this phase was to develop biomarkers that could predict cognitive decline [Weiner et al., 2015]. The most recent phase of ADNI, called ADNI-3, began in 2016 to study the use of PET and functional imaging in clinical trials. Existing participants in ADNI-2 were carried on to the new phase, and 371 new participants (133 HC, 151 MCI, and 87 AD) have been recruited till date [Weiner et al., 2017]. An overview of subject demographics has been shown in Figure 2.6, excluding the age groups that contained very few participants (e.g. under two years old). An estimate of the proportion of participants in each group and gender may be made from the figure.

Several types of data have been collected from ADNI participants at baseline and regular follow-ups. They can be categorised into one of the following [Weiner et al., 2017, 2010]:

- Clinical: Information in this category may include subject demographics (e.g. age, gender), medical history, and results of physical and cognitive examinations. Initially collected during the baseline visit, the data has been updated as required after each follow-up visit.

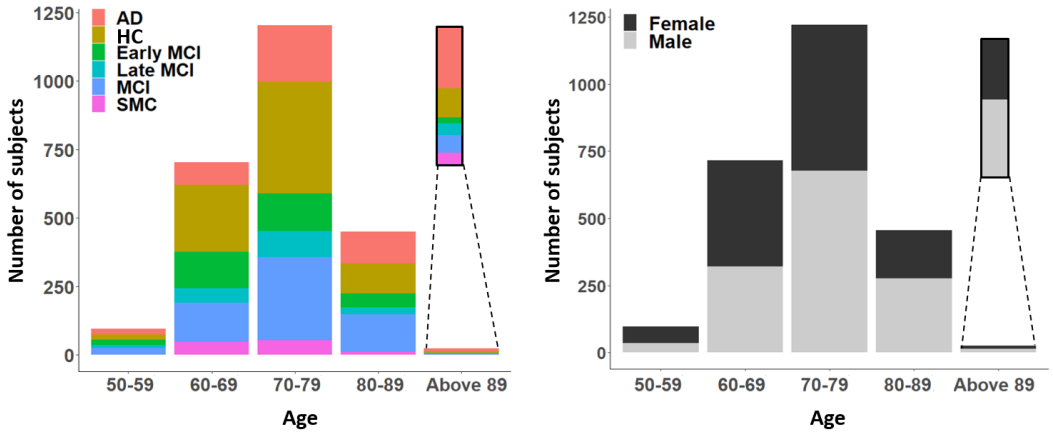

Figure 2.6: A visual summary of subject demographics, plotted with participant summary data obtained from ADNI. Subjects have been shown stratified according to their disease group, as well as gender.

- Genetic: Genotyping and sequencing data have been generated at the time of participant recruitment to capture information on genetic risk factors such as the APOE ε4 allele.
- MRI: Collection of MRI scans during baseline and follow-up visits is critical to the primary goal of ADNI, i.e., development of biomarkers that can predict cognitive outcomes. Different types of MRI scans have been acquired to support different avenues of research, including structural MRI for measurement of atrophy, DTI for investigation of white matter changes, and high-resolution MRI of the hippocampus for measurement of atrophy of its sub-regions.
- PET: Similar to MRI, PET is also critical for biomarker development in ADNI. Both amyloid and tau PET scans have been acquired, with the tau-PET scan scheduled depending on the amount of amyloid detected in the brain. Because of potential harmful effects from ionising radiations, a lower number of PET scans have been acquired for each subject compared to MRI.
- Bio-specimen: This includes blood, urine and CSF collected from participants during recruitment and follow-up visits. The samples have been analysed to extract information on different factors such as homocysteine (an amino acid linked to heart disease), tau levels, and amyloid precursor protein (involved in Aβ generation).

The breadth of multi-modal information collected by ADNI has played a significant role in making advances in the field of AD research [Weiner et al., 2015,

2013]. Pathological mechanisms, including amyloid deposition and brain atrophy, are now known to be present much before symptoms start to appear. Cognitive decline has been associated more closely with the deposition of tau and neurofibrillary tangles than with Aβ. The pathogenesis of AD has been reported to be heterogeneous, with different individuals following different patterns of changes in the brain to progress to AD.

2.6 Conclusions

In this chapter, the fundamental principles of DW-MRI and DTI have been introduced, and different potential sources of anisotropy as observed in the white matter have been discussed. It must be noted that the biological mechanisms giving rise to specific patterns of changes on a DTI scan have not yet been established. It is important to keep this in mind while interpreting the results of a DTI study.

The goals, scope, and extent of data available through ADNI have been introduced and described. Being the first of its kind, ADNI is a large-scale collaborative partnership supported by funding from both the government and pharmaceutical industry. It has played a significant role in advancing biomarker development in AD by making its collection of data to researchers around the world free of charge. Throughout the three phases, the overarching goals of ADNI have remained the same: development of biomarkers to track disease progression, support treatment development, and uphold the open-access data sharing policy.

Chapter 3

Methodological Considerations in DTI Analysis

3.1 Introduction

The results of a DTI study may be influenced by several factors associated with the analysis methodology, ranging from scan acquisition parameters to the algorithm used to fit tensors to image voxels. While a study protocol would be established and followed in an investigation, an inter-centre bias may still exist in multi-centre studies due to reasons such as different scanner manufacturers. This chapter has focused on such factors in the context of ADNI to understand how they might affect measurements. A DTI analysis protocol has been developed based on this to be followed throughout this thesis.

3.2 Scan parameters

The effects of scan acquisition parameters on DTI have been studied extensively. In general, the following factors have been found to impact the results of DTI studies:

1. **Number of gradient directions**: Although a minimum of six directions are theoretically required for DTI (section 2.2), increasing the number of gradient directions has been found to increase the accuracy of tensor estimation [**?**]. However, this has been observed to be true only to a certain extent [Tristán-Vega et al., 2012]. A few studies have reported that at least 20 unique directions are required for a robust estimation of FA, while a minimum of 30 directions are required for robust estimations of tensor orientations and MD [Ni et al., 2006; Jones and Basser, 2004]. The FA of highly anisotropic structures have been

observed to increase and that of low anisotropic structures to decrease, with an increase in the number of gradient directions [Giannelli et al., 2010]. However, a few studies have reported no impact of the number of gradient directions on FA and MD measured in highly anisotropic regions, and suggested that clinical studies using similar protocols but different well-balanced diffusion weighting schemes may be comparable [Lebel et al., 2012b; Landman et al., 2007].

2. **Signal to noise ratio**: SNR of the acquired signal describes the relative contributions of the true signal and random noise. It is often unclear how to define SNR in DTI studies since diffusion weighted and non-diffusion weighted images have different signal and noise characteristics. Given the fact that diffusion is represented by attenuation of the acquired signal (section 2.2), it is easy in suboptimal settings for the signal to drop below noise level. This may lead to an underestimation of measured diffusion through a systematic shift in the eigen vectors of the diffusion tensor, and a subsequent underestimation of anisotropy [Laun et al., 2009]. An important recommendation made by Farrell et al. (2007) is that patients and controls be scanned with equal number of gradient directions to keep SNR profiles similar when investigating group differences. Deviations from the true value in DTI parameters due to reasons such as different number of gradient directions are reportedly prominent at a lower SNR [Landman et al., 2007]. In fact, it has been shown that the effect of SNR plays an important role in determining the robustness of obtained results when other scan parameters are suboptimal [Tijssen et al., 2009]. Efficient receiver coils or signal averaging may help increase the SNR.

3. **b-value**: The diffusion weighting of an MRI scan is determined by the b-value estimated from the pulse sequence (equation 2.3). Simulation studies have reported that an increasing b-value leads to an underestimation of FA due to a co-existing decrease in SNR [Alexander, 2005; Jones, 2004]. Confirming these findings are results of experimental studies where increasing the applied b-value has been associated with decreasing FA and MD [Chung et al., 2013; Hui et al., 2010]. This has been attributed to a non-mono-exponential decay of the diffusion weighted signal with at a higher b-value, caused by complex underlying biological mechanisms [Hui et al., 2010]. However, this effect may vary depending on the type of tissue being probed. At a magnetic field strength of 3 T, a b-value of 1000 s/mm^2 has been reported to be optimal for clinical studies of the white matter [Chung et al., 2013].

4. **TE and TR**: A DTI is fundamentally a T_2-weighted MRI. Therefore, a typical

DTI scan sequence has a very long TE and TR (section 2.1). The effects of TE and TR on DTI measurements have not been thoroughly investigated. Linear correlations of TE with FA, RD, and AxD have been reported, where a decrease in RD and an increase in AxD were observed with increasing TE potentially resulting in an increase in FA and absence of variations in MD [Qin et al., 2009]. It has been postulated that an increase in TE might affect DTI in three possible ways: a decrease in SNR, an increase in the time period over which diffusion is observed, and a significant decay of short-T_2 compartments in the tissue [Qin et al., 2009]. While TE is usually of the order of a few milliseconds, typical values of TR are in seconds. It is likely that relatively small differences in TR may not have any impact on the acquired signal. However, this has not been corroborated by experimental studies.

5. **Resolution**: Another factor that may affect the accuracy of measurement in DTI is spatial resolution. This is closely associated with SNR for a given set of scan sequence parameters. Increasing the spatial resolution may lead to a low SNR and impact the estimation of FA as described above in (2). On the other hand, a smaller resolution or a larger voxel size may result in partial volume effects that also impacts FA measurements. It has been reported that using a non-isotropic voxel resolution may affect the estimation of DTI parameters [Oouchi et al., 2007]. An isotropic resolution of 2 mm has been found to give the best SNR in clinical DTI settings [Jahanshad et al., 2010; Kim et al., 2006].

When using images acquired by a multi-centre study such as ADNI, care must be taken to ensure that the images are quantitatively comparable with each other. A report by Zavaliangos-Petropulu et al. in 2019 has acknowledged that although spatial resolution of images remains consistent across ADNI sites, other factors including the number of gradient directions may vary depending on the scanner to accommodate scanning sessions under 60 minutes. The report showed that images from multiple sites may be used together in studies but after harmonising them across protocols.

Images from multiple ADNI sites have been used in this thesis, if they have been acquired with the same scanner manufacturer and model, as well as the same scan parameters. This is to ensure the elimination of potential confounding factors so that differences observed between cohorts may be attributed to changes in the brain with a degree of confidence.

3.3 Software

Several software packages have been developed in response to the need for tools to process and analyse DTI. Some are generic image analysis tool kits capable of processing MRI and DTI while others are dedicated programs. The processing algorithms used vary from software to software with some performing better than others for specific tasks. This thesis has explored several tool kits and used them as required for the studies described in the following chapters. Details of these software have been given in appendix section A.1.

3.4 Tensor fitting methods

The diffusion tensor **D** can be estimated by solving equation 2.9 to obtain the values of D_{xx}, D_{yy}, D_{zz}, D_{xy}, D_{xz} and D_{yz}:

$$S = S_0\, exp[-b_{xx}D_{xx} - b_{yy}D_{yy} - b_{zz}D_{zz} - 2b_{xy}D_{xy} - 2b_{xz}D_{xz} - 2b_{yz}D_{yz}]$$

As described in section 2.2, a minimum of six gradient directions is required to solve this system of equations containing six unknowns. Standard methods such as Cramer's rule may be used to estimate **D** as described below, assuming a DTI scan with M images, in which N have been acquired with diffusion gradients (b $>$ 0) and $M - N$ without (b = 0).

$$\mathbf{D} = \mathbf{H}^{-1}\mathbf{Y} \tag{3.1}$$

where **H** is the gradient matrix given by

$$\mathbf{H} = \begin{bmatrix} g_{x1}^2 & g_{y1}^2 & g_{z1}^2 & 2g_{x1}g_{y1} & 2g_{x1}g_{z1} & 2g_{y1}g_{z1} \\ g_{x2}^2 & g_{y2}^2 & g_{z2}^2 & 2g_{x2}g_{y2} & 2g_{x2}g_{z2} & 2g_{y2}g_{z2} \\ . & . & . & . & . & . \\ . & . & . & . & . & . \\ . & . & . & . & . & . \\ g_{xN}^2 & g_{yN}^2 & g_{zN}^2 & 2g_{xN}g_{yN} & 2g_{xN}g_{zN} & 2g_{yN}g_{zN} \end{bmatrix} \tag{3.2}$$

where g_i represents the normalised i$^{\text{th}}$ gradient component of the scan sequence and **Y** represents the logarithm of signal intensities, given by

$$\mathbf{Y} = \frac{1}{b}\begin{bmatrix} ln(S_1/S_0) & ln(S_2/S_0) & . & . & . & ln(S_N/S_0) \end{bmatrix}^T \tag{3.3}$$

With six gradient directions, $\mathbf{H}$ is a square matrix with an inverse. When there are more than six gradients, $\mathbf{H}$ is no longer square and does not have an inverse. Instead, a pseudo-inverse $\mathbf{H}^{\psi}$ may be calculated as follows.

$$\mathbf{H}^{\psi} = (\mathbf{H}^T\mathbf{H})^{-1}\mathbf{H}^T \tag{3.4}$$

This method of solving for the diffusion tensor is called linear least squares fitting. All acquired signal intensities (S_i) are treated as if they were equally accurate. In contrast, weighted linear least squares is another method where more weight (or importance) is given to higher values of lnS_i, and lower weight to lower values of lnS_i. This is due to the fact that although the original signal intensities may be equally true, this is not the case for their logarithms - if signal intensities have been acquired with the same variance, the uncertainty in lnS_i is proportional to $1/S_i$. Mathematically, weighted least squared fitting may be carried out using a matrix containing the b-values as follows.

$$\mathbf{D} = (\mathbf{B}^T\Sigma^{-1}\mathbf{B})^{-1}(\mathbf{B}^T\Sigma^{-1})\mathbf{x} \tag{3.5}$$

where $\mathbf{B}$ is the b-value matrix given by

$$\mathbf{B} = \begin{bmatrix} -b_{xx1} & -b_{yy1} & -b_{zz1} & -2b_{xy1} & -2b_{xz1} & -2b_{yz1} & 1 \\ . & . & . & . & . & . & \\ . & . & . & . & . & . & \\ -b_{xxM} & -b_{yyM} & -b_{zzM} & -2b_{xyM} & -2b_{xzM} & -2b_{yzM} & 1 \end{bmatrix} \tag{3.6}$$

and Σ is an M x M diagonal matrix given by the following equation for i ranging from 1 to M.

$$\Sigma^{-1} = diag(S_i^2/\sigma_i^2) \tag{3.7}$$

If each value of S_i^2/σ_i^2 is 1 defining Σ^{-1} to be the identity matrix, the above is equivalent to a non-weighted linear least squares fitting. The matrix $\mathbf{B}^T\Sigma^{-1}\mathbf{B}$ is called the covariance matrix and is useful in computing the propagation of error and optimising DTI parameters.

Another method of diffusion tensor estimation is through the non-linear least squares fitting of the acquired signal. This is commonly used in cases where the noise is high. One of the common methods used for non-linear fitting of data is the Levenberg-Marquardt algorithm. It attempts to reduce the error between

estimated and measured data using two minimisation methods, i.e., the gradient descent and the Gauss-Newton. It is an iterative algorithm with the output of a linear least squared fit typically being the starting point. A detailed description of the Levenberg-Marquardt algorithm is out of scope for this thesis but may be obtained in Moré [1978].

More recently developed methods of tensor estimation include bi-exponential fitting [Maier et al., 2004] and the robust estimation of tensors by outlier rejection (RESTORE) [Chang et al., 2012]. Bi-exponential models provide a more accurate estimation of **D** by assuming a non-mono-exponential relationship between the MR signal and the b-value. However, this method requires the DTI to be acquired at multiple b-values. On the other hand, RESTORE iteratively carries out a weighted least squares fit of the data, identifies potential outliers in each step, and exclude them in the next iteration.

3.4.1 Comparison of linear (weighted and non-weighted) and non-linear tensor estimation

In this section, linear least squares (both weighted and non-weighted) as well as non-linear fitting methods have been compared to evaluate their performance on ADNI images. Advanced methods have not been tested due to their input requirements (e.g. multiple b-values) that have not been satisfied by ADNI. DTI scans of 10 HC and 10 AD participants (5 females and 5 males each, aged 70-75 years old) from ADNI-2, acquired with the same set of scan parameters (field strength = 3 T, TE = 56 ms, TR = 7200 ms, voxel size = 1.3 mm x 1.3 mm x 2.7 mm, number of gradient directions = 55), were selected for this study. The following steps were carried out.

1. For each image, eddy current artefacts were eliminated and the brain was extracted using FSL commands '*eddy_correct*' and '*bet*' respectively.

2. Diffusion tensors were estimated in Camino. Linear least squares models (both weighted and non-weighted) and a non-linear model using the Levenberg-Marquardt algorithm were employed to obtain three different estimates of the tensor **D** for each image. In weighted linear fitting, the standard deviation of each log-transformed DW-MRI intensity (σ_{ln}) has been approximated as σ/S_m where S_m is the non-log-transformed DW-MRI intensity and σ is its standard deviation. Each observation has then been weighted by the corresponding σ_{ln}. Non-linear fitting has been implemented with the imposition of a positive-definiteness constraint on **D**.

3. For each estimate of **D**, a metric describing the quality of fit called pixel chi-squared (χ_p^2) was calculated for every slice in the volume, averaged for the gradient directions as described below.

Estimation of pixel chi-squared

A 'goodness of fit' metric is required to quantitatively assess how well the estimated tensor can reconstruct the acquired image. The traditional metric chi-squared (χ^2) has been adapted specifically for DTI as pixel chi-squared (χ_p^2) [Papadakis et al., 2003]. It is given by:

$$\chi_p^2 = \sum_{j=1}^{J} \frac{(S_{m,j} - S_{f,j})^2}{\sum_{j=1}^{J} S_{m,j}^2} \tag{3.8}$$

where $j = 1...J$ is the gradient direction, $S_{m,j}$ and $S_{f,j}$ are the acquired DW-MRI signal and the signal reconstructed using the tensor respectively, in the j^{th} direction. The errors in fitting have been normalised using $S_{m,j}$. Data with high noise or poor fit are mapped to higher values of χ_p^2 with the noise region centred around $\chi_p^2 = 0.2$, while data with a good fit of the tensor are mapped to smaller values of χ_p^2.

A MATLAB code to estimate χ_p^2 was generated and has been given in appendix section A.2. For each image, the three steps previously explained were carried out to estimate non-weighted and weighted linear, and non-linear fits of the

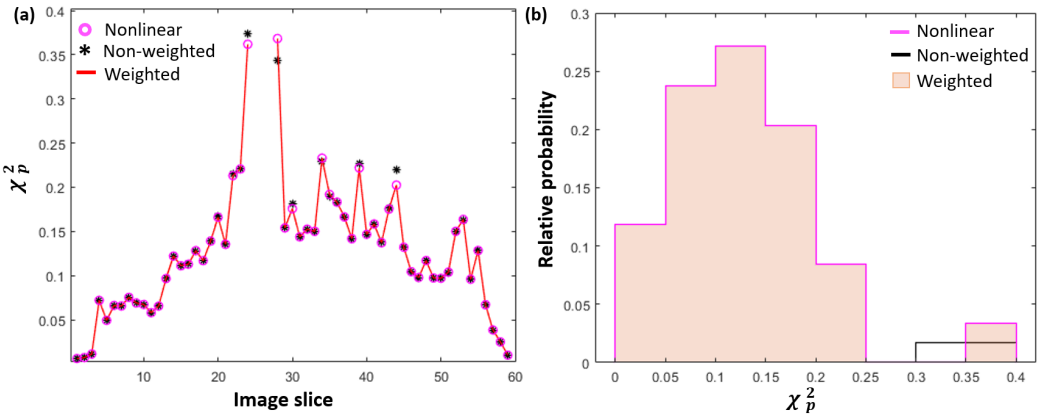

Figure 3.1: (a) χ_p^2 plotted for each slice in an ADNI-2 image (b) Histogram of χ_p^2 with lower values indicating a good fit of the data, and values equal to and greater than 0.2 indicating noise. The three fitting methods have been represented in different ways for better visualisation in overlapping regions. The non-weighted and weighted linear fits have similar histograms in (b), with the non-weighted fit not visualised due to the overlap.

tensor in Camino. The χ_p^2 maps of the three fits were qualitatively compared to evaluate their performance on ADNI images. An example of a χ_p^2 map for a DW-MRI image from ADNI-2 has been given in Figure 3.1. It may be noted that both the weighted linear fit and the non-linear fit showed similar performance on the images, while the non-weighted linear fit gave a slightly greater χ_p^2. A few studies have reported superior performance of the weighted least squares fit of diffusion tensors compared to non-linear and non-weighted linear fits [Veraart et al., 2013; Salvador et al., 2005]. Therefore, throughout this thesis, weighted linear least squares fitting has been implemented to estimate the diffusion tensor. Performance of the three methods may vary on images acquired with different scan parameters.

Since FSL does not offer a non-linear estimation of the diffusion tensor, this study has used Camino to compare different fitting methods. However, it must be noted that Camino and FSL have implemented different algorithms for weighted fitting. A lack of consensus has been reported in the community on the best available algorithm for weighted linear least squares estimation of the tensor [Veraart et al., 2013]. The algorithm as implemented in FSL has been used throughout this thesis, chosen over Camino for its simpler user-interface, which may contribute to the portability of the analysis protocol described in the next section.

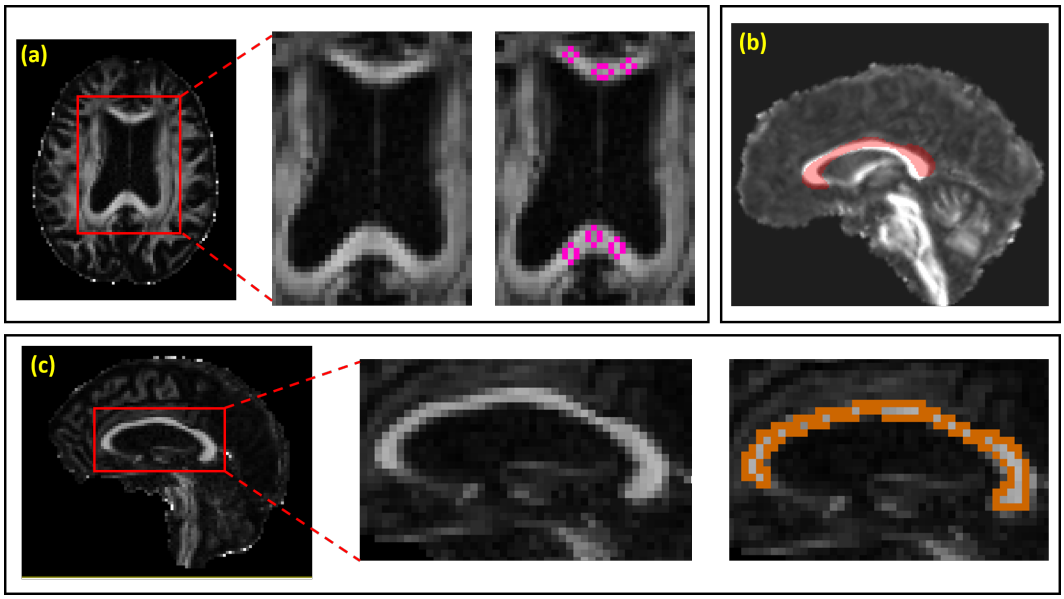

Figure 3.2: (a) Manual sampling of FA values in the corpus callosum in the axial plane using circles placed as ROI. Measurements taken from this ROI have been considered as the ground truth for comparison (b) Atlas-based ROI of the corpus callosum (c) Manual segmentation of corpus callosum in the FA image in the sagittal plane.

3.5 Comparison between segmentation methods

Segmentation of an ROI on a DTI scan may be performed using automated, semi-automated or manual methods. A comparison study was carried out between three different segmentation strategies to investigate their performance and impact on results. The corpus callosum has been chosen as the ROI for this study since it is the largest white matter tract in the human brain, can be easily identified on an FA image, and has been studied in detail in subsequent chapters in the context of ageing and diseases. Several DTI investigations of the corpus callosum have employed automated segmentation of the ROI [Bennett et al., 2017; Ma et al., 2009]. A few studies have also investigated the corpus callosum by sub-regions often using automated methods including tractography [Feng et al., 2018; Lebel et al., 2010; Ota et al., 2006]. With several methods available to analyse and interpret DTI parameters in the corpus callosum, it is important to establish a protocol to be consistently followed. To this end, a cohort of 10 healthy adults aged between 55 and 95 years was selected from ADNI-3, with their DTI scans acquired using the same parameters: field strength = 3 T, number of gradient directions = 54, voxel size = 2 mm x 2 mm x 2 mm, TE = 56 ms, TR = 7200 ms.

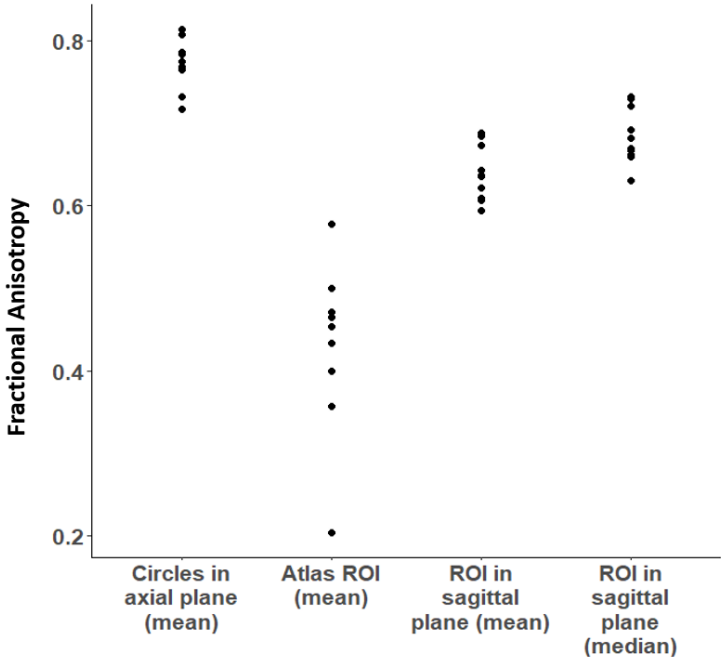

Figure 3.3: Plot showing measured values of FA in the cohort with 10 randomly selected healthy subjects when different segmentation schemes are used.

Since ADNI-3 scans have been acquired in the axial plane, ideally the definition of the corpus callosum ROI would likewise have been performed in the axial plane. However, segmenting the whole structure in the axial plane would likely lead to an inaccurate ROI due to the lack of visible boundaries. Therefore, circular ROI of varying radii were placed in the corpus callosum to sample mean FA values, which were then considered to be the ground truth (Figure 3.2a) [Bartzokis et al., 2010; Li et al., 2009]. The mean FA measured in the circular ROI were used to estimate a final average representing the corpus callosum, which has been plotted in Figure 3.3 ('Circles in axial plane (mean)').

An ROI of the corpus callosum was defined in FSL using the ICBM-DTI-81 atlas [Mori et al., 2008]. Labelled regions corresponding to different parts of the corpus callosum were used to threshold the atlas and obtain a binary mask. Subject images were registered to the Montreal Neurological Institute (MNI) coordinate system and the mean value of FA in the corpus callosum was measured using the mask for each subject. However, it was noted that the mask did not always accurately define the ROI, often including regions outside the corpus callosum such as the ventricles (Figure 3.2b). This resulted in a drastic reduction in the estimated mean FA values which have been plotted in Figure 3.3 ('Atlas ROI (mean)'). The possibility of ICBM-DTI-81 being inaccurate has been addressed by Rohlfing in 2013.

A manual segmentation strategy was tested in ROIEditor as follows. The FA image originally estimated in the axial plane was reconstructed in the sagittal plane. The mid-sagittal slice of the brain was estimated using the method reported by Freitas et al. in 2011 which has been described in appendix section A.3. The corpus callosum was then segmented on the mid-sagittal slice as well as two slices each on either side of it. The manual segmentation method thus yielded a volume of five sagittal slices defining the corpus callosum. A slice from this volume has been shown in Figure 3.2c. Mean and median of FA values in this ROI were estimated and plotted in Figure 3.3 ('ROI in sagittal plane (mean)' and 'ROI in sagittal plane (median)' respectively).

Median values of FA in the ROI generated in the sagittal plane were found to be the closest to ground truth. An approximately consistent offset of 0.1 was observed between the ground truth and the medians, suggesting that measurements in these cases would follow similar distributions. The manually segmented sagittal ROI may also used to obtain the median of MD, RD, and AxD values in the corresponding parameter maps.

3.6 Segmentation and analysis protocol for the corpus callosum

Using the results described in the previous sections, the segmentation and DTI parameter estimation protocols developed for the corpus callosum in ADNI images may be summarised in the following steps:

1. For the axially acquired DW-MRI in ADNI, generate the FA map in FSL using a weighted fit of the diffusion tensor and reconstruct it in the sagittal plane using ImageJ.

2. Estimate the mid-sagittal slice of the FA map in MATLAB using the method described in appendix section A.3.

3. Manually segment the corpus callosum on the mid-sagittal slice and two slices to either side of it in ROIEditor to obtain a segmented volume of five slices.

4. Measure pixel-wise FA in the ROI in ROIEditor and estimate their median value (carried out in MATLAB for this thesis).

5. Save the estimated median as the FA of the corpus callosum for the subject analysed.

6. Repeat steps 4 and 5 on MD, RD, and AxD maps using the same ROI to obtain median MD, RD, and AxD in the corpus callosum.

In subsequent chapters of this thesis, the corpus callosum has also been studied by sub-region. Several different schemes of sub-division have been proposed, one of

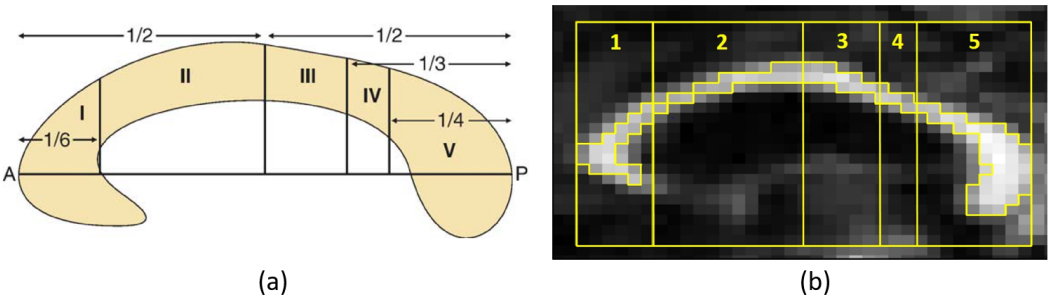

Figure 3.4: (a) Diagram showing the Hofer and Frahm scheme of sub-division. 'A' denotes the anterior and 'P' denotes the posterior ends of the corpus callosum. The anterior-posterior length has been divided into sub-regions as shown. Picture has been adapted with permission from Hofer and Frahm [2006] (b) Sub-division using the Hofer and Frahm scheme carried out in ImageJ.

the most widely used being the Witelson scheme which has been used as a reference in numerous studies [Tanaka-Arakawa et al., 2015; Witelson, 1989]. However, this scheme is based on the anterior-posterior extent of the corpus callosum and data obtained from primates. Another method of sub-division, called the Hofer and Frahm scheme [Hofer and Frahm, 2006], is based on the results of tractography analysis of human DW-MRI. Five sub-regions have been defined in the corpus callosum in this scheme, with fibres projecting to (i) prefrontal, (ii) premotor and supplementary motor, (iii) primary motor, (iv) sensory, and (v) parietal, temporal and occipital regions of the brain. This manner of subdivision enables investigation of changes occurring in a corpus callosum region in relation to the corresponding part of the brain it projects to. A diagram of Hofer and Frahm sub-division scheme is given in Figure 3.4a.

Manual segmentation protocol for the corpus callosum may be modified by adding the following steps to divide it into sub-regions using the Hofer and Frahm scheme (Figure 3.4b):

1. Carry out steps 1 - 3 from the original protocol to manually segment 5 sagittal slices containing the corpus callosum on the FA image.

2. Use the rectangle drawing tool in ImageJ to create a bounding box extending from the anterior end to the posterior end of the corpus callosum. Knowing the width of the rectangle, create smaller rectangles of sizes $1/6^{th}$, 1/2, $1/3^{rd}$ and $1/4^{th}$ of the width and place them as shown in Figure 3.4 to visualise the sub-divisions.

3. Manually segment the corpus callosum in each of these sub-divisions to create five ROI volumes for the five sub-regions.

4. Carry out steps 4 - 6 from the protocol described previously to estimate median FA, MD, RD and AxD in each of the sub-regions.

3.7 Feasibility study

A feasibility study was conducted with images from ADNI-2 to explore their scope and suitability for investigations of the corpus callosum carried out in this thesis. This study did not use the protocol developed in the previous section, rather it was carried out using TBSS to obtain initial data on group differences in HC, MCI, and AD.

3.7.1 Power analysis

An *a priori* estimation of sample size was made using power analysis in G*Power before carrying out the feasibility study [Faul et al., 2009]. This provided the number of study subjects required to reveal significant differences in DTI parameters between HC, MCI, and AD cohorts. A mean effect size was estimated by averaging the effect sizes of FA in different white matter regions as reported in a meta-analysis study [Sexton et al., 2011], which was 0.605 for AD versus HC and 0.503 for MCI versus HC. A liberal statistical power of 0.8 and a significance level of 0.05 were set. Sample sizes were assumed to be equal between groups. Details of the analysis have been given in appendix section A.4. A sample size of 35 each for HC and AD groups and 50 each for HC and MCI groups were estimated using the above parameters for a one-tailed two-sample test for differences between two independent means.

Given that the aim of this feasibility study was to detect group differences in the corpus callosum of ADNI subjects as a starting point for detailed ROI analysis, the sample sizes were kept small at 10 subjects in each group. The sample size estimated using power analysis has been considered in later studies described in this thesis.

3.7.2 Analysis using TBSS

DTI scan acquisition details of ADNI-2 participants included in the study have been given in Table 3.1. 10 age- and gender-matched subjects (5 males and 5 females) between 65 and 80 years old were included in each group (HC, MCI, and AD). TBSS was used to study cohort differences in white matter tracts by carrying out voxel-wise statistical analysis of DTI parameters between two groups at a time. All the necessary steps including pre-processing have been carried out in FSL as described below.

Table 3.1: Scan acquisition details of ADNI-2 images used in the feasibility study.

Image size	256 x 256 x 59	Voxel size	1.3 mm x 1.3 mm x 2.7 mm
Field strength	3 T	Flip angle	90°
Number of gradients	41	Number of non-diffusion-weighted images	7
Scanner manufacturer/model	GE/ Signa HDxt	Pulse sequence	EP/ SE
Echo time	68.3 ms	Repetition time	12500 ms

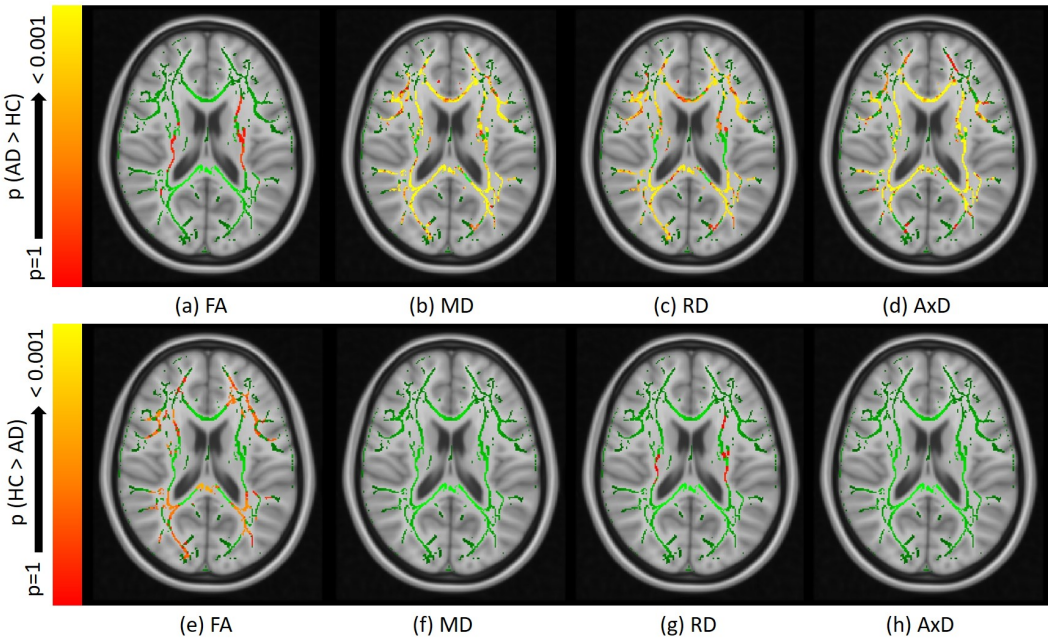

Figure 3.5: Results of TBSS analysis between AD and HC groups. First row represents p-value images testing for whether (a) FA, (b) MD, (c) RD, and (d) AxD of patients with AD were greater than that in HC. The second row represents p-value images testing for whether (e) FA, (f) MD, (g) RD, and (h) AxD of HC were greater than that in patients with AD. The p-values have been represented using a colour map with the colour scale as shown on the left and voxels in yellow showing significant differences between the groups.

Raw DW-MRI were corrected for eddy current artefacts using the *eddy_correct* tool. The skull region was removed and the brain extracted from this image using the *bet* command. FA, MD, RD, and AxD maps were generated by weighted fitting of the tensor using the *dtifit* tool. They were then registered to a 1 mm x 1 mm x 1 mm standard space using *flirt*. A mean FA image was then estimated and a mean FA skeleton generated from this, to represent the centres of all tracts common to the groups being studied. Each subject's FA data was projected onto this skeleton and voxel-wise cross-subject statistics was carried out. The FSL codes written to implement these processes have been given in the appendix as Figure A.8.

3.7.2.1 Group differences between AD and HC

The results of TBSS analysis between AD and HC have been shown in Figure 3.5. Differences were observed in FA between the two groups, though these were not statistically significant. This may be due to the low sensitivity of FA to detect

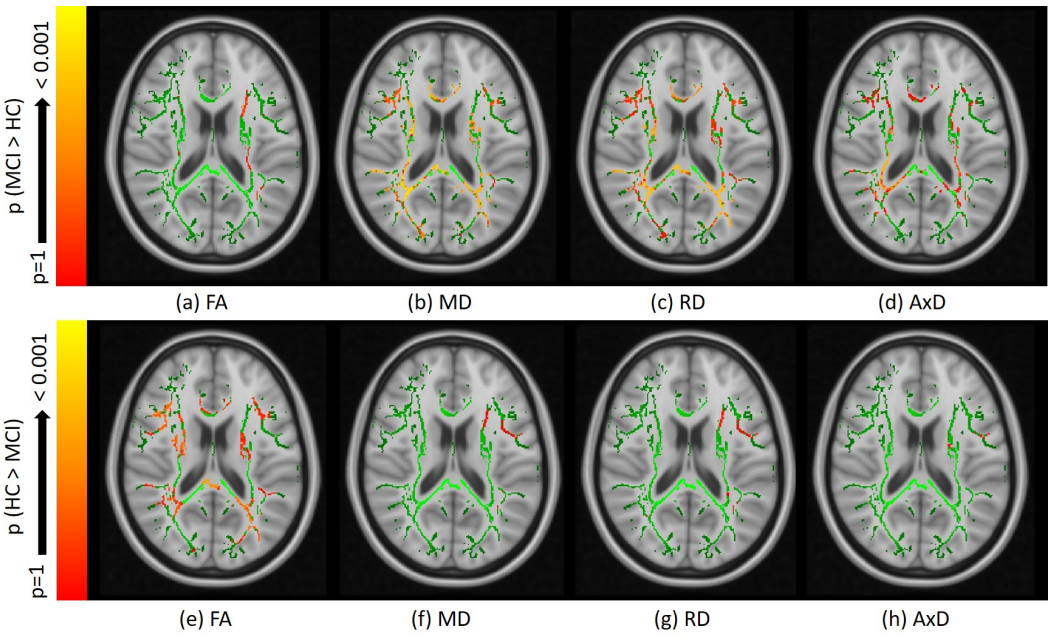

Figure 3.6: Results of TBSS between MCI and HC carried out in the feasibility study. First row represents p-value images testing for whether (a) FA, (b) MD, (c) RD, and (d) AxD of patients with MCI were greater than that in HC. The second row represents p-value images testing for whether (e) FA, (f) MD, (g) RD, and (h) AxD of HC were greater than that in patients with MCI. The p-values have been represented using a colour map with the colour scale as shown on the left and voxels in yellow showing significant differences between the groups.

changes as previously reported (section 2.4) or the sample size being insufficient to detect differences or a combination of both. Widespread significant ($p < 0.05$) increases in MD were observed in patients with AD including in the genu, splenium, and body of the corpus callosum, cingulum, superior longitudinal fasciculus, internal capsule, posterior thalamic radiation, and the posterior corona radiata. These regions have been identified on DTI parameter maps using the ICBM-DTI-81 white matter labels provided with FSL, with the possibility of errors, as discussed previously, kept in mind [Mori et al., 2008]. Significant differences were observed for RD and AxD ($p < 0.05$) in the corpus callosum, internal capsule, posterior thalamic radiation, and the superior longitudinal fasciculus. Changes observed in the white matter for patients with AD in this feasibility study (increases in MD, RD, and AxD with no significant differences in FA) have not been identified as a pattern by Burzynska et al. (section 2.3). However, several published studies, described in section 2.4, have reported similar observations.

3.7.2.2 Group Differences between MCI and HC

The results of TBSS analysis between MCI and HC have been shown in Figure 3.6. Widespread differences were observed in FA, MD, RD, and AxD between MCI and HC including in the corpus callosum, cingulum, superior longitudinal fasciculus, internal capsule, posterior thalamic radiation and the posterior corona radiata. However, not all differences were found to be statistically significant. Similar to the results in patients with AD, FA decreased in MCI compared to HC while MD, RD and AxD increased, although not to the level of statistical significance. This may be attributed to subjects with MCI being very early in their disease stage to exhibit significant white matter changes. A larger sample size may be required to detect changes in MCI accurately and reliably.

3.7.3 DTI analysis of the corpus callosum

The feasibility study described above has demonstrated the suitability of ADNI images to detect changes in DTI parameters in the corpus callosum of 30 participants belonging to HC, MCI, and AD groups. A detailed analysis of the corpus callosum was carried out using the protocol developed in section 3.6 with the same subject images. Each of these images were processed as follows:

1. Eddy current artefacts were eliminated using the '*eddy_correct*' command of FSL; brain was extracted using '*bet*' and DTI parameter maps (FA, MD, RD, and AxD) were estimated using '*dtifit*'.

2. The estimated FA map was used to manually segment the corpus callosum in the sagittal plane (as shown in Figure 3.2c). The median of pixel-wise FA in the ROI was estimated in MATLAB.

3. Similar to step 2, the median of pixel values of MD, RD, and AxD in the corpus callosum were also estimated using the same ROI.

The MATLAB code used to estimate the medians has been given in appendix section A.6. Once the median FA, MD, RD, and AxD were calculated, statistical analysis was carried out in R. Box plots were used to visualise the distribution of data (Figure 3.7) and independent samples t-tests were used to check if they significantly differed between cohorts. A statistically significant difference was observed between HC and AD groups for FA, MD, and RD ($p < 0.05$), but not for AxD. However, such a difference was not observed between HC and MCI or between AD and MCI. The details of the three pair-wise t-tests have been given in Tables 3.2 and 3.3.

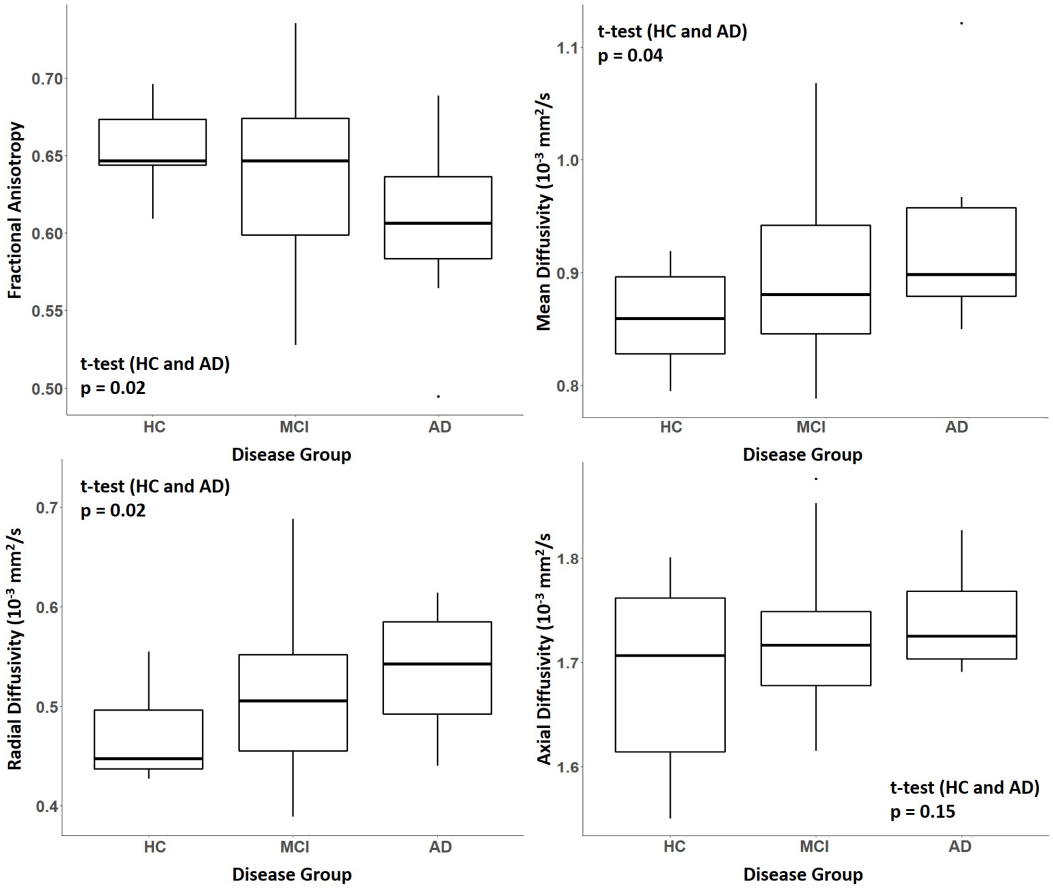

Figure 3.7: Box plots showing the distribution of FA, MD, RD, and AxD in HC, MCI and AD groups. The estimated median values of the four parameters have been used to plot these figures. The p-values of t-tests between AD and HC have been shown on corresponding plots which were considered significant if less than 0.05. The p-values of t-tests between AD and MCI, and between HC and MCI did not reach a level of statistical significance, but have been given in Table 3.3.

The number of pixels segmented as ROI for each image was extracted using the tools available in ROIEditor. The volume of ROI for each image was then computed in mm^3 using the pixel dimensions given in Table 3.1. The total brain volume was also estimated in mm^3 by extracting the number of pixels in the brain mask image computed by FSL. The normalised volume of the corpus callosum ROI was then calculated using equation 3.9 and has been plotted for each cohort in Figure 3.8.

$$\text{Normalised volume} = \frac{\text{Volume of ROI}}{\text{Total brain volume}} \tag{3.9}$$

Although differences in cohort ROI volumes were observed from Figure 3.8, they did

Table 3.2: Average values of the median DTI parameters in the study cohorts. Independent sample t-tests were conducted to test for significant differences in these values and results have been given in Table 3.3.

Parameter	Healthy Controls	Mild Cognitive Impairment	Alzheimer's Disease
Fractional Anisotropy	0.652	0.636	0.603
Mean Diffusivity (10^{-3} mm^2/s)	0.859	0.896	0.925
Radial Diffusivity (10^{-3} mm^2/s)	0.471	0.511	0.552
Axial Diffusivity (10^{-3} mm^2/s)	1.69	1.729	1.738
ROI Volume (mm^3)	2992.9	3061.4	3327.9
Total Brain Volume (mm^3)	1770487	2097965	1949474
Normalised Volume	0.169	0.152	0.173

Table 3.3: Results (p-values) of t-tests conducted between HC, MCI, and AD groups. A difference between groups was considered significant if $p < 0.05$.

Pair-wise t-test	Fractional Anisotropy	Mean Diffusivity	Radial Diffusivity	Axial Diffusivity	Normalised Volume
HC - AD	0.02	0.04	0.02	0.15	0.68
HC - MCI	0.45	0.23	0.22	0.31	0.13
AD - MCI	0.22	0.42	0.32	0.78	0.09

not reach the level of statistical significance between any of the groups (Table 3.3). Estimating volumes using anatomical T_1-weighted MRI is usually preferred [Cho et al., 2018; Westlye et al., 2010] but this has also been carried out using DW-MRI in a few studies [Rotarska-Jagiela et al., 2008; Alexander et al., 2007]. The corpus callosum volume of patients with MCI was found to be slightly lower than that of both HC and AD (Figure 3.8). This may be attributed to the pathological processes in MCI and AD such as neuroinflammation and atrophy, or relatively simpler reasons such as a low sample size. Analysis using larger cohort sizes as well as T_1-weighted MRI of corresponding subjects are required to confirm the validity of these findings.

3.8 Conclusions

This chapter has discussed several factors affecting the results of DTI studies and developed a protocol to be consistently followed across investigations. The latter has been carried out in the context of the corpus callosum. While this protocol may

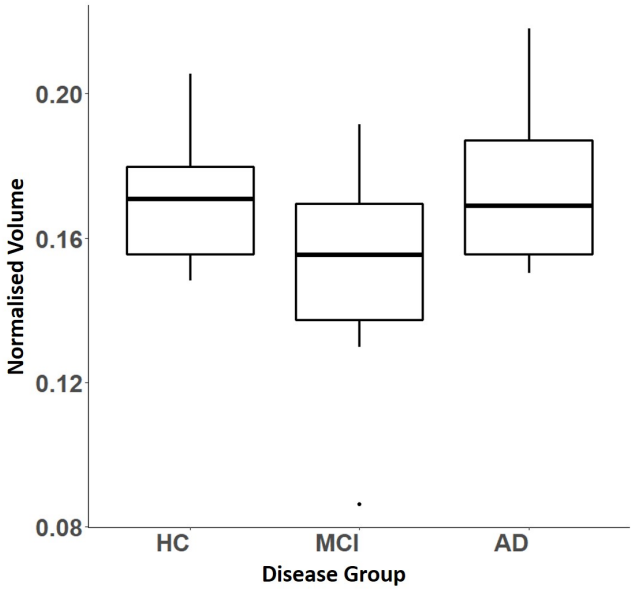

Figure 3.8: Box plots showing the volumes of segmented corpus callosum ROI for HC, MCI, and AD groups

be extended to other white matter tracts in the brain, manual segmentation may be a more demanding method for these structures. For instance, boundaries of the tracts may not be sufficiently visible or the structure itself may be too small to be accurately identified on the image. In such cases, TBSS or atlas-based ROI may provide initial information on group-wise differences. If an atlas-based ROI is used, it is good practice to overlay it on top of the image for visual verification.

DTI scans from ADNI-2 have been explored in a feasibility study using TBSS. Statistically significant group differences were revealed between patients with AD and HC in different white matter regions. A decrease in FA accompanied by increases in MD, RD, and AxD has not been attributed to any specific pathological process, although this is a pattern observed by many studies including the feasibility study described in this chapter. More detailed analysis of the observed group differences have been investigated using the developed protocol in the corpus callosum of HC, MCI, and AD cohorts. Results indicated a significant decrease in FA and a significant increase in MD and RD for patients with AD compared to HC. Although box plots indicated similar differences between HC and MCI groups, they did not reach the level of statistical significance. The developed segmentation and analysis protocol was thus demonstrated through a DTI analysis of HC, MCI, and AD subjects. The measured parameters have been given in appendix B.

Chapter 4

Corpus callosum in mild cognitive impairment and Alzheimer's disease

4.1 Introduction

The segmentation and analysis protocol described in section 3.6 has been applied in a feasibility study in section 3.7.3, and the results revealed differences in DTI parameters in the corpus callosum between HC and AD cohorts. In this chapter, a detailed analysis of the corpus callosum has been carried out to investigate alterations in DTI parameters occurring in MCI and AD. The first set of images from the third phase of ADNI (called ADNI-3) had just been released before this study commenced. DTI scans in ADNI-3 have been acquired with an isotropic resolution of 2 mm which has been suggested to give a good SNR on clinical scanners (section 3.2). Therefore, although the analysis in section 3.7 has been conducted with data from ADNI-2, this study has utilised DTI scans from ADNI-3.

4.2 Imaging studies of the corpus callosum

Corpus callosum is the largest white matter tract connecting the two hemispheres of the human brain (section 1.2.4). Post-mortem studies have found altered properties of the corpus callosum in normal ageing and neurological diseases including AD [Køster et al., 2018; Hou and Pakkenberg, 2012]. Corpus callosum atrophy has been commonly reported and a loss of fibres have been found to be the major factor contributing to atrophy [Hou and Pakkenberg, 2012].

Non-invasive MRI studies have strengthened the significance of post-mortem results described above. For instance, corpus callosum atrophy is a feature that has been reported in several studies of neurological disorders including MCI and AD [Wang et al., 2015b]. Annual rates of this atrophy have been used to develop a logistic regression model to predict conversion of patients with MCI to AD [Lee et al., 2016]. The prediction accuracy of the model was reportedly higher for females than males suggesting that discriminating regions of the corpus callosum differed between genders. MRI studies have also reported morphological changes of the corpus callosum using properties such as 'circularity', which is a parameter that captures both area and deformity of the structure [Ardekani et al., 2014]. In contrast to these observations in adults, the corpus callosum area and thickness have been observed to increase in children with neurological conditions compared to matched controls [Wolff et al., 2015].

DTI has been used by several studies to investigate the microstructural properties of the corpus callosum. Typically, an increase in FA and a decrease in MD have been reported in studies of normal ageing [Bennett et al., 2017; Ota et al., 2006; Hasan et al., 2005] similar to other white matter structures. FA and MD in the corpus callosum have been modelled as a function of age to evaluate their patterns of change in mid to later years of life; a negative linear relationship has been observed between FA and age and a positive linear relationship between MD and age [Ota et al., 2006]. Some studies have suggested a better fit for data using non-linear models [Sala et al., 2012; Lebel et al., 2012b]. In general, an increasing FA and a decreasing MD have been reported in childhood and adolescence, gradually reversing trajectories in older age [Lebel et al., 2012b].

Altered DTI properties of the corpus callosum have also been observed in MCI and AD [Mayo et al., 2017; Stricker et al., 2016; Genc et al., 2016]. Results of DTI studies have established that changes occurring in the corpus callosum in degenerative diseases exceeded that arising from normal ageing. Atrophy of the corpus callosum as observed in MRI studies has correlated well with cognitive decline in MCI and AD [Lee et al., 2016; Wang et al., 2015a], but DTI parameters have predicted subtle changes in the corpus callosum that preceded atrophy [Sala et al., 2012].

DTI studies have also suggested that corpus callosum may be the white matter structure most affected by age, but the extent to which it is affected varies by sub-region [Ota et al., 2006]. These variations have been suggested to be indicative of the differing effects of age in the corresponding parts of the brain each sub-region projects to [Lebel et al., 2010]. While some studies have reported a larger effect of

age (typically indicated by a decrease in FA and an increase in MD) in the anterior parts of the corpus callosum such as the genu [Lebel et al., 2010; Ota et al., 2006; Hasan et al., 2005], other studies have observed this in the posterior parts such as the splenium [Bennett et al., 2017]. In this chapter, analysis of the corpus callosum will be carried out by sub-region to account for this heterogeneity in its microstructure.

4.2.1 Corpus callosum sub-regions

Imaging as well as proteomics studies of the human corpus callosum have confirmed its heterogeneous structure [Kashem et al., 2009; Bartzokis et al., 2004]. However, no macroscopic landmarks exist to differentiate between regions. An introduction to different schemes of sub-division of the corpus callosum has been given in section 3.6. A simple method is to divide the corpus callosum into the anterior genu, the body, and the posterior splenium [Weis et al., 1993]. The most widely used

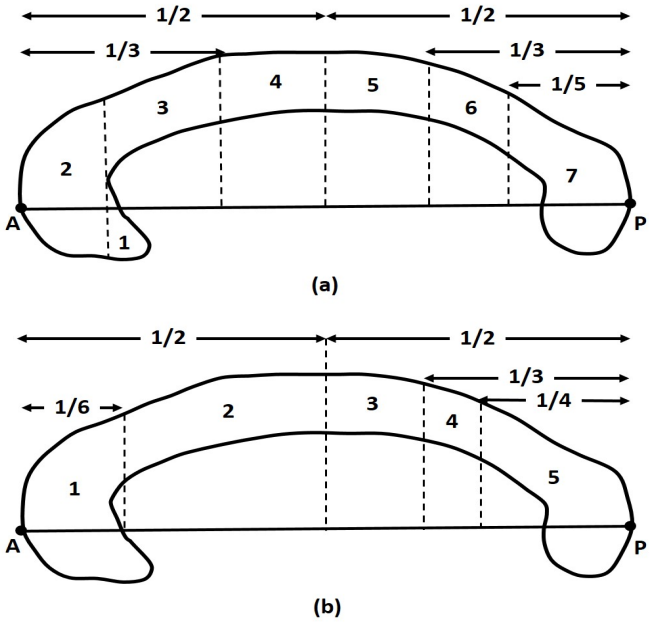

Figure 4.1: Subdivision of the corpus callosum using (a) Witelson's scheme: 1. Rostrum 2. Genu 3. Rostral body 4. Anterior body 5. Posterior body 6. Isthmus 7. Splenium. Regions 1-3 project to prefrontal, premotor and supplementary motor areas, region 4 to motor areas, region 5 to somaesthetic and posterior parietal areas, region 6 to posterior parietal and superior temporal areas, and region 7 to occipital and inferior temporal areas. (b) Hofer scheme: 1. Prefrontal 2. Premotor and supplementary motor 3. Motor 4. Sensory 5. Parietal, temporal, and occipital projections.

geometrical subdivision is the Witelson's classification [Witelson, 1989]. It divides the corpus callosum into seven regions, namely rostrum, genu, rostral body, anterior body, posterior body, isthmus, and splenium, as shown in Figure 4.1a. The main limitations of this scheme are its geometrical method of classification, and its development based on data obtained from non-human primates.

Several studies have used tractography based parcellations of the corpus callosum to identify sub-divisions based on the regions of the brain they project to. The scheme developed by Hofer and Frahm (2006) is one such method, where after parcellation through the corpus callosum of 8 healthy subjects, sub-divisions were proposed based on the average results of tractography. They found differences between Witelson's classification and the results of their tractography analysis, which has motivated the development of their scheme. It divides the corpus callosum into five regions based on the areas of the brain they project to; namely, prefrontal (region 1), premotor and supplementary motor (region 2), motor (region 3), sensory (region 4), and parietal, temporal and occipital (region 5) areas. A diagrammatic representation of the Hofer and Frahm sub-division method has been given in Figure 4.1b.

In this chapter, the Hofer and Frahm scheme of sub-division has been used to analyse the corpus callosum by sub-region. This scheme has been chosen since it offers a means to investigate alterations in DTI parameters in the sub-regions and their potential roles in impacting the brain areas they project to. This may play a significant role in associating clinical symptoms with DTI parameter alterations in the corpus callosum. A careful analysis by sub-region may reveal minor pathological changes in MCI and AD that may otherwise be missed.

4.3 Materials and methods

Images used in this study have been obtained from ADNI-3. Since they have been acquired from multiple scan sites, the inclusion criteria were designed to select images with fully matched scan parameters. This was necessary to eliminate confounding factors since scan parameters have been reported to affect tensor estimation in DTI as described previously (section 3.2). Scan sequence details of images included in this study are: field strength = 3 T, TE = 56 ms, TR = 7200 ms, b = 0, 1000 s/mm^2, number of diffusion weighted images = 48, number of non-diffusion weighted images = 7, voxel size = 2 mm x 2 mm x 2 mm, and approximate scan time = 7 minutes 30 seconds. Diffusion weighted scans of 107 HC, 28 subjects with MCI, and 5 patients with AD matched the inclusion criteria. This resulted in unbalanced cohort sizes with

subject numbers not equal to that estimated in section 3.7.1, although the unequal sample sizes were accounted for in the statistical analysis. Subject demographics have been summarised in Table 4.1.

A subset of subjects from HC, that included only age- and gender-matched participants, was selected to investigate the effects of gender on changes in DTI parameters. This group consisted of 74 subjects (37 males and 37 females) and was called HC_{sub}. The demographics of this group have also been given in Table 4.1. The cohort of healthy subjects to be studied was selected (HC or HC_{sub}) after analysing the effects of gender on changes in DTI parameters of the corpus callosum with age. If gender proved to be a significant factor, the cohort HC_{sub} was studied along with MCI and AD; otherwise, cohort HC was selected.

Once the healthy subject group (HC or HC_{sub}) was selected, analysis of the corpus callosum with ageing, MCI, and AD was carried out as described in the following sections. The analysis protocol developed in section 3.6 was used to extract values of FA, MD, RD, and AxD in the whole corpus callosum as well as its

Table 4.1: Age and gender distribution of subjects in the study (M: male, F: female).

		HC		MCI		AD	
Age Range	Cohort	M	F	M	F	M	F
55-60	HC	-	1	-	2	1	-
	HC_{sub}	-	-				
61-65	HC	5	8	1	-	-	-
	HC_{sub}	5	5				
66-70	HC	7	24	2	1	1	-
	HC_{sub}	7	7				
71-75	HC	5	10	4	4	-	1
	HC_{sub}	5	5				
76-80	HC	11	9	3	4	1	-
	HC_{sub}	9	9				
81-85	HC	8	9	1	-	-	
	HC_{sub}	8	8				
86-90	HC	6	2	1	2	-	1
	HC_{sub}	2	2				
90-96	HC	1	1	1	2	-	-
	HC_{sub}	1	1				
Total	**HC**	**43**	**64**	**13**	**15**	**3**	**2**
	HC_{sub}	**37**	**37**				

sub-regions. Statistical tests including linear regression and analysis of covariance (ANCOVA) were then carried out for each DTI parameter to detect significant deviations from healthy ageing in MCI and AD.

4.4 Testing for the effects of gender on DTI parameters

Previous studies of the corpus callosum, and the white matter in general, have reported mixed results regarding the effects of gender on changes in DTI parameters with age. Although gender has been observed to have a significant effect in different age ranges, the absolute differences between DTI parameters of males and females were very small [Lebel et al., 2010]. Even among studies reporting these differences, there is no clear consensus on how gender affects the measurements. For instance,

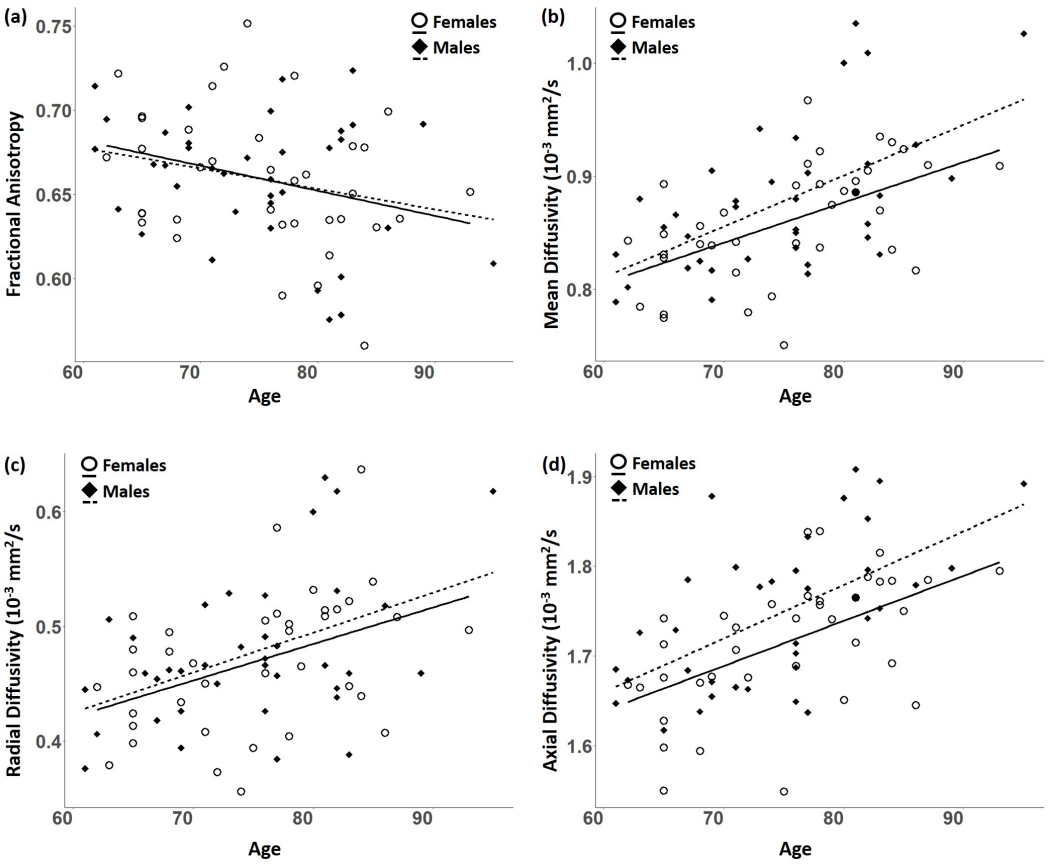

Figure 4.2: Linear regression plots of (a) FA, (b) MD, (c) RD, and (d) AxD in the corpus callosum of subjects from HC_{sub}. Observations have been stratified according to gender.

some studies have reported a higher FA in the white matter of healthy adult males compared to females [Lebel et al., 2010], while others have observed a higher FA in males in some white matter regions and lower in others [Kanaan et al., 2012]. Contrasting these findings are the results of investigations that found no significant differences between genders in DTI parameters [Inano et al., 2011; Davis et al., 2009; Ota et al., 2006]. Even among studies focusing specifically on the corpus callosum, similar contrasting results have been reported on the effects of gender [Muetzel et al., 2008; Westerhausen et al., 2004]. Individual differences in subject data may account for these discrepancies. Therefore, it is important that any effects of gender on DTI parameters should be tested on the study data before the main investigations are carried out.

Multiple linear regression analysis was carried out on FA, MD, RD, and AxD values estimated using the protocol described in section 3.6 from the subjects in cohort HC_{sub}. Age, gender, and the effects of their interaction were considered as factors. All four DTI parameters exhibited linear trends with age in the age range analysed (Figure 4.2), consistent with previously reported observations [Lebel et al., 2010; Ota et al., 2006]. An offset was noted between the regression lines plotted for male and female patterns of change for MD, RD, and AxD, but not for FA. However, these gender-related differences were not found to be statistically significant (Table 4.2). Neither gender, nor the effects of interaction between age and gender, were found to be significant factors contributing to changes in DTI parameters with age.

Since gender was not found to be a significant factor impacting DTI measurements in the present dataset, cohort HC was used for further analysis instead of HC_{sub}. This enabled a larger sample size to be studied which may lead to a lower variance in the fitted regression models. Unequal sample sizes for HC, MCI, and AD may be accounted for in the statistical tests carried out.

Table 4.2: The contributions of age, gender, and their interaction, to observed linear trends in Figure 4.2 were analysed using a null hypothesis that tests their correlation with the DTI parameters (FA, MD, RD, and AxD) and outputs a probability 'p'. The factor is considered significant if 'p' is less than 0.05. p(age:gender) denotes the p-value for the effects of interaction of age and gender on the DTI parameters.

DTI parameter	p(age)	p(gender)	p(age:gender)
FA	0.06	0.8	0.8
MD	< 0.001	0.63	0.51
RD	< 0.01	0.91	0.85
AxD	< 0.001	0.8	0.62

4.5 Analysis of the corpus callosum in ageing

The cohort HC was used to analyse the effects of healthy ageing on DTI parameters in the corpus callosum. Results of linear regression analysis have been given in Figure 4.3(a-d). For all four DTI parameters, age was found to be a significant factor contributing to changes observed ($p < 0.001$). This agreed with previous studies where a negative correlation of FA and positive correlations of MD, RD, and AxD with age have been reported (see section 2.4). It is likely that although a linear relationship existed in the age range analysed, a non-linear fit may better describe the data as more subjects (younger and older) are added [Lebel et al., 2012a; Sala et al., 2012; Lebel et al., 2010].

Regression analysis was also carried out by corpus callosum sub-region to investigate whether patterns of change in DTI parameters with age were similar throughout the white matter tract (Figure 4.3(e-h)). Tests using ANCOVA on the region-wise data revealed that the measured values of FA, MD, and RD differed significantly ($p < 0.001$) between sub-regions after controlling for the effects of age. Tukey's multiple comparison tests between FA, MD, RD, and AxD of the five regions supported these observations, although AxD remained fairly constant between the regions (Figure 4.4). The effect sizes of region as a contributing factor to the variance observed in the DTI parameters have been given in Table 4.3.

A post-mortem study has shown that the corpus callosum is a bundle of fibres with different diameters connecting the left and the right hemispheres. The anterior corpus callosum has the highest density of thin fibres. This decreases towards the posterior regions with a rising presence of larger fibres, and reaches a minimum before increasing again towards the posterior end; an opposite trend has been observed for the density of fibres with larger diameters (Figure 4.5a) [Aboitiz et al., 1992]. Another study [Barazany et al., 2009] has reported a positive correlation between the axon diameter and RD in the corpus callosum of rat brain, potentially due to larger diameters leading to a lower density and a subsequent increase in perpendicular diffusion. This relationship was found to hold true in the present study in the human corpus callosum (Figure 4.5b), even though the schemes of subdivision used were different.

Regional variations observed in DTI parameters in the corpus callosum ROI (Table 4.3) may likely be due to the varying density of axons with larger and smaller diameters. However, these regional variations in microstructure were not found to significantly impact the values of AxD in the corpus callosum. This may be due to the manner of segmentation of the ROI itself; variations in fibre size between

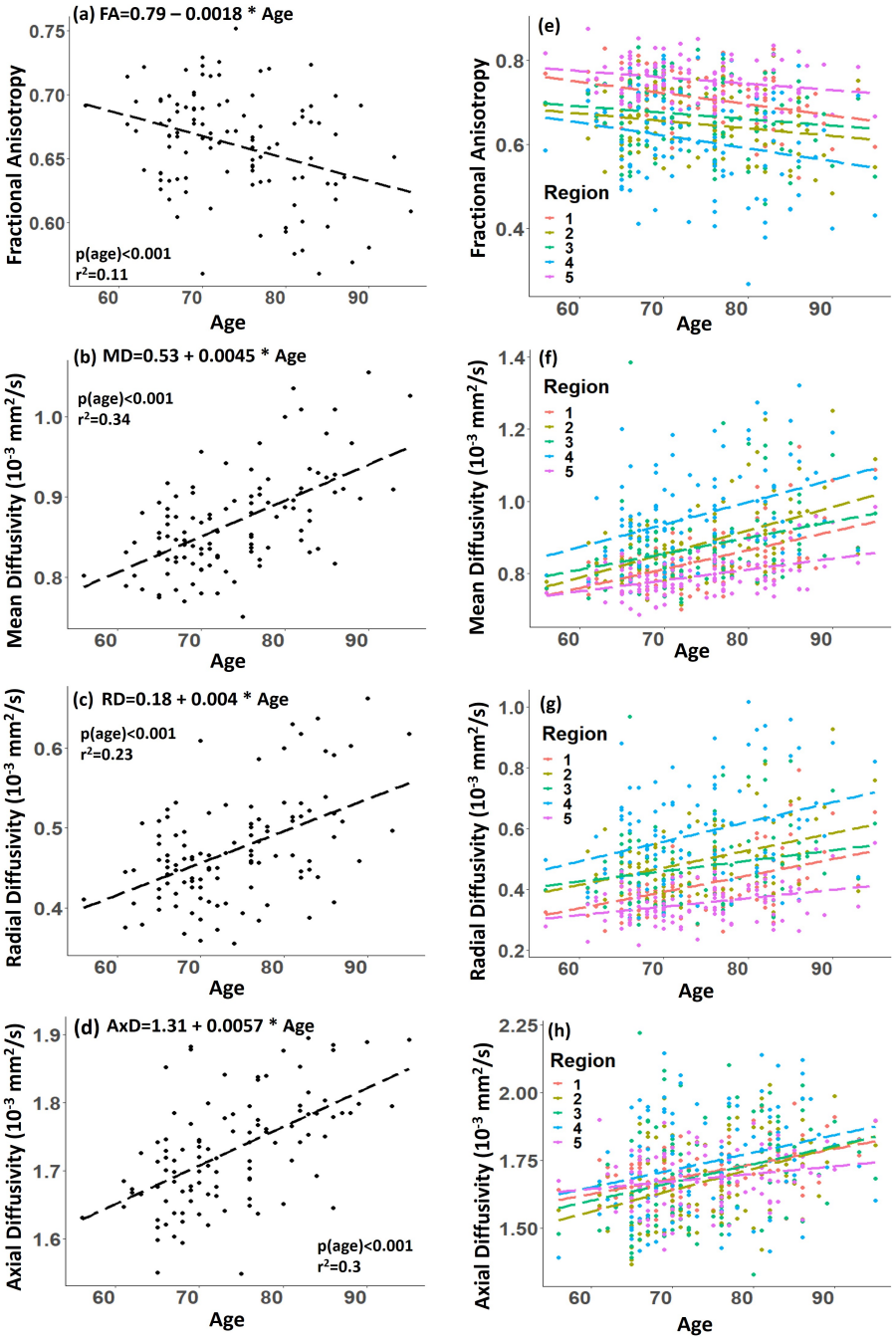

Figure 4.3: Linear regression plots of (a) FA, (b) MD, (c) RD, and (d) AxD in the whole corpus callosum. The p-values from testing age as a contributing factor to the observed trends have been shown on the plots with their corresponding r-squared values. Figures (e), (f), (g), and (h) show the parameters stratified by sub-region. The results of corresponding statistical tests have been given in Table 4.3.

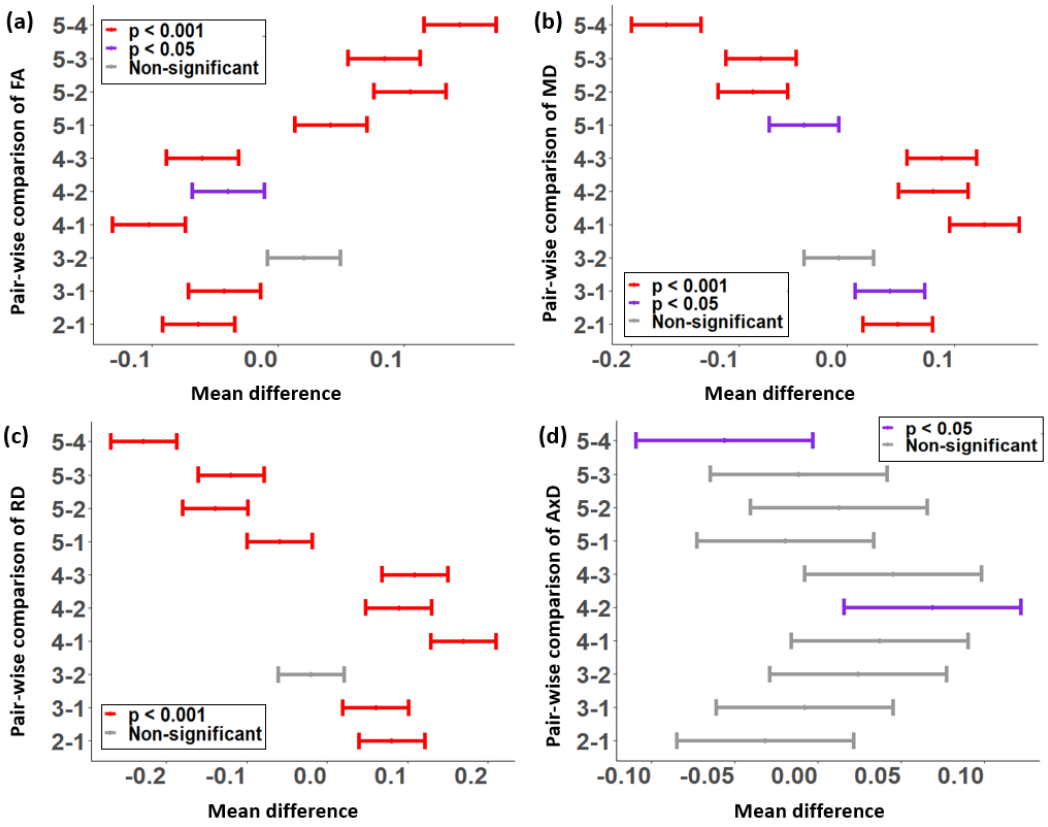

Figure 4.4: Results of Tukey's multiple comparison tests between FA, MD, RD, and AxD of corpus callosum sub-regions with different colours indicating different significance levels.

Table 4.3: Results of ANCOVA between regions 1 - 5 in HC, testing for regional differences after controlling for the effects of age. Partial omega squared (ω^2) is a measure of effect size; it is an estimate of how much variance in the output variables are accounted for by the explanatory variable, i.e., corpus callosum sub-region. ω^2 has values between 1 and -1, with 0 indicating no effect.

DTI parameter	Cumulative p-value (ANCOVA)	ω^2
FA	< 0.001	0.285
MD	< 0.001	0.252
RD	< 0.001	0.306
AxD	0.006	0.017

anterior and posterior regions may not have an impact on AxD, which measures the diffusivity in a direction parallel to the fibre orientation, i.e., from one hemisphere to the other. It is important to keep in mind that the anterior-posterior segmentation of the corpus callosum ROI does not represent the direction of fibre orientation.

The analysis carried out in this section has revealed that regional variations in DTI properties in the corpus callosum are statistically significant. Results given in Table 4.3 have suggested that at least 25% of variance in FA, MD, and RD measurements may be explained by regional variations. Therefore, studies investigating the diffusion properties of the corpus callosum in ageing or disease may be better served by analysing each sub-region separately.

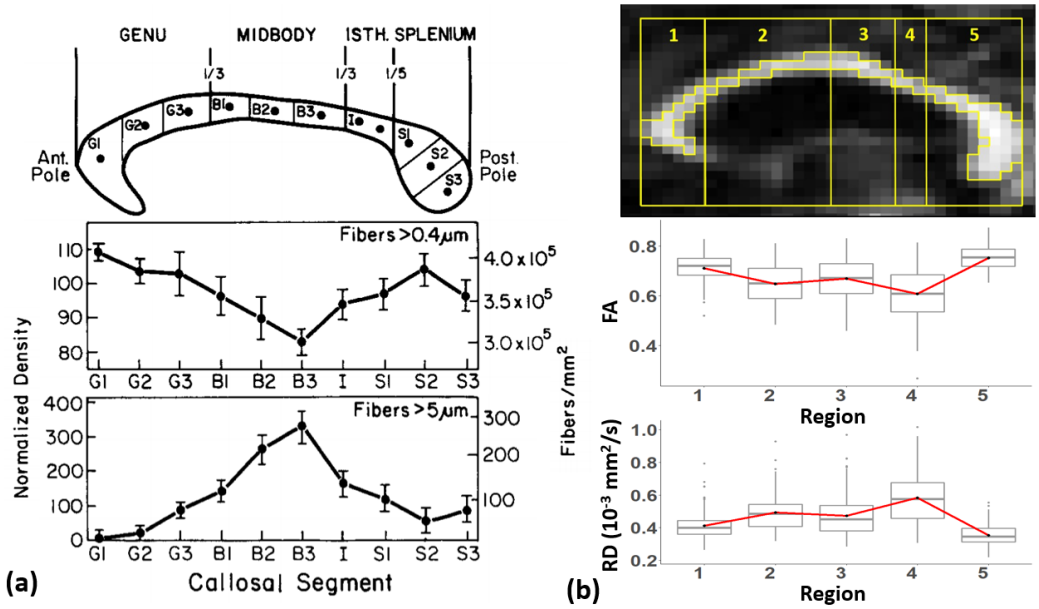

Figure 4.5: (a) Density distribution of small and large diameter axons in the corpus callosum. Picture has been adapted with permission from Aboitiz et al. [1992]. (b) Distribution of FA and RD values in the corpus callosum sub-regions were observed to follow a similar trajectory. Although the sub-division scheme used in this study is different to that used in (a), it may be observed that the minimum and maximum density for smaller and larger diameter fibres occur in region B3 (isthmus) and the minimum and maximum for FA and RD distributions occur in region 4 in the Hofer and Frahm scheme. These regions may be observed from the figures to be the same.

4.6 Analysis of the corpus callosum in MCI and AD

The cohorts MCI and AD described in section 4.3 were used to analyse the effects of disease-related microstructural changes on DTI parameters in the corpus callosum. Linear regression plots of FA, MD, RD, and AxD in the whole corpus callosum ROI have been shown in Figure 4.6. Initial tests were carried out in this ROI using ANCOVA. They revealed subtle but significant changes in FA, RD, and AxD of patients with MCI compared to HC after controlling for the effects of age (Table 4.4). A decrease in RD accompanied by an increase in AxD likely had opposing effects on MD measurements, which were not statistically significant between MCI and HC. This has been shown in Figure 4.7 where the linear relationship between MD and RD + AxD implied by the equations using diffusion tensor eigen values

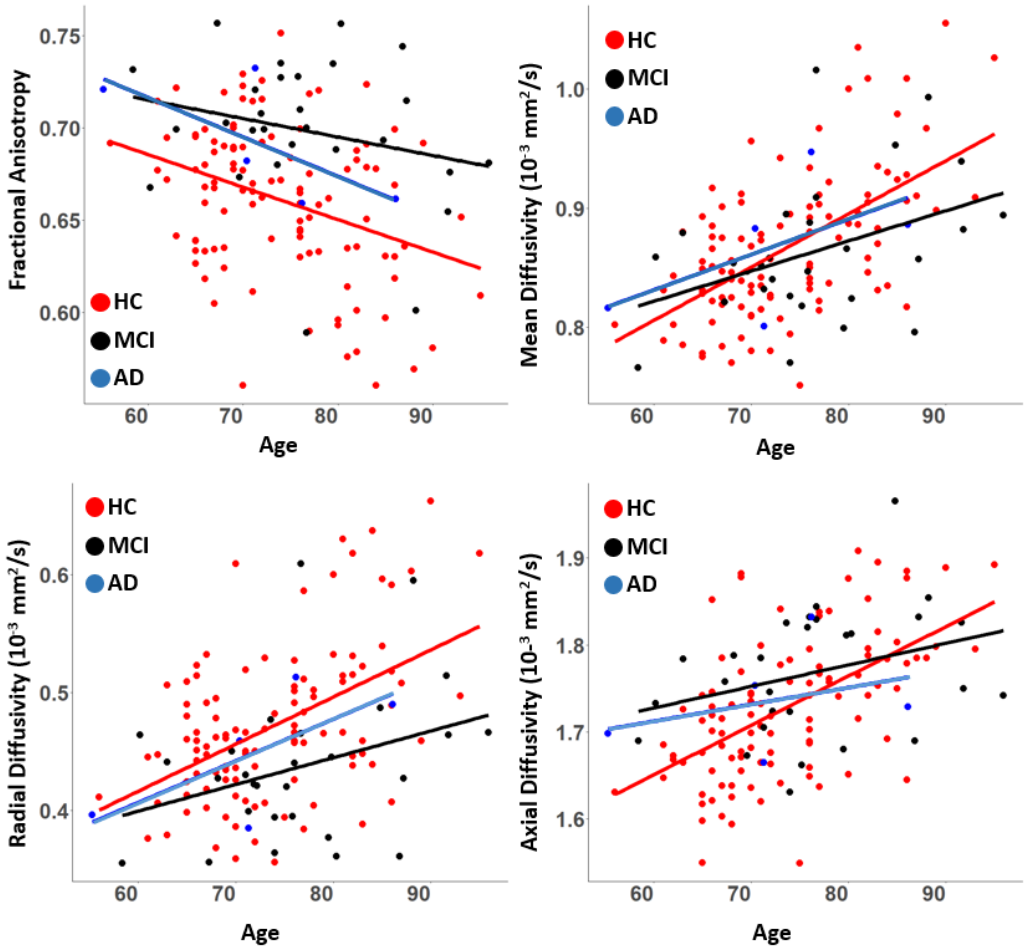

Figure 4.6: Linear regression plots of DTI parameters with age in the whole corpus callosum ROI of HC, MCI, and AD groups.

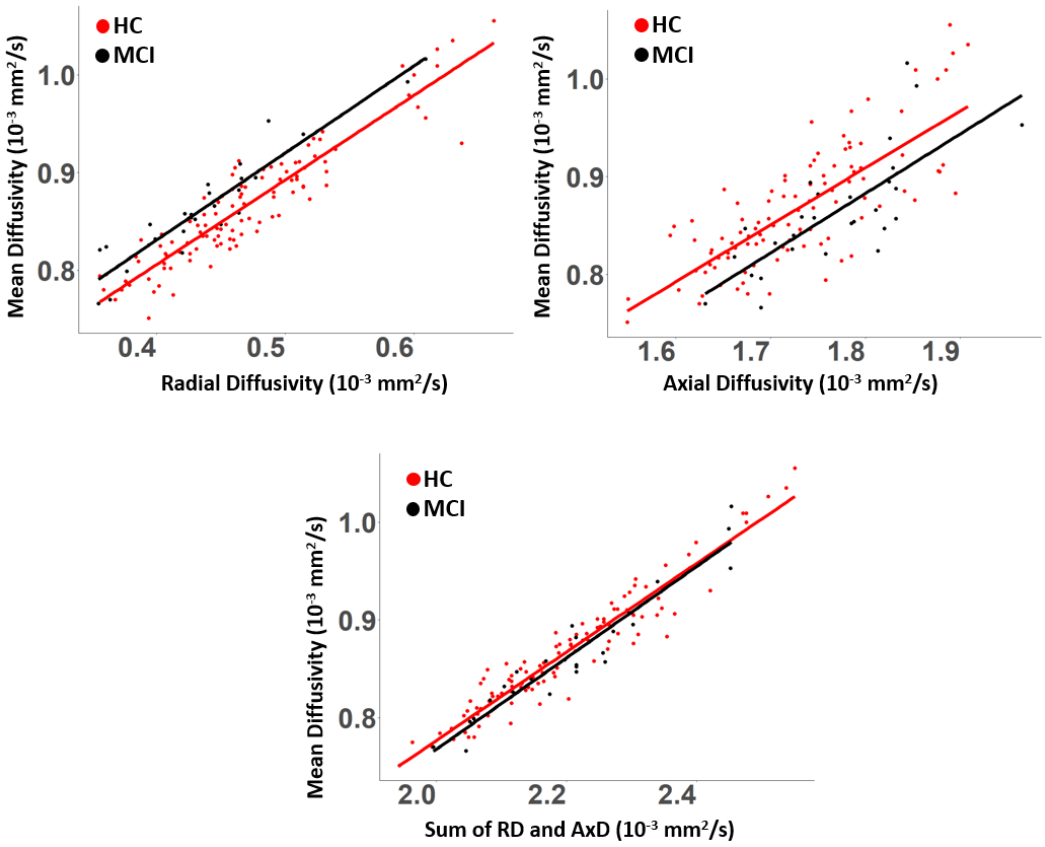

Figure 4.7: Plots showing the relationships between MD, RD, and AxD of HC and MCI subjects.

Table 4.4: Results of ANCOVA tests between HC, MCI, and AD groups with age and disease group as factors. Effect sizes of disease on the parameters have been represented by ω^2. Tukey's test was used to obtain a p-value for pairwise comparisons between groups.

DTI parameter	Pairwise comparison		Effect size (ω^2)
	HC-MCI	HC-AD	
FA	< 0.001	0.2	0.119
MD	0.91	0.99	-0.009
RD	0.013	0.65	0.036
AxD	0.02	0.98	0.026

[RD = $(\lambda_2 + \lambda_3)/2$, AxD = λ_1, and MD = $(\lambda_1 + \lambda_2 + \lambda_3)/3$] may be observed. These equations have been used to generate plots that show a smaller RD and a larger AxD in MCI patients compared to HC, for a given value of MD. The third plot in Figure 4.7 suggests that these opposing patterns (represented by RD + AxD) bring the MD values of HC and MCI subjects closer to each other, resulting in a non-significant difference.

Measurements from patients with AD were not found to be significantly different from either HC or MCI patients. However, this was more likely due to insufficient number of subjects rather than the absence of pathological changes. Nevertheless, the data obtained from patients with AD were plotted alongside that from HC and MCI to visualise the regression trends (Figure 4.6). Results of ANCOVA comparing data from AD and HC cohorts have been given in Table 4.4.

It is worth noting that the measured FA values in patients with MCI were higher than that in HC on average, and the values for MD and RD were lower (Figure 4.6). This contradicted previous reports which showed trends of lower FA and higher diffusivities in degeneration (see section 2.4), but seemed to suggest a role for inflammation in MCI as indicated by increasing FA and decreasing diffusivities [Gupta et al., 2008; Nath et al., 2007]. This has been reported to be suggestive of either intracellular inflammation with inflow of extracellular water in the axons, or decreased extracellular space due to cellular infiltration by inflammatory cells [Renoux et al., 2006]. Neuroinflammation in MCI and AD has not been extensively studied in the context of DTI. Advanced diffusion models of the brain such as those quantifying extracellular free-water volume are being used to develop markers to study neuroinflammation [Pasternak et al., 2016, 2012].

An investigation into region-wise measurements provided a better insight into the differences between DTI parameters in HC and MCI. Density plots or smoothed histograms were plotted for DTI parameters in each region to visualise the distribution of measured values and the heterogeneity (Figures 4.8 and 4.9). Significant differences were observed in MD ($p < 0.05$), RD ($p < 0.1$), and AxD ($p < 0.05$) between HC and MCI in region 2 and only AxD ($p < 0.1$) in region 3. This indicated that degenerative changes observed in MCI were dominant in regions 2 and 3 of the corpus callosum and that they might be more extensive in region 2 than in region 3. No significant differences were observed between HC and AD groups at $p < 0.05$ but this may likely be due to the low sample size. Results of ANCOVA analysis on region-wise DTI parameters of HC, MCI, and AD groups have been given in Table 4.5. It should be noted that although the effect sizes of disease in regions 2 and 3 for the significantly different parameters (see Table 4.5) were higher

than in other regions, their absolute values were still small. This may be attributed to the subtle differences between HC and MCI during the early stages of cognitive impairment.

Physiological interpretations for RD have included demyelination and that for AxD have included axonal degeneration [Song et al., 2003]. This implies a diminished corpus callosum integrity in MCI, potentially playing a role in progression to AD. Alterations in DTI parameters in the corpus callosum of patients with AD could not be investigated thoroughly in this study due to the low sample size. This may be carried out in a future study after ADNI-3 releases more patient data. Nevertheless, several DTI studies have reported corpus callosum degeneration in AD [Doan et al.,

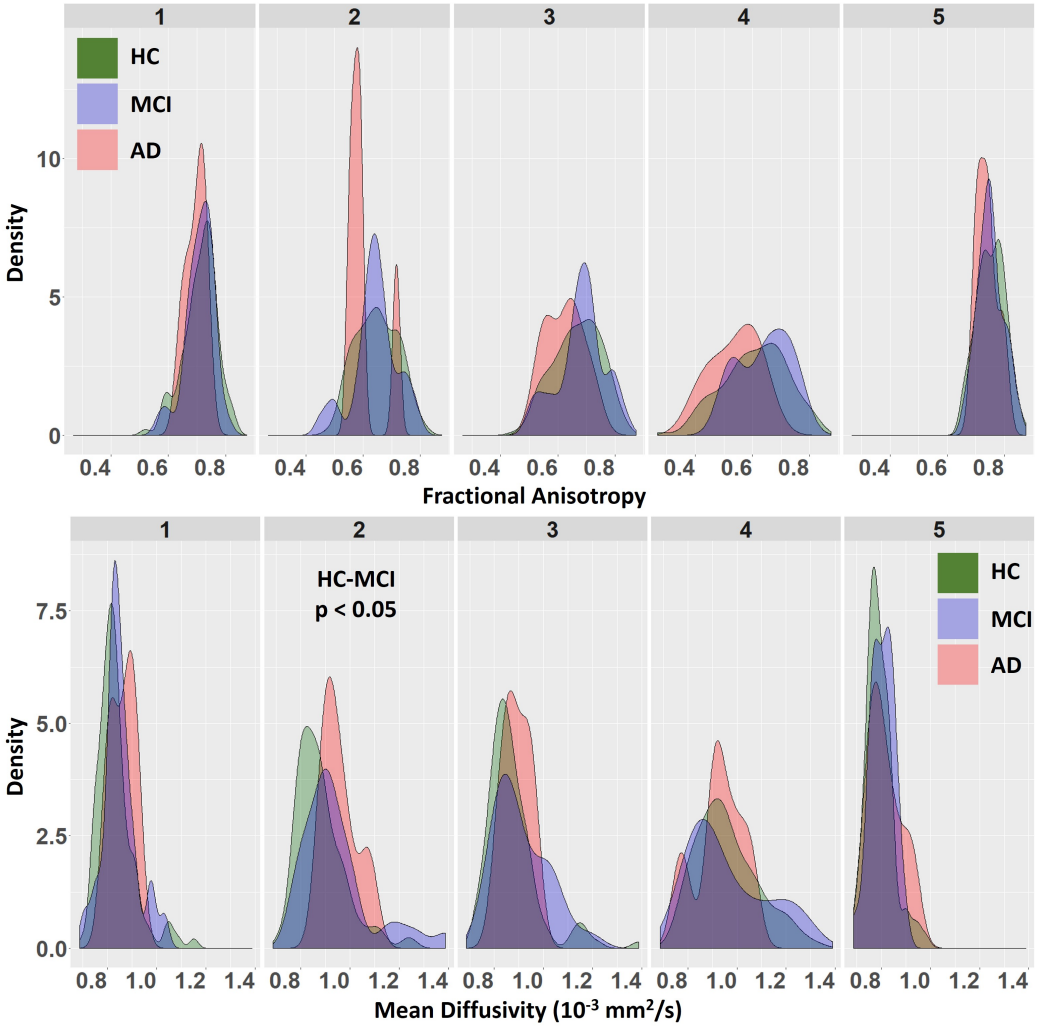

Figure 4.8: Density plots of FA and MD visualised separately in the corpus callosum sub-regions.

2017; Demey et al., 2015; Preti et al., 2012] using images obtained from other sources.

4.6.1 Associations with clinical observations

The results of the DTI analysis indicated that corpus callosum sub-regions 2 and 3 were affected in MCI. Region 2 of the corpus callosum projects to pre-motor and supplementary motor areas, and region 3 to primary motor areas of the brain [Hofer and Frahm, 2006]. An effect of disease in MCI, indicated by altered values of DTI parameters in these regions, may help explain motor impairments observed in patients with MCI and pre-clinical AD [de Paula et al., 2016; Buchman and

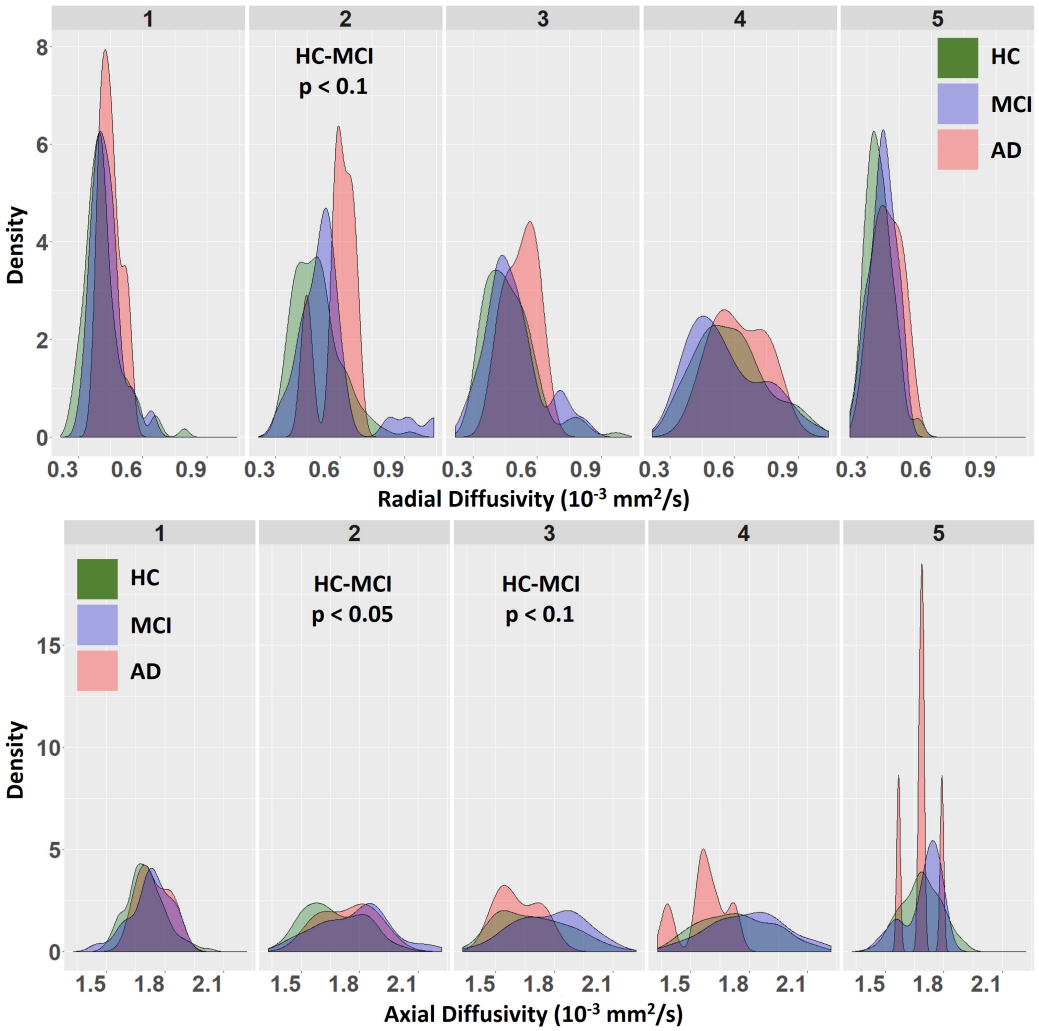

Figure 4.9: Density plots of RD and AxD visualised separately in the corpus callosum sub-regions.

Bennett, 2011]. Neurophysiological examination results accompanying participant data in ADNI-3 were used to test this hypothesis. They have been collected as part of subject screening process and provide preliminary information about a range of functional networks including motor, visual, and auditory systems.

The results of neurophysiological examinations have been summarised in Table 4.6. They showed that a higher proportion of tremors, abnormal reflexes and impaired gait were reported in MCI patients compared to HC. It is interesting to note that this pattern was observed only in motor-related functions and not in the results of visual or auditory examinations. This agreed with the study results that indicated altered DTI parameters only in regions 2 and 3, which are regions projecting to motor areas of the brain. The study also supported results from previous investigations that show significant correlations between altered FA in the anterior parts of the

Table 4.5: Effect size (ω^2) and significance (p-values) of disease on the corpus callosum. Tukey's test was used to obtain a p-value from pairwise comparisons of MCI and AD with HC.

Region	DTI parameter	Cumulative p-value	Effect size	Pairwise comparison	
				HC-MCI	HC-AD
1	FA	0.79	-0.01	0.98	0.77
	MD	0.32	0.002	0.41	0.61
	RD	0.42	-0.001	0.61	0.56
	AxD	0.36	0	0.46	0.62
2	FA	0.38	0	0.92	0.36
	MD	0.003	0.05	0.005	0.19
	RD	0.03	0.03	0.09	0.18
	AxD	0.006	0.05	0.005	0.57
3	FA	0.33	0.001	0.74	0.44
	MD	0.25	0.005	0.23	0.92
	RD	0.62	-0.007	0.88	0.64
	AxD	0.05	0.03	0.08	0.59
4	FA	0.1	0.02	0.32	0.3
	MD	0.84	-0.011	0.99	0.83
	RD	0.67	-0.008	0.78	0.86
	AxD	0.03	0.03	0.31	0.09
5	FA	0.79	-0.011	0.98	0.77
	MD	0.37	0	0.54	0.55
	RD	0.16	0.01	0.37	0.3
	AxD	0.86	-0.012	0.85	0.99

corpus callosum and abnormal gait function [Snir et al., 2019; de Laat et al., 2011; Bhadelia et al., 2009]. However, it must be noted that an increase in FA in the ROI was observed in this study, whereas previous studies have reported a decrease in FA. Although results from AD group show a similar increase in motor related abnormalities, they have not been considered while interpreting the data due to the low sample size of the cohort.

Due to a lack of specificity in DTI, the nature of pathological changes giving rise to alterations in measured parameters in the corpus callosum could not be established. Prior associations of DTI parameters with demyelination and axonal degeneration suggest these processes may occur in the anterior parts of the corpus callosum in MCI and AD, resulting in diminished processing of information in the pre-motor, supplementary motor and primary motor areas of the brain [Song et al., 2003].

4.7 Evidence for retrogenesis

The results of the study described in this chapter agreed with the retrogenesis theory, which suggests that white matter fibres that myelinated later in life were more susceptible to damage from ageing and diseases than those that myelinated earlier in life (see section 2.4.1.1). In other words, it postulates that degeneration of the white matter follows an opposite trajectory to that of myelogenesis. In the human corpus callosum, posterior areas such as the splenium have been found to myelinate earlier in life compared to anterior regions such as the genu and are therefore thought to be more resilient in ageing and disease [Knyazeva, 2013].

In the corpus callosum analysis carried out in this chapter, FA values in the

Table 4.6: Summary of neurophysiological examination data from ADNI-3 subjects, showing the % of subjects with abnormal results.

Examination	HC	MCI	AD
Visual impairment	5.6	3.6	0
Auditory impairment	6.5	7.1	0
Presence of tremors	8.4	21.4	40
Abnormal tendon reflexes	7.5	10.7	20
Abnormal plantar reflexes	0.9	3.6	0
Abnormal gait	8.4	21.4	40
Motor strength	2.8	0	20
Sensory reflexes	12.1	10.7	20

anterior parts of the corpus callosum were observed to be lower and MD values higher than in the posterior parts (Figures 4.10 and 4.11). Welch's two-sample t-tests were carried out to quantify the significance of this difference; this test was chosen to account for unequal variances in measurements in different regions of the corpus callosum. The results of t-tests have been summarised in Table 4.7. Significant differences were observed between regions 1 and 5 in FA, MD, and RD ($p < 0.001$), but not for AxD. These results supported the retrogenesis theory by indicating that the anterior parts of the corpus callosum which myelinate later in life may be more susceptible to degeneration with ageing than the posterior parts.

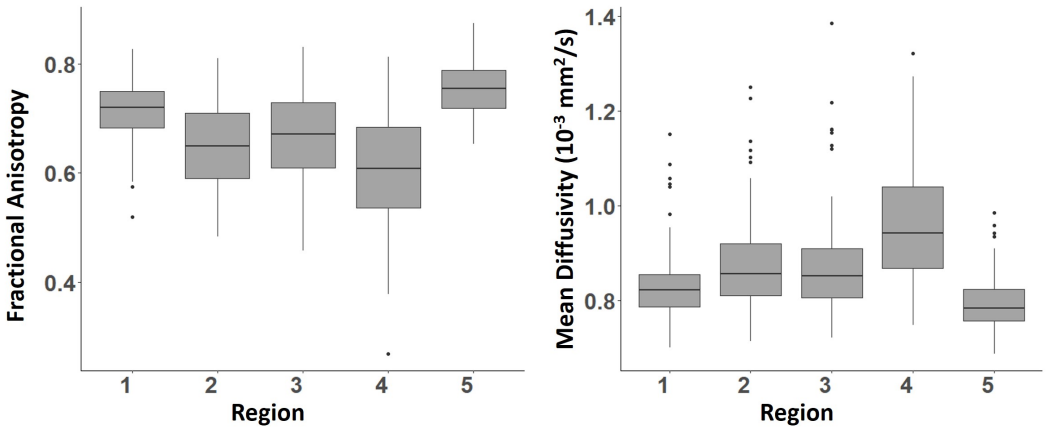

Figure 4.10: Region-wise box plots of FA and MD in the corpus callosum of HC subjects.

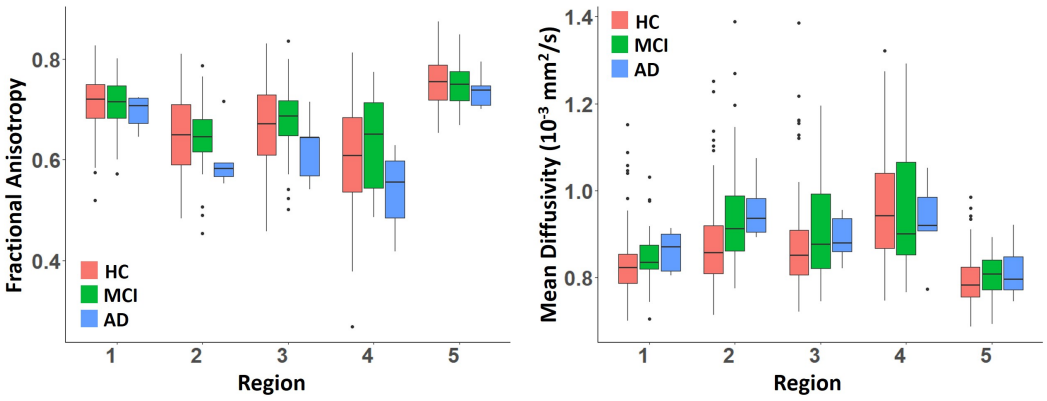

Figure 4.11: Region-wise box plots of FA and MD in the corpus callosum of HC subjects and patients with MCI and AD.

Table 4.7: Results of Welch's two-sample t-tests carried out between regions 1 and 5 of the corpus callosum.

DTI Parameter	Mean in Region 1	Mean in Region 5	p-value
FA	0.71	0.75	< 0.001
MD	0.83	0.79	< 0.001
RD	0.41	0.35	< 0.001
AxD	1.7	1.68	0.15

4.8 Conclusions

The effects of normal ageing as well as pathological effects of MCI and AD have been analysed in the corpus callosum using DTI. Corpus callosum was divided into sub-regions to account for its microstructural heterogeneity in measurements. Age-related alterations in diffusion properties have been observed to be significantly different between the sub-regions. A careful and detailed analysis of FA, MD, RD, and AxD, which also accounted for the AD risk factors age and gender, has shown that the DTI properties of the corpus callosum were best characterised when investigated by sub-region rather than as a single structure. The analysis has also revealed alterations in DTI parameters occurring in the corpus callosum due to MCI, predominantly in regions 2 and 3. This suggested a potential role of the corpus callosum in motor-related deficits seen in MCI and early AD, as regions 2 and 3 project to motor areas of the brain. The results have been supported by evidence from neurophysiological exam data archived in ADNI-3, where patients with MCI were more likely than HC to experience motor-related deficits compared to other impairments.

The results described in this chapter have demonstrated a role for the corpus callosum in a symptom that is observed early in AD pathogenesis, i.e., motor related abnormalities. They have showed the utility of the segmentation and analysis protocol developed in chapter 3 in detecting clinically relevant, subtle alterations in DTI parameters in disease. A limitation of this study is the lack of detailed information about motor functions in ADNI-3 neurophysiological exams, which were collected as part of screening. The results indicate only the presence or absence of abnormalities. Availability of detailed test results may help estimate the correlation between DTI parameters, tremors, reflexes and gait, providing insight into the extent of the role of corpus callosum in motor impairment as observed in MCI and potentially, pre-clinical AD. The measurements collected have been given in appendix C.

Chapter 5

Advanced DTI methods for clinical scans

5.1 Introduction

A detailed study of the corpus callosum was carried out in chapter 4 using the protocol developed in chapter 3. The corpus callosum was observed to be a heterogeneous structure with its properties varying between sub-regions. Alterations in DTI properties were also measured in specific sub-regions of the corpus callosum projecting to motor areas of the brain in patients with MCI and AD as compared to HC. In this chapter, two advanced methods of DTI analysis have been applied on the same cohorts of subjects to investigate the feasibility of extracting more specific information about ageing and disease-related changes in the corpus callosum. Although these methods have originally been proposed for DTI scans acquired using multiple HARDI shells or a higher resolution, prior studies have adapted them for application to clinically acquired scans.

5.2 NODDI-DTI

5.2.1 Neurite Orientation Dispersion and Density Imaging (NODDI)

NODDI has been developed by Zhang et al. (2012) as a method to investigate the integrity of axons through indices that are more specific to variations in microstructure than the common DTI parameters (FA, MD, RD, AxD). The NODDI model of the white matter may be represented by a modified version of the composite hindered and restricted model of diffusion (CHARMED, Assaf and Basser [2005]). CHARMED attributed the MR signal decay observed in white matter to

both Gaussian (hindered) and non-Gaussian (restricted) diffusion compartments, with hindered diffusion thought to occur in the extra-axonal space and restricted diffusion in the intra-axonal space [Assaf and Basser, 2005]. NODDI has generalised this model by representing the white matter as a bundle of impermeable cylindrical axons with an orientation distribution and equal diameters [Zhang et al., 2011]. It has approximated the acquired signal as contributed to by three compartments - intra-cellular, extra-cellular, and CSF.

The DW-MRI scan acquisition protocol for NODDI requires a minimum of two HARDI shells to create a model of the white matter that includes intra-cellular, extra-cellular, and CSF compartments. The intra-cellular space has been modelled using a set of cylinders with zero radii to capture the highly anisotropic diffusion in the axons. On the other hand, the extra-cellular space has been described by an anisotropic Gaussian diffusion and the CSF space by an isotropic Gaussian diffusion [Zhang et al., 2012]. The CSF compartment in the model allows for the estimation of CSF partial volume fraction in the signal, which may result in more accurate measurements in white matter structures close to the ventricles such as the corpus callosum.

The NODDI model may be mathematically described as follows [Zhang et al., 2012]:

$$A = (1 - \nu_{iso})(\nu_{ic}A_{ic} + (1 - \nu_{ic})A_{ec}) + \nu_{iso}A_{iso} \tag{5.1}$$

where ν represents the volume fraction, A represents the normalised signal, and ic, ec, and iso are the intra-cellular, extra-cellular, and CSF compartments respectively. The intra-cellular compartment has been modelled using a Watson distribution to describe the ODF of the fibre bundle:

$$f(\mathbf{n}) = M\left(\frac{1}{2}, \frac{3}{2}, \kappa\right)^{-1} e^{\kappa(\boldsymbol{\mu}.\mathbf{n})^2} \tag{5.2}$$

where M is a special mathematical function known as the confluent hypergeometric function, $\boldsymbol{\mu}$ is the mean fibre orientation and κ is a parameter measuring the dispersion of orientation around $\boldsymbol{\mu}$. The extra-cellular compartment has been modelled using a symmetric tensor with the principal direction of diffusion $\mathbf{n}$ and diffusion coefficients $d_{\parallel}$ and $d_{\perp}$. The CSF compartment has been described using an isotropic Gaussian diffusion with diffusivity d_{iso}. The model has then been fitted to the acquired image using non-linear optimisation [Zhang et al., 2012; Alexander and Seunarine, 2010] and the parameter κ has been used to compute the orientation dispersion index

[Zhang et al., 2012] (OD) as follows:

$$OD = \frac{2}{\pi}\arctan\left[\frac{1}{\kappa}\right] \tag{5.3}$$

The performance of NODDI has been tested under different scan acquisition protocols with multiple shells and one protocol with a single shell. It has been established that the neurite density as measured by ν_{ic} cannot be estimated accurately with single shell DTI acquisition, rather a minimum of two shells was required. NODDI may be applied to scans acquired with typical clinical b-values, provided the signal has been sampled using more than one HARDI shell.

5.2.2 The NODDI-DTI model

The NODDI-DTI model has been proposed as a modification to NODDI that enabled its application to single-shell DTI. It has eliminated the CSF compartment from the model and recommended application on voxels without CSF partial volume contamination [Edwards et al., 2017]. The parameter OD has been redefined as τ [Edwards et al., 2017; Zhang et al., 2012]:

$$\tau = \frac{1}{\sqrt{\pi\kappa}\,\exp(-\kappa)\,\mathrm{erfi}(\sqrt{\kappa})} - \frac{1}{2\kappa}, \quad \tau \in [1/3, 1] \tag{5.4}$$

The value of τ may vary from 1/3 in isotropic structures (κ=0) to 1 in strictly anisotropic structures ($\kappa = \infty$). The eigen values of the diffusion tensor has been used to express ν_{ic} and τ in terms of FA and MD [Edwards et al., 2017], leading to the following equations:

$$\nu_{ic} = 1 - \sqrt{\frac{1}{2}\left(\frac{3\ \mathrm{MD}}{d} - 1\right)} \tag{5.5}$$

$$\tau = \frac{1}{3}\left[1 + \frac{4}{|\ d - \mathrm{MD}\ |}\frac{\mathrm{MD}\ .\ \mathrm{FA}}{\sqrt{3 - 2\ \mathrm{FA}^2}}\right] \tag{5.6}$$

Since $\nu_{ic} \in [0, 1]$ and $\tau \in [1/3, 1]$, this implies [Edwards et al., 2017]:

$$\mathrm{MD} \in [d/3, d], \quad \mathrm{FA} \in \left[0, \sqrt{\frac{3}{2}}\frac{|\ d\ -\ \mathrm{MD}\ |}{\sqrt{2\ \mathrm{MD}^2 - (d - \mathrm{MD})^2}}\right] \tag{5.7}$$

A heuristic correction has been applied to MD to account for diffusion kurtosis [Edwards et al., 2017] that may be present in single-shell DTI. Kurtosis is a measure of the tails of a probability distribution, with a higher kurtosis implying heavier tails

or outliers. Heuristically corrected MD has been defined as:

$$\mathrm{MD}_h = \mathrm{MD} + \frac{b}{6}\left[\sum_{i,j=1}^{3} \frac{1+2\delta_{ij}}{15}\lambda_i\lambda j\right] \tag{5.8}$$

where λ_i is the i^{th} eigen value of the diffusion tensor and δ_{ij} is the Kronecker delta function.

The heuristic correction applied to MD has been based on several assumptions: (a) diffusional kurtosis is the dominant factor contributing to the observed bias, (b) the square of ADC is not correlated with the apparent diffusional kurtosis, (c) the mean diffusional kurtosis is 1, and (d) the effect of diffusional kurtosis on each individual eigen value is negligible. The kurtosis bias may not be completely eliminated due to the nature of these assumptions, and the residual effects may push the values of MD outside its normal range of $[d/3, d]$. This is a major limitation of the NODDI-DTI model. The value of MD_h may be substituted in equation 5.5 to estimate values of ν_{ic}. A heuristic correction has not been recommended for FA since it was found to reduce the upper bound of values leading to unphysical estimates of τ. The parameters ν_{ic} and τ estimated using NODDI-DTI have been found to be close to that estimated using NODDI, demonstrating the utility of NODDI-DTI method in images acquired using typical clinical scan parameters [Edwards et al., 2017].

It must be noted that the NODDI-DTI model may often give rise to unphysical estimates of ν_{ic} and τ. Some explanations for this have been proposed by Edwards et al.. They include errors in the estimation of FA and MD using the diffusion tensor, partial volume effects of CSF in the image after setting its contribution to zero in the model, residual bias after heuristic kurtosis correction as described above, and cases where model assumptions of NODDI itself are invalid. Edwards et al. has further stipulated that ageing or pathological mechanisms in the white matter may lead to one or more of the above situations and subsequent unphysical parameter estimates, and has recommended that the NODDI-DTI model be applied only to healthy subject data. Here, the cohort HC from chapter 4 has been used to explore the scope of NODDI-DTI model in extracting specific information that enriches the DTI analysis of the corpus callosum.

5.2.3 Analysis of ADNI-3 HC group

Images used in this study belong to the cohort HC obtained from ADNI-3 and has been described in chapter 4. Briefly, the scan sequence parameters of the images are:

field strength = 3 T, TE = 56 ms, TR = 7200 ms, b = 0, 1000 s/mm^2, number of diffusion weighted images = 48, number of non-diffusion weighted images = 7, voxel size = 2 mm x 2 mm x 2 mm, and approximate scan time = 7 minutes 30 seconds. Subject demographics have been summarised in Table 4.1 in chapter 4.

The following steps have been followed for analysis of HC data using NODDI-DTI. They have been derived from the segmentation and analysis protocol developed in section 3.6. To ensure the accuracy of the NODDI-DTI model, the corpus callosum was manually segmented ensuring no CSF contamination in the ROI.

1. Using the steps described in section 3.6, FA and MD were estimated for every pixel in the corpus callosum ROI.

2. For each image, a heuristic correction was applied to estimate pixel-wise MD_h, and used instead of MD in equation 5.5 to estimate pixel-wise ν_{ic}. Such a correction was not carried out for the estimation of τ (equation 5.6) as it was not recommended by Edwards et al..

3. The median of pixel-wise ν_{ic} and τ were estimated to represent these parameters in the ROI of each image.

The above steps were carried out for the corpus callosum both as a single ROI and by sub-regions similar to the analysis in chapter 4. The corresponding plots of ν_{ic} and τ have been given in Figure 5.1. A decrease in ν_{ic} was observed with ageing, with the patterns of change differing between the sub-regions of the corpus callosum; this was observed to be similar to the changes in FA (Figure 4.3). On the other hand, variations in τ with ageing were not found to be statistically significant in the whole corpus callosum ROI or the sub-regions. The estimation of τ using equation 5.6 resulted in a few values outside the range of feasible bounds as discussed by Edwards et al. and has been ignored for the calculations carried out in this study.

Some of the different sources of diffusion anisotropy have been discussed previously (see section 2.3). A decrease in ν_{ic} or an increase in τ have been proposed as factors contributing to a reduction in FA observed in DTI studies of the white matter [Beaulieu, 2014]. The similarity in patterns of change observed in FA and ν_{ic} supports this hypothesis and was further investigated using a correlation analysis. The values of Pearson's correlation coefficient for each sub-region have been given in Table 5.1. The results described in the table suggest a high degree of correlation between FA and ν_{ic}, especially in the anterior sub-region 1 of the corpus callosum. Linear regression analysis was carried out to obtain the values of r^2 in different

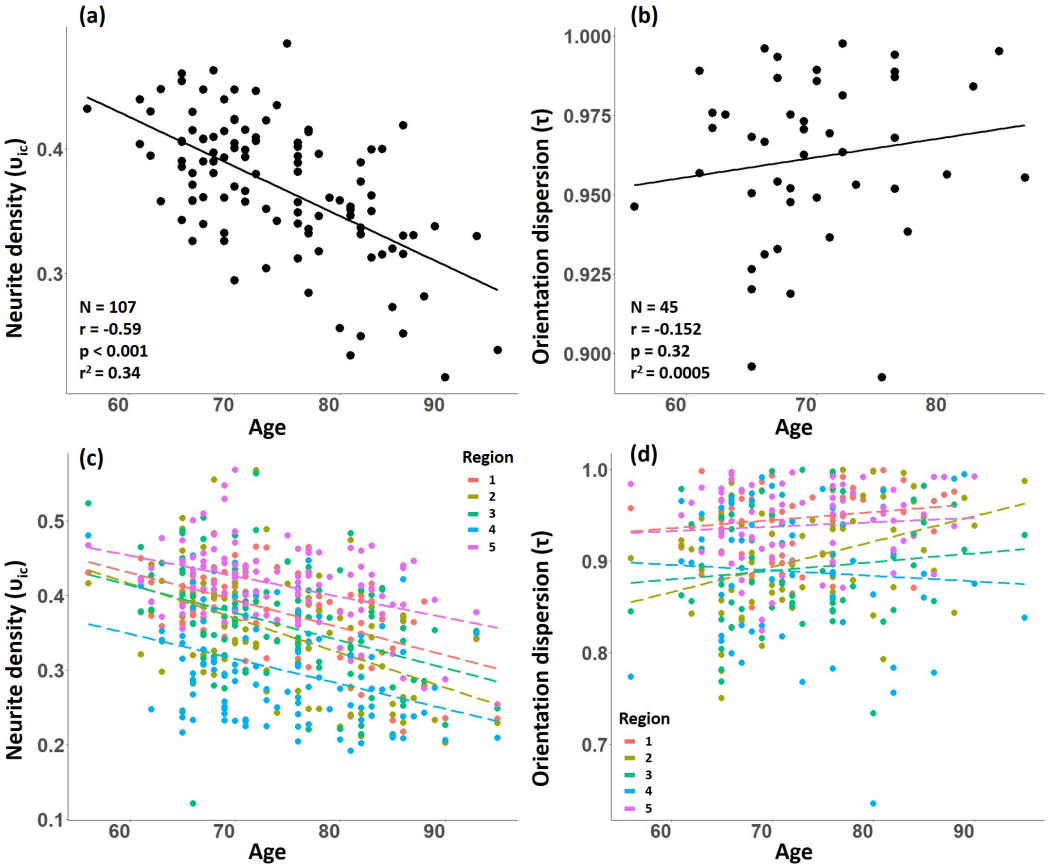

Figure 5.1: (a) Plot of neurite density ν_{ic} showing a decrease with age. (b) Plot of the orientation dispersion τ with age. Plots (c) and (d) show region-wise distribution of values of ν_{ic} and τ. Only values within physically feasible bounds have been plotted for τ. The correlation coefficient and r^2 values have been shown for the whole corpus callosum in the figure, and for the sub-regions in Table 5.1.

regions; these results (Table 5.1) indicate a high r^2 in region 1 of the corpus callosum and suggest ν_{ic} as a major factor contributing to the changes observed in FA in this region.

The retrogenesis theory postulates that the anterior regions of the corpus callosum may be more susceptible to the effects of ageing than the posterior regions (section 2.4.1.1). The evidence for a reduced neurite density in region 1 compared to region 5 of the corpus callosum (Figure 5.1) supported this hypothesis. A prior study of neurite density across the human lifespan (7 - 63 years) has observed a similar trajectory as FA, i.e., increasing in childhood and plateauing in adulthood [Chang et al., 2015]. In this study, a decline in FA with age that corresponds to a decline in

ν_{ic} was observed. The scope of NODDI-DTI, to improve specificity and extend the results of conventional DTI analysis, has been demonstrated on clinically acquired images of the HC cohort from ADNI-3. While the original NODDI model may offer a more accurate and comprehensive picture, it also requires images to be acquired using multiple HARDI shells. This has not yet become a routine clinical practice.

5.3 TractSeg

A widely adopted method of white matter tract segmentation uses tractography followed by manual delineation to obtain an ROI. Automated segmentation methods have also been proposed to follow tractography and obtain the ROI. These may include atlases, anatomy-based clustering, template matching, and geometric flow-based segmentation [Wasserthal et al., 2018b]. TractSeg is an algorithm based on a convolutional neural network for white matter segmentation and tractography that has aimed to surpass the performance of these automated methods by using a fully convolutional neural network (FCNN). Training data for the algorithm has been produced by a semi-automated segmentation of 72 white matter tracts in a cohort of 105 HC subjects from the Human Connectome Project (HCP) database [Van Essen et al., 2013]. Thus, TractSeg is capable of segmenting 72 white matter tracts in total. It has been made available free of charge at *www.github.com/MIC-DKFZ/TractSeg*.

DTI scans have been acquired by the HCP at 3 T with 1.25 mm x 1.25 mm x 1.25 mm isotropic voxel resolution, 270 diffusion weighted directions evenly distributed over 3 HARDI shells with b-values of 1000, 2000, and 3000 s/mm^2, and 18 images without diffusion weighting. These scan parameters are state-of-the-art and not typical for clinical scanners. To ensure a good performance of TractSeg on clinical datasets as well, the HCP images have been down-sampled to 2.5 mm isotropic resolution with only 32 diffusion weighted directions retained at b=1000 s/mm^2. This reduced quality data was then used to validate the performance of TractSeg

Table 5.1: Results of Pearson's test and linear regression for the corpus callosum sub-regions between FA and ν_{ic}.

Region	Pearson's r	Adjusted r^2	p-value
1	0.72	0.52	< 0.001
2	0.38	0.14	< 0.001
3	0.31	0.089	0.001
4	0.49	0.23	< 0.001
5	0.4	0.15	< 0.001

on clinically acquired images. In this study, TractSeg has been implemented on the ADNI-3 cohort to analyse corpus callosum tracts in HC, MCI, and AD subject images. These are the same cohorts that have been analysed in the DTI study in chapter 4. Here, TractSeg has been used to extract information that may complement the results already obtained from conventional DTI analysis.

An important fact to keep in mind is the difference in the corpus callosum ROI as processed by the DTI analysis and TractSeg. While the protocol developed in chapter 3 has proposed an ROI on a mid-sagittal volume extending from anterior to posterior regions of the brain, TractSeg parses the corpus callosum from one hemisphere of the brain to the other (Figure 1.2). In other words, while DTI analysis in chapter 4 has revealed changes in MCI and AD across the corpus callosum fibre bundle, TractSeg has been used to extract the same information along the length of the bundle.

5.3.1 TractSeg model and architecture

5.3.1.1 Model architecture and training

The FCNN model proposed by TractSeg has been based on the widely used U-Net architecture [Ronneberger et al., 2015]. The input is in the form of a 2D image with 144 x 144 voxels and 9 channels to represent the extracted orientation peaks. The FCNN generates an output image with 144 x 144 voxels and 72 channels, with each channel carrying the voxel-wise probabilities for one of the 72 possible white matter tracts, which may be converted to binary outcomes by thresholding at 0.5.

The model has not been extended to 3D images to retain memory efficiency. However, the 2D image slices are randomly sampled in axial, sagittal and coronal orientations to ensure a good performance of the model independent of the image acquisition plane. Three predictions are made based on the orientation peaks which are later averaged to obtain a single final prediction of the white matter tract each pixel belongs to. Rather than directly taking the mean of the predictions, an optional second FCNN stage has been proposed, which may offer an optimum combination of slice orientations to obtain the best prediction.

Data augmentation of the ODF peak images, including rotation, elastic deformation, displacement, zoom, noise addition, contrast, and brightness augmentation have been carried out on the training data to improve the performance of the FCNN [Wasserthal et al., 2018b]. Different types of ODF peak images have been generated for training including using: (a) multi-shell multi-tissue constrained spherical deconvolution (CSD) using all gradient directions, (b) single-shell CSD using all

gradient directions at b=1000 s/mm^2, and (c) single-shell CSD using only 12 gradient directions at b=1000 s/mm^2. Training data for the network has been randomly sampled from these peak images to ensure an overall good performance.

The images of 105 subjects from HCP have been used to generate segmentations of 72 white matter tracts to train and validate the FCNN. These images have been put through the following processing steps - (a) tractography using the ODF generated by multi-shell CSD, (b) initial extraction of the tracts using a dictionary of anatomical definitions describing each of them, (c) tract refinement using manually defined inclusion and exclusion ROI, (d) manual inspection for quality control, and (e) generation of binary masks for the 72 tracts.

5.3.1.2 Pre-processing

The input to TractSeg is required to be in the form of 3 fibre directions per voxel, each represented by a 3D vector, resulting in 9 input channels. Fibre directions may be extracted using CSD, that expresses the acquired HARDI signal from a fibre bundle with a specific ODF as the convolution of a response function in a spherical coordinate system [Tournier et al., 2004]. A non-negativity constraint has been found to result in a robust determination of the fibre orientations using CSD [Tournier et al., 2007]. A multi-shell version of this algorithm has also been proposed [Jeurissen et al., 2014]. If an image voxel contains fibres with only one orientation, such as in the corpus callosum, the other two are set to zero. The images from HCP with spatial resolution 145 x 174 x 145 voxels have been cropped to 144 x 144 x 144 voxels without losing brain tissue, to fit them to the FCNN input size.

The three stages of TractSeg, as explained below, have been based on the same FCNN receiving fibre ODF as input. However, they differ based on the training target or the expected outcome. The workflow of TractSeg algorithm is shown in Figure 5.2 and is explained in the following sections.

5.3.1.3 Tract segmentation

The FCNN, trained as described in the previous section, carries out voxel-wise classification of white matter tracts in this stage of TractSeg. It has 72 output channels, each producing a binary image with voxel labels of 0 or 1 depending on whether they belong to the corresponding tract. Therefore, the FCNN at this stage has an output in the form of 144 x 144 voxels and 72 channels.

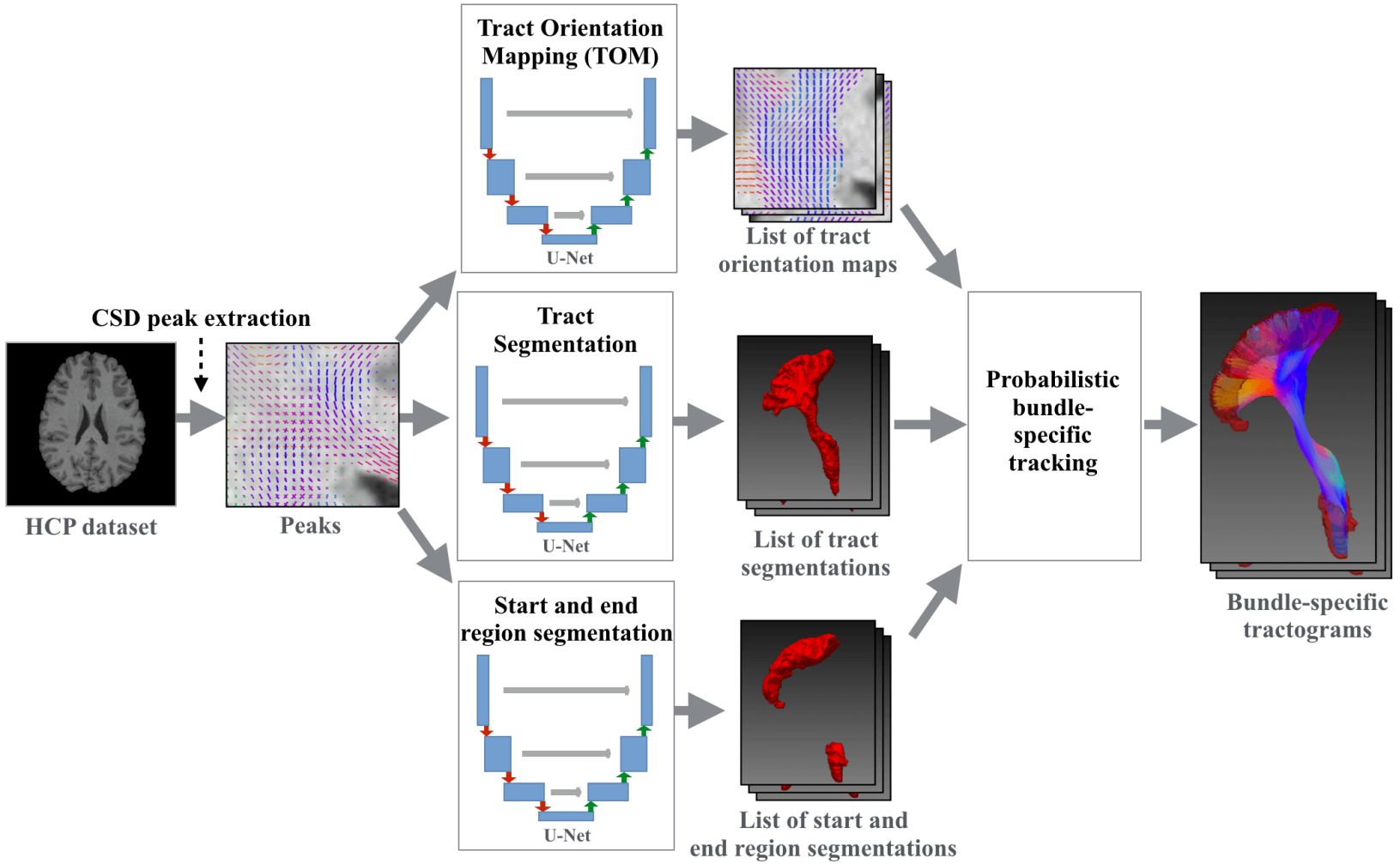

Figure 5.2: Schematic of the TractSeg workflow. Picture has been obtained with permission under the Creative Commons CC-BY license [Wasserthal et al., 2019].

5.3.1.4 Start and end segmentation

The FCNN has been trained to segment the start and end regions of each tract in this stage of TractSeg. Thus, a total of 144 output channels are required for 72 white matter tracts. Training of the network has been carried out similar to that of the tract segmentation stage, except for the fact that 2 outputs per tract are generated - one start and one end region. These regions have been derived from the binary masks obtained from the tract fibres by setting each voxel to 1 if at least one fibre streamline passes through it [Wasserthal et al., 2019].

5.3.1.5 Tract orientation mapping

Tract orientation mapping (TOM) is carried out as the third stage of TractSeg using an FCNN. [Wasserthal et al., 2018a, 2019]. The network has been trained to learn tract-specific orientations from the ODF, which are then used to generate tract orientation maps (also abbreviated TOM). Each voxel in a TOM carries a 3D vector representing a single tract and its orientation, constituting 72 x 3 = 216 output channels in total. However, since this has been found to lead to problems with convergence, four separate FCNN models have been trained for TOM, with 18 tracts and 18 x 3 = 54 output channels per model.

5.3.1.6 Tractometry

Tractometry is a method through with FA and other DTI parameters may be measured along the fibres of white matter tracts [Yeatman et al., 2012]. In TractSeg, the method proposed by Chandio et al. has been implemented to carry out tractometry through the following steps:

1. All fibre streamlines in the white matter tract being studied are resampled to an equal number of points, that may be specified by the user.
2. The centroids of these streamlines are determined.
3. For each streamline, each sampled segment is assigned to the nearest centroid segment.
4. The FA is evaluated at each segment of each streamline.
5. The average FA is then calculated from the centroid segments.

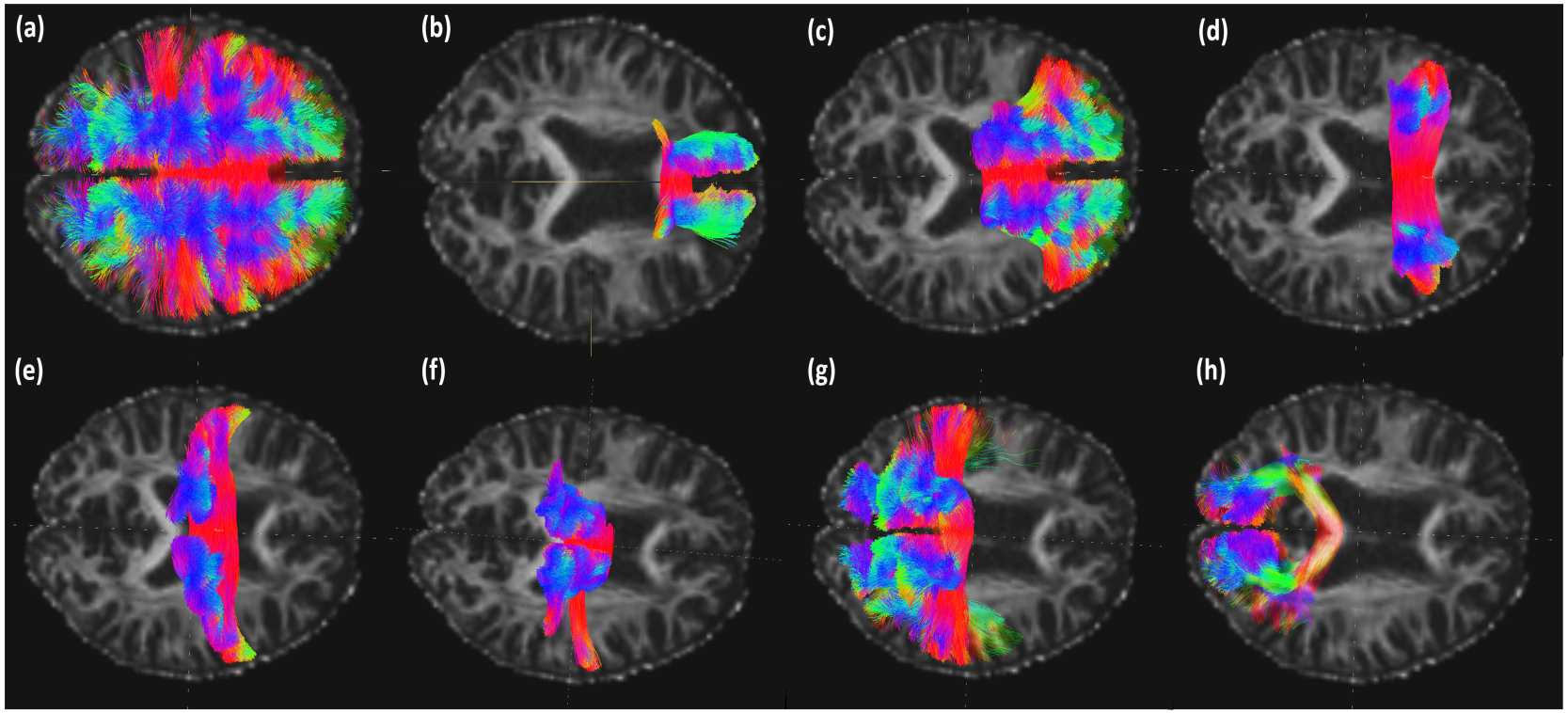

Figure 5.3: Tractography results of the corpus callosum and its sub-regions from an HC subject overlaid on the FA map. All images have been shown on the axial plane. (a) The whole corpus callosum (b) - (h) are regions 1 - 7 in the Witelson's scheme of subdivision.

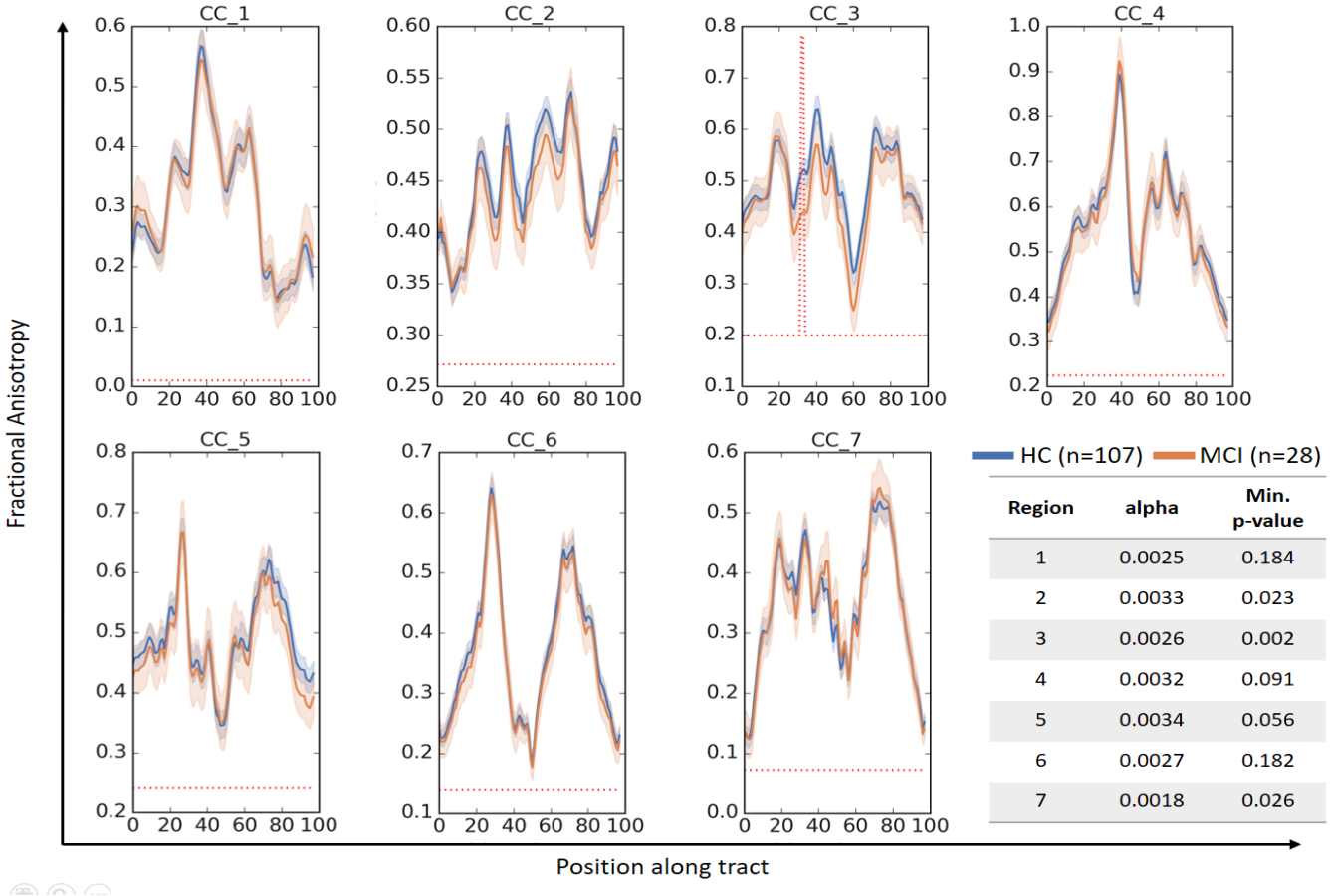

Region	alpha	Min. p-value
1	0.0025	0.184
2	0.0033	0.023
3	0.0026	0.002
4	0.0032	0.091
5	0.0034	0.056
6	0.0027	0.182
7	0.0018	0.026

Figure 5.4: Results from TractSeg analysis of HC and MCI data from ADNI-3. The differences between HC and MCI groups along the corpus callosum fibre streamlines are statistically significant if the minimum p-value observed $<$ alpha, after corrections for multiple comparisons. The red dotted line (CC_3) indicates the areas where p $<$ alpha.

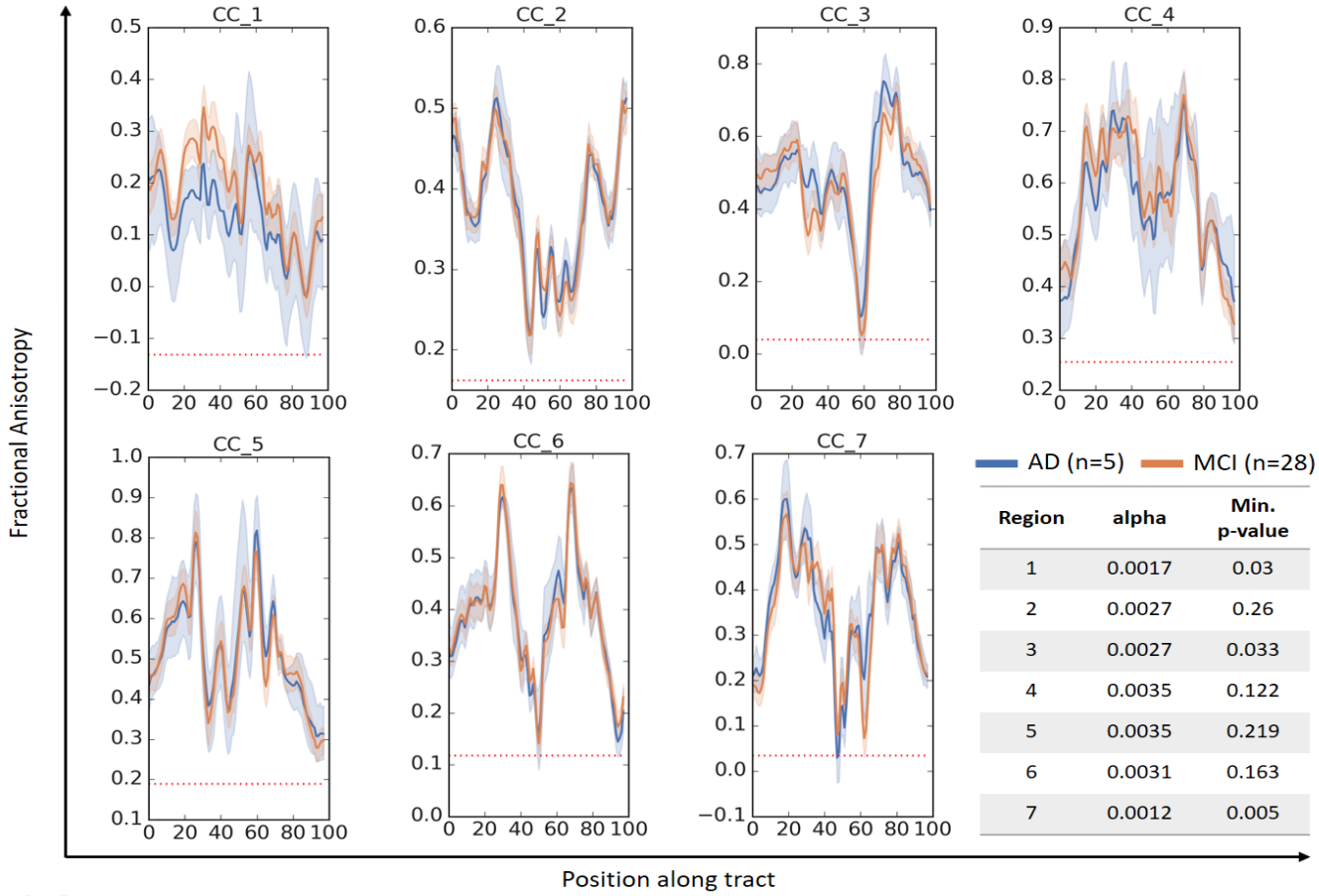

Region	alpha	Min. p-value
1	0.0017	0.03
2	0.0027	0.26
3	0.0027	0.033
4	0.0035	0.122
5	0.0035	0.219
6	0.0031	0.163
7	0.0012	0.005

Figure 5.5: Results from TractSeg analysis of AD and MCI data from ADNI-3. The differences between HC and MCI groups along the corpus callosum fibre streamlines are statistically significant if the minimum p-value observed $<$ alpha, after corrections for multiple comparisons.

5.3.2 Analysis of ADNI-3 data

The TractSeg model trained on images from HCP was downloaded and used in a study on images from ADNI-3. The corpus callosum was tracked on the DW-MRI scans obtained from 107 HC, 28 MCI, and 5 AD subjects, which is the same cohort that has been studied in chapter 4. Briefly, the scan sequence details of ADNI-3 image are: field strength = 3 T, echo time (TE) = 56 ms, repetition time (TR) = 7200 ms, b = 0, 1000 s/mm^2, number of diffusion weighted images = 48, number of non-diffusion weighted images = 7, voxel size = 2 mm x 2 mm x 2 mm, and approximate scan time = 7 minutes 30 seconds. Subject demographics have been summarised in Table 4.1. Since these images have been acquired by ADNI-3 at a lower resolution than HCP, the protocol recommended by the authors of TractSeg for use in 'standard cases' was followed (see TractSeg tutorial by Wasserthal, accessed 14/09/2018). This includes altering the threshold value for small, incomplete tracts as required to convert probability masks to complete binary masks, and post-processing of tracked bundles to remove regions containing very few voxels.

TractSeg tracks the fibre bundles of the corpus callosum according to Witelson's classification into 7 sub-regions (section 4.2.1). Although the results in chapter 4 has been obtained using Hofer scheme of subdivision, they may be compared with the results of TractSeg using an approximation of coinciding regions. For instance, it can be observed from Figure 4.1 that regions 1 and 2 in the Witelson scheme corresponds to region 1 in the Hofer scheme, regions 3 and 4 in the Witelson scheme to region 2 in the Hofer scheme, and regions 5, 6, and 7 in the Witelson scheme to regions 3, 4, and 5 respectively in the Hofer scheme. The tractography results have been shown in Figure 5.3.

The results of TractSeg analysis on images from HC and MCI groups have been given in Figure 5.4. It shows a statistically significant difference in FA along the tract for Witelson's region 3 of the corpus callosum, which corresponds to region 2 in the Hofer scheme. This agreed with the analysis in chapter 4, where a difference in DTI parameters have been noted in region 2 of the corpus callosum. Statistical significance has been evaluated by TractSeg after correcting for multiple comparisons. It must be noted that significant differences were estimated in a small portion of the fibre bundle in Witelson's region 3, although further deviations were present in other parts (Figure 5.4). This was attributed to the unequal sample sizes of HC and MCI groups and a corresponding larger variance observed in measurements from the MCI group.

The results of TractSeg analysis on images from AD and MCI groups have been given in Figure 5.5. Although separate patterns of change may be observed

between the groups in the corpus callosum sub-regions, these were not found to be statistically significant. The variance in data measured from patients with AD were found to be high - a few measurements were observed to carry negative values as is the case when the acquired data does not follow the diffusion tensor model due to noise or signal drop [Niethammer et al., 2006]. The observed patterns in FA may be validated by carrying out the study with sufficient number of participants in the AD cohort.

5.4 Conclusions

In this chapter, two advanced analysis methods have been implemented for ADNI DTI images to demonstrate the extent of information that may be extracted to enrich conventional DTI analysis. Application of NODDI-DTI to images from the HC cohort has suggested that neurite density in the ageing corpus callosum varied between sub-regions and that it may be a major contributing factor to changes observed in FA with age. It has also offered some support to the retrogenesis theory with evidence of a reduced neurite density in the anterior regions compared to the posterior regions of the corpus callosum. While the results of TractSeg analysis may not be directly compared to the DTI study due to differences in the way the corpus callosum has been parsed, they were in agreement with the findings in chapter 4. Statistically significant differences were observed in Witelson's region 3 of the corpus callosum, which projects to motor areas of the brain. This agreed with the results from chapter 4 where similar differences have been found in Hofer's regions 2 and 3 that also project to motor areas of the brain. The measured parameters have been given in appendix C.

Chapter 6

Modelling white matter DTI

6.1 Introduction

In previous chapters, DTI analyses of the corpus callosum have revealed alterations in FA, MD, RD, and AxD resulting from age-related changes as well as neurodegenerative mechanisms of MCI and AD. A significant outcome from these investigations has been the association of specific corpus callosum sub-regions with motor-related impairments observed in patients with MCI and AD. These findings have further been supported by results of advanced analyses using NODDI-DTI and TractSeg.

DTI has proved to be an invaluable tool in clinical practice to diagnose and monitor various conditions. However, DTI is a technique known for its lack of specificity in measurements. It is not currently feasible to associate changes in DTI parameters such as FA, MD, RD, and AxD, with underlying pathophysiological mechanisms in routine clinical settings. Advanced tools are being developed which may provide more specific measures of physiological parameters such as axon or myelin diameters, but they often require image acquisition using state-of-the-art scan settings, and may not always be applicable in clinical practice [Jung et al., 2018; Zhang et al., 2012; Assaf et al., 2008]. Investigating biological processes in the white matter and their associations with DTI is not a trivial task *in vivo*; and this becomes even more complicated under typical clinical imaging conditions.

The white matter has been modelled in a prior study using various parameters to represent the physiology, including axon and myelin radii, fibre packing density, and myelin membrane permeability, to predict the sensitivity of diffusion metrics to changes in these parameters [Sen and Basser, 2005]. An analysis of this model revealed that diffusion metrics were largely dependent on the axon radius, the extra-cellular volume fraction, and the spacing between the axons. The study also

concluded that the myelin sheath presented a diffusion barrier to water molecules in the axon, resulting in the extra-cellular fluid being the major determinant of the estimated metrics. This theoretical model was later used to design a computational study, based on the fact that DTI metrics measured *in vivo* are dependent also on the properties of the scan pulse sequence [Baxter and Frank, 2013], rather than solely on the physiological parameters.

A strategy to correlate clinically acquired DTI with physiological parameters of the white matter was proposed by Davoodi-Bojd and Soltanian-Zadeh [2011]. They first estimated the eigen values, FA, and ADC from the diffusion tensor and then fitted these metrics to the analytical model of Sen and Basser [2005]. Their study concluded that the analytical fibre model needed modifications to enable a more precise association with underlying physiology when using typical clinical DTI scan settings.

The analytical model of Sen and Basser [2005] has held true for DTI pulse sequences with low b-values and long diffusion times, which is typically not the case in clinical scans. Deviations from predicted values have been observed for diffusion metrics in simulation experiments, specifically at clinically relevant b-values, carrying significant implications for data interpretation in DTI studies [Baxter and Frank, 2013]. These observations are compounded by the fact that a voxel of DTI signal acquired from the white matter is a composite of signal contributions from several compartments, of which the axon, myelin, and extracellular compartments are thought to be the most significant [Beaulieu, 2002]. In these compartments, the overall mobility of water molecules undergoing diffusion is different and is determined by the tissue structure.

It has also been established that the longitudinal (T_1) and transverse (T_2) relaxation properties of water molecules in these white matter compartments are different [Peled, 2007; Does and Gore, 2002]. Both relaxation and diffusion appear as signal attenuation; therefore, it is critical that their effects are separated and only the attenuation due to diffusion is considered while estimating DTI metrics. Studies looking at relaxation properties of the white matter have typically estimated them separately using MRI and then compared them with DTI metrics. For instance, two-compartment T_2 decay models have been fitted to MRI signal resulting in a short and a long T_2 compartment; it has now been established that the short T_2 compartment belonged to the myelin layer and the long T_2 compartment to the intra/extra-cellular water [MacKay et al., 2006; Mädler et al., 2008; Laule et al., 2004; Laule and Moore, 2018]. However, a thorough search of relevant literature revealed no studies that accounted for the effects of relaxation while estimating the

diffusion tensor.

The study described in this chapter is based on the computational framework previously developed [Baxter and Frank, 2013] which in turn, was based on the theoretical model of the white matter proposed by Sen and Basser [2005]. Simulations of the model have been carried out, both with and without accounting for T_2 relaxation, and the results compared. The parameters of the model have been varied (as described later) to represent healthy tissue, chronic and acute demyelination, and neuroinflammation to investigate the impact of T_2 relaxation on the estimated DTI metrics and their interpretation. The results of this study will be significant in understanding how T_2 relaxation in the white matter affects DTI, thereby improving the specificity of results obtained from *in vivo* DTI studies. The experiment has been carried out using both single and multi-compartment fitting of the acquired signal, as explained in later sections.

6.2 White matter model

6.2.1 Model assumptions

The geometry of the model was designed based on the following assumptions, which have been derived from the original computational framework [Baxter and Frank, 2013].

1. An axon was represented using a straight cylinder of a constant diameter throughout; with the myelin sheath represented using a larger cylinder enclosing the axon completely.

2. Diameters of all axon cylinders in the model are constant.

3. Diameters of all myelin cylinders in the model are constant, and greater than that of axon cylinders.

4. Axons are packed in a hexagonal array with constant spacing between adjacent cylinders throughout the array.

The selection of geometrical and other physiological parameters describing the model have been explained in detail in the following section. Several parameters, such as the diffusion coefficients of water in various compartments, have not been conclusively estimated for the white matter. In this study, they have been chosen either based on studies investigating similar properties for other cell types, or results from *in vivo* studies where available, as explained later.

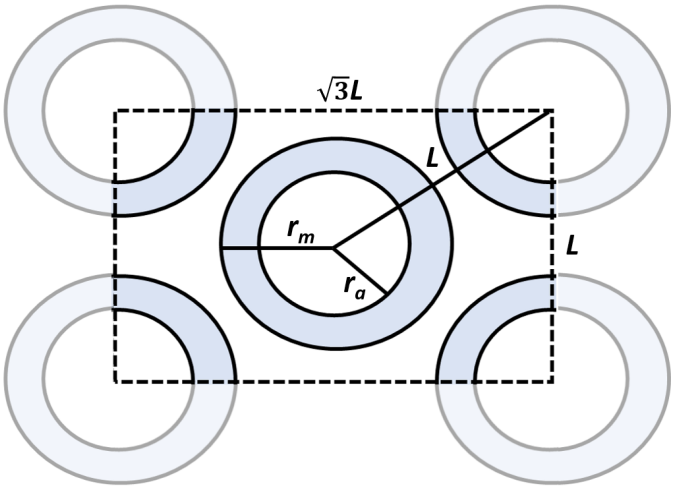

Figure 6.1: Schematic of the white matter model using cylinders to represent axon and myelin. Adjacent cylinders were spaced L μm apart. The rectangular region was infinitely replicated to create an array of cylinders. The schematic is based on Figure 1 in Baxter and Frank [2013].

6.2.2 Model design

The model consisted of a hexagonally packed array of axons represented by cylinders of radius r_a wrapped around by myelin layers represented by cylinders with a larger radius r_m. Adjacent cylinders in the array were spaced at a distance $L\mu$m apart. The packing density f of the hexagonal array was defined as the area fraction occupied by the axon-myelin structure.

$$f = \frac{2\pi r_m^2}{L * \sqrt{3}L} \tag{6.1}$$

The model as shown in Figure 6.1 constituted of three media - the axon, the myelin, and the ECS. Different parameters of the model included the diffusion coefficients of water molecules in the axon (D_a), the myelin (D_m), and the ECS (D_e), and the corresponding concentration of water molecules (C_a, C_m, C_e). Derived from Fick's first and second laws of diffusion, the probability of transition of a water molecule from one medium to the other has been proposed as a function of its concentration and diffusion coefficient [Baxter and Frank, 2013]:

$$p_{AB} = \frac{C_B\sqrt{D_B}}{C_A\sqrt{D_A}} \tag{6.2}$$

where A is a medium with a higher flux than medium B, C_A, C_B, D_A, and D_B represent the concentrations and diffusion coefficients of water molecules in A and B respectively, and p_{AB} is the probability of transition of a molecule from A to B. The probability of water diffusion through the membrane in the opposite direction, i.e., from a low flux medium to a high flux medium was set as 1. With the probabilities of transition or permeability having been so defined, a model implemented with an initial condition will achieve a quasi steady state within a given time. Quasi steady state is when the conditions within a system change slowly enough to be considered constant. The range of values used in this experiment for the model parameters have been shown in Table 6.1 and the rationale for choosing these values have been given below.

For all experiments, the transverse relaxation time (T_2) of water molecules in the whole white matter was set as 110 ms [Wansapura et al., 1999], and that of various compartments were set as: $T_{2m} = 12$ ms, $T_{2a} = T_{2e} = 90$ ms, where 'm' denotes myelin water and 'a' and 'e' denote the axonal and extra-cellular water molecules respectively. These values agreed with results of several prior *in vivo* and *in vitro* studies [MacKay and Laule, 2016; Andrews et al., 2006; Laule and Moore, 2018; Does and Gore, 2002; Lancaster et al., 2003] but were set based on a prior study carried out at 3 T [Deoni et al., 2013]. Since DTI is a T_2-weighted MRI, the effects of longitudinal relaxation (T_1) are considered negligible and were therefore not accounted for in this study.

Myelin and axon radii were similarly estimated based on published literature. Specifically, they were based on fibre sizes in the corpus callosum, where radii of around 0.7 μm have been observed to make up the major portion [De Santis et al., 2016; Liewald et al., 2014; Aboitiz et al., 1992]. To represent larger diameter fibres, axon radii of $r_a = 1.2$ μm, 1.75 μm, 2.2 μm, and 3 μm (reported largest diameter in the corpus callosum by De Santis et al. [2016])) were simulated for all sets of initial conditions. This enabled mapping the patterns of observed changes with variations in fibre diameter.

The g-ratio, which is the ratio of axon radius to myelin radius, has been reported to be fairly constant in the white matter. Theoretically, the optimum g-ratio has been estimated to be 0.65 [Rushton, 1951]; and several studies have reported *in vivo* g-ratios close to this value [Berman et al., 2018; Thapaliya et al., 2018; Mohammadi et al., 2015]. This gave myelin radii of 1.076 μm, 1.85 μm, 2.7 μm, 3.38 μm, and 4.615 μm for corresponding axon radii.

The arrangement of axons *in vivo* has not yet been conclusively established, although studies have hinted at complex morphologies that include dispersion,

Table 6.1: Summary table containing the range of values of parameters used in the model (for healthy white matter and disease cases). A full list of the different model conditions simulated is given in appendix section A.7.4.

Parameter	**Value**	**Parameter**	**Value**
T_2	110 ms at 3 T	f	0.55 - 0.8
T_{2m}	12 ms at 3 T	L	1.752 - 2.76 μm for r_a = 0.7 μm, 7.517 - 11.85 μm for r_a = 3 μm
$T_{2a} = T_{2e}$	90 ms at 3 T	C_m	8% - 13 %
r_a	0.7 - 3 μm	g	0.65 - 0.85
r_m	0.823 - 1.076 μm for r_a = 0.7 μm, 3.53 - 4.615 μm for r_a = 3 μm	D_m	$0.3 * 10^{-5}$ cm^2/s
D_e	$0.05 * 10^{-5} - 2 * 10^{-5}$ cm^2/s	D_a	$2 * 10^{-5}$ cm^2/s

undulation, and bends [Abdollahzadeh et al., 2019]. In this study, the axons were arranged in a hexagonal packing array, following several prior studies [Baxter and Frank, 2013; Peled, 2007] since it offered a maximum packing density of 0.907 which may support packing densities as observed in physiology. Since extra-cellular volume has been reported to be about 20% of the total brain volume [Nicholson, 2001], assuming the same in the white matter gave a fibre packing density (f) of 0.8. Using equation 6.1, this results in a fibre spacing (L) of 2.29 μm for $r_a = 0.7$ μm and 9.827 μm for $r_a = 3$ μm. The values of L for the remaining axon radii have been given in appendix section A.7.4.

The concentrations of water molecules in various model compartments were estimated based on prior *in vivo* and post-mortem studies on myelin water fraction [Meyers et al., 2017; Hwang et al., 2010; Du et al., 2007; Whittall et al., 1997], which has been estimated to be about 0.13. Based on this, a base concentration of C (100 particles per μm^3) and $C_m = 0.13C$ in healthy tissue were defined. Following Peled [2007], the remaining 87% was distributed between axonal and ECS compartments weighted by their volume. For each value of r_a in healthy tissue, this gave $C_a = 0.55C$ and $C_e = 0.32C$ in healthy tissue. The diffusion coefficients of water molecules in these compartments were estimated as $D_m = 0.3{*}10^{-5}$ cm^2/s, and $D_a = D_e = 2{*}10^{-5}$ cm^2/s [Peled, 2007; Andrews et al., 2006; Latour et al., 1994].

Several of the above parameter values differ from that used in the original theoretical model by Sen and Basser [2005] and later by Baxter and Frank [2013]. However Sen and Basser [2005] has acknowledged that their values were based on reasonable approximations, often based on values estimated in other cell types. In

this study, the model parameters have been based on results from several published studies, both *in vivo* and post-mortem, so they may represent the physiology more accurately. While the above values represent healthy physiology, variations in these parameters representing demyelination and neuroinflammation have been modelled as described below.

6.2.2.1 Demyelination

Demyelination is the process of disintegration of the myelin layers around an axon due to pathological or physiological processes. It was represented in this study following the process in multiple sclerosis (MS), which has been established to be a disease affecting the white matter. In MS, demyelination has been reported to be followed by the body's attempts at remyelination, however the myelin sheaths typically remain thinner than before [Franklin and ffrench-Constant, 2008].

In this study, the g-ratio has been increased from 0.65 (healthy) up to 0.85 to represent MS demyelinating lesions – with the higher values representing newer lesions. These values have been based on prior *in vivo* and post-mortem studies on MS [Yu et al., 2019; Stikov et al., 2015; Albert et al., 2007; Campbell et al., 2018]. Accompanying this loss of myelin, a decrease in myelin water fraction down to 8% and less has also been reported in MS [Vavasour et al., 2018; Kolind et al., 2012]. Based on this, the value of C_m has been progressively reduced from 13% to 8% with increasing g-ratio in demyelination. Values of C_a and C_e have been varied accordingly. No corresponding changes in T_{2m} have been reported in demyelination. Rather, an absence of changes in T_{2m} in demyelination in MS has been observed in a few prior studies [Vavasour et al., 2018; Tozer et al., 2005].

Two types of demyelination mechanisms have been modelled in this study – acute and chronic. Acute lesions are typically softer than healthy tissue; this has been represented by an increase in the extracellular space and therefore the water content (varying f and keeping L constant at its healthy tissue value). Chronic lesions are typically stiffer than healthy tissue; this has been represented by a shrinkage of the fibre tract and therefore increased cellular deposits (varying L and keeping f constant at its healthy value) [Pietsch and Tournier, 2015; Urbanski et al., 2019]. These two types of demyelination mechanisms have been shown in a schematic in Figure 6.2. The model parameters for different values of r_a have been given in appendix section A.7.4.

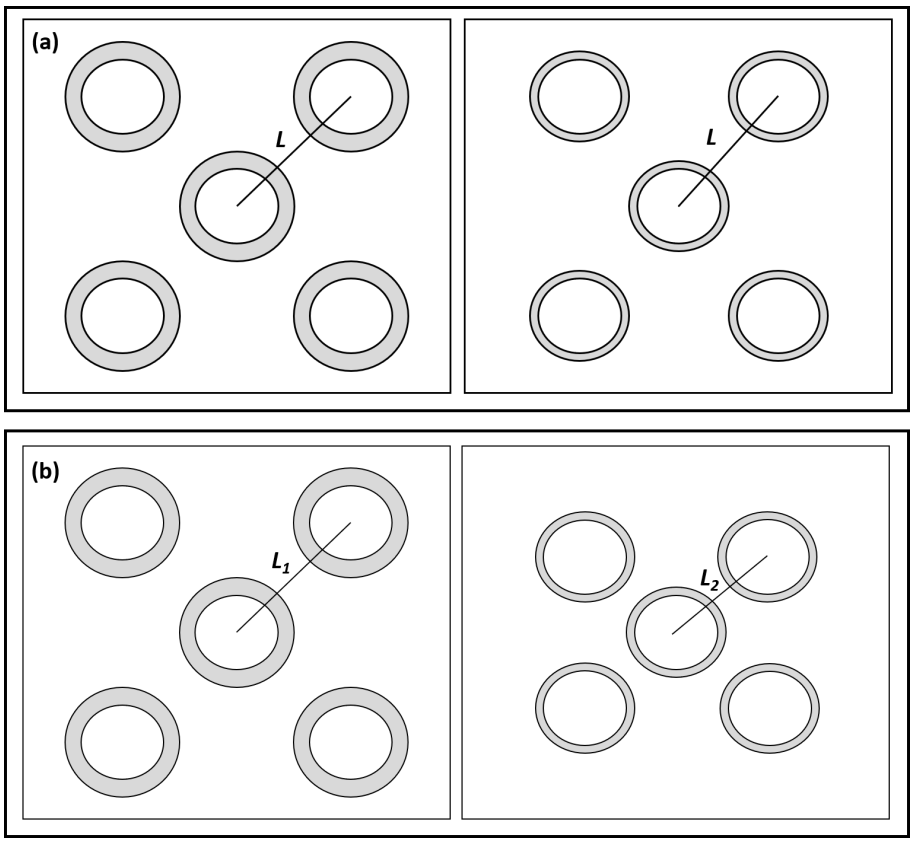

Figure 6.2: (a) Left: Healthy tissue; Right: Tissue in acute demyelinating lesions – the extracellular volume fraction increases while the spacing between axons stays constant (b) Left: Healthy tissue; Right: Tissue in chronic demyelinating lesions – the extracellular volume fraction is kept constant by shrinking the fibre tract so that axonal spacing decreases.

6.2.2.2 Neuroinflammation

Neuroinflammation is defined as an inflammatory process in the central nervous system, regulated by microglia and astrocytes. When this process is successfully controlled, it may have protective effects such as promoting recovery and tissue regrowth after infections [DiSabato et al., 2016]. However, in pathological conditions the process of neuroinflammation is triggered but often not terminated, leading to oedema and tissue damage. The detrimental mechanisms and effects of neuroinflammation have been widely studied [Tohidpour et al., 2017]. Recent findings using DTI and other advanced techniques based on diffusion have revealed the significance of neuroinflammation in several diseases including schizophrenia, multiple sclerosis, and Alzheimer's disease [Pasternak et al., 2016; Wang et al., 2015a, 2019].

An increased cellularity (number of cells) and an increased ECS volume in

the white matter are two features of neuroinflammation that have been reported in several studies [Samara et al., 2020; Pasternak et al., 2015; Wang et al., 2011; Chiang et al., 2014; Taquet et al., 2019]. Based on these findings, neuroinflammation has been modelled through decreasing values of f and D_e. While a reduction in f represents an ECS expansion to accommodate cellular deposits, a reduction in D_e represents the corresponding increase in the number of cells within ECS hindering diffusion. Published literature on alterations in white matter parameters due to neuroinflammation, including in f and D_e, is not as extensive as that on demyelination. In this study, f has been varied with values 0.8, 0.75, 0.7, 0.65, 0.6, and 0.55 while correspondingly varying D_e with values 2, 1.5, 1, 0.5, 0.1, and 0.05 (10^{-5} cm^2/s). All other parameters have been kept the same as that of healthy tissue, except for L which will vary with f. These models were then simulated at different values of r_a; the corresponding parameter values have been given in appendix section A.7.4.

6.2.3 Model implementation

Several software packages are available for numerical modelling and DTI simulation of the white matter. For instance, Camino has implemented an algorithm that can acquire a DTI signal through the simulated diffusion of water molecules in simple or complex environments. Camino represents the white matter fibres using cylinders, with options to specify the packing arrangement, membrane permeability, and whether the fibres are crossing. It also allows specification of the DTI pulse sequence to simulate the scan. However, some limitations of Camino have been demonstrated previously including better simulation in simplified designs of the white matter, more number of time steps within a scan pulse, and a larger computing time to finish simulations [Balls and Frank, 2009]. Other numerical simulation approaches have also been proposed for both model and DTI design and simulation, such as SpinDoctor, Diffusion Microscopist Simulator (DMS) and its upgraded version Microstructure Environment Designer with Unified Sphere Atoms (MEDUSA) [Ginsburger et al., 2019; Yeh et al., 2013; Li et al., 2019]. In the study described in this chapter, the Monte Carlo diffusion simulator 'MCell' was used to simulate the white matter structure, and the software 'DIFSIM' to acquire the DTI signal. The open source graphics software 'Blender' was used to design the model, which was then used by MCell for simulation. Descriptions of Blender, MCell, and DIFSIM along with relevant details of their diffusion and DTI simulation algorithms have been provided in appendix section A.7.1.

In MCell, the concentrations of water molecules in the three compartments

were required to be in the units of mols/L. At each boundary, the transition of water molecules from one compartment to the other was achieved using MCell reactions. The reaction or transition probability p_{AB} at each boundary was calculated for each simulation using equation 6.2 and the corresponding reaction rate to be set in MCell was estimated as p_{AB}/pbf, where the probability factor pbf was computed using the equation [Gupta et al., 2018]:

$$pbf = \frac{10^{11} * A}{2 * N_{av}} \sqrt{(\frac{\pi * \Delta t}{D})} \tag{6.3}$$

where A is the surface grid density in MCell, N_{av} is the Avogadro's constant, Δt is the simulation time step, and D is the diffusion coefficient of the molecule undergoing transition at the boundary.

For the main simulation study, the DTI signal was acquired using a spin echo pulse of G = 4 G/cm at three different b-values (1000, 4000, and 8000 s/mm^2), and an echo time (TE) of 100 ms determined by the highest b-value used [Peled et al., 2009]. The corresponding pulse sequence parameters were: (i) Δ = 25.2 ms, δ = 22.2 ms for b = 1000 s/mm^2 (ii) Δ = 38.96 ms, δ = 36 ms for b = 4000 s/mm^2, and (iii) Δ = 48.69 ms, δ = 45.7 ms for b = 8000 s/mm^2. The schematic of a diffusion pulse is shown in Figure 2.4. Each simulation was run 5 times with different seed points to estimate experiment uncertainty in terms of standard deviation of measurements.

To unravel the associations between different model parameters and the signal acquired by DIFSIM, two simple systems were initially designed and simulated at a b-value of 1000 s/mm^2. The results have been given in section A.7.2 in the appendix. The patterns of change observed in simple geometries such as those simulated in section A.7.2 supported data interpretation in more complex geometries such as the white matter model. The cylinder radius, diffusion or simulation time, diffusion coefficient of the molecules, and permeability of the cylinder surface were observed to have an impact on FA, MD, RD, and AxD. Interestingly, axial diffusion was found to rise when diffusion in radial directions was increased by changing the cylinder radius or permeability. This was in agreement with the findings of Baxter and Frank [2013] where an increase in the longitudinal diffusion coefficient was observed as the exchange between compartments or permeability was increased. Although this could not be predicted by the theoretical model of Sen and Basser [2005], it appeared that an increase in radial diffusion may cause a corresponding increase in axial diffusion, detectable at a b-value of 1000 s/mm^2.

The simulations were run on a Tinis high performance computing system based on Lenovo NeXtScale nx360 M5 servers with 2 Intel Xeon E5-2630 v3 2.4

GHz (Haswell) 8-core processors constituting a node. In total, 70 models were designed with each of them representing either healthy tissue, demyelination, or neuroinflammation at a specific value of r_a (see section A.7.4 in appendix). Each model was simulated at three different b-values, with each simulation using one node of the Tinis system and taking an average of 10,000 seconds to complete. The total computing hours required to carry out this study was about 25 days.

6.2.3.1 Diffusion Tensor Estimation

In a typical DTI experiment the signal acquired is affected by diffusion in three dimensions, and the diffusion is represented by a tensor **D**. This has been given in equation 2.2:

$$S = S_0 e^{-b\mathbf{D}}$$

where **D** is the diffusion tensor characterising the diffusion in x, y, and z directions as well as the correlation between diffusion in these directions (equation 2.7):

$$\mathbf{D} = \begin{bmatrix} D_{xx} & D_{xy} & D_{xz} \\ D_{yx} & D_{yy} & D_{yz} \\ D_{zx} & D_{zy} & D_{zz} \end{bmatrix}$$

More details on the diffusion tensor has been given in chapter 2. The above equations do not account for the effects of T_2 relaxation on the acquired signal, and may lead to an over-estimation of molecular diffusion. In order to account for T_2 in DTI, equation 2.2 may be re-written as:

$$S = S_0 e^{-TE/T_2} e^{-b\mathbf{D}} \tag{6.4}$$

Deriving a compartmental model for equation 6.4, the acquired signal can be described as a sum of signal contributions from the different model compartments as given below:

$$S = S_0 \left[f_a e^{-TE/T_{2a}} e^{-b\mathbf{D}_a} + f_m e^{-TE/T_{2m}} e^{-b\mathbf{D}_m} + f_e e^{-TE/T_{2e}} e^{-b\mathbf{D}_e} \right] \tag{6.5}$$

where the ECS volume fraction $f_e = 1 - f$ and f_a and f_m are the axon and myelin volume fractions in the model schematic shown in Figure 6.1. The diffusion tensor and DTI metrics were estimated separately using equations 2.2 and 6.4 at three different b-values (1000, 4000, and 8000 s/mm^2) to compare results obtained with and without accounting for T_2 (110 ms). Compartmental diffusion tensors were

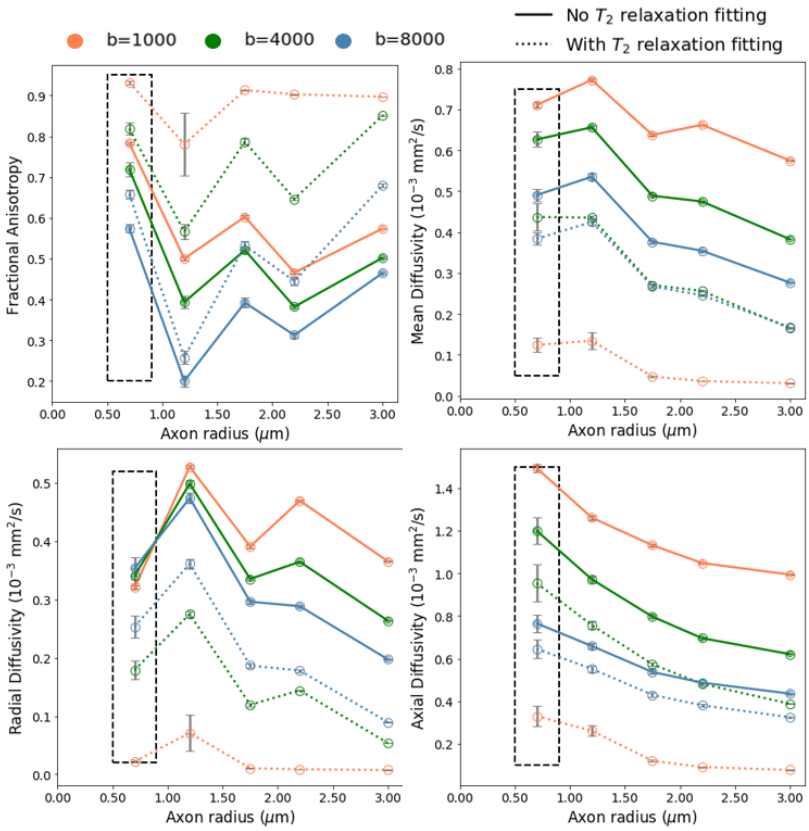

Figure 6.3: Variations in FA, MD, RD, and AxD with increasing axon radius. The rectangular region represents an average axon radius centred around 0.7 μm, which is the average size of fibres in the corpus callosum. Error bars represent the standard deviation of measurements taken from five repetitions of each experiment.

estimated using equation 6.5 containing three unknowns (D_a, D_m, D_e), with the signals acquired at three b-values and $T_{2m} = 12$ ms, $T_{2a} = T_{2e} = 90$ ms. Custom codes written in MATLAB using the fanDTasia toolbox [Barmpoutis and Vemuri, 2010], to fit the acquired signal to equations 2.2, 6.4, and 6.5 have been given in appendix section A.7.3.

6.3 Simulation Results

6.3.1 Healthy Tissue

It can be seen from the results in Figure 6.3 that for all three b-values, accounting for T_2 relaxation (equation 6.4)) resulted in a greater FA, and lower MD, RD, and AxD, than when not accounting for T_2 relaxation (equation 2.2)). Since both relaxation

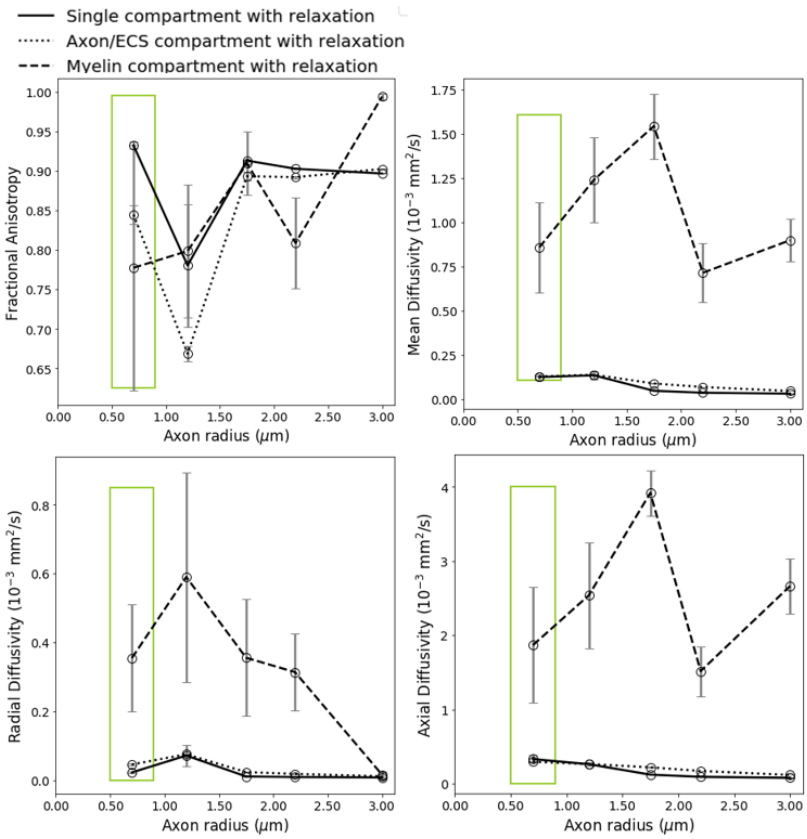

Figure 6.4: Data simulated from models representing healthy tissue, of different r_a. Data obtained from both single (at b = 1000 s/mm^2) and multi-compartment fitting have been plotted. The rectangular region represents an average axon radius centred around 0.7 μm, which is the average size of fibres in the corpus callosum. Error bars represent the standard deviation of measurements taken from five repetitions of each experiment.

and diffusion appears as signal attenuation, it is likely that accounting for relaxation in equation 6.4 provided a more accurate estimation of diffusion. It was observed that the disparity between DTI metrics computed using equations 2.2 and 6.4 decreased with increasing b-value.

The DTI metrics estimated using equation 6.4 was compared with that obtained through compartmental fitting of the signal (equation 6.5)) in Figure 6.4. Since $D_a = D_e$ and $T_{2a} = T_{2e}$ in the model, the signal acquired from axon and ECS as well as the DTI metrics estimated in these compartments had very similar values and therefore were plotted together in Figure 6.4. It was observed that the metrics calculated using compartmental fitting of the diffusion tensor differed from that obtained using single compartment fitting, although the general pattern of change

was preserved. The results showed the metrics computed from single-compartment fitting of the signal closely following the metrics of the ECS compartment, supporting prior hypothesis that the acquired DTI signal is dominated by the properties of water molecules in the ECS [Sen and Basser, 2005].

An interesting observation was made regarding the pattern of changes in FA, MD, RD, and AxD in Figures 6.3 and 6.4. The scientific consensus point to a decrease in FA and an increase in MD, RD, and AxD with increasing fibre size in the corpus callosum and other white matter tracts [Beaulieu, 2002, 2014]. While this was found to be the case for $r_a = 0.7 - 1$ μm (average fibre size in the white matter tract), deviations from this pattern were observed for other values of r_a. Rather, an oscillatory nature was observed in measurements, especially FA, with the oscillations appearing to plateau with increasing r_a. While this oscillatory pattern can be observed in results from prior studies [Berry et al., 2018], it has not been addressed in discussions. The underlying mechanisms giving rise to this pattern is not yet known, but more studies may be required to understand whether it is caused by uncertainties or discretisation in simulations or tensor calculations, or related to the diffusion process itself.

The increased measurement uncertainty observed specifically in the myelin compartment in multi-compartment fitting (Figure 6.4) may rise from the fact that the acquired signal S (equation 6.5) is heavily influenced by the water molecules in the ECS (and therefore also the axon compartment since their parameters are set equal in the model). This can be observed in Figure 6.4 where the total signal (single-compartment fitting) closely follows the signal from the axon/ECS compartments. Therefore, fitting this signal using a multi-compartment model probably attributed all uncertainty to the myelin compartment. Although the uncertainty is high, it is clear from Figure 6.4 that the variations in DTI metrics in the myelin compartment is different to that in the axon/ECS compartment or that obtained using single compartment fitting.

The choice of single or multi-compartment fitting of the acquired DTI signal may depend on different factors such as measurement uncertainty and utility in clinical practice. However, Figures 6.3 and 6.4 indicate that accounting for T_2 relaxation while estimating the diffusion tensor may result in more accurate estimates of FA, MD, RD, and AxD in *in vivo* studies.

6.3.2 Chronic Demyelination

Chronic demyelination has been modelled in this study by varying L with g-ratio while keeping f constant at its healthy value. Figures 6.5 and 6.6 shows the variations

in DTI metrics estimated with and without T_2 relaxation terms (equations 2.2 and 6.4) for an axon radius of $r_a = 1.75$ μm and b = 1000 s/mm^2. It may be observed that accounting for T_2 relaxation (equation 6.4) resulted in a greater FA, and lower MD, RD, and AxD, than when not accounting for T_2 relaxation, similar to results observed for healthy tissue. Slopes between data points were also different for the two cases, suggesting that the DTI metrics showing large variations in demyelination may in fact, be only slightly affected due to disease; and that the variations seen may likely be due to relaxation effects. Not accounting for these effects may therefore result in incorrect interpretations of results where changes in DTI metrics arising from T_2 relaxation are attributed to pathological mechanisms in demyelination.

If the DTI metrics obtained from the diffusion tensor estimated by accounting for T_2 relaxation are considered, there appears to be minimal to no variation with increasing g-ratio. This is in contrast to a decreasing FA and increasing diffusivities typically reported in demyelination [Pietsch and Tournier, 2015; Inglese and Bester, 2010]. This might be related to the way chronic demyelination has been modelled in this study – it has been compared with the results from acute demyelination model in the next section to interpret the findings together.

Figures 6.5 and 6.6 also show the DTI metrics, estimated using single and multi-compartment fitting accounting for T_2 relaxation, for $r_a = 1.75$ μm. It was observed that DTI metrics differed in both cases, although the general pattern of change was preserved. Similar to the observations made for healthy tissue, these results also showed the metrics computed from single-compartment fitting of the signal closely following the metrics of the ECS compartment. The uncertainty in measurement was higher in the case of multi-compartment fitting due to reasons explained in the previous section.

6.3.3 Acute Demyelination

Acute demyelination has been modelled in this study by varying f with the g-ratio and keeping L constant at its healthy value. Figures 6.7 and 6.8 shows the variations in DTI metrics estimated with and without T_2 relaxation terms (equations 2.2 and 6.4) for an axon radius of $r_a = 1.75$ μm and b = 1000 s/mm^2. It may be observed that accounting for T_2 relaxation (equation 6.4) resulted in a greater FA, and lower MD, RD, and AxD, than when not accounting for T_2 relaxation, similar to results observed for healthy tissue and chronic demyelination.

For chronic demyelination, minimal to no changes were observed in the DTI metrics when considering the measurements obtained by accounting for T_2 relaxation. In contrast, variations were observed in acute demyelination, although the intensity

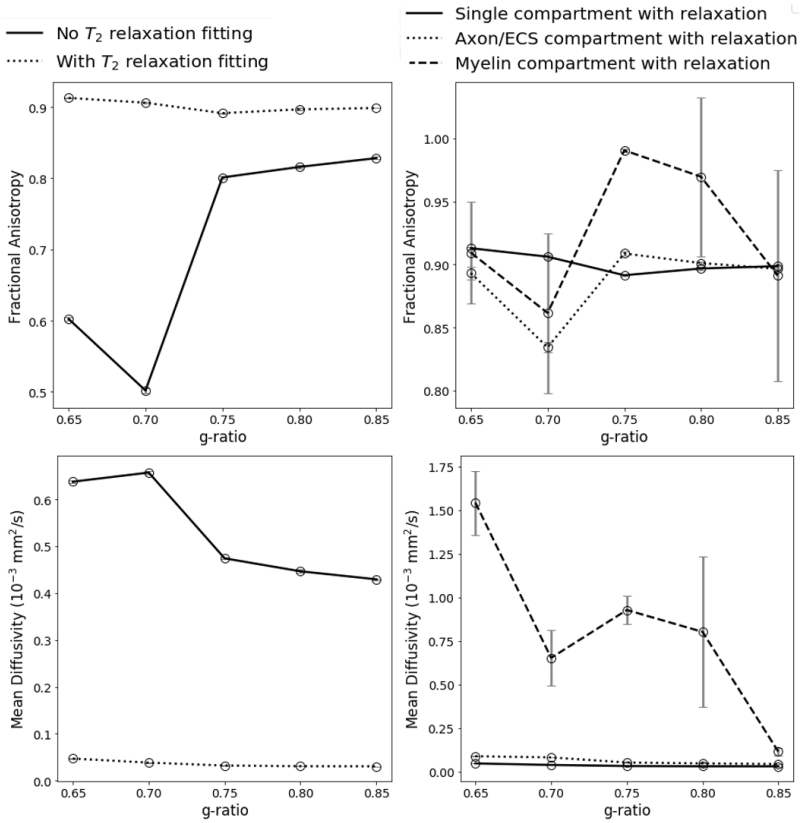

Figure 6.5: Variations in FA and MD with increasing g-ratio which represents an increasing severity of chronic demyelination. Error bars represent the standard deviation of measurements taken from five repetitions of each experiment. On the left: data from single compartment fitting at b=1000 s/mm^2 and r_a=1.75 μm, with and without accounting for T_2 relaxation. Error bars are not visible since the standard deviation is very small compared to the y-axis scale. On the right: data from single vs. multi-compartment fitting for r_a=1.75 μm. Single compartment data has been plotted for b=1000 s/mm^2. Legends for both columns have been given at the top of the figure.

of these variations was lower than when not accounting for T_2 relaxation. It may be due to the fact that while equation 2.2 estimated a diffusion tensor by attributing all signal attenuation to diffusion, equation 6.4 differentiated between the two processes and estimated a more accurate tensor using attenuation that may belong to diffusion. An increase in MD, RD, and AxD were observed which have been associated with demyelination in several published *in vivo* DTI studies [Pietsch and Tournier, 2015; Inglese and Bester, 2010]. In contrast to a decrease in FA typically reported, a very small increase in FA was observed.

When comparing the results from acute and chronic demyelination models

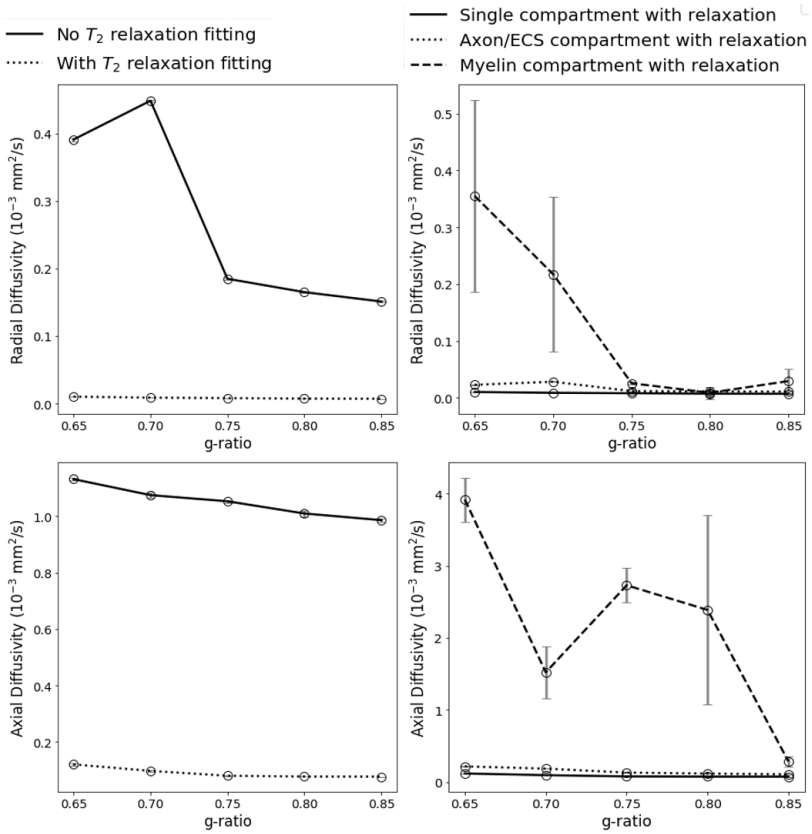

Figure 6.6: Variations in RD and AxD with increasing g-ratio which represents an increasing severity of chronic demyelination. Detailed plot descriptions can be found in Figure 6.5 caption.

with that from prior studies, it appeared that the mechanisms giving rise to reported results aligned more with acute rather than chronic demyelination. It was clear from the simulation results that accounting for T_2 relaxation while estimating the diffusion tensor may lead to more accurate measurements of diffusion. This may carry significant implications for interpretation of results in quantitative *in vivo* DTI studies of demyelination.

Figures 6.7 and 6.8 also show the DTI metrics, estimated using single and multi-compartment fitting accounting for T_2 relaxation, for $r_a = 1.75$ μm. Similar to the observations made for healthy tissue and chronic demyelination, these results also showed the metrics computed from single-compartment fitting of the signal closely following the metrics of the ECS compartment. The uncertainty in measurement was higher in the case of multi-compartment fitting due to reasons previously explained.

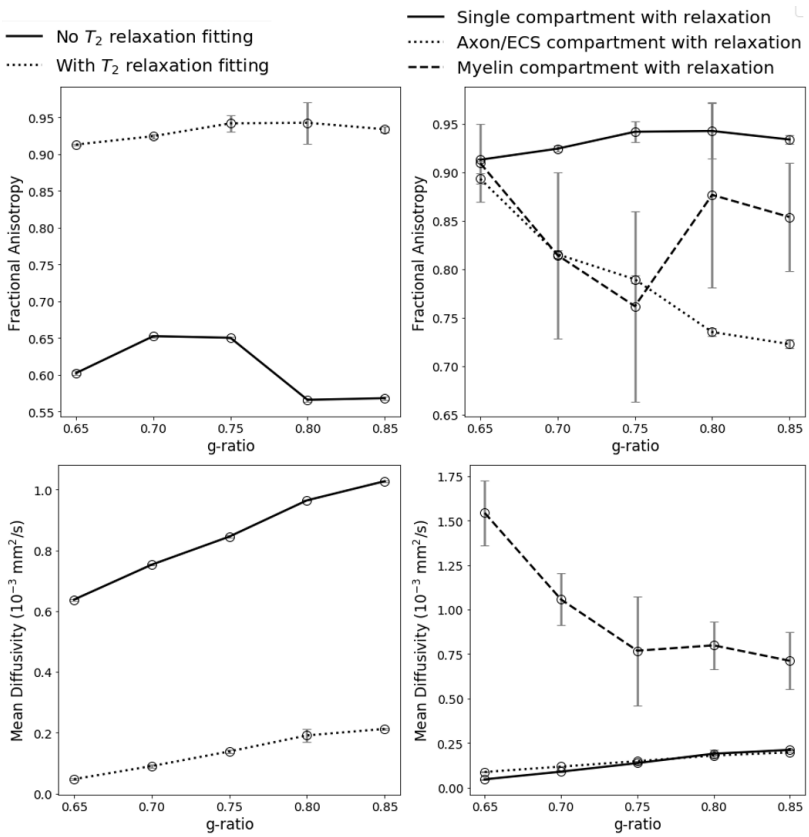

Figure 6.7: Variations in FA, MD, RD, and AxD with increasing g-ratio which represents an increasing severity of acute demyelination. Error bars represent the standard deviation of measurements taken from five repetitions of each experiment. On the left: data from single compartment fitting at b=1000 s/mm^2 and r_a=1.75 μm, with and without accounting for T_2 relaxation. Some error bars are not visible since the standard deviation is very small compared to the y-axis scale. On the right: data from single vs. multi-compartment fitting for r_a=1.75 μm. Single compartment data has been plotted for b=1000 s/mm^2. Legends for both columns have been given at the top of the figure.

6.3.4 Neuroinflammation

Neuroinflammation has been modelled in this study by an increasing f accompanied by a decreasing D_e. Figures 6.9 and 6.10 show the variations in DTI metrics estimated with and without accounting for T_2 relaxation (equations 2.2 and 6.4) for an axon radius of $r_a = 1.75$ μm and b = 1000 s/mm^2. Like previous results, the FA is underestimated whereas MD, RD, and AxD are overestimated when not accounting for T_2 while tracking acute demyelination. It can also be clearly seen that while there is little to no variation in the DTI metrics in the model of neuroinflammation,

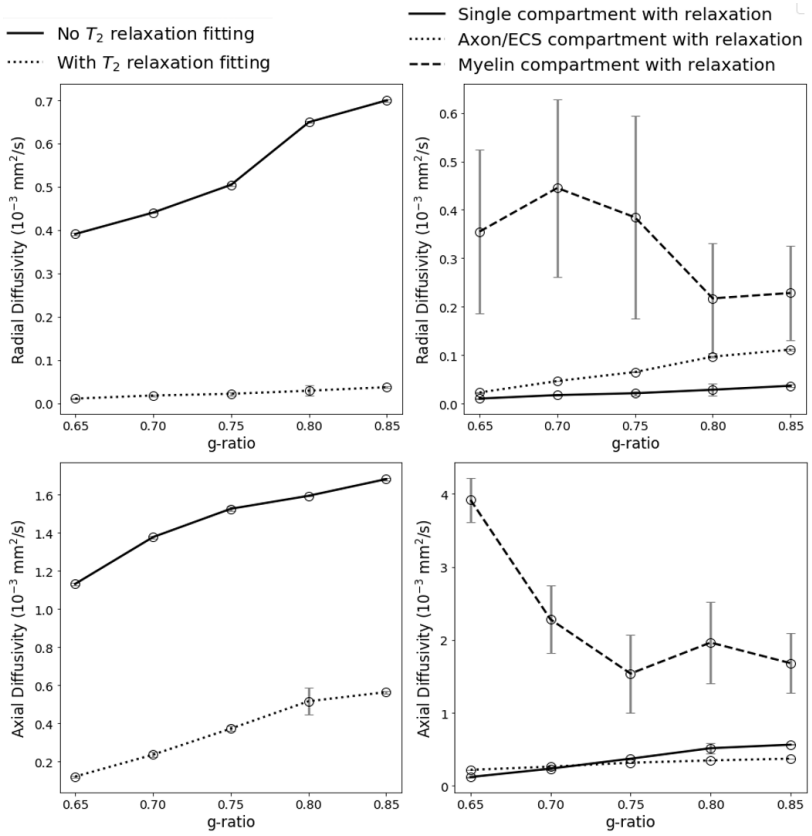

Figure 6.8: Variations in RD and AxD with increasing g-ratio which represents an increasing severity of acute demyelination. Detailed plot descriptions can be found in Figure 6.7 caption.

estimating the diffusion tensor without accounting for relaxation resulted in big variations, which may be misinterpreted as pathological changes in the tissue. This model of neuroinflammation clearly demonstrates the importance of accounting for T_2 relaxation in *in vivo* studies.

Figures 6.9 and 6.10 also shows the differences in single and multi-compartment fitting of data in the neuroinflammation model. The increased experimental uncertainty seen in the previous models may be observed here as well, localised to the myelin compartment. It is interesting to note that although parameters of the ECS compartment are varied to represent increasing inflammation, the resulting variations in DTI metrics are observed largely in the myelin compartment. This may likely be due to changes in myelin membrane permeability occurring because of changes in flux in the ECS (equation 6.2). However, the DTI metrics measured in the ECS compartment and therefore, that measured using single compartment fitting of the tensor, remain fairly constant with increasing f.

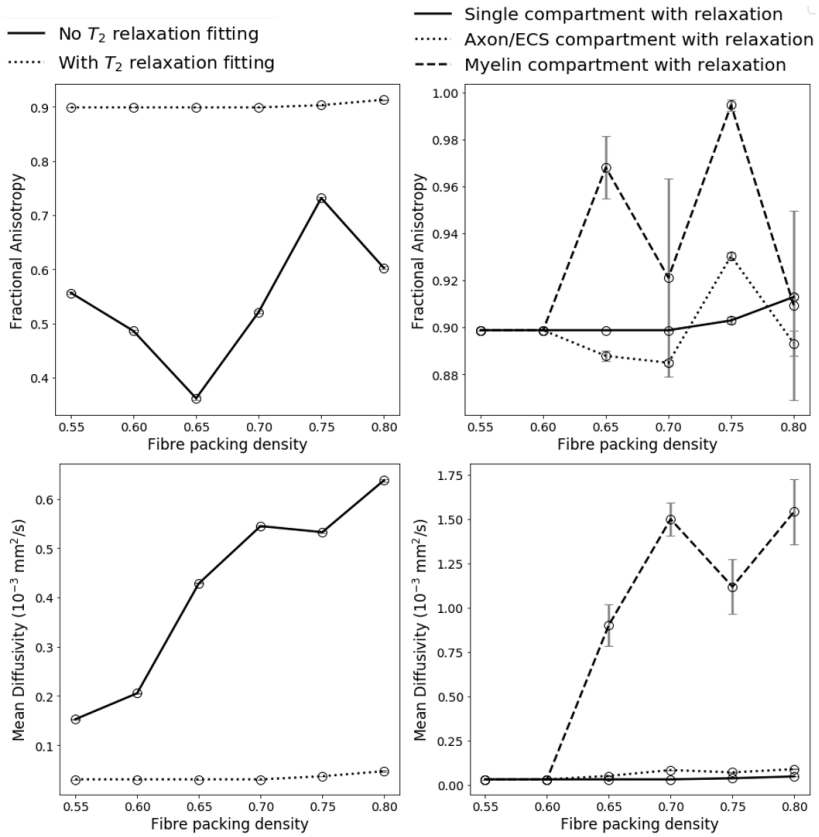

Figure 6.9: Variations in FA, MD, RD, and AxD with increasing fibre packing density which represents an increasing severity of neuroinflammation. Error bars represent the standard deviation of measurements taken from five repetitions of each experiment. On the left: data from single compartment fitting at b=1000 s/mm^2 and r_a=1.75 μm, with and without accounting for T_2 relaxation. Error bars are not visible since the standard deviation is very small compared to the y-axis scale. On the right: data from single vs. multi-compartment fitting for r_a=1.75 μm. Single compartment data has been plotted for b=1000 s/mm^2. Legends for both columns have been given at the top of the figure.

6.4 Conclusions

This chapter has demonstrated the significance as well as feasibility of accounting for T_2 relaxation effects when estimating the diffusion tensor. The impact of T_2 relaxation and water diffusion both appear as signal attenuation in DTI; therefore, it is likely that the attenuation due to relaxation is mistakenly attributed to diffusion and incorrect estimates of anisotropy and diffusivity are made. Several studies have now been published that report the values of $T2$ of the white matter at different magnetic field strengths [Wansapura et al., 1999]. A simple modification of the

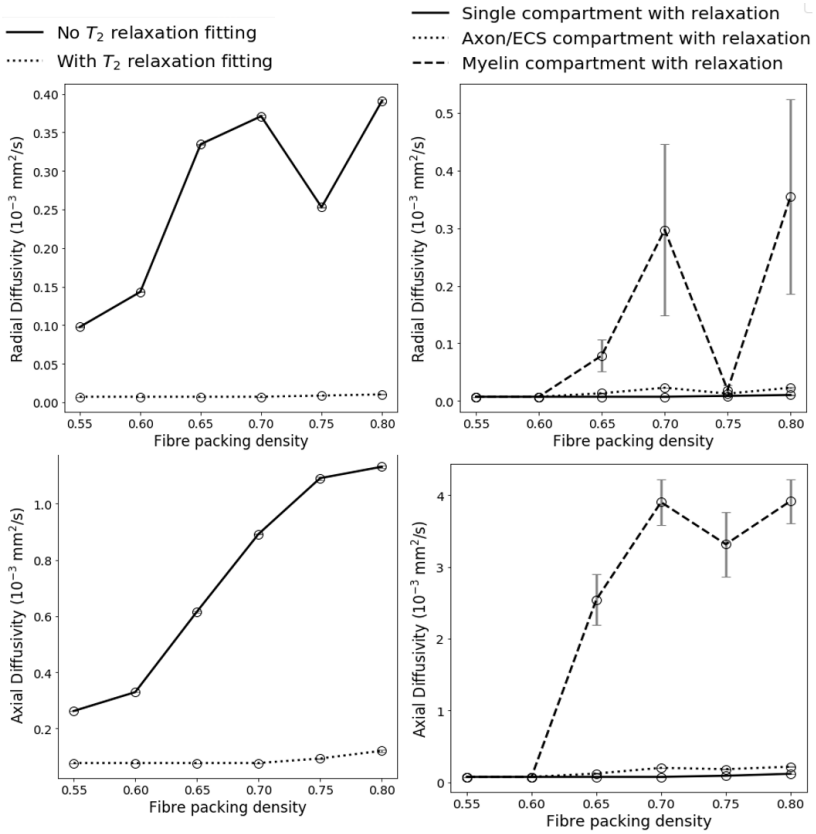

Figure 6.10: Variations in RD and AxD with increasing fibre packing density which represents an increasing severity of neuroinflammation. Detailed plot descriptions can be found in Figure 6.9 caption.

typical diffusion tensor equation might provide more accurate measurements of FA, MD, RD, and AxD; and this was shown to be feasible at a typical clinical b-value of 1000 s/mm^2.

An even more accurate picture of diffusion may be obtained by compartmental fitting of the diffusion tensor. In this chapter, three (axon, myelin, ECS) compartments were fitted to the acquired DTI signal to obtain separate diffusion tensors for each compartment (equation 6.5). However, this may not be suitable for clinical scans as the equation contains three unknowns and therefore, require signal acquired with at least three b-values to solve them. In this chapter, the signal was acquired at b=1000, 4000, and 8000 s/mm^2. However, b=4000 and 8000 s/mm^2 are not typically feasible in clinical scans due to gradient limitations or increased scan time.

A summary plot showing the values of FA, MD, RD, and AxD has been shown in Figure 6.11. The data used to plot this figure has been taken from

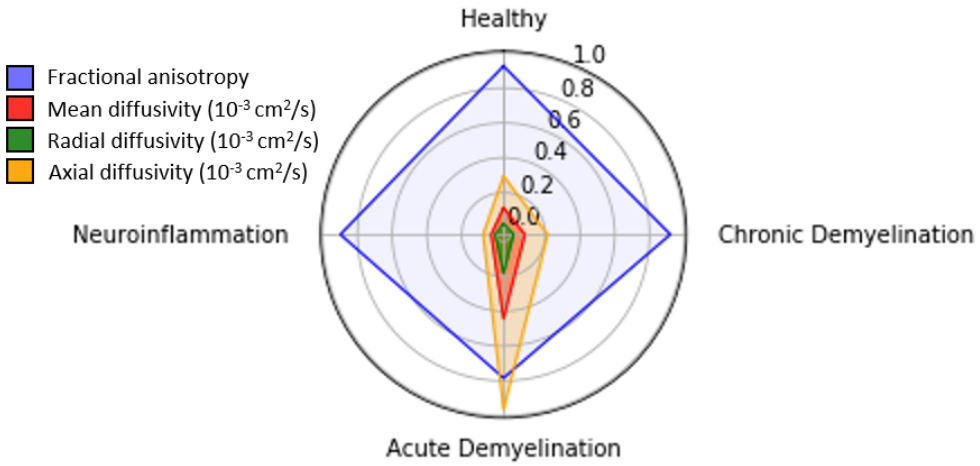

Figure 6.11: Radar plot showing variations in the four DTI parameters in the simulated healthy and disease cases.

model numbers 1, 5, 9, and 14 (models with $r_a = 0.7$ μm, b=1000 s/mm^2 and the most severe disease state modelled in case of demyelination and neuroinflammation, see appendix section A.7.4). It can be observed that compared to the values measured for the healthy tissue model, the largest deviations are present in the case of acute demyelination for all four DTI metrics. This plot indicates a greater likelihood in *in vivo* DTI studies of the reported changes in FA, MD, RD, and AxD occurring as a result of acute demyelination compared to chronic demyelination or neuroinflammation. Further disease states could be modelled, such as hydrocephalus or cytotoxic/cytogenic oedema as demonstrated by Sen and Basser [2005]. However, the model parameters used in their study are not representative of physiologically plausible values as discussed before and a thorough search of literature provided no studies that investigated changes in physiological factors such as g-ratio or packing density in these conditions. Therefore, a direct comparison of these disease states as modelled in Sen and Basser [2005] with that modelled in this study would not be appropriate.

A model of healthy tissue at different values of axon radius was presented in this chapter, along with models of three commonly found neurological mechanisms – chronic and acute demyelination, and neuroinflammation. It was observed that not accounting for T_2 relaxation when estimating the DTI metrics may lead to misinterpretation of results. This was clearly demonstrated in the neuroinflammation

model, where large variations seen in DTI metrics with disease severity disappeared when T_2 relaxation was accounted for. The results of this chapter has emphasised the significance of including T_2 relaxation terms in diffusion tensor estimation and the need to adopt this practice widely across the scientific community to obtain accurate metrics of diffusion.

There were some limitations to this study. Firstly, the model used to simulate healthy and diseased tissue was a very simplified model of the actual tissue geometry in the white matter. Secondly, the experimental uncertainty was estimated as the standard deviation of measurements from five repetitions of each simulation with different seed points. However, the uncertainty present in each experiment was not known. While this is partially accounted for in DIFSIM [Berry et al., 2018], there is a possibility that some uncertainty was associated with each simulation. Thirdly, the models of healthy and diseased tissue were simplified views of normal and pathological mechanisms occurring in the white matter. However, even with these limitations, the study presented in this chapter has clearly demonstrated the need to adopt T_2 relaxation terms in diffusion tensor estimation.

Chapter 7

Conclusions

7.1 Outcomes

The work carried out in this thesis focused on methodological and analysis aspects of clinically acquired DTI, and their utility in detecting subtle changes in the corpus callosum microstructure in patients with MCI and AD. The studies discussed in chapters 3, 4, 5, and 6 investigated several aspects of DTI and tackled the aims described in section 1.5. The novel contributions made by the thesis are summarised below and described in detail in the following sections.

1. The study carried out in Chapter 3 addresses Aim 1 (see Chapter 1). Several strategies to segment the corpus callosum on DTI were compared in terms of their impact on quantitative measurements made. It was found that atlas-based segmentation, which is a widely used method to delineate the corpus callosum, gave less accurate results when compared with other methods. This suggested that results of quantitative DTI studies that have used atlas-based segmentation of the corpus callosum may carry a greater level of uncertainty than initially thought. This is likely to be the case for other white matter tracts as well.

2. The study described in Chapter 4 tackles Aim 2. DTI metrics (FA, MD, RD, AxD) measured from the corpus callosum of patients with MCI and AD were compared with that of healthy individuals. While the whole corpus callosum ROI showed differences, these were localised to the sub-regions involved in motor functions of the brain. The results were also supported by neurophysiological assessments of participants where impairments in motor functions were observed. The results from this study have been published (see

section D.4) and contribute to understanding the early stages of Alzheimer's disease where non-memory related functions of the brain may be affected.

3. Chapter 5 addresses Aim 3. Two advanced DTI analysis methods were applied on clinical scans from ADNI to demonstrate the feasibility of their application in routine practice. The results from these studies supported the findings made in chapter 4, and also suggested that the alterations in the corpus callosum seen in MCI and AD may arise from a decreasing packing density of fibres which in turn, may be caused by underlying pathological mechanisms. These results demonstrated the scope of improving the specificity of clinical DTI studies using existing advanced analysis methods.

4. The experiments described in Chapter 6 tackles Aim 4. A model of the white matter was developed to investigate the impact of varying physiological parameters on the widely used DTI metrics (FA, MD, RD, AxD). Using this model, healthy tissue as well as various disease conditions were simulated. While fitting the diffusion tensor to the acquired signal, the impact of T_2 relaxation time was considered. It was found that not including T_2 relaxation terms while estimating the tensor led to less accurate results, as signal attenuation which in fact, was arising from relaxation was also considered to be arising from diffusion. While comparing results from healthy and disease models, it was found that acute demyelination (reduction in packing density) may be the dominating factor behind white matter alterations seen in *in vivo* studies, which supported results from previous chapters. Estimation of the diffusion tensor by including T_2 relaxation terms is a novel contribution of this thesis, as a thorough search of published literature revealed that this has not been carried out previously.

7.1.1 Segmentation strategies

Segmentation strategies were found to impact quantitative measurements of DTI parameters in chapter 3. The measured values of FA from atlas-based ROI of the corpus callosum were drastically reduced compared to the ground truth values although the patterns in change were preserved. This may have implications for future DTI studies as ROI derived from white matter atlases are widely used for analyses. Median value of the pixels in the ROI obtained by manual segmentation of the corpus callosum on sagittal FA images were observed to be closest to the ground truth.

The contribution of Chapter 3 is the development of a protocol for segmentation and analysis of data measured from the corpus callosum ROI and its sub-regions. The Hofer and Frahm scheme of sub-division was chosen as it divided the corpus callosum based on the region of the brain the fibres project to [Hofer and Frahm, 2006]. This enabled association of changes in DTI parameters with clinical and neurophysiological observations.

7.1.2 Corpus callosum in MCI and AD

The novel contribution from Chapter 4 (published, see section D.4) is the use of the above segmentation approach to delineate the corpus callosum in healthy controls and individuals with MCI and AD; and to use the measurements from this ROI to reveal alterations in motor-related sub-regions.

In healthy controls, the heterogeneity in the corpus callosum microstructure was revealed through variations in measured DTI parameters between sub-regions. This was associated with the presence of fibres of varying sizes with differing regional density in the tract. Regional differences were found to be a major source of variance in measurements in the corpus callosum and it was recommended that future investigations be carried out by sub-region.

Alterations in each of the corpus callosum sub-regions was investigated using MCI and AD patient data from ADNI. A decrease in FA and increases in MD, RD, and AxD was observed in specific regions that project to pre-motor, supplementary motor, and motor areas of the brain. The implications of these findings were revealed through the results of neurophysiological assessments that indicated a higher proportion of patients with MCI exhibited motor-related deficits including gait imbalances and tremors. A similar pattern was also observed for patients with AD although they were not considered conclusive due to the small cohort size.

7.1.3 Advanced methods for clinical DTI

The contribution made by Chapter 5 is the demonstration of the feasibility and utility of translating advanced DTI analysis tools to clinical practice. While these advanced methods have already been developed and validated, their use on clinical DTI scans have not yet been highlighted. The results obtained in Chapter 5 using NODDI-DTI and TractSeg analyses demonstrate the fact that albeit with limitations, these techniques improve the specificity of results obtained from conventional DTI analysis.

NODDI-DTI, a previously proposed adaptation of the more widely used

NODDI, showed a decrease in neurite density in a cohort of healthy subjects with ageing. This, accompanied by the simulation results from chapter 6, supported the interpretation of results in chapter 4 - a reduced packing density was revealed to be the dominant factor contributing to the decrease in FA and increases in MD, RD, and AxD observed with ageing, and potentially MCI and AD.

TractSeg, a machine learning approach to tractography, provided a different perspective to the results obtained in chapters 4 and 5, as it tracked the corpus callosum fibres along its length from one hemisphere to the other in contrast to an anterior-posterior direction. A reduction in FA was observed in MCI subjects compared to HC specifically in the fibres projecting to motor areas of the brain, supporting the results of the DTI analysis in chapter 4.

7.1.4 Modelling the white matter

The novel contributions made by Chapter 6 are two - (a) develop a model of healthy white matter, acute/chronic demyelination, and neuroinflammation using parameters that are as physiologically accurate as possible, (b) account for the effects of T_2 relaxation when estimating the diffusion tensor.

The white matter model developed in Chapter 6 was based on the theoretical model proposed by Sen and Basser [2005] and its numerical implementation by Baxter and Frank [2013]. While Baxter and Frank [2013] have used the values of physiological parameters proposed by Sen and Basser [2005], they were not physiologically accurate and were based on values estimated for other cell types. In Chapter 6, although the model framework is based on Sen and Basser [2005], the physiological parameters have been based on values reported in published *in vivo* and post mortem studies of the white matter. By implementing the model in this way, it is now possible to use it to derive conclusions regarding observations made in clinical DTI studies, enhancing the specificity offered by routine clinical DTI scans. In fact, the results indicated that white matter alterations, such as those seen in MCI and early AD (Chapter 4), may arise from acute demyelination, which has been modelled as a reduction in fibre packing density.

The other major contribution made by Chapter 6 is accounting for the effects of T_2 relaxation when estimating the diffusion tensor and DTI metrics (FA, MD, RD, AxD). While it has been acknowledged in prior studies that there is an effect of T_2 relaxation on DTI scans, it has not yet been quantified. The results described in Chapter 6 indicate that if the effects of T_2 relaxation are not accounted for, the FA might be under-estimated and the diffusivity metrics over-estimated. They highlight the importance of including T_2 terms in the diffusion tensor equation as well as the

need to estimate the value of T_2 in the white matter. While the study in Chapter 6 has also estimated the diffusion tensor in each white matter compartment by accounting for relaxation separately, it has shown that a single field-dependent value of T_2 for the white matter can improve the physiological relevance of the estimated diffusion by separating out the effects of relaxation.

7.2 Overarching themes, limitations, and scope for future work

Outcomes from the studies carried out in this thesis may be categorised into one of three overarching themes as described in the following sections. Some implications of these outcomes and scope for future work have been discussed.

7.2.1 Standardisation of analysis protocols

The comparison study between different segmentation strategies in section 3.5 has revealed that methodology plays a crucial role in the outcomes of quantitative DTI investigations including in the corpus callosum. Although patterns of change were preserved, absolute values of DTI parameters differed from the ground truth. This may carry implications for quantitative comparisons between studies with different methodologies, for instance in a meta-analysis. Manual segmentation has widely been thought of as the gold standard in image analysis and has been preferred for the work carried out in chapters 3, 4, and 5. However, manual delineation of white matter ROI is a demanding task and is limited in terms of reproducibility owing to human bias.

Automated segmentation of white matter structures including the corpus callosum may be developed based on the contrast between grey and white matter structures on FA images. Methods available include simple intensity thresholding and active contouring. It may be easier to automate the segmentation of the corpus callosum, compared to smaller white matter tracts due to their size and absence of clear boundaries. This limits the amount of detailed ROI analysis that may be carried out for smaller but important tracts such as the parahippocampal cingulum or the fornix which have been previously implicated in AD. A potential starting point to develop automated methods to delineate smaller tracts is TBSS, which compares white matter regions common to the subject images analysed. Atlas labels are currently used to identify tracts after carrying out TBSS, but as seen from section 3.5 this may be susceptible to errors. Semi-automated methods of segmentation that

ensures visual inspection of the ROI may be the best approach for smaller tracts.

The FSL tool '*eddy_correct*' has been used throughout in this thesis for consistency since its upgraded version '*eddy*' was released after the initial processing of data had been completed. The new tool '*eddy*' is computationally intensive and requires phase encoding information to eliminate eddy current artefacts and susceptibility distortions [Andersson and Sotiropoulos, 2016]. This has been validated to perform better than '*eddy_correct*' and recommended to be substituted in its place in future studies [Andersson and Sotiropoulos, 2016; Graham et al., 2016].

7.2.1.1 Involvement of corpus callosum in MCI and AD

Subtle alterations in DTI parameters were observed in specific corpus callosum sub-regions that suggested its involvement in motor impairments observed in MCI and potentially AD. Motor-related deficits in early stages of dementia have not been so extensively studied as cognitive impairments. The study outcomes in chapter 4 emphasised the importance of considering MCI and AD as part of a spectrum of neurodegenerative disorders that include other diseases such as Parkinson's disease, Huntington's disease, and multiple sclerosis. Symptoms characteristic of any one of these diseases may appear in the course of progression of others; for instance motor deficits have been observed in patients with pre-clinical AD while cognitive impairment has been observed in Parkinson's disease patients. Some support for retrogenesis was also obtained from the results in chapter 4 that suggested later-myelinating regions of the corpus callosum were more susceptible to ageing and disease-related mechanisms compared to those that myelinated earlier. Age and gender, two risk factors for AD as described in chapter 1, have been carefully considered in the study to account for their relationship with changes in DTI parameters.

A more detailed analysis of the AD cohort may be carried out when ADNI-3 releases further patient data. Once the required sample sizes are available, the inclusion criteria may be modified to select subjects who are both age and gender matched. This will enable a more accurate modelling of the data using regression or other statistical methods, with a reduced variance in measurements with a higher sample size.

7.2.2 Translation of research advances to clinical practice

Advances in the field of DTI offer sophisticated modelling of the acquired signal to provide more specific information on the white matter compared to conventional DTI

analysis. A majority of these techniques require that the images be acquired with advanced scan settings such as multiple HARDI shells, which may not be typical in clinical practice. There is a need to translate research advances into clinical settings to improve specificity in diagnosis and monitoring of patients. Mathematical adaptations and assumptions regarding the tissue model may enable this and offer a bridge between research advances and clinical practice. To demonstrate this, NODDI-DTI and TractSeg were applied on ADNI images to extract information on the corpus callosum that extended the results obtained from conventional DTI analysis.

A limitation of using modifications of advanced methods as described above, is the alterations made to the core assumptions of the original methods. This may quantitatively impact the measured parameters even if patterns in change are preserved. On the other hand, acquisition of superior DTI scans that are required by these methods may not be feasible in clinical settings. Translation of research advances to the clinic is thus susceptible to inaccuracies, but this is a trade-off with the amount of information that may be extracted.

7.2.3 Specificity of DTI

Advances in the field of DTI offer methods with a higher specificity compared to conventional analysis. However, it is equally important to improve this in a clinical setting. The white matter model developed in Chapter 6 offers a way to model healthy and pathological mechanisms and understand their impact on the DTI metrics. Moreover, it highlights the necessity of adopting T_2 terms in diffusion tensor equations as standard practice in order to obtain accurate estimates of diffusion.

While the simple white matter model was designed as a proof of concept, it offers flexibility for extension including more physiological variables such as cells in the ECS including astrocytes and microglia. The model may also be improved by extending the concept of cylindrical axons and myelin to truly reflect the physiology. The myelin layer may be modelled as a spiralling structure encapsulating single or multiple axons. Axons in turn may be modelled not as elongated cylindrical structures, but as fibres with bends, twists, undulations, and crossings. A more complete model of the white matter may help unravel its associations with DTI and investigate the sources contributing to different patterns in DTI parameter changes as described section 2.3 [Burzynska et al., 2010].

It must also be noted that the scan pulse used by DIFSIM was a pulsed gradient spin echo, whereas a quicker and advanced scan sequence may be used in clinical scanners. This may carry an implication for the modelling results, but

the nature of its impact is not currently known. This may be tested within the framework of DIFSIM in the future. When accounting for the effects of T_2, it is important that the value of T_2 used in the diffusion tensor equations is as accurate as possible. Although several studies have investigated this, the exact value of T_2 for a given field strength (including 3 T as used in this chapter) is still under debate; only a range of possible values is currently known.

7.3 Conclusions

This chapter has presented an overarching view of the work carried out in this thesis. Age, gender, and other risk factors may lead to courses of disease progression being different between individuals in MCI and AD. This implies a need to monitor patients longitudinally using advanced methods that may offer information about the underlying physiological mechanisms. This in turn requires consistent methodology and translation of research advances into clinical practice. The work carried out in this thesis demonstrates the feasibility of extracting subtle information from study cohorts using conventional DTI analysis, supported by more specific results obtained from advanced methods, and interprets this in a physiological context using results obtained from simulation. The data extracted using this approach revealed a key role of the fibre packing density in the corpus callosum in motor-related impairments in patients with MCI and potentially, AD.

References

Ali Abdollahzadeh, Ilya Belevich, Eija Jokitalo, Jussi Tohka, and Alejandra Sierra. Automated 3D Axonal Morphometry of White Matter. *Scientific Reports*, 9(1):6084, April 2019. ISSN 2045-2322. doi: 10.1038/s41598-019-42648-2.

F. Aboitiz, A. B. Scheibel, R. S. Fisher, and E. Zaidel. Fiber composition of the human corpus callosum. *Brain Research*, 598:143--153, 1992.

J. Acosta-Cabronero, G. B. Williams, G. Pengas, and P. J. Nestor. Absolute diffusivities define the landscape of white matter degeneration in Alzheimer's disease. *Brain*, 133(2):529--539, February 2010. ISSN 1460-2156 (Electronic) 0006-8950 (Linking). doi: 10.1093/brain/awp257.

J. Acosta-Cabronero, S. Alley, G. B. Williams, G. Pengas, and P. J. Nestor. Diffusion tensor metrics as biomarkers in Alzheimer's disease. *PLoS One*, 7(11):e49072, 2012. ISSN 1932-6203 (Electronic) 1932-6203 (Linking). doi: 10.1371/journal.pone.0049072.

F. Agosta, M. Pievani, S. Sala, C. Geroldi, S. Galluzzi, G. B. Frisoni, and M. Filippi. White matter damage in Alzheimer disease and its relationship to gray matter atrophy. *Radiology*, 258(3):853--863, March 2011. ISSN 1527-1315 (Electronic) 0033-8419 (Linking). doi: 10.1148/radiol.10101284.

Federica Agosta, Francesca Caso, Daniele Mattavelli, Massimiliano Copetti, Giuseppe Magnani, Elisa Canu, Alessandra Marcone, Monica Falautano, Giancarlo Comi, Andrea Falini, and Massimo Filippi. Grey matter and white matter MRI markers of cognitive progression in early and late onset variants of Alzheimer's disease. *Neurology*, 84(14 Supplement):P4.090, April 2015.

M. W. Albers, G. C. Gilmore, J. Kaye, C. Murphy, A. Wingfield, D. A. Bennett, A. L. Boxer, A. S. Buchman, K. J. Cruickshanks, D. P. Devanand, C. J. Duffy, C. M. Gall, G. A. Gates, A. C. Granholm, T. Hensch, R. Holtzer, B. T. Hyman, F. R. Lin, A. C. McKee, J. C. Morris, R. C. Petersen, L. C. Silbert, R. G. Struble, J. Q. Trojanowski, J. Verghese, D. A. Wilson, S. Xu, and L. I. Zhang. At the interface of sensory and motor dysfunctions and Alzheimer's disease. *Alzheimers Dement*, 11(1):70--98, January 2015. ISSN 1552-5279 (Electronic) 1552-5260 (Linking). doi: 10.1016/j.jalz.2014.04.514.

M. S. Albert, S. T. DeKosky, D. Dickson, B. Dubois, H. H. Feldman, N. C. Fox, A. Gamst, D. M. Holtzman, W. J. Jagust, R. C. Petersen, P. J. Snyder, M. C. Carrillo, B. Thies, and C. H. Phelps. The diagnosis of mild cognitive impairment due to Alzheimer's disease: Recommendations from the National Institute on Aging-Alzheimer's Association workgroups on diagnostic guidelines for Alzheimer's disease. *Alzheimers Dement*, 7(3):270--279, May 2011. ISSN 1552-5279 (Electronic) 1552-5260 (Linking). doi: 10.1016/j.jalz.2011.03.008.

Monika Albert, Jack Antel, Wolfgang Brück, and Christine Stadelmann. Extensive Cortical Remyelination in Patients with Chronic Multiple Sclerosis. *Brain Pathology*, 17(2):129--138, April 2007. ISSN 1015-6305. doi: 10.1111/j.1750-3639.2006.00043.x.

A. L. Alexander, J. E. Lee, M. Lazar, and A. S. Field. Diffusion tensor imaging of the brain. *Neurotherapeutics*, 4(3):316--29, July 2007. ISSN 1933-7213 (Print) 1878-7479 (Linking). doi: 10.1016/j.nurt.2007.05.011.

D. C. Alexander, P. L. Hubbard, M. G. Hall, E. A. Moore, M. Ptito, G. J. Parker, and T. B. Dyrby. Orientationally invariant indices of axon diameter and density from diffusion MRI. *Neuroimage*, 52(4):1374--1389, October 2010. ISSN 1095-9572 (Electronic) 1053-8119 (Linking).

doi: 10.1016/j.neuroimage.2010.05.043.

Daniel C Alexander. Multiple-fiber reconstruction algorithms for diffusion MRI. *White Matter in Cognitive Neuroscience: Advances in Diffusion Tensor Imaging and Its Applications*, 1064: 113--133, 2005. ISSN 0077-8923.

DANIEL C Alexander and KIRAN K Seunarine. Mathematics of crossing fibers. *Diffusion MRI: theory, methods, and applications. Oxford University Press, New York*, pages 451--464, 2010.

I. K. Amlien and A. M. Fjell. Diffusion tensor imaging of white matter degeneration in Alzheimer's disease and mild cognitive impairment. *Neuroscience*, 276:206--215, September 2014. ISSN 1873-7544 (Electronic) 0306-4522 (Linking). doi: 10.1016/j.neuroscience.2014.02.017.

J. L. Andersson and S. N. Sotiropoulos. An integrated approach to correction for off-resonance effects and subject movement in diffusion MR imaging. *Neuroimage*, 125:1063--1078, January 2016. ISSN 1095-9572 (Electronic) 1053-8119 (Linking). doi: 10.1016/j.neuroimage.2015.10.019.

Trevor J. Andrews, Michael T. Osborne, and Mark D. Does. Diffusion of myelin water. *Magnetic Resonance in Medicine*, 56(2):381--385, August 2006. ISSN 0740-3194. doi: 10.1002/mrm.20945.

B. A. Ardekani, A. H. Bachman, K. Figarsky, and J. J. Sidtis. Corpus callosum shape changes in early Alzheimer's disease: An MRI study using the OASIS brain database. *Brain Struct Funct*, 219(1):343--352, January 2014. ISSN 1863-2661 (Electronic) 1863-2653 (Linking). doi: 10.1007/s00429-013-0503-0.

Benjamin S. Aribisala, Maria C. Valdés Hernández, Natalie A. Royle, Zoe Morris, Susana Muñoz Maniega, Mark E. Bastin, Ian J. Deary, and Joanna M. Wardlaw. Brain atrophy associations with white matter lesions in the ageing brain: The Lothian Birth Cohort 1936. *Eur Radiol*, 23(4): 1084--1092, April 2013. ISSN 1432-1084. doi: 10.1007/s00330-012-2677-x.

Y. Assaf and P. J. Basser. Composite hindered and restricted model of diffusion (CHARMED) MR imaging of the human brain. *Neuroimage*, 27(1):48--58, August 2005. ISSN 1053-8119 (Print) 1053-8119 (Linking). doi: 10.1016/j.neuroimage.2005.03.042.

Y. Assaf, T. Blumenfeld-Katzir, Y. Yovel, and P. J. Basser. AxCaliber: A method for measuring axon diameter distribution from diffusion MRI. *Magn Reson Med*, 59(6):1347--1354, June 2008. ISSN 0740-3194 (Print) 0740-3194 (Linking). doi: 10.1002/mrm.21577.

G. T. Balls and L. R. Frank. A simulation environment for diffusion weighted MR experiments in complex media. *Magn Reson Med*, 62(3):771--778, September 2009. ISSN 1522-2594 (Electronic) 0740-3194 (Linking). doi: 10.1002/mrm.22033.

M. L. Balthazar, C. L. Yasuda, F. R. Pereira, T. Pedro, B. P. Damasceno, and F. Cendes. Differences in grey and white matter atrophy in amnestic mild cognitive impairment and mild Alzheimer's disease. *Eur J Neurol*, 16(4):468--474, April 2009. ISSN 1468-1331 (Electronic) 1351-5101 (Linking). doi: 10.1111/j.1468-1331.2008.02408.x.

D. Barazany, P. J. Basser, and Y. Assaf. In vivo measurement of axon diameter distribution in the corpus callosum of rat brain. *Brain*, 132(Pt 5):1210--1220, May 2009. ISSN 1460-2156 (Electronic) 0006-8950 (Linking). doi: 10.1093/brain/awp042.

A. Barmpoutis and B.C. Vemuri. A unified framework for estimating diffusion tensors of any order with symmetric positive-definite constraints. In *2010 IEEE International Symposium on Biomedical Imaging: From Nano to Macro*, pages 1385--1388. IEEE, 2010.

J. Barnes, B. C. Dickerson, C. Frost, L. C. Jiskoot, D. Wolk, and W. M. van der Flier. Alzheimer's disease first symptoms are age dependent: Evidence from the NACC dataset. *Alzheimers Dement*, 11(11):1349--1357, November 2015. ISSN 1552-5279 (Electronic) 1552-5260 (Linking). doi: 10.1016/j.jalz.2014.12.007.

G. Bartzokis. Alzheimer's disease as homeostatic responses to age-related myelin breakdown. *Neurobiol Aging*, 32(8):1341--1371, August 2011. ISSN 1558-1497 (Electronic) 0197-4580 (Linking). doi: 10.1016/j.neurobiolaging.2009.08.007.

G. Bartzokis, D. Sultzer, P. H. Lu, K. H. Nuechterlein, J. Mintz, and J. L. Cummings. Heterogeneous age-related breakdown of white matter structural integrity: Implications for cortical

‘‘disconnection" in aging and Alzheimer’s disease. *Neurobiol Aging*, 25(7):843--851, August 2004. ISSN 0197-4580 (Print) 0197-4580 (Linking). doi: 10.1016/j.neurobiolaging.2003.09.005.

G. Bartzokis, P. H. Lu, K. Tingus, M. F. Mendez, A. Richard, D. G. Peters, B. Oluwadara, K. A. Barrall, J. P. Finn, P. Villablanca, P. M. Thompson, and J. Mintz. Lifespan trajectory of myelin integrity and maximum motor speed. *Neurobiol Aging*, 31(9):1554--1562, September 2010. ISSN 1558-1497 (Electronic) 0197-4580 (Linking). doi: 10.1016/j.neurobiolaging.2008.08.015.

George Bartzokis. Age-related myelin breakdown: A developmental model of cognitive decline and Alzheimer’s disease. *Neurobiology of Aging*, 25(1):5--18, 2004. ISSN 01974580. doi: 10.1016/j.neurobiolaging.2003.03.001.

P. J. Basser, J. Mattiello, and D. Le Bihan. Estimation of the effective self-diffusion tensor from the NMR spin echo. *J Magn Reson B*, 103(3):247--254, 1994a. ISSN 1064-1866 (Print) 1064-1866 (Linking).

P. J. Basser, J. Mattiello, and D. Le Bihan. MR diffusion tensor spectroscopy and imaging. *Biophysical Journal*, 66:259--267, 1994b.

Peter J Basser and Carlo Pierpaoli. Microstructural and physiological features of tissues elucidated by quantitative-diffusion-tensor MRI. *J Magn Reson B*, 111:209--219, 1996. ISSN 1090-7807.

Seyed Amir Hossein Batouli and Valiallah Saba. At least eighty percent of brain grey matter is modifiable by physical activity: A review study. *Behav Brain Res*, 332:204--217, August 2017. ISSN 0166-4328. doi: 10.1016/j.bbr.2017.06.002.

F. Bature, B. Guinn, D. Pang, and Y. Pappas. Signs and symptoms preceding the diagnosis of Alzheimer’s disease: A systematic scoping review of literature from 1937 to 2016. *BMJ Open*, 7(8):e015746, August 2017. ISSN 2044-6055 (Electronic) 2044-6055 (Linking). doi: 10.1136/bmjopen-2016-015746.

G. T. Baxter and L. R. Frank. A computational model for diffusion weighted imaging of myelinated white matter. *Neuroimage*, 75:204--212, July 2013. ISSN 1095-9572 (Electronic) 1053-8119 (Linking). doi: 10.1016/j.neuroimage.2013.02.076.

C. Beaulieu. The basis of anisotropic water diffusion in the nervous system - a technical review. *NMR Biomed*, 15(7-8):435--455, November 2002. ISSN 0952-3480 (Print) 0952-3480 (Linking). doi: 10.1002/nbm.782.

C. Beaulieu and P. S. Allen. Determinants of anisotropic water diffusion in nerves. *Magnetic Resonance in Medicine*, 31(4):394--400, April 1994a. ISSN 0740-3194 (Print) 0740-3194 (Linking).

C. Beaulieu and P. S. Allen. Water diffusion in the giant axon of the squid: Implications for diffusion-weighted MRI of the nervous system. *Magn Reson Med*, 32(5):579--583, 1994b.

Christian Beaulieu. The Biological Basis of Diffusion Anisotropy. In *Diffusion MRI: From Quantitative Measurement to In Vivo Neuroanatomy*, pages 155--183. Academic Press, 2014. ISBN 978-0-12-396460-1. doi: 10.1016/b978-0-12-396460-1.00008-1.

I. J. Bennett, D. E. Greenia, P. Maillard, S. A. Sajjadi, C. DeCarli, M. M. Corrada, and C. H. Kawas. Age-related white matter integrity differences in oldest-old without dementia. *Neurobiol Aging*, 56:108--114, August 2017. ISSN 1558-1497 (Electronic) 0197-4580 (Linking). doi: 10.1016/j.neurobiolaging.2017.04.013.

S. Berman, K. L. West, M. D. Does, J. D. Yeatman, and A. A. Mezer. Evaluating g-ratio weighted changes in the corpus callosum as a function of age and sex. *Neuroimage*, 182:304--313, November 2018. ISSN 1095-9572 (Electronic) 1053-8119 (Linking). doi: 10.1016/j.neuroimage.2017.06.076.

David B Berry, Benjamin Regner, Vitaly Galinsky, Samuel R Ward, and Lawrence R Frank. Relationships between tissue microstructure and the diffusion tensor in simulated skeletal muscle. *Magn Reson Med*, 80(1):317--329, July 2018. ISSN 1522-2594. doi: 10.1002/mrm.26993.

R. A. Bhadelia, L. L. Price, K. L. Tedesco, T. Scott, W. Q. Qiu, S. Patz, M. Folstein, I. Rosenberg, L. R. Caplan, and P. Bergethon. Diffusion tensor imaging, white matter lesions, the corpus callosum, and gait in the elderly. *Stroke*, 40(12):3816--3820, December 2009. ISSN 1524-4628 (Electronic) 0039-2499 (Linking). doi: 10.1161/STROKEAHA.109.564765.

KATHERINE M. Bishop and DOUGLAS Wahlsten. Sex Differences in the Human Corpus Callosum: Myth or Reality? *Neurosci Biobehav Rev*, 21(5):581--601, January 1997. ISSN 0149-7634. doi: 10.1016/S0149-7634(96)00049-8.

Kim T. Blackwell. Particle-Based Stochastic Simulators. In Dieter Jaeger and Ranu Jung, editors, *Encyclopedia of Computational Neuroscience*. Springer, New York, NY, 2014. ISBN 978-1-4614-7320-6. doi: 10.1007/978-1-4614-7320-6_191-1.

F. Bloch. Nuclear Induction. *Phys. Rev.*, 70(7-8):460--474, October 1946. doi: 10.1103/PhysRev.70.460.

B. Bosch, E. M. Arenaza-Urquijo, L. Rami, R. Sala-Llonch, C. Junqué, C. Solé-Padullés, C. Peña-Gómez, N. Bargalló, J. L. Molinuevo, and D. Bartrés-Faz. Multiple DTI index analysis in normal aging, amnestic MCI and AD. Relationship with neuropsychological performance. *Neurobiol Aging*, 33(1):61--74, January 2012. ISSN 1558-1497 (Electronic) 0197-4580 (Linking). doi: 10.1016/j.neurobiolaging.2010.02.004.

N. Boublay, A. M. Schott, and P. Krolak-Salmon. Neuroimaging correlates of neuropsychiatric symptoms in Alzheimer's disease: A review of 20 years of research. *Eur J Neurol*, 23(10):1500--1509, October 2016. ISSN 1468-1331 (Electronic) 1351-5101 (Linking). doi: 10.1111/ene.13076.

F. Branzoli, E. Ercan, R. Valabregue, E. T. Wood, M. Buijs, A. Webb, and I. Ronen. Differentiating between axonal damage and demyelination in healthy aging by combining diffusion-tensor imaging and diffusion-weighted spectroscopy in the human corpus callosum at 7 T. *Neurobiol Aging*, 47:210--217, November 2016. ISSN 1558-1497 (Electronic) 0197-4580 (Linking). doi: 10.1016/j.neurobiolaging.2016.07.022.

A. M. Brickman, I. B. Meier, M. S. Korgaonkar, F. A. Provenzano, S. M. Grieve, K. L. Siedlecki, B. T. Wasserman, L. M. Williams, and M. E. Zimmerman. Testing the white matter retrogenesis hypothesis of cognitive aging. *Neurobiol Aging*, 33(8):1699--1715, August 2012. ISSN 1558-1497 (Electronic) 0197-4580 (Linking). doi: 10.1016/j.neurobiolaging.2011.06.001.

J. P. Brion. Neurofibrillary tangles and Alzheimer's disease. *Eur Neurol*, 40(3):130--140, October 1998. ISSN 0014-3022. doi: 10.1159/000007969.

Robert W Brown, Y-C Norman Cheng, E Mark Haacke, Michael R Thompson, and Ramesh Venkatesan. *Magnetic Resonance Imaging: Physical Principles and Sequence Design*. John Wiley & Sons, 2014. ISBN 0-471-72085-2.

P. D. Bruen, W. J. McGeown, M. F. Shanks, and A. Venneri. Neuroanatomical correlates of neuropsychiatric symptoms in Alzheimer's disease. *Brain*, 131(Pt 9):2455--2463, September 2008. ISSN 1460-2156 (Electronic) 0006-8950 (Linking). doi: 10.1093/brain/awn151.

P. Bublak, P. Redel, C. Sorg, A. Kurz, H. Förstl, H. J. Müller, W. X. Schneider, and K. Finke. Staged decline of visual processing capacity in mild cognitive impairment and Alzheimer's disease. *Neurobiol Aging*, 32(7):1219--1230, July 2011. ISSN 1558-1497 (Electronic) 0197-4580 (Linking). doi: 10.1016/j.neurobiolaging.2009.07.012.

Aron S. Buchman and David A. Bennett. Loss of motor function in preclinical Alzheimer's disease. *Expert Rev Neurother*, 11(5):665--676, May 2011. ISSN 1473-7175. doi: 10.1586/ern.11.57.

A. Z. Burzynska, C. Preuschhof, L. Bäckman, L. Nyberg, S. C. Li, U. Lindenberger, and H. R. Heekeren. Age-related differences in white matter microstructure: Region-specific patterns of diffusivity. *Neuroimage*, 49(3):2104--2112, February 2010. ISSN 1095-9572 (Electronic) 1053-8119 (Linking). doi: 10.1016/j.neuroimage.2009.09.041.

Miguel Ángel Araque Caballero, Marc Suárez-Calvet, Marco Duering, Nicolai Franzmeier, Tammie Benzinger, Anne M. Fagan, Randall J. Bateman, Clifford R. Jack, Johannes Levin, Martin Dichgans, Mathias Jucker, Celeste Karch, Colin L. Masters, John C. Morris, Michael Weiner, Martin Rossor, Nick C. Fox, Jae Hong Lee, Stephen Salloway, Adrian Danek, Alison Goate, Igor Yakushev, Jason Hassenstab, Peter R. Schofield, Christian Haass, and Michael Ewers. White matter diffusion alterations precede symptom onset in autosomal dominant Alzheimer's disease. *Brain*, 141(10):3065--3080, October 2018. ISSN 0006-8950. doi: 10.1093/brain/awy229.

Carlos Cabral, Pedro M. Morgado, Durval Campos Costa, and Margarida Silveira. Predicting conversion from MCI to AD with FDG-PET brain images at different prodromal stages. *Comput Biol Med*, 58:101--109, March 2015. ISSN 0010-4825. doi: 10.1016/j.compbiomed.2015.01.003.

Jennifer S. W. Campbell, Ilana R. Leppert, Sridar Narayanan, Mathieu Boudreau, Tanguy Duval, Julien Cohen-Adad, G. Bruce Pike, and Nikola Stikov. Promise and pitfalls of g-ratio estimation with MRI. *NeuroImage*, 182:80--96, November 2018. ISSN 1053-8119. doi: 10.1016/j.neuroimage.2017.08.038.

Thomas Champney. Essential Clinical Neuroanatomy Resources. http://www.wileyessential.com/neuroanatomy/flashcards/c17_1/c17_1.html.

Bramsh Qamar Chandio, Jaroslaw Harezlak, Serge Koudoro, David Reagan, and Eleftherios Garyfallidis. Bundle analytics: A computational and statistical analysis framework for tractometric studies. In *ISMRM 27th Annual Meeting & Exhibition*, Montreal, Canada, 2019.

L. C. Chang, L. Walker, and C. Pierpaoli. Informed RESTORE: A method for robust estimation of diffusion tensor from low redundancy datasets in the presence of physiological noise artifacts. *Magn Reson Med*, 68(5):1654--1663, November 2012. ISSN 1522-2594 (Electronic) 0740-3194 (Linking). doi: 10.1002/mrm.24173.

Y. S. Chang, J. P. Owen, N. J. Pojman, T. Thieu, P. Bukshpun, M. L. Wakahiro, J. I. Berman, T. P. Roberts, S. S. Nagarajan, E. H. Sherr, and P. Mukherjee. White Matter Changes of Neurite Density and Fiber Orientation Dispersion during Human Brain Maturation. *PLoS One*, 10(6):e0123656, 2015. ISSN 1932-6203 (Electronic) 1932-6203 (Linking). doi: 10.1371/journal.pone.0123656.

C. Cheignon, M. Tomas, D. Bonnefont-Rousselot, P. Faller, C. Hureau, and F. Collin. Oxidative stress and the amyloid beta peptide in Alzheimer's disease. *Redox Biol*, 14:450--464, April 2018. ISSN 2213-2317 (Electronic) 2213-2317 (Linking). doi: 10.1016/j.redox.2017.10.014.

Chia-Wen Chiang, Yong Wang, Peng Sun, Tsen-Hsuan Lin, Kathryn Trinkaus, Anne H. Cross, and Sheng-Kwei Song. Quantifying white matter tract diffusion parameters in the presence of increased extra-fiber cellularity and vasogenic edema. *NeuroImage*, 101:310--319, November 2014. ISSN 1053-8119. doi: 10.1016/j.neuroimage.2014.06.064.

Hanna Cho, Jae Yong Choi, Mi Song Hwang, Jae Hoon Lee, You Jin Kim, Hye Mi Lee, Chul Hyoung Lyoo, Young Hoon Ryu, and Myung Sik Lee. Tau PET in Alzheimer disease and mild cognitive impairment. *Neurology*, 87(4):375--383, July 2016. doi: 10.1212/WNL.0000000000002892.

Nicholas S Cho, Mehrnaz Jenabi, Julio Arevalo-Perez, Nicole Brennan, Robert J Young, Sasan Karimi, Andrei I Holodny, and Kyung K Peck. Diffusion Tensor Imaging Shows Corpus Callosum Differences between High-Grade Gliomas and Metastases. *J Neuroimaging*, 28(2):199--205, 2018. ISSN 1051-2284.

A. W. Chung, D. L. Thomas, R. J. Ordidge, and C. A. Clark. Diffusion tensor parameters and principal eigenvector coherence: Relation to b-value intervals and field strength. *Magn Reson Imaging*, 31(5):742--747, June 2013. ISSN 1873-5894 (Electronic) 0730-725X (Linking). doi: 10.1016/j.mri.2012.11.014.

E. A. Codling, M. J. Plank, and S. Benhamou. Random walk models in biology. *J R Soc Interface*, 5(25):813--834, August 2008. ISSN 1742-5689 (Print) 1742-5662 (Linking). doi: 10.1098/rsif.2008.0014.

J. H. Cole, S. J. Ritchie, M. E. Bastin, M. C. Valdés Hernández, S. Muñoz Maniega, N. Royle, J. Corley, A. Pattie, S. E. Harris, Q. Zhang, N. R. Wray, P. Redmond, R. E. Marioni, J. M. Starr, S. R. Cox, J. M. Wardlaw, D. J. Sharp, and I. J. Deary. Brain age predicts mortality. *Molecular Psychiatry*, 23(5):1385--1392, May 2018. ISSN 1476-5578. doi: 10.1038/mp.2017.62.

P A Cook, Y Bai, S Nedjati-Gilani, K K Seunarine, M G Hall, G J Parker, and D C Alexander. Camino: Open-source diffusion-MRI reconstruction and processing. In *14th Scientific Meeting of the International Society for Magnetic Resonance in Medicine*. Seattle WA, USA, 2006.

G. S. Cover, W. G. Herrera, M. P. Bento, S. Appenzeller, and L. Rittner. Computational methods for corpus callosum segmentation on MRI: A systematic literature review. *Comput Methods*

Programs Biomed, 154:25--35, 2018. ISSN 01692607. doi: 10.1016/j.cmpb.2017.10.025.

S. R. Cox, S. J. Ritchie, E. M. Tucker-Drob, D. C. Liewald, S. P. Hagenaars, G. Davies, J. M. Wardlaw, C. R. Gale, M. E. Bastin, and I. J. Deary. Ageing and brain white matter structure in 3,513 UK Biobank participants. *Nat Commun*, 7:13629, December 2016. ISSN 2041-1723 (Electronic) 2041-1723 (Linking). doi: 10.1038/ncomms13629.

P Cras, M Kawai, D Lowery, P Gonzalez-DeWhitt, B Greenberg, and G Perry. Senile plaque neurites in Alzheimer disease accumulate amyloid precursor protein. *Proc Natl Acad Sci U S A*, 88(17):7552--7556, September 1991. ISSN 0027-8424. doi: 10.1073/pnas.88.17.7552.

Lotte G. M. Cremers, Marius de Groot, Albert Hofman, Gabriel P. Krestin, Aad van der Lugt, Wiro J. Niessen, Meike W. Vernooij, and M. Arfan Ikram. Altered tract-specific white matter microstructure is related to poorer cognitive performance: The Rotterdam Study. *Neurobiol Aging*, 39:108--117, March 2016. ISSN 0197-4580. doi: 10.1016/j.neurobiolaging.2015.11.021.

Simon W. Davis, Nancy A. Dennis, Norbou G. Buchler, Leonard E. White, David J. Madden, and Roberto Cabeza. Assessing the effects of age on long white matter tracts using diffusion tensor tractography. *NeuroImage*, 46(2):530--541, 2009. ISSN 10538119. doi: 10.1016/j.neuroimage.2009.01.068.

E. Davoodi-Bojd and H. Soltanian-Zadeh. Evaluation of diffusion models of fiber tracts using diffusion tensor magnetic resonance imaging. *Magn Reson Imaging*, 29(9):1175--1185, November 2011. ISSN 1873-5894 (Electronic) 0730-725X (Linking). doi: 10.1016/j.mri.2011.07.006.

K. F. de Laat, A. M. Tuladhar, A. G. van Norden, D. G. Norris, M. P. Zwiers, and F. E. de Leeuw. Loss of white matter integrity is associated with gait disorders in cerebral small vessel disease. *Brain*, 134(Pt 1):73--83, January 2011. ISSN 1460-2156 (Electronic) 0006-8950 (Linking). doi: 10.1093/brain/awq343.

J. J. de Paula, M. R. Albuquerque, G. M. Lage, M. A. Bicalho, M. A. Romano-Silva, and L. F. Malloy-Diniz. Impairment of fine motor dexterity in mild cognitive impairment and Alzheimer's disease dementia: Association with activities of daily living. *Braz J Psychiatry*, 38(3):235--238, July 2016. ISSN 1809-452X (Electronic) 1516-4446 (Linking). doi: 10.1590/1516-4446-2015-1874.

Silvia De Santis, Derek K. Jones, and Alard Roebroeck. Including diffusion time dependence in the extra-axonal space improves in vivo estimates of axonal diameter and density in human white matter. *NeuroImage*, 130:91--103, April 2016. ISSN 1053-8119. doi: 10.1016/j.neuroimage.2016.01.047.

Stéphanie Debette and H. S. Markus. The clinical importance of white matter hyperintensities on brain magnetic resonance imaging: Systematic review and meta-analysis. *BMJ*, 341(c3666), July 2010. ISSN 0959-8138, 1468-5833. doi: 10.1136/bmj.c3666.

Ignacio Demey, Fernando Ventrice, Galeno Rojas, Victoria Zubiri, and Veronica Somale. Alzheimer's Disease Dementia involves the Corpus Callosum and the Cingulum: A Diffusion Tensor Imaging Study (P6.210). *Neurology*, 84(14 Supplement):P6.210, April 2015.

Sean C. L. Deoni, Lucy Matthews, and Shannon H. Kolind. One component? Two components? Three? The effect of including a nonexchanging ''free'' water component in multicomponent driven equilibrium single pulse observation of T1 and T2. *Magnetic Resonance in Medicine*, 70 (1):147--154, July 2013. ISSN 0740-3194. doi: 10.1002/mrm.24429.

Maxime Descoteaux. *High Angular Resolution Diffusion MRI: From Local Estimation to Segmentation and Tractography*. PhD thesis, Univ. de Nice-Sophia Antipolis, Nice-Sophia Antipolis, France, 2008.

Maxime Descoteaux, Elaine Angelino, Shaun Fitzgibbons, and Rachid Deriche. Regularized, fast, and robust analytical Q-ball imaging. *Magn Reson Med*, 58(3):497--510, 2007. ISSN 0740-3194.

Margherita Di Paola, Eileen Luders, Fulvia Di Iulio, Andrea Cherubini, Domenico Passafiume, Paul M. Thompson, Carlo Caltagirone, Arthur W. Toga, and Gianfranco Spalletta. Callosal atrophy in mild cognitive impairment and Alzheimer's disease: Different effects in different stages. *NeuroImage*, 49(1):141--149, January 2010. ISSN 1053-8119. doi: 10.1016/j.neuroimage.2009.07.

050.

Ellen Dicks, Lisa Vermunt, Wiesje M. van der Flier, Pieter Jelle Visser, Frederik Barkhof, Philip Scheltens, and Betty M. Tijms. Modeling grey matter atrophy as a function of time, aging or cognitive decline show different anatomical patterns in Alzheimer's disease. *Neuroimage Clin*, 22: 101786, January 2019. ISSN 2213-1582. doi: 10.1016/j.nicl.2019.101786.

Olaf Dietrich. MRI from k-Space to parallel imaging. In Stefan O. Schoenberg, Olaf Dietrich, and Maximilian F. Reiser, editors, *Parallel Imaging in Clinical MR Applications*, pages 3--17. Springer, Berlin, Heidelberg, 2007. ISBN 978-3-540-68879-2. doi: 10.1007/978-3-540-68879-2_1.

Damon J DiSabato, Ning Quan, and Jonathan P Godbout. Neuroinflammation: The devil is in the details. *J Neurochem*, 139 Suppl 2(Suppl 2):136--153, October 2016. ISSN 1471-4159. doi: 10.1111/jnc.13607.

N. T. Doan, A. Engvig, K. Persson, D. Alnæs, T. Kaufmann, J. Rokicki, A. Córdova-Palomera, T. Moberget, A. Brækhus, M. L. Barca, K. Engedal, O. A. Andreassen, G. Selbæk, and L. T. Westlye. Dissociable diffusion MRI patterns of white matter microstructure and connectivity in Alzheimer's disease spectrum. *Sci Rep*, 7:45131, March 2017. ISSN 2045-2322 (Electronic) 2045-2322 (Linking). doi: 10.1038/srep45131.

Mark D. Does and John C. Gore. Compartmental study of T1 and T2 in rat brain and trigeminal nerve in vivo. *Magnetic Resonance in Medicine*, 47(2):274--283, February 2002. ISSN 0740-3194. doi: 10.1002/mrm.10060.

Takehiko Doi, Hyuma Makizako, Hiroyuki Shimada, Kota Tsutsumimoto, Ryo Hotta, Sho Nakakubo, Hyuntae Park, and Takao Suzuki. Objectively measured physical activity, brain atrophy, and white matter lesions in older adults with mild cognitive impairment. *Exp Gerontol*, 62:1--6, February 2015. ISSN 0531-5565. doi: 10.1016/j.exger.2014.12.011.

Y. Dong and E. N. Benveniste. Immune function of astrocytes. *Glia*, 36(2):180--190, November 2001. ISSN 0894-1491 (Print) 0894-1491 (Linking).

G. Douaud, R. A. Menke, A. Gass, A. U. Monsch, A. Rao, B. Whitcher, G. Zamboni, P. M. Matthews, M. Sollberger, and S. Smith. Brain microstructure reveals early abnormalities more than two years prior to clinical progression from mild cognitive impairment to Alzheimer's disease. *J Neurosci*, 33(5):2147--2155, January 2013. ISSN 1529-2401 (Electronic) 0270-6474 (Linking). doi: 10.1523/JNEUROSCI.4437-12.2013.

Yiping P. Du, Renxin Chu, Dosik Hwang, Mark S. Brown, Bette K. Kleinschmidt-DeMasters, Debra Singel, and Jack H. Simon. Fast multislice mapping of the myelin water fraction using multicompartment analysis of T decay at 3T: A preliminary postmortem study. *Magnetic Resonance in Medicine*, 58(5):865--870, November 2007. ISSN 0740-3194. doi: 10.1002/mrm.21409.

J. Dubois, G. Dehaene-Lambertz, S. Kulikova, C. Poupon, P. S. Hüppi, and L. Hertz-Pannier. The early development of brain white matter: A review of imaging studies in fetuses, newborns and infants. *Neuroscience*, 276:48--71, September 2014. ISSN 1873-7544 (Electronic) 0306-4522 (Linking). doi: 10.1016/j.neuroscience.2013.12.044.

L. J. Edwards, K. J. Pine, I. Ellerbrock, N. Weiskopf, and S. Mohammadi. NODDI-DTI: Estimating Neurite Orientation and Dispersion Parameters from a Diffusion Tensor in Healthy White Matter. *Front Neurosci*, 11:720, 2017. ISSN 1662-4548 (Print) 1662-453X (Linking). doi: 10.3389/fnins.2017.00720.

Michael Ewers, Philip S. Insel, Yaakov Stern, and Michael W. Weiner. Cognitive reserve associated with FDG-PET in preclinical Alzheimer disease. *Neurology*, 80(13):1194--1201, March 2013. doi: 10.1212/WNL.0b013e31828970c2.

J. A. Farrell, B. A. Landman, C. K. Jones, S. A. Smith, J. L. Prince, P. C. van Zijl, and S. Mori. Effects of signal-to-noise ratio on the accuracy and reproducibility of diffusion tensor imaging-derived fractional anisotropy, mean diffusivity, and principal eigenvector measurements at 1.5 T. *J Magn Reson Imaging*, 26(3):756--767, September 2007. ISSN 1053-1807 (Print) 1053-1807 (Linking). doi: 10.1002/jmri.21053.

F. Faul, E. Erdfelder, A. Buchner, and A. G. Lang. Statistical power analyses using G*Power 3.1: Tests for correlation and regression analyses. *Behav Res Methods*, 41(4):1149--1160, November 2009. ISSN 1554-3528 (Electronic) 1554-351X (Linking). doi: 10.3758/BRM.41.4.1149.

Qi Feng, Zhengluan Liao, Hongyang Jiang, Dewang Mao, Mei Wang, Enyan Yu, and Zhongxiang Ding. Corpus callosum radiomics-based classification model in Alzheimer's disease: A Case-control study. *Frontiers in neurology*, 9:618, 2018. ISSN 1664-2295.

Florian Udo Fischer, Dominik Wolf, Armin Scheurich, and Andreas Fellgiebel. Altered whole-brain white matter networks in preclinical Alzheimer's disease. *Neuroimage Clin*, 8:660--666, January 2015. ISSN 2213-1582. doi: 10.1016/j.nicl.2015.06.007.

Robin J. M. Franklin and Charles ffrench-Constant. Remyelination in the CNS: From biology to therapy. *Nature Reviews Neuroscience*, 9(11):839--855, November 2008. ISSN 1471-0048. doi: 10.1038/nrn2480.

Pedro Freitas, Leticia Rittner, Simone Appenzeller, and Roberto Lotufo. Watershed-Based Segmentation of the Midsagittal Section of the Corpus Callosum in Diffusion MRI. In *2011 24th SIBGRAPI Conference on Graphics, Patterns and Images*, pages 274--280, 2011. doi: 10.1109/sibgrapi.2011.46.

Giovanni B. Frisoni, Martina Bocchetta, Gael Chételat, Gil D. Rabinovici, Mony J. de Leon, Jeffrey Kaye, Eric M. Reiman, Philip Scheltens, Frederik Barkhof, Sandra E. Black, David J. Brooks, Maria C. Carrillo, Nick C. Fox, Karl Herholz, Agneta Nordberg, Clifford R. Jack, William J. Jagust, Keith A. Johnson, Christopher C. Rowe, Reisa A. Sperling, William Thies, Lars-Olof Wahlund, Michael W. Weiner, Patrizio Pasqualetti, and Charles DeCarli. Imaging markers for Alzheimer disease: Which vs how. *Neurology*, 81(5):487--500, July 2013. doi: 10.1212/WNL.0b013e31829d86e8.

Serge Gauthier, Barry Reisberg, Michael Zaudig, Ronald C. Petersen, Karen Ritchie, Karl Broich, Sylvie Belleville, Henry Brodaty, David Bennett, Howard Chertkow, Jeffrey L. Cummings, Mony de Leon, Howard Feldman, Mary Ganguli, Harald Hampel, Philip Scheltens, Mary C. Tierney, Peter Whitehouse, and Bengt Winblad. Mild cognitive impairment. *Lancet*, 367(9518):1262--1270, 2006. ISSN 01406736. doi: 10.1016/s0140-6736(06)68542-5.

Bryce L. Geeraert, Robert Marc Lebel, and Catherine Lebel. A multiparametric analysis of white matter maturation during late childhood and adolescence. *Hum Brain Mapp*, 40:4345--4356, October 2019. ISSN 1065-9471. doi: 10.1002/hbm.24706.

Tamar Gefen, Garam Kim, Kabriya Bolbolan, Andrew Geoly, Daniel Ohm, Carly Oboudiyat, Ryan Shahidehpour, Alfred Rademaker, Sandra Weintraub, Eileen H. Bigio, M Marsel Mesulam, Emily Rogalski, and Changiz Geula. Activated Microglia in Cortical White Matter Across Cognitive Aging Trajectories. *Front Aging Neurosci*, 11(94), 2019. ISSN 1663-4365. doi: 10.3389/fnagi.2019.00094.

S. Genc, C. E. Steward, C. B. Malpas, D. Velakoulis, T. J. O'Brien, and P. M. Desmond. Short-term white matter alterations in Alzheimer's disease characterized by diffusion tensor imaging. *J Magn Reson Imaging*, 43(3):627--634, March 2016. ISSN 1522-2586 (Electronic) 1053-1807 (Linking). doi: 10.1002/jmri.25017.

M. Giannelli, M. Cosottini, M. C. Michelassi, G. Lazzarotti, G. Belmonte, C. Bartolozzi, and M. Lazzeri. Dependence of brain DTI maps of fractional anisotropy and mean diffusivity on the number of diffusion weighting directions. *J Appl Clin Med Phys*, 11(1):176--190, 2010. ISSN 1526-9914 (Electronic) 1526-9914 (Linking).

Florent Ginhoux, Shawn Lim, Guillaume Hoeffel, Donovan Low, and Tara Huber. Origin and differentiation of microglia. *Front Cell Neurosci*, 7:45, April 2013. ISSN 1662-5102. doi: 10.3389/fncel.2013.00045.

K. Ginsburger, F. Matuschke, F. Poupon, J. F. Mangin, M. Axer, and C. Poupon. MEDUSA: A GPU-based tool to create realistic phantoms of the brain microstructure using tiny spheres. *Neuroimage*, 193:10--24, June 2019. ISSN 1095-9572 (Electronic) 1053-8119 (Linking). doi: 10.1016/j.neuroimage.2019.02.055.

G. Giulietti, M. Torso, L. Serra, B. Spanò, C. Marra, C. Caltagirone, M. Cercignani, M. Bozzali, and Initiative Alzheimer's Disease Neuroimaging. Whole brain white matter histogram analysis of diffusion tensor imaging data detects microstructural damage in mild cognitive impairment and alzheimer's disease patients. *J Magn Reson Imaging*, page Epub, January 2018. ISSN 1522-2586 (Electronic) 1053-1807 (Linking). doi: 10.1002/jmri.25947.

B. T. Gold, N. F. Johnson, D. K. Powell, and C. D. Smith. White matter integrity and vulnerability to Alzheimer's disease: Preliminary findings and future directions. *Biochim Biophys Acta*, 1822 (3):416--422, March 2012. ISSN 0006-3002 (Print) 0006-3002 (Linking). doi: 10.1016/j.bbadis.2011.07.009.

H. L. Golden, J. M. Nicholas, K. X. Yong, L. E. Downey, J. M. Schott, C. J. Mummery, S. J. Crutch, and J. D. Warren. Auditory spatial processing in Alzheimer's disease. *Brain*, 138(1):189--202, January 2015. ISSN 1460-2156 (Electronic) 0006-8950 (Linking). doi: 10.1093/brain/awu337.

R. E. González-Reyes, M. O. Nava-Mesa, K. Vargas-Sánchez, D. Ariza-Salamanca, and L. Mora-Muñoz. Involvement of Astrocytes in Alzheimer's Disease from a Neuroinflammatory and Oxidative Stress Perspective. *Front Mol Neurosci*, 10:427, 2017. ISSN 1662-5099 (Print) 1662-5099 (Linking). doi: 10.3389/fnmol.2017.00427.

Catriona D. Good, Ingrid S. Johnsrude, John Ashburner, Richard N. A. Henson, Karl J. Friston, and Richard S. J. Frackowiak. A Voxel-Based Morphometric Study of Ageing in 465 Normal Adult Human Brains. *NeuroImage*, 14(1):21--36, July 2001. ISSN 1053-8119. doi: 10.1006/nimg.2001.0786.

M. S. Graham, I. Drobnjak, and H. Zhang. Realistic simulation of artefacts in diffusion MRI for validating post-processing correction techniques. *Neuroimage*, 125:1079--1094, January 2016. ISSN 1095-9572 (Electronic) 1053-8119 (Linking). doi: 10.1016/j.neuroimage.2015.11.006.

V. Gulani, A. G. Webb, I. D. Duncan, and P. C. Lauterbur. Apparent diffusion tensor measurements in myelin-deficient rat spinal cords. *Magn Reson Med*, 45(2):191--195, February 2001. ISSN 0740-3194 (Print) 0740-3194 (Linking).

R. K. Gupta, K. Nath, A. Prasad, K. N. Prasad, M. Husain, R. K. Rathore, N. Husain, C. Srivastava, P. Khetan, R. Trivedi, and P. A. Narayana. In vivo demonstration of neuroinflammatory molecule expression in brain abscess with diffusion tensor imaging. *AJNR Am J Neuroradiol*, 29(2):326--332, February 2008. ISSN 1936-959X (Electronic) 0195-6108 (Linking). doi: 10.3174/ajnr.A0826.

Sanjana Gupta, Jacob Czech, Robert Kuczewski, Thomas M. Bartol, Terrence J. Sejnowski, Robin E. C. Lee, and James R. Faeder. Spatial Stochastic Modeling with MCell and CellBlender. arXiv preprint arXiv:1810.00499, 2018.

G. Gyebnár, Á. Szabó, E. Sirály, Z. Fodor, A. Sákovics, P. Salacz, Z. Hidasi, É. Csibri, G. Rudas, L. R. Kozák, and G. Csukly. What can DTI tell about early cognitive impairment? - Differentiation between MCI subtypes and healthy controls by diffusion tensor imaging. *Psychiatry Res Neuroimaging*, 272:46--57, 2018. ISSN 1872-7123 (Electronic) 0165-1781 (Linking). doi: 10.1016/j.pscychresns.2017.10.007.

Erwin L. Hahn. Spin echoes. *Phys Rev*, 80(4):580, 1950.

Matt G Hall and Daniel C Alexander. Convergence and parameter choice for Monte-Carlo simulations of diffusion MRI. *IEEE Trans Med Imaging*, 28(9):1354--1364, 2009. ISSN 0278-0062.

Haruo Hanyu, Hirofumi Sakurai, Toshihiko Iwamoto, Masaru Takasaki, Hiroaki Shindo, and Kimihiko Abeb. Diffusion-weighted MR imaging of the hippocampus and temporal white matter in Alzheimer's disease. *J Neurol Sci*, 156:195--200, 1998.

K. M. Hasan, R. K. Gupta, R. M. Santos, J. S. Wolinsky, and P. A. Narayana. Diffusion tensor fractional anisotropy of the normal-appearing seven segments of the corpus callosum in healthy adults and relapsing-remitting multiple sclerosis patients. *J Magn Reson Imaging*, 21(6):735--743, June 2005. ISSN 1053-1807 (Print) 1053-1807 (Linking). doi: 10.1002/jmri.20296.

Michael T. Heneka, Monica J. Carson, Joseph El Khoury, Gary E. Landreth, Frederic Brosseron, Douglas L. Feinstein, Andreas H. Jacobs, Tony Wyss-Coray, Javier Vitorica, Richard M. Ran-

sohoff, Karl Herrup, Sally A. Frautschy, Bente Finsen, Guy C. Brown, Alexei Verkhratsky, Koji Yamanaka, Jari Koistinaho, Eicke Latz, Annett Halle, Gabor C. Petzold, Terrence Town, Dave Morgan, Mari L. Shinohara, V. Hugh Perry, Clive Holmes, Nicolas G. Bazan, David J. Brooks, Stéphane Hunot, Bertrand Joseph, Nikolaus Deigendesch, Olga Garaschuk, Erik Boddeke, Charles A. Dinarello, John C. Breitner, Greg M. Cole, Douglas T. Golenbock, and Markus P. Kummer. Neuroinflammation in Alzheimer's disease. *Lancet Neurol*, 14(4):388--405, 2015. ISSN 14744422. doi: 10.1016/s1474-4422(15)70016-5.

Karl Herrup. The case for rejecting the amyloid cascade hypothesis. *Nat Neurosci*, 18(6):794--799, June 2015. ISSN 1546-1726. doi: 10.1038/nn.4017.

H. Hippius and G. Neundörfer. The discovery of Alzheimer's disease. *Dialogues Clin Neurosci*, 5(1): 101--108, 2003.

S. Hofer and J. Frahm. Topography of the human corpus callosum revisited--comprehensive fiber tractography using diffusion tensor magnetic resonance imaging. *Neuroimage*, 32(3):989--994, September 2006. ISSN 1053-8119 (Print) 1053-8119 (Linking). doi: 10.1016/j.neuroimage.2006.05.044.

Y. J. Hong, B. Yoon, S. C. Lim, Y. S. Shim, J. Y. Kim, K. J. Ahn, I. W. Han, and D. W. Yang. Microstructural changes in the hippocampus and posterior cingulate in mild cognitive impairment and Alzheimer's disease: A diffusion tensor imaging study. *Neurol Sci*, 34(7):1215--1221, July 2013. ISSN 1590-3478 (Electronic) 1590-1874 (Linking). doi: 10.1007/s10072-012-1225-4.

J. Hou and B. Pakkenberg. Age-related degeneration of corpus callosum in the 90+ years measured with stereology. *Neurobiol Aging*, 33(5):1009 e1--9, May 2012. ISSN 1558-1497 (Electronic) 0197-4580 (Linking). doi: 10.1016/j.neurobiolaging.2011.10.017.

K. Hua, J. Zhang, S. Wakana, H. Jiang, X. Li, D. S. Reich, P. A. Calabresi, J. J. Pekar, P. C. van Zijl, and S. Mori. Tract probability maps in stereotaxic spaces: Analyses of white matter anatomy and tract-specific quantification. *Neuroimage*, 39(1):336--347, January 2008. ISSN 1053-8119 (Print) 1053-8119 (Linking). doi: 10.1016/j.neuroimage.2007.07.053.

Juebin Huang and Alexander P. Auchus. Diffusion Tensor Imaging of Normal Appearing White Matter and Its Correlation with Cognitive Functioning in Mild Cognitive Impairment and Alzheimer's Disease. *Annals of the New York Academy of Sciences*, 1097(1):259--264, 2007. ISSN 1749-6632. doi: 10.1196/annals.1379.021.

W. J. Huang, X. Zhang, and W. W. Chen. Role of oxidative stress in Alzheimer's disease. *Biomed Rep*, 4(5):519--522, May 2016. ISSN 2049-9434 (Print) 2049-9434 (Linking). doi: 10.3892/br.2016.630.

E. S. Hui, M. M. Cheung, K. C. Chan, and E. X. Wu. B-value dependence of DTI quantitation and sensitivity in detecting neural tissue changes. *Neuroimage*, 49(3):2366--2374, February 2010. ISSN 1095-9572 (Electronic) 1053-8119 (Linking). doi: 10.1016/j.neuroimage.2009.10.022.

Dosik Hwang, Dong-Hyun Kim, and Yiping P. Du. In vivo multi-slice mapping of myelin water content using T2* decay. *NeuroImage*, 52(1):198--204, August 2010. ISSN 1053-8119. doi: 10.1016/j.neuroimage.2010.04.023.

Leonardo Iaccarino, Arianna Sala, and Daniela Perani. Predicting long-term clinical stability in amyloid-positive subjects by FDG-PET. *Annals of Clinical and Translational Neurology*, 6(6): 1113--1120, 2019. ISSN 2328-9503. doi: 10.1002/acn3.782.

S. Inano, H. Takao, N. Hayashi, O. Abe, and K. Ohtomo. Effects of age and gender on white matter integrity. *AJNR Am J Neuroradiol*, 32(11):2103--2109, December 2011. ISSN 1936-959X (Electronic) 0195-6108 (Linking). doi: 10.3174/ajnr.A2785.

M Inglese and Maxim Bester. Diffusion imaging in multiple sclerosis: Research and clinical implications. *NMR Biomed*, 23(7):865--872, August 2010. ISSN 1099-1492. doi: 10.1002/nbm.1515.

L. M. Ittner and J. Götz. Amyloid-beta and tau - a toxic pas de deux in Alzheimer's disease. *Nat Rev Neurosci*, 12(2):65--72, February 2011. ISSN 1471-0048 (Electronic) 1471-003X (Linking). doi: 10.1038/nrn2967.

Clifford R. Jack Jr., David S. Knopman, William J. Jagust, Ronald C. Petersen, Michael W. Weiner,

Paul S. Aisen, Leslie M. Shaw, Prashanthi Vemuri, Heather J. Wiste, Stephen D. Weigand, Timothy G. Lesnick, Vernon S. Pankratz, Michael C. Donohue, and John Q. Trojanowski. Tracking pathophysiological processes in Alzheimer's disease: An updated hypothetical model of dynamic biomarkers. *The Lancet Neurology*, 12(2):207--216, 2013. ISSN 14744422. doi: 10.1016/s1474-4422(12)70291-0.

Clifford R Jack Jr., Heather J Wiste, Stephen D Weigand, Walter A Rocca, David S Knopman, Michelle M Mielke, Val J Lowe, Matthew L Senjem, Jeffrey L Gunter, Gregory M Preboske, Vernon S Pankratz, Prashanthi Vemuri, and Ronald C Petersen. Age-specific population frequencies of cerebral β-amyloidosis and neurodegeneration among people with normal cognitive function aged 50–89 years: A cross-sectional study. *Lancet Neurol*, 13(10):997--1005, October 2014. ISSN 1474-4422. doi: 10.1016/S1474-4422(14)70194-2.

W. Jagust, B. Reed, D. Mungas, W. Ellis, and C. DeCarli. What does fluorodeoxyglucose PET imaging add to a clinical diagnosis of dementia? *Neurology*, 69(9):871--877, August 2007. doi: 10.1212/01.wnl.0000269790.05105.16.

N. Jahanshad, L. Zhan, M. A. Bernstein, B. J. Borowski, C. R. Jack Jr., A. W. Toga, and P. M. Thompson. Diffusion tensor imaging in seven minutes: Determining trade-offs between spatial and directional resolution. In *2010 IEEE International Symposium on Biomedical Imaging: From Nano to Macro*, pages 1161--1164, April 2010. ISBN 1945-8452. doi: 10.1109/ISBI.2010.5490200.

F. Z. Javaid, J. Brenton, L. Guo, and M. F. Cordeiro. Visual and Ocular Manifestations of Alzheimer's Disease and Their Use as Biomarkers for Diagnosis and Progression. *Front Neurol*, 7: 55, 2016. ISSN 1664-2295 (Print) 1664-2295 (Linking). doi: 10.3389/fneur.2016.00055.

I. O. Jelescu and M. D. Budde. Design and validation of diffusion MRI models of white matter. *Front Phys*, 5:61, 2017. ISSN 2296-424X (Print) 2296-424X (Linking). doi: 10.3389/fphy.2017.00061.

M. Jenkinson, C. F. Beckmann, T. E. Behrens, M. W. Woolrich, and S. M. Smith. FSL. *Neuroimage*, 62(2):782--790, August 2012. ISSN 1095-9572 (Electronic) 1053-8119 (Linking). doi: 10.1016/j.neuroimage.2011.09.015.

B. Jeurissen, J. D. Tournier, T. Dhollander, A. Connelly, and J. Sijbers. Multi-tissue constrained spherical deconvolution for improved analysis of multi-shell diffusion MRI data. *Neuroimage*, 103:411--426, December 2014. ISSN 1095-9572 (Electronic) 1053-8119 (Linking). doi: 10.1016/j.neuroimage.2014.07.061.

B. Jeurissen, M. Descoteaux, S. Mori, and A. Leemans. Diffusion MRI fiber tractography of the brain. *NMR Biomed*, 32(4):e3785, April 2019. ISSN 1099-1492 (Electronic) 0952-3480 (Linking). doi: 10.1002/nbm.3785.

D. K. Jones. The effect of gradient sampling schemes on measures derived from diffusion tensor MRI: A Monte Carlo study. *Magn Reson Med*, 51(4):807--815, April 2004. ISSN 0740-3194 (Print) 0740-3194 (Linking). doi: 10.1002/mrm.20033.

D. K. Jones and P. J. Basser. "Squashing peanuts and smashing pumpkins": How noise distorts diffusion-weighted MR data. *Magn Reson Med*, 52(5):979--993, November 2004. ISSN 0740-3194 (Print) 0740-3194 (Linking). doi: 10.1002/mrm.20283.

W. Jung, J. Lee, H. G. Shin, Y. Nam, H. Zhang, S. H. Oh, and J. Lee. Whole brain g-ratio mapping using myelin water imaging (MWI) and neurite orientation dispersion and density imaging (NODDI). *Neuroimage*, 2018. ISSN 1095-9572 (Electronic) 1053-8119 (Linking). doi: 10.1016/j.neuroimage.2017.09.053.

F. Kametani and M. Hasegawa. Reconsideration of Amyloid Hypothesis and Tau Hypothesis in Alzheimer's Disease. *Front Neurosci*, 12:25, 2018. ISSN 1662-4548 (Print) 1662-453X (Linking). doi: 10.3389/fnins.2018.00025.

R. A. Kanaan, M. Allin, M. Picchioni, G. J. Barker, E. Daly, S. S. Shergill, J. Woolley, and P. K. McGuire. Gender differences in white matter microstructure. *PLoS One*, 7(6):e38272, 2012. ISSN 1932-6203 (Electronic) 1932-6203 (Linking). doi: 10.1371/journal.pone.0038272.

G. B. Karas, P. Scheltens, S. A. Rombouts, P. J. Visser, R. A. van Schijndel, N. C. Fox, and

F. Barkhof. Global and local gray matter loss in mild cognitive impairment and Alzheimer's disease. *Neuroimage*, 23(2):708--716, October 2004. ISSN 1053-8119 (Print) 1053-8119 (Linking). doi: 10.1016/j.neuroimage.2004.07.006.

M. A. Kashem, R. Sarker, H. Des Etages, R. Machaalani, N. King, I. S. McGregor, and I. Matsumoto. Comparative proteomics in the corpus callosal sub-regions of postmortem human brain. *Neurochem Int*, 55(7):483--490, December 2009. ISSN 1872-9754 (Electronic) 0197-0186 (Linking). doi: 10.1016/j.neuint.2009.04.017.

Alar Kaskikallio, Mira Karrasch, Juha O. Rinne, Terhi Tuokkola, Riitta Parkkola, and Petra Grönholm-Nyman. Domain-specific cognitive effects of white matter pathology in old age, mild cognitive impairment and Alzheimer's disease. *Aging, Neuropsychology, and Cognition*, DOI: 10.1080/13825585.2019.1628916, June 2019. ISSN 1382-5585. doi: 10.1080/13825585.2019.1628916.

Rex A Kerr, Thomas M Bartol, Boris Kaminsky, Markus Dittrich, Jen-Chien Jack Chang, Scott B Baden, Terrence J Sejnowski, and Joel R Stiles. Fast monte carlo simulation methods for biological reaction-diffusion systems in solution and on surfaces. *SIAM J Sci Comput*, 30(6):3126, October 2008. ISSN 1064-8275. doi: 10.1137/070692017.

I. Kilimann, J. R. Thyrian, W. Hoffmann, and S. J. Teipel. Translation of imaging biomarkers from clinical research to healthcare. *Z Gerontol Geriatr*, 50:84--88, May 2017. ISSN 1435-1269 (Electronic) 0948-6704 (Linking). doi: 10.1007/s00391-017-1225-3.

M. Kim, I. Ronen, K. Ugurbil, and D. S. Kim. Spatial resolution dependence of DTI tractography in human occipito-callosal region. *Neuroimage*, 32(3):1243--1249, September 2006. ISSN 1053-8119 (Print) 1053-8119 (Linking). doi: 10.1016/j.neuroimage.2006.06.006.

S. Kitamura, K. Kiuchi, T. Taoka, K. Hashimoto, S. Ueda, F. Yasuno, M. Morikawa, K. Kichikawa, and T. Kishimoto. Longitudinal white matter changes in Alzheimer's disease: A tractography-based analysis study. *Brain Res*, 1515:12--18, June 2013. ISSN 1872-6240 (Electronic) 0006-8993 (Linking). doi: 10.1016/j.brainres.2013.03.052.

Maria G Knyazeva. Splenium of corpus callosum: Patterns of interhemispheric interaction in children and adults. *Neural Plast*, 639430, 2013. ISSN 1687-5443. doi: 10.1155/2013/639430.

Shannon Kolind, Lucy Matthews, Heidi Johansen-Berg, M. Isabel Leite, Steven C.R. Williams, Sean Deoni, and Jackie Palace. Myelin water imaging reflects clinical variability in multiple sclerosis. *NeuroImage*, 60(1):263--270, March 2012. ISSN 1053-8119. doi: 10.1016/j.neuroimage.2011.11.070.

Rimvall Nicolai Køster, Riise Jesper, and Pakkenberg Bente. The total number of myelinated nerve fibers is reduced in corpus callosum in brains from patients with Alzheimer´s disease. *Neurobiol Aging*, 69:58--64, 2018. ISSN 01974580. doi: 10.1016/j.neurobiolaging.2018.04.016.

Rajesh Kumar, Haidang D. Nguyen, Paul M. Macey, Mary A. Woo, and Ronald M. Harper. Regional brain axial and radial diffusivity changes during development. *J Neurosci Res*, 90(2):346--355, February 2012. ISSN 0360-4012. doi: 10.1002/jnr.22757.

J. L. Lancaster, T. Andrews, L. J. Hardies, S. Dodd, and P. T. Fox. Three-pool model of white matter. *J Magn Reson Imaging*, 17(1):1--10, January 2003. ISSN 1053-1807 (Print) 1053-1807 (Linking). doi: 10.1002/jmri.10230.

Susan M. Landau, Danielle Harvey, Cindee M. Madison, Robert A. Koeppe, Eric M. Reiman, Norman L. Foster, Michael W. Weiner, and William J. Jagust. Associations between cognitive, functional, and FDG-PET measures of decline in AD and MCI. *Neurobiol Aging*, 32(7):1207--1218, July 2011. ISSN 0197-4580. doi: 10.1016/j.neurobiolaging.2009.07.002.

B. A. Landman, J. A. Farrell, C. K. Jones, S. A. Smith, J. L. Prince, and S. Mori. Effects of diffusion weighting schemes on the reproducibility of DTI-derived fractional anisotropy, mean diffusivity, and principal eigenvector measurements at 1.5T. *Neuroimage*, 36(4):1123--1138, July 2007. ISSN 1053-8119 (Print) 1053-8119 (Linking). doi: 10.1016/j.neuroimage.2007.02.056.

L L Latour, K Svoboda, P P Mitra, and C H Sotak. Time-dependent diffusion of water in a biological model system. *Proc Natl Acad Sci U S A*, 91(4):1229--1233, February 1994. ISSN 0027-8424. doi: 10.1073/pnas.91.4.1229.

C. H. Latta, H. M. Brothers, and D. M. Wilcock. Neuroinflammation in Alzheimer's disease; A source of heterogeneity and target for personalized therapy. *Neuroscience*, 302:103--111, August 2015. ISSN 1873-7544 (Electronic) 0306-4522 (Linking). doi: 10.1016/j.neuroscience.2014.09.061.

C. Laule, I. M. Vavasour, G. R. Moore, J. Oger, D. K. Li, D. W. Paty, and A. L. MacKay. Water content and myelin water fraction in multiple sclerosis. A T2 relaxation study. *J Neurol*, 251(3):284--93, March 2004. ISSN 0340-5354 (Print) 0340-5354 (Linking). doi: 10.1007/s00415-004-0306-6.

Cornelia Laule and G.R. Wayne Moore. Myelin water imaging to detect demyelination and remyelination and its validation in pathology. *Brain Pathology*, 28(5):750--764, September 2018. ISSN 1015-6305. doi: 10.1111/bpa.12645.

Frederik Bernd Laun, Lothar Rudi Schad, Jan Klein, and Bram Stieltjes. How background noise shifts eigenvectors and increases eigenvalues in DTI. *MAGMA*, 22(3):151--158, 2009.

C. B. Lauzon, A. J. Asman, M. L. Esparza, S. S. Burns, Q. Fan, Y. Gao, A. W. Anderson, N. Davis, L. E. Cutting, and B. A. Landman. Simultaneous analysis and quality assurance for diffusion tensor imaging. *PLoS One*, 8(4):e61737, 2013. ISSN 1932-6203 (Electronic) 1932-6203 (Linking). doi: 10.1371/journal.pone.0061737.

D. Le Bihan and E. Breton. In vivo magnetic resonance imaging of diffusion. *Comptes Rendus des Seances de l'Academie des Sciences Serie 2*, 301(15):1109--1112, 1985.

D. Le Bihan, R. Turner, P. Douek, and N. Patronas. Diffusion MR imaging: Clinical applications. *Am J Roentgenol*, 159(3):591--599, September 1992. ISSN 0361-803X (Print) 0361-803X (Linking). doi: 10.2214/ajr.159.3.1503032.

Denis Le Bihan, Eric Breton, Denis Lallemand, Philippe Grenier, Emmanuel Cabanis, and Maurice %J Radiology Laval-Jeantet. MR imaging of intravoxel incoherent motions: Application to diffusion and perfusion in neurologic disorders. *Radiology*, 161(2):401--407, 1986. ISSN 0033-8419.

Denis Le Bihan, Eric Breton, Denis Lallemand, ML Aubin, J Vignaud, and M Laval-Jeantet. Separation of diffusion and perfusion in intravoxel incoherent motion MR imaging. *Radiology*, 168(2):497--505, 1988. ISSN 0033-8419.

Denis Le Bihan, Jean Francois Mangin, Cyril Poupon, Chris A. Clark, Sabina Pappata, Nicolas Molko, and Hughes Chabriat. Diffusion tensor imaging: Concepts and applications. *J Magn Reson Imaging*, 13:534--546, 2001.

C. Lebel, S. Caverhill-Godkewitsch, and C. Beaulieu. Age-related regional variations of the corpus callosum identified by diffusion tensor tractography. *Neuroimage*, 52(1):20--31, August 2010. ISSN 1095-9572 (Electronic) 1053-8119 (Linking). doi: 10.1016/j.neuroimage.2010.03.072.

C. Lebel, T. Benner, and C. Beaulieu. Six is enough? Comparison of diffusion parameters measured using six or more diffusion-encoding gradient directions with deterministic tractography. *Magn Reson Med*, 68(2):474--483, August 2012a. ISSN 1522-2594 (Electronic) 0740-3194 (Linking). doi: 10.1002/mrm.23254.

C. Lebel, M. Gee, R. Camicioli, M. Wieler, W. Martin, and C. Beaulieu. Diffusion tensor imaging of white matter tract evolution over the lifespan. *Neuroimage*, 60(1):340--352, March 2012b. ISSN 1095-9572 (Electronic) 1053-8119 (Linking). doi: 10.1016/j.neuroimage.2011.11.094.

Catherine Lebel, Sarah Treit, and Christian Beaulieu. A review of diffusion MRI of typical white matter development from early childhood to young adulthood. *NMR in Biomedicine*, 32(4):e3778, 2019. ISSN 1099-1492. doi: 10.1002/nbm.3778.

H. G. Lee, G. Perry, P. I. Moreira, M. R. Garrett, Q. Liu, X. Zhu, A. Takeda, A. Nunomura, and M. A. Smith. Tau phosphorylation in Alzheimer's disease: Pathogen or protector? *Trends Mol Med*, 11(4):164--169, April 2005. ISSN 1471-4914 (Print) 1471-4914 (Linking). doi: 10.1016/j.molmed.2005.02.008.

S. H. Lee, A. H. Bachman, D. Yu, J. Lim, and B. A. Ardekani. Predicting progression from mild cognitive impairment to Alzheimer's disease using longitudinal callosal atrophy. *Alzheimers Dement (Amst)*, 2:68--74, 2016. ISSN 2352-8729 (Print). doi: 10.1016/j.dadm.2016.01.003.

J. Q. Li, L. Tan, H. F. Wang, M. S. Tan, L. Tan, W. Xu, Q. F. Zhao, J. Wang, T. Jiang, and J. T. Yu.

Risk factors for predicting progression from mild cognitive impairment to Alzheimer's disease: A systematic review and meta-analysis of cohort studies. *J Neurol Neurosurg Psychiatry*, 87(5):476--484, May 2016. ISSN 1468-330X (Electronic) 0022-3050 (Linking). doi: 10.1136/jnnp-2014-310095.

J. R. Li, V. D. Nguyen, T. N. Tran, J. Valdman, C. B. Trang, K. V. Nguyen, D. T. S. Vu, H. A. Tran, H. T. A. Tran, and T. M. P. Nguyen. SpinDoctor: A MATLAB toolbox for diffusion MRI simulation. *Neuroimage*, 202:116120, August 2019. ISSN 1095-9572 (Electronic) 1053-8119 (Linking). doi: 10.1016/j.neuroimage.2019.116120.

Tie-Qiang Li, Bing Yao, Peter van Gelderen, Hellmut Merkle, Stephen Dodd, Lalith Talagala, Alan P. Koretsky, and Jeff Duyn. Characterization of T2* Heterogeneity in Human Brain White Matter. *Magn Reson Med.*, 62(6):1652--1657, 2009.

Daniel Liewald, Robert Miller, Nikos Logothetis, Hans-Joachim Wagner, and Almut Schüz. Distribution of axon diameters in cortical white matter: An electron-microscopic study on three human brains and a macaque. *Biol Cybern*, 108(5):541--557, October 2014. ISSN 1432-0770. doi: 10.1007/s00422-014-0626-2.

K. A. Lin, K. R. Choudhury, B. G. Rathakrishnan, D. M. Marks, J. R. Petrella, P. M. Doraiswamy, and Alzheimer's Disease Neuroimaging Initiative. Marked gender differences in progression of mild cognitive impairment over 8 years. *Alzheimers Dement (N Y)*, 1(2):103--110, September 2015. ISSN 2352-8737 (Print) 2352-8737 (Linking). doi: 10.1016/j.trci.2015.07.001.

J. Liu, C. Yin, S. Xia, L. Jia, Y. Guo, Z. Zhao, X. Li, Y. Han, and J. Jia. White matter changes in patients with amnestic mild cognitive impairment detected by diffusion tensor imaging. *PLoS One*, 8(3):e59440, 2013. ISSN 1932-6203 (Electronic) 1932-6203 (Linking). doi: 10.1371/journal.pone.0059440.

Eileen Luders, Paul M. Thompson, and Arthur W. Toga. The Development of the Corpus Callosum in the Healthy Human Brain. *J Neurosci*, 30(33):10985--10990, August 2010. ISSN 0270-6474, 1529-2401. doi: 10.1523/JNEUROSCI.5122-09.2010.

Liangsuo Ma, Khader M Hasan, Joel L Steinberg, Ponnada A Narayana, Scott D Lane, Edward A Zuniga, Larry A Kramer, and F Gerard Moeller. Diffusion tensor imaging in cocaine dependence: Regional effects of cocaine on corpus callosum and effect of cocaine administration route. *Drug Alcohol Depend*, 104(3):262--267, 2009. ISSN 0376-8716.

R. B. Maccioni, G. Farias, I. Morales, and L. Navarrete. The revitalized tau hypothesis on Alzheimer's disease. *Arch Med Res*, 41(3):226--231, April 2010. ISSN 1873-5487 (Electronic) 0188-4409 (Linking). doi: 10.1016/j.arcmed.2010.03.007.

A. MacKay, C. Laule, I. Vavasour, T. Bjarnason, S. Kolind, and B. Madler. Insights into brain microstructure from the T2 distribution. *Magn Reson Imaging*, 24(4):515--25, May 2006. ISSN 0730-725X (Print) 0730-725X (Linking). doi: 10.1016/j.mri.2005.12.037.

Alex L MacKay and Cornelia Laule. Magnetic Resonance of Myelin Water: An in vivo Marker for Myelin. *Brain Plast*, 2(1):71--91, December 2016. ISSN 2213-6312. doi: 10.3233/BPL-160033.

Burkhard Mädler, Sylvia A. Drabycz, Shannon H. Kolind, Kenneth P. Whittall, and Alexander L. MacKay. Is diffusion anisotropy an accurate monitor of myelination?: Correlation of multicomponent T2 relaxation and diffusion tensor anisotropy in human brain. *Magnetic Resonance Imaging*, 26(7):874--888, September 2008. ISSN 0730-725X. doi: 10.1016/j.mri.2008.01.047.

S. E. Maier, S. Vajapeyam, H. Mamata, C. F. Westin, F. A. Jolesz, and R. V. Mulkern. Biexponential diffusion tensor analysis of human brain diffusion data. *Magn Reson Med*, 51(2):321--330, February 2004. ISSN 0740-3194 (Print) 0740-3194 (Linking). doi: 10.1002/mrm.10685.

Susana Muñoz Maniega, Maria C. Valdés Hernández, Jonathan D. Clayden, Natalie A. Royle, Catherine Murray, Zoe Morris, Benjamin S. Aribisala, Alan J. Gow, John M. Starr, Mark E. Bastin, Ian J. Deary, and Joanna M. Wardlaw. White matter hyperintensities and normal-appearing white matter integrity in the aging brain. *Neurobiol Aging*, 36(2):909--918, February 2015. ISSN 0197-4580. doi: 10.1016/j.neurobiolaging.2014.07.048.

C. D. Mayo, E. L. Mazerolle, L. Ritchie, J. D. Fisk, J. R. Gawryluk, and Alzheimer's Disease

Neuroimaging Initiative. Longitudinal changes in microstructural white matter metrics in Alzheimer's disease. *Neuroimage Clin*, 13:330--338, 2017. ISSN 2213-1582 (Electronic) 2213-1582 (Linking). doi: 10.1016/j.nicl.2016.12.012.

Kirsty E. McAleese, Lauren Walker, Sophie Graham, Elisa L. J. Moya, Mary Johnson, Daniel Erskine, Sean J. Colloby, Madhurima Dey, Carmen Martin-Ruiz, John Paul Taylor, Alan J. Thomas, Ian G. McKeith, Charles De Carli, and Johannes Attems. Parietal white matter lesions in Alzheimer's disease are associated with cortical neurodegenerative pathology, but not with small vessel disease. *Acta Neuropathol*, 134(3):459--473, September 2017. ISSN 1432-0533. doi: 10.1007/s00401-017-1738-2.

G. McKhann, D. Drachman, M. Folstein, R. Katzman, D. Price, and E. M. Stadlan. Clinical diagnosis of Alzheimer's disease: Report of the NINCDS-ADRDA Work Group under the auspices of Department of Health and Human Services Task Force on Alzheimer's Disease. *Neurology*, 34 (7):939--944, July 1984. ISSN 0028-3878 (Print) 0028-3878 (Linking). doi: 10.1212/wnl.34.7.939.

G. M. McKhann, D. S. Knopman, H. Chertkow, B. T. Hyman, C. R. Jack Jr., C. H. Kawas, W. E. Klunk, W. J. Koroshetz, J. J. Manly, R. Mayeux, R. C. Mohs, J. C. Morris, M. N. Rossor, P. Scheltens, M. C. Carrillo, B. Thies, S. Weintraub, and C. H. Phelps. The diagnosis of dementia due to Alzheimer's disease: Recommendations from the National Institute on Aging-Alzheimer's Association workgroups on diagnostic guidelines for Alzheimer's disease. *Alzheimers Dement*, 7(3):263--269, May 2011. ISSN 1552-5279 (Electronic) 1552-5260 (Linking). doi: 10.1016/j.jalz.2011.03.005.

David Medina, Leyla deToledo-Morrell, Fabio Urresta, John D. E. Gabrieli, Michael Moseley, Debra Fleischman, David A. Bennett, Sue Leurgans, David A. Turner, and Glenn T. Stebbins. White matter changes in mild cognitive impairment and AD: A diffusion tensor imaging study. *Neurobiol Aging*, 27(5):663--672, May 2006. ISSN 0197-4580. doi: 10.1016/j.neurobiolaging.2005.03.026.

Sandra M. Meyers, Shannon H. Kolind, and Alex L. MacKay. Simultaneous measurement of total water content and myelin water fraction in brain at 3T using a T2 relaxation based method. *Magnetic Resonance Imaging*, 37:187--194, April 2017. ISSN 0730-725X. doi: 10.1016/j.mri.2016.12.001.

M. M. Mielke. Sex and Gender Differences in Alzheimer's Disease Dementia. *Psychiatr Times*, 35 (11):14--17, November 2018. ISSN 0893-2905 (Print) 0893-2905 (Linking).

M. M. Mielke, N. A. Kozauer, K. C. Chan, M. George, J. Toroney, M. Zerrate, K. Bandeen-Roche, M. C. Wang, P. van Zijl, J. J. Pekar, S. Mori, C. G. Lyketsos, and M. Albert. Regionally-specific diffusion tensor imaging in mild cognitive impairment and Alzheimer's disease. *Neuroimage*, 46(1): 47--55, May 2009. ISSN 1095-9572 (Electronic) 1053-8119 (Linking). doi: 10.1016/j.neuroimage.2009.01.054.

Siawoosh Mohammadi, Daniel Carey, Fred Dick, Joern Diedrichsen, Martin I. Sereno, Marco Reisert, Martina F. Callaghan, and Nikolaus Weiskopf. Whole-Brain In-vivo Measurements of the Axonal G-Ratio in a Group of 37 Healthy Volunteers. *Frontiers in Neuroscience*, 9:441, 2015. ISSN 1662-453X. doi: 10.3389/fnins.2015.00441.

H. J. Möller and M. B. Graeber. The case described by Alois Alzheimer in 1911. *Eur Arch Psychiatry Clin Neurosci*, 248(3):111--122, 1998.

Jorge J. Moré. The Levenberg-Marquardt algorithm: Implementation and theory. In G. A. Watson, editor, *Numerical Analysis. Lecture Notes in Mathematics*, pages 105--116. Springer Berlin Heidelberg, 1978. ISBN 978-3-540-35972-2.

S. Mori, K. Oishi, H. Jiang, L. Jiang, X. Li, K. Akhter, K. Hua, A. V. Faria, A. Mahmood, R. Woods, A. W. Toga, G. B. Pike, P. R. Neto, A. Evans, J. Zhang, H. Huang, M. I. Miller, P. van Zijl, and J. Mazziotta. Stereotaxic white matter atlas based on diffusion tensor imaging in an ICBM template. *Neuroimage*, 40(2):570--582, April 2008. ISSN 1053-8119 (Print) 1053-8119 (Linking). doi: 10.1016/j.neuroimage.2007.12.035.

Susumu Mori and Donald J. Tournier. Moving Beyond DTI: High Angular Resolution Diffusion Imaging (HARDI). In *Introduction to Diffusion Tensor Imaging (Second Edition)*,

pages 65--78. Academic Press, San Diego, January 2014. ISBN 978-0-12-398398-5. doi: 10.1016/B978-0-12-398398-5.00008-4.

Susumu Mori, Setsu Wakana, Lidia M. Nagae-Poetscher, and Peter C. M. van Zijl. *MRI Atlas of Human White Matter*. Elsevier, Amsterdam, The Netherlands, 2005.

R. L. Muetzel, P. F. Collins, B. A. Mueller, M. Schissel A, K. O. Lim, and M. Luciana. The development of corpus callosum microstructure and associations with bimanual task performance in healthy adolescents. *Neuroimage*, 39(4):1918--1925, February 2008. ISSN 1053-8119 (Print) 1053-8119 (Linking). doi: 10.1016/j.neuroimage.2007.10.018.

Claire Murphy. Olfactory and other sensory impairments in Alzheimer disease. *Nature Reviews Neurology*, 15(1):11--24, January 2019. ISSN 1759-4766. doi: 10.1038/s41582-018-0097-5.

Kavindra Nath, Mazhar Husain, Richa Trivedi, Raj Kumar, Kashi N Prasad, RKS Rathore, and Rakesh K Gupta. Clinical implications of increased fractional anisotropy in meningitis associated with brain abscess. *J Comput Assist Tomogr*, 31(6):888--893, 2007. ISSN 0363-8715.

R. A. Nebel, N. T. Aggarwal, L. L. Barnes, A. Gallagher, J. M. Goldstein, K. Kantarci, M. P. Mallampalli, E. C. Mormino, L. Scott, W. H. Yu, P. M. Maki, and M. M. Mielke. Understanding the impact of sex and gender in Alzheimer's disease: A call to action. *Alzheimers Dement*, 14(9):1171--1183, September 2018. ISSN 1552-5279 (Electronic) 1552-5260 (Linking). doi: 10.1016/j.jalz.2018.04.008.

H. Ni, V. Kavcic, T. Zhu, S. Ekholm, and J. Zhong. Effects of number of diffusion gradient directions on derived diffusion tensor imaging indices in human brain. *AJNR Am J Neuroradiol*, 27(8): 1776--1781, September 2006. ISSN 0195-6108 (Print) 0195-6108 (Linking).

Charles Nicholson. Diffusion and related transport mechanisms in brain tissue. *Rep Prog Phys*, 64 (7):815--884, 2001.

M. Niethammer, R. San Jose Estepar, S. Bouix, M. Shenton, and C. F. Westin. On diffusion tensor estimation. *Conf Proc IEEE Eng Med Biol Soc*, 1:2622--2625, 2006. ISSN 1557-170X (Print) 1557-170X (Linking). doi: 10.1109/IEMBS.2006.259826.

T. M. Nir, N. Jahanshad, J. E. Villalon-Reina, A. W. Toga, C. R. Jack Jr., M. W. Weiner, P. M. Thompson, and Alzheimer's Disease Neuroimaging Initiative. Effectiveness of regional DTI measures in distinguishing Alzheimer's disease, MCI, and normal aging. *Neuroimage Clin*, 3: 180--195, 2013. ISSN 2213-1582 (Linking). doi: 10.1016/j.nicl.2013.07.006.

C. Nishioka, C. Poh, and S. W. Sun. Diffusion tensor imaging reveals visual pathway damage in patients with mild cognitive impairment and Alzheimer's disease. *J Alzheimers Dis*, 45(1): 97--107, 2015. ISSN 1875-8908 (Electronic) 1387-2877 (Linking). doi: 10.3233/JAD-141239.

H. Niu, I. Álvarez-Álvarez, F. Guillén-Grima, and I. Aguinaga-Ontoso. Prevalence and incidence of Alzheimer's disease in Europe: A meta-analysis. *Neurología*, 32(8):523--532, 2017. ISSN 21735808. doi: 10.1016/j.nrleng.2016.02.009.

M. A. Nowrangi, C. G. Lyketsos, J. M. Leoutsakos, K. Oishi, M. Albert, S. Mori, and M. M. Mielke. Longitudinal, region-specific course of diffusion tensor imaging measures in mild cognitive impairment and Alzheimer's disease. *Alzheimers Dement*, 9(5):519--528, September 2013. ISSN 1552-5279 (Electronic) 1552-5260 (Linking). doi: 10.1016/j.jalz.2012.05.2186.

H. Oouchi, K. Yamada, K. Sakai, O. Kizu, T. Kubota, H. Ito, and T. Nishimura. Diffusion anisotropy measurement of brain white matter is affected by voxel size: Underestimation occurs in areas with crossing fibers. *AJNR Am J Neuroradiol*, 28(6):1102--1106, June 2007. ISSN 0195-6108 (Print) 0195-6108 (Linking). doi: 10.3174/ajnr.A0488.

M. Ota, T. Obata, Y. Akine, H. Ito, H. Ikehira, T. Asada, and T. Suhara. Age-related degeneration of corpus callosum measured with diffusion tensor imaging. *Neuroimage*, 31(4):1445--1452, July 2006. ISSN 1053-8119 (Print) 1053-8119 (Linking). doi: 10.1016/j.neuroimage.2006.02.008.

Adeoye A. Oyefiade, Stephanie Ameis, Jason P. Lerch, Conrad Rockel, Kamila U. Szulc, Nadia Scantlebury, Alexandra Decker, Jaleel Jefferson, Simon Spichak, and Donald J. Mabbott. Development of short-range white matter in healthy children and adolescents. *Hum Brain Mapp*, 39

(1):204--217, January 2018. ISSN 1065-9471. doi: 10.1002/hbm.23836.

E. Panagiotaki, T. Schneider, B. Siow, M. G. Hall, M. F. Lythgoe, and D. C. Alexander. Compartment models of the diffusion MR signal in brain white matter: A taxonomy and comparison. *Neuroimage*, 59(3):2241--2254, February 2012. ISSN 1095-9572 (Electronic) 1053-8119 (Linking). doi: 10.1016/j.neuroimage.2011.09.081.

Nikos G. Papadakis, Kay M. Martin, Iain D. Wilkinson, and Chris L. H. Huang. A measure of curve fitting error for noise filtering diffusion tensor MRI data. *J Magn Reson*, 164(1):1--9, 2003. ISSN 10907807. doi: 10.1016/s1090-7807(03)00202-7.

Peter Parbo, Rola Ismail, Kim V. Hansen, Ali Amidi, Frederik H. Mårup, Hanne Gottrup, Hans Brændgaard, Bengt O. Eriksson, Simon F. Eskildsen, Torben E. Lund, Anna Tietze, Paul Edison, Nicola Pavese, Morten G. Stokholm, Per Borghammer, Rainer Hinz, Joel Aanerud, and David J. Brooks. Brain inflammation accompanies amyloid in the majority of mild cognitive impairment cases due to Alzheimer's disease. *Brain*, 140(7):2002--2011, July 2017. ISSN 0006-8950. doi: 10.1093/brain/awx120.

Peter Parbo, Rola Ismail, Michael Sommerauer, Morten G. Stokholm, Allan K. Hansen, Kim V. Hansen, Ali Amidi, Jeppe L. Schaldemose, Hanne Gottrup, Hans Brændgaard, Simon F. Eskildsen, Per Borghammer, Rainer Hinz, Joel Aanerud, and David J. Brooks. Does inflammation precede tau aggregation in early Alzheimer's disease? A PET study. *Neurobiol Dis*, 117:211--216, September 2018. ISSN 0969-9961. doi: 10.1016/j.nbd.2018.06.004.

Geoff J.M. Parker. Probabilistic Fiber Tracking. In *Diffusion MRI: Theory, Methods, and Applications*. Oxford University Press, Oxford, UK, September 2012. ISBN 978-0-19-536977-9. doi: 10.1093/med/9780195369779.003.0023.

O. Pasternak, C. F. Westin, S. Bouix, L. J. Seidman, J. M. Goldstein, T. U. Woo, T. L. Petryshen, R. I. Mesholam-Gately, R. W. McCarley, R. Kikinis, M. E. Shenton, and M. Kubicki. Excessive extracellular volume reveals a neurodegenerative pattern in schizophrenia onset. *J Neurosci*, 32(48):17365--17372, November 2012. ISSN 1529-2401 (Electronic) 0270-6474 (Linking). doi: 10.1523/JNEUROSCI.2904-12.2012.

O. Pasternak, M. Kubicki, and M. E. Shenton. In vivo imaging of neuroinflammation in schizophrenia. *Schizophr Res*, 173(3):200--212, June 2016. ISSN 1573-2509 (Electronic) 0920-9964 (Linking). doi: 10.1016/j.schres.2015.05.034.

Ofer Pasternak, Carl-Fredrik Westin, Brian Dahlben, Sylvain Bouix, and Marek Kubicki. The extent of diffusion MRI markers of neuroinflammation and white matter deterioration in chronic schizophrenia. *Schizophrenia Research*, 161(1):113--118, January 2015. ISSN 0920-9964. doi: 10.1016/j.schres.2014.07.031.

Sharon Peled. New perspectives on the sources of white matter DTI signal. *IEEE Trans Med Imaging*, 26(11):1448--1455, November 2007. ISSN 0278-0062. doi: 10.1109/TMI.2007.906787.

Sharon Peled, Stephen Whalen, Ferenc A Jolesz, and Alexandra J Golby. High b-value apparent diffusion-weighted images from CURVE-ball DTI. *J Magn Reson Imaging*, 30(1):243--248, July 2009. ISSN 1053-1807. doi: 10.1002/jmri.21808.

C. Pennanen, C. Testa, M. P. Laakso, M. Hallikainen, E. L. Helkala, T. Hanninen, M. Kivipelto, M. Kononen, A. Nissinen, S. Tervo, M. Vanhanen, R. Vanninen, G. B. Frisoni, and H. Soininen. A voxel based morphometry study on mild cognitive impairment. *J Neurol Neurosurg Psychiatry*, 76(1):11--14, January 2005. ISSN 0022-3050 (Print) 0022-3050 (Linking). doi: 10.1136/jnnp.2004.035600.

Ronald C. Petersen, Heather J. Wiste, Stephen D. Weigand, Walter A. Rocca, Rosebud O. Roberts, Michelle M. Mielke, Val J. Lowe, David S. Knopman, Vernon S. Pankratz, Mary M. Machulda, Yonas E. Geda, and Clifford R. Jack Jr. Association of Elevated Amyloid Levels With Cognition and Biomarkers in Cognitively Normal People From the Community. *JAMA Neurol*, 73(1):85--92, January 2016. ISSN 2168-6149. doi: 10.1001/jamaneurol.2015.3098.

Jeffrey S. Phillips, Fulvio Da Re, David J. Irwin, Corey T. McMillan, Sanjeev N. Vaishnavi, Sharon X. Xie, Edward B. Lee, Philip A. Cook, James C. Gee, Leslie M. Shaw, John Q. Trojanowski,

David A. Wolk, and Murray Grossman. Longitudinal progression of grey matter atrophy in non-amnestic Alzheimer's disease. *Brain*, 142(6):1701--1722, June 2019. ISSN 0006-8950. doi: 10.1093/brain/awz091.

Maximilian Pietsch and J-Donald Tournier. Effect of demyelination on diffusion tensor indices: A Monte Carlo simulation study. In *Proceedings of the International Society for Magnetic Resonance in Medicine*, volume 23, 23rd Annual Meeting & Exhibition, ISMRM, Toronto, 2015.

O. Piguet, K. L. Double, J. J. Kril, J. Harasty, V. Macdonald, D. A. McRitchie, and G. M. Halliday. White matter loss in healthy ageing: A postmortem analysis. *Neurobiol Aging*, 30(8):1288--1295, August 2009. ISSN 1558-1497 (Electronic) 0197-4580 (Linking). doi: 10.1016/j.neurobiolaging.2007.10.015.

C. Pozzilli, S. Bastianello, A. Bozzao, A. Pierallini, F. Giubilei, C. Argentino, and L. Bozzao. No Differences in Corpus Callosum Size by Sex and Aging. *J Neuroimaging*, 4(4):218--221, 1994. ISSN 1552-6569. doi: 10.1111/jon199444218.

D Prayer, T Roberts, AJ Barkovich, L Prayer, J Kucharczyk, M Moseley, and A. Arieff. Diffusion-weighted MRI of myelination in the rat brain following treatment with gonadal hormones. *Neuroradiology*, 39(5):320--325, 1997. ISSN 0028-3940.

D. M. Prendergast, B. Ardekani, T. Ikuta, M. John, B. Peters, P. DeRosse, R. Wellington, A. K. Malhotra, and P. R. Szeszko. Age and sex effects on corpus callosum morphology across the lifespan. *Hum Brain Mapp*, 36(7):2691--2702, July 2015. ISSN 1097-0193 (Electronic) 1065-9471 (Linking). doi: 10.1002/hbm.22800.

M. G. Preti, F. Baglio, M. M. Laganà, L. Griffanti, R. Nemni, M. Clerici, M. Bozzali, and G. Baselli. Assessing corpus callosum changes in Alzheimer's disease: Comparison between tract-based spatial statistics and atlas-based tractography. *PLoS One*, 7(4):e35856, 2012. ISSN 1932-6203 (Electronic) 1932-6203 (Linking). doi: 10.1371/journal.pone.0035856.

W. Qin, C. S. Yu, F. Zhang, X. Y. Du, H. Jiang, Y. X. Yan, and K. C. Li. Effects of echo time on diffusion quantification of brain white matter at 1.5 T and 3.0 T. *Magn Reson Med*, 61(4):755--760, April 2009. ISSN 1522-2594 (Electronic) 0740-3194 (Linking). doi: 10.1002/mrm.21920.

Yingwei Qiu, Siwei Liu, Saima Hilal, Yng Miin Loke, Mohammad Kamran Ikram, Xin Xu, Boon Yeow Tan, Narayanaswamy Venketasubramanian, Christopher Li-Hsian Chen, and Juan Zhou. Inter-hemispheric functional dysconnectivity mediates the association of corpus callosum degeneration with memory impairment in AD and amnestic MCI. *Sci Rep*, 6(1):1--12, September 2016. ISSN 2045-2322. doi: 10.1038/srep32573.

Eric M. Reiman, Kewei Chen, Xiaofen Liu, Daniel Bandy, Meixiang Yu, Wendy Lee, Napatkamon Ayutyanont, Jennifer Keppler, Stephanie A. Reeder, Jessica B. S. Langbaum, Gene E. Alexander, William E. Klunk, Chester A. Mathis, Julie C. Price, Howard J. Aizenstein, Steven T. DeKosky, and Richard J. Caselli. Fibrillar amyloid-beta burden in cognitively normal people at 3 levels of genetic risk for Alzheimer's disease. *Proc Natl Acad Sci USA*, 106(16):6820--6825, April 2009. doi: 10.1073/pnas.0900345106.

Katherine Reiter, Kristy A. Nielson, Sally Durgerian, John L. Woodard, J. Carson Smith, Michael Seidenberg, Dana A. Kelly, and Stephen M. Rao. Five-Year Longitudinal Brain Volume Change in Healthy Elders at Genetic Risk for Alzheimer's Disease. *J Alzheimers Dis*, 55(4):1363--1377, January 2017. ISSN 1387-2877. doi: 10.3233/JAD-160504.

Christiane Reitz. Alzheimer's Disease and the Amyloid Cascade Hypothesis: A Critical Review. *Int J Alzheimers Dis*, 369808, 2012. doi: 10.1155/2012/369808.

J. Renoux, D. Facon, P. Fillard, I. Huynh, P. Lasjaunias, and D. Ducreux. MR diffusion tensor imaging and fiber tracking in inflammatory diseases of the spinal cord. *AJNR Am J Neuroradiol*, 27(9):1947--1951, October 2006. ISSN 0195-6108 (Print) 0195-6108 (Linking).

B. C. Riedel, P. M. Thompson, and R. D. Brinton. Age, APOE and sex: Triad of risk of Alzheimer's disease. *J Steroid Biochem Mol Biol*, 160:134--147, June 2016. ISSN 1879-1220 (Electronic) 0960-0760 (Linking). doi: 10.1016/j.jsbmb.2016.03.012.

Stuart J. Ritchie, David Alexander Dickie, Simon R. Cox, Maria del C. Valdes Hernandez, Janie Corley, Natalie A. Royle, Alison Pattie, Benjamin S. Aribisala, Paul Redmond, Susana Muñoz Maniega, Adele M. Taylor, Ruth Sibbett, Alan J. Gow, John M. Starr, Mark E. Bastin, Joanna M. Wardlaw, and Ian J. Deary. Brain volumetric changes and cognitive ageing during the eighth decade of life. *Human Brain Mapping*, 36(12):4910--4925, 2015. ISSN 1097-0193. doi: 10.1002/hbm.22959.

T. Rohlfing. Incorrect ICBM-DTI-81 atlas orientation and white matter labels. *Front Neurosci*, 7:4, 2013. ISSN 1662-4548 (Print) 1662-453X (Linking). doi: 10.3389/fnins.2013.00004.

Olaf Ronneberger, Philipp Fischer, and Thomas Brox. U-Net: Convolutional Networks for Biomedical Image Segmentation. *arXiv:1505.04597*, 2015.

P. B. Rosenberg, M. A. Nowrangi, and C. G. Lyketsos. Neuropsychiatric symptoms in Alzheimer's disease: What might be associated brain circuits? *Mol Aspects Med*, 43-44:25--37, June 2015. ISSN 1872-9452 (Electronic) 0098-2997 (Linking). doi: 10.1016/j.mam.2015.05.005.

Anna Rotarska-Jagiela, Ralf Schönmeyer, Viola Oertel, Corinna Haenschel, Kai Vogeley, and David EJ Linden. The corpus callosum in schizophrenia-volume and connectivity changes affect specific regions. *Neuroimage*, 39(4):1522--1532, 2008. ISSN 1053-8119.

W A H Rushton. A theory of the effects of fibre size in medullated nerve. *J Physiol*, 115(1):101--122, September 1951. ISSN 0022-3751. doi: 10.1113/jphysiol.1951.sp004655.

Henry Rusinek, Susan de Santi, Dina Frid, Wai-Hon Tsui, Chaim Y. Tarshish, Antonio Convit, and Mony J. de Leon. Regional Brain Atrophy Rate Predicts Future Cognitive Decline: 6-year Longitudinal MR Imaging Study of Normal Aging. *Radiology*, 229(3):691--696, December 2003. ISSN 0033-8419. doi: 10.1148/radiol.2293021299.

C. Ryberg, E. Rostrup, M. B. Stegmann, F. Barkhof, P. Scheltens, E. C. W. van Straaten, F. Fazekas, R. Schmidt, J. M. Ferro, H. Baezner, T. Erkinjuntti, H. Jokinen, L. O. Wahlund, J. O'Brien, A. M. Basile, L. Pantoni, D. Inzitari, and G. Waldemar. Clinical significance of corpus callosum atrophy in a mixed elderly population. *Neurobiol Aging*, 28(6):955--963, June 2007. ISSN 0197-4580. doi: 10.1016/j.neurobiolaging.2006.04.008.

S. Sala, F. Agosta, E. Pagani, M. Copetti, G. Comi, and M. Filippi. Microstructural changes and atrophy in brain white matter tracts with aging. *Neurobiol Aging*, 33(3):488--498 e2, March 2012. ISSN 1558-1497 (Electronic) 0197-4580 (Linking). doi: 10.1016/j.neurobiolaging.2010.04.027.

R. Salvador, A. Pena, D. K. Menon, T. A. Carpenter, J. D. Pickard, and E. T. Bullmore. Formal characterization and extension of the linearized diffusion tensor model. *Hum Brain Mapp*, 24(2):144--155, February 2005. ISSN 1065-9471 (Print) 1065-9471 (Linking). doi: 10.1002/hbm.20076.

Amjad Samara, Tatianna Murphy, Jeremy Strain, Jerrel Rutlin, Peng Sun, Olga Neyman, Nitya Sreevalsan, Joshua S. Shimony, Beau M. Ances, Sheng-Kwei Song, Tamara Hershey, and Sarah A. Eisenstein. Neuroinflammation and White Matter Alterations in Obesity Assessed by Diffusion Basis Spectrum Imaging. *Frontiers in Human Neuroscience*, 13:464, 2020. ISSN 1662-5161. doi: 10.3389/fnhum.2019.00464.

P. N. Sen and P. J. Basser. A model for diffusion in white matter in the brain. *Biophys J*, 89(5):2927--2938, November 2005. ISSN 0006-3495 (Print) 0006-3495 (Linking). doi: 10.1529/biophysj.105.063016.

Yoshiteru Seo, Hadassah Shinar, Yasushi Morita, and Gil Navon. Anisotropic and restricted diffusion of water in the sciatic nerve: A 2H double-quantum-filtered NMR study. *Magn Reson Med*, 42(3):461--466, 1999. ISSN 0740-3194.

Kiran K. Seunarine and Daniel C. Alexander. Multiple Fibers: Beyond the Diffusion Tensor. In *Diffusion MRI: From Quantitative Measurement to in-Vivo Neuroanatomy*. Academic Press, 2009.

C. E. Sexton, C. E. Mackay, J. A. Lonie, M. E. Bastin, E. Terrière, R. E. O'Carroll, and K. P. Ebmeier. MRI correlates of episodic memory in Alzheimer's disease, mild cognitive impairment, and healthy aging. *Psychiatry Res*, 184(1):57--62, October 2010. ISSN 0165-1781 (Print) 0165-1781

(Linking). doi: 10.1016/j.pscychresns.2010.07.005.

C. E. Sexton, U. G. Kalu, N. Filippini, C. E. Mackay, and K. P. Ebmeier. A meta-analysis of diffusion tensor imaging in mild cognitive impairment and Alzheimer's disease. *Neurobiol Aging*, 32(12):2322 e5--18, December 2011. ISSN 1558-1497 (Electronic) 0197-4580 (Linking). doi: 10.1016/j.neurobiolaging.2010.05.019.

C. E. Sexton, K. B. Walhovd, A. B. Storsve, C. K. Tamnes, L. T. Westlye, H. Johansen-Berg, and A. M. Fjell. Accelerated changes in white matter microstructure during aging: A longitudinal diffusion tensor imaging study. *J Neurosci*, 34(46):15425--15436, November 2014. ISSN 1529-2401 (Electronic) 0270-6474 (Linking). doi: 10.1523/JNEUROSCI.0203-14.2014.

David A. Slater, Lester Melie-Garcia, Martin Preisig, Ferath Kherif, Antoine Lutti, and Bogdan Draganski. Evolution of white matter tract microstructure across the life span. *Hum Brain Mapp*, 40(7):2252--2268, 2019. ISSN 1097-0193. doi: 10.1002/hbm.24522.

S. A. Small and K. Duff. Linking Abeta and tau in late-onset Alzheimer's disease: A dual pathway hypothesis. *Neuron*, 60(4):534--542, November 2008. ISSN 1097-4199 (Electronic) 0896-6273 (Linking). doi: 10.1016/j.neuron.2008.11.007.

S. M. Smith, M. Jenkinson, M. W. Woolrich, C. F. Beckmann, T. E. Behrens, H. Johansen-Berg, P. R. Bannister, M. De Luca, I. Drobnjak, D. E. Flitney, R. K. Niazy, J. Saunders, J. Vickers, Y. Zhang, N. De Stefano, J. M. Brady, and P. M. Matthews. Advances in functional and structural MR image analysis and implementation as FSL. *Neuroimage*, 23 Suppl 1:S208--219, 2004. ISSN 1053-8119 (Print) 1053-8119 (Linking). doi: 10.1016/j.neuroimage.2004.07.051.

Jonatan A. Snir, Robert Bartha, and Manuel Montero-Odasso. White matter integrity is associated with gait impairment and falls in mild cognitive impairment. Results from the gait and brain study. *NeuroImage Clin*, 24:101975, 2019. ISSN 22131582. doi: 10.1016/j.nicl.2019.101975.

S. K. Song, S. W. Sun, W. K. Ju, S. J. Lin, A. H. Cross, and A. H. Neufeld. Diffusion tensor imaging detects and differentiates axon and myelin degeneration in mouse optic nerve after retinal ischemia. *Neuroimage*, 20(3):1714--1722, November 2003. ISSN 1053-8119 (Print) 1053-8119 (Linking). doi: 10.1016/S1053-8119(03)00440-3.

P. Staempfli, T. Jaermann, G. R. Crelier, S. Kollias, A. Valavanis, and P. Boesiger. Resolving fiber crossing using advanced fast marching tractography based on diffusion tensor imaging. *Neuroimage*, 30(1):110--120, March 2006. ISSN 1053-8119 (Print) 1053-8119 (Linking). doi: 10.1016/j.neuroimage.2005.09.027.

L. Steardo, Jr., M. R. Bronzuoli, A. Iacomino, G. Esposito, L. Steardo, and C. Scuderi. Does neuroinflammation turn on the flame in Alzheimer's disease? Focus on astrocytes. *Front Neurosci*, 9:259, 2015. ISSN 1662-4548 (Print) 1662-453X (Linking). doi: 10.3389/fnins.2015.00259.

E. O. Stejskal and J. E. Tanner. Spin diffusion measurements: Spin echoes in the presence of a time-dependent field gradient. *J Chem Phys*, 42(1), 1965.

Nikola Stikov, Jennifer S.W. Campbell, Thomas Stroh, Mariette Lavelée, Stephen Frey, Jennifer Novek, Stephen Nuara, Ming-Kai Ho, Barry J. Bedell, Robert F. Dougherty, Ilana R. Leppert, Mathieu Boudreau, Sridar Narayanan, Tanguy Duval, Julien Cohen-Adad, Paul-Alexandre Picard, Alicja Gasecka, Daniel Côté, and G. Bruce Pike. In vivo histology of the myelin g-ratio with magnetic resonance imaging. *NeuroImage*, 118:397--405, September 2015. ISSN 1053-8119. doi: 10.1016/j.neuroimage.2015.05.023.

Joel R Stiles and Thomas M Bartol. Monte Carlo methods for simulating realistic synaptic microphysiology using MCell. In *Computational Neuroscience: Realistic Modeling for Experimentalists*, pages 87--127. E. CRC Press, Boca Raton, 2001.

Joel R Stiles, Dirk Van Helden, Thomas M Bartol, Edwin E Salpeter, and Miriam M Salpeter. Miniature endplate current rise times less than 100 microseconds from improved dual recordings can be modeled with passive acetylcholine diffusion from a synaptic vesicle. *PNAS*, 93(12): 5747--5752, 1996. ISSN 0027-8424.

N. H. Stricker, B. C. Schweinsburg, L. Delano-Wood, C. E. Wierenga, K. J. Bangen, K. Y. Haaland,

L. R. Frank, D. P. Salmon, and M. W. Bondi. Decreased white matter integrity in late-myelinating fiber pathways in Alzheimer's disease supports retrogenesis. *Neuroimage*, 45(1):10--16, March 2009. ISSN 1095-9572 (Electronic) 1053-8119 (Linking). doi: 10.1016/j.neuroimage.2008.11.027.

N. H. Stricker, D. H. Salat, T. P. Kuhn, J. M. Foley, J. S. Price, L. T. Westlye, M. S. Esterman, R. E. McGlinchey, W. P. Milberg, and E. C. Leritz. Mild Cognitive Impairment is Associated With White Matter Integrity Changes in Late-Myelinating Regions Within the Corpus Callosum. *Am J Alzheimers Dis Other Demen*, 31(1):68--75, February 2016. ISSN 1938-2731 (Electronic) 1533-3175 (Linking). doi: 10.1177/1533317515578257.

E. V. Sullivan, M. J. Rosenbloom, J. E. Desmond, and A. Pfefferbaum. Sex differences in corpus callosum size: Relationship to age and intracranial size. *Neurobiol Aging*, 22(4):603--611, July 2001. ISSN 0197-4580 (Print) 0197-4580 (Linking).

I. Suridjan, B. G. Pollock, N. P. L. G. Verhoeff, A. N. Voineskos, T. Chow, P. M. Rusjan, N. J. Lobaugh, S. Houle, B. H. Mulsant, and R. Mizrahi. In-vivo imaging of grey and white matter neuroinflammation in Alzheimer's disease: A positron emission tomography study with a novel radioligand, [18 F]-FEPPA. *Molecular Psychiatry*, 20(12):1579--1587, December 2015. ISSN 1476-5578. doi: 10.1038/mp.2015.1.

M. M. Tanaka-Arakawa, M. Matsui, C. Tanaka, A. Uematsu, S. Uda, K. Miura, T. Sakai, and K. Noguchi. Developmental changes in the corpus callosum from infancy to early adulthood: A structural magnetic resonance imaging study. *PLoS One*, 10(3):e0118760, 2015. ISSN 1932-6203 (Electronic) 1932-6203 (Linking). doi: 10.1371/journal.pone.0118760.

Y Tang, J. R Nyengaard, B Pakkenberg, and H. J. G Gundersen. Age-Induced White Matter Changes in the Human Brain: A Stereological Investigation. *Neurobiol Aging.*, 18(6):609--615, November 1997. ISSN 0197-4580. doi: 10.1016/S0197-4580(97)00155-3.

Maxime Taquet, Aleksandar Jankovski, Gaëtan Rensonnet, Damien Jacobs, Anne des Rieux, Benoît Macq, Simon K. Warfield, and Benoît Scherrer. Extra-axonal restricted diffusion as an in-vivo marker of reactive microglia. *Scientific Reports*, 9(1):13874, September 2019. ISSN 2045-2322. doi: 10.1038/s41598-019-50432-5.

K. Thapaliya, V. Vegh, S. Bollmann, and M. Barth. Assessment of microstructural signal compartments across the corpus callosum using multi-echo gradient recalled echo at 7 T. *Neuroimage*, 182:407--416, November 2018. ISSN 1095-9572 (Electronic) 1053-8119 (Linking). doi: 10.1016/j.neuroimage.2017.11.029.

Carsten Thomsen, O. Henriksen, and P. Ring. In vivo measurement of water self diffusion in the human brain by magnetic resonance imaging. *Acta Radiol*, 28(3):353--361, 1987. ISSN 0284-1851 1600-0455. doi: 10.3109/02841858709177362.

R. H. Tijssen, J. F. Jansen, and W. H. Backes. Assessing and minimizing the effects of noise and motion in clinical DTI at 3 T. *Hum Brain Mapp*, 30(8):2641--2655, August 2009. ISSN 1097-0193 (Electronic) 1065-9471 (Linking). doi: 10.1002/hbm.20695.

Abolghasem Tohidpour, Andrey V Morgun, Elizaveta B Boitsova, Natalia A Malinovskaya, Galina P Martynova, Elena D Khilazheva, Natalia V Kopylevich, Galina E Gertsog, and Alla B Salmina. Neuroinflammation and Infection: Molecular Mechanisms Associated with Dysfunction of Neurovascular Unit. *Front Cell Infect Microbiol*, 7:276--276, June 2017. ISSN 2235-2988. doi: 10.3389/fcimb.2017.00276.

Henry C. Torrey. Bloch equations with diffusion terms. *Phys Rev*, 104(3):563--565, 1956.

J. D. Tournier, F. Calamante, D. G. Gadian, and A. Connelly. Direct estimation of the fiber orientation density function from diffusion-weighted MRI data using spherical deconvolution. *Neuroimage*, 23(3):1176--1185, November 2004. ISSN 1053-8119 (Print) 1053-8119 (Linking). doi: 10.1016/j.neuroimage.2004.07.037.

J. D. Tournier, F. Calamante, and A. Connelly. Robust determination of the fibre orientation distribution in diffusion MRI: Non-negativity constrained super-resolved spherical deconvolution. *Neuroimage*, 35(4):1459--1472, May 2007. ISSN 1053-8119 (Print) 1053-8119 (Linking). doi: 10.1016/j.neuroimage.2007.02.016.

J. Donald Tournier, Fernando Calamante, and Alan Connelly. MRtrix: Diffusion tractography in crossing fiber regions. *Int J Img Syst Tech*, 22(1):53--66, 2012. ISSN 08999457. doi: 10.1002/ima.22005.

D.J. Tozer, G.R. Davies, D.R. Altmann, D.H. Miller, and P.S. Tofts. Correlation of apparent myelin measures obtained in multiple sclerosis patients and controls from magnetization transfer and multicompartmental T2 analysis. *Magnetic Resonance in Medicine*, 53(6):1415--1422, June 2005. ISSN 0740-3194. doi: 10.1002/mrm.20479.

A. Tristán-Vega, S. Aja-Fernández, and C. F. Westin. Least squares for diffusion tensor estimation revisited: Propagation of uncertainty with Rician and non-Rician signals. *Neuroimage*, 59(4):4032--4043, February 2012. ISSN 1095-9572 (Electronic) 1053-8119 (Linking). doi: 10.1016/j.neuroimage.2011.09.074.

M. Ukmar, E. Makuc, M. L. Onor, G. Garbin, M. Trevisiol, and M. A. Cova. Evaluation of white matter damage in patients with Alzheimer's disease and in patients with mild cognitive impairment by using diffusion tensor imaging. *Radiol med*, 113(6):915--922, July 2008. ISSN 1826-6983. doi: 10.1007/s11547-008-0286-1.

Mateusz M. Urbanski, Matthew B. Brendel, and Carmen V. Melendez-Vasquez. Acute and chronic demyelinated CNS lesions exhibit opposite elastic properties. *Scientific Reports*, 9(1):999, January 2019. ISSN 2045-2322. doi: 10.1038/s41598-018-37745-7.

L. J. Van Eldik, M. C. Carrillo, P. E. Cole, D. Feuerbach, B. D. Greenberg, J. A. Hendrix, M. Kennedy, N. Kozauer, R. A. Margolin, J. L. Molinuevo, R. Mueller, R. M. Ransohoff, D. M. Wilcock, L. Bain, and K. Bales. The roles of inflammation and immune mechanisms in Alzheimer's disease. *Alzheimers Dement (N Y)*, 2(2):99--109, June 2016. ISSN 2352-8737 (Print) 2352-8737 (Linking). doi: 10.1016/j.trci.2016.05.001.

D. C. Van Essen, S. M. Smith, D. M. Barch, T. E. Behrens, E. Yacoub, K. Ugurbil, and WU-Minn HCP Consortium. The WU-Minn Human Connectome Project: An overview. *Neuroimage*, 80:62--79, October 2013. ISSN 1095-9572 (Electronic) 1053-8119 (Linking). doi: 10.1016/j.neuroimage.2013.05.041.

Irene M. Vavasour, Sophie C. Huijskens, David K. B. Li, Anthony L. Traboulsee, Burkhard Mädler, Shannon H. Kolind, Alexander Rauscher, G. R. Wayne Moore, Alex L. MacKay, and Cornelia Laule. Global loss of myelin water over 5 years in multiple sclerosis normal-appearing white matter. *Multiple Sclerosis Journal*, 24(12):1557--1568, October 2018. ISSN 1352-4585. doi: 10.1177/1352458517723717.

J. Veraart, J. Sijbers, S. Sunaert, A. Leemans, and B. Jeurissen. Weighted linear least squares estimation of diffusion MRI parameters: Strengths, limitations, and pitfalls. *Neuroimage*, 81:335--346, November 2013. ISSN 1095-9572 (Electronic) 1053-8119 (Linking). doi: 10.1016/j.neuroimage.2013.05.028.

Nicolas Villain, Marine Fouquet, Jean Claude Baron, Florence Mézenge, Brigitte Landeau, Vincent de La Sayette, Fausto Viader, Francis Eustache, Béatrice Desgranges, and Gaël Chételat. Sequential relationships between grey matter and white matter atrophy and brain metabolic abnormalities in early Alzheimer's disease. *Brain*, 133(11):3301--3314, November 2010. ISSN 0006-8950. doi: 10.1093/brain/awq203.

Ashwati Vipin, Kwun Kei Ng, Fang Ji, Hee Youn Shim, Joseph K. W. Lim, Ofer Pasternak, and Juan Helen Zhou. Amyloid burden accelerates white matter degradation in cognitively normal elderly individuals. *Hum Brain Mapp*, 40(7):2065--2075, 2019. ISSN 1097-0193. doi: 10.1002/hbm.24507.

Setsu Wakana, Hangyi Jiang, Lidia M Nagae-Poetscher, Peter CM van Zijl, and Susumu Mori. Fiber tract–based atlas of human white matter anatomy. *Radiology*, 230(1):77--87, 2004. ISSN 0033-8419.

Setsu Wakana, Arvind Caprihan, Martina M. Panzenboeck, James H. Fallon, Michele Perry, Randy L. Gollub, Kegang Hua, Jiangyang Zhang, Hangyi Jiang, Prachi Dubey, Ari Blitz, Peter van Zijl, and Susumu Mori. Reproducibility of quantitative tractography methods applied to

cerebral white matter. *Neuroimage*, 36(3):630--644, 2007.

Maggie Wang, Jennifer E Norman, Vivek J Srinivasan, and John C Rutledge. Metabolic, inflammatory, and microvascular determinants of white matter disease and cognitive decline. *Am J Neurodegener Dis*, 5(5):171--177, November 2016. ISSN 2165-591X.

Qing Wang, Yong Wang, Jingxia Liu, Courtney L. Sutphen, Carlos Cruchaga, Tyler Blazey, Brian A. Gordon, Yi Su, Charlie Chen, Joshua S. Shimony, Beau M. Ances, Nigel J. Cairns, Anne M. Fagan, John C. Morris, and Tammie L. S. Benzinger. Quantification of white matter cellularity and damage in preclinical and early symptomatic Alzheimer's disease. *NeuroImage: Clinical*, 22, 2019. ISSN 22131582. doi: 10.1016/j.nicl.2019.101767.

W. Y. Wang, M. S. Tan, J. T. Yu, and L. Tan. Role of pro-inflammatory cytokines released from microglia in Alzheimer's disease. *Ann Transl Med*, 3(10):136, June 2015a. ISSN 2305-5839 (Print) 2305-5839 (Linking). doi: 10.3978/j.issn.2305-5839.2015.03.49.

X. D. Wang, M. Ren, M. W. Zhu, W. P. Gao, J. Zhang, H. Shen, Z. G. Lin, H. L. Feng, C. J. Zhao, and K. Gao. Corpus callosum atrophy associated with the degree of cognitive decline in patients with Alzheimer's dementia or mild cognitive impairment: A meta-analysis of the region of interest structural imaging studies. *J Psychiatr Res*, 63:10--19, April 2015b. ISSN 1879-1379 (Electronic) 0022-3956 (Linking). doi: 10.1016/j.jpsychires.2015.02.005.

Yong Wang, Qing Wang, Justin P. Haldar, Fang-Cheng Yeh, Mingqiang Xie, Peng Sun, Tsang-Wei Tu, Kathryn Trinkaus, Robyn S. Klein, Anne H. Cross, and Sheng-Kwei Song. Quantification of increased cellularity during inflammatory demyelination. *Brain*, 134(12):3590--3601, December 2011. ISSN 0006-8950. doi: 10.1093/brain/awr307.

Janaka P. Wansapura, Scott K. Holland, R. Scott Dunn, and William S. Ball. NMR Relaxation Times in the Human Brain at 3.0 Tesla. *Journal of Magnetic Resonance Imaging*, 9:531--538, 1999.

J. Wasserthal, P. Neher, and K. H. Maier-Hein. TractSeg - Fast and accurate white matter tract segmentation. *Neuroimage*, 183:239--253, December 2018a. ISSN 1095-9572 (Electronic) 1053-8119 (Linking). doi: 10.1016/j.neuroimage.2018.07.070.

J. Wasserthal, P. F. Neher, D. Hirjak, and K. H. Maier-Hein. Combined tract segmentation and orientation mapping for bundle-specific tractography. *Med Image Anal*, 58:101559, December 2019. ISSN 1361-8423 (Electronic) 1361-8415 (Linking). doi: 10.1016/j.media.2019.101559.

Jakob Wasserthal. TractSeg Tutorial. https://github.com/MIC-DKFZ/TractSeg/blob/master/resources/Tutorial.md, accessed 14/09/2018.

Jakob Wasserthal, Peter F. Neher, and Klaus H. Maier-Hein. Tract orientation mapping for bundle-specific tractography. *arXiv:1806.05580*, 2018b.

M. W. Weiner, P. S. Aisen, C. R. Jack Jr., W. J. Jagust, J. Q. Trojanowski, L. Shaw, A. J. Saykin, J. C. Morris, N. Cairns, L. A. Beckett, A. Toga, R. Green, S. Walter, H. Soares, P. Snyder, E. Siemers, W. Potter, P. E. Cole, M. Schmidt, and Alzheimer's Disease Neuroimaging Initiative. The Alzheimer's disease neuroimaging initiative: Progress report and future plans. *Alzheimers Dement*, 6(3):202--211 e7, May 2010. ISSN 1552-5279 (Electronic) 1552-5260 (Linking). doi: 10.1016/j.jalz.2010.03.007.

M. W. Weiner, D. P. Veitch, P. S. Aisen, L. A. Beckett, N. J. Cairns, R. C. Green, D. Harvey, C. R. Jack Jr., W. Jagust, E. Liu, J. C. Morris, R. C. Petersen, A. J. Saykin, M. E. Schmidt, L. Shaw, L. Shen, J. A. Siuciak, H. Soares, A. W. Toga, J. Q. Trojanowski, and Alzheimer's Disease Neuroimaging Initiative. The Alzheimer's Disease Neuroimaging Initiative: A review of papers published since its inception. *Alzheimers Dement*, 8(1 Suppl):S1--68, September 2013. ISSN 1552-5279 (Electronic) 1552-5260 (Linking). doi: 10.1016/j.jalz.2013.05.1769.

M. W. Weiner, D. P. Veitch, P. S. Aisen, L. A. Beckett, N. J. Cairns, J. Cedarbaum, M. C. Donohue, R. C. Green, D. Harvey, C. R. Jack Jr., W. Jagust, J. C. Morris, R. C. Petersen, A. J. Saykin, L. Shaw, P. M. Thompson, A. W. Toga, J. Q. Trojanowski, and Alzheimer's Disease Neuroimaging Initiative. Impact of the Alzheimer's Disease Neuroimaging Initiative, 2004 to 2014. *Alzheimers Dement*, 11(7):865--884, July 2015. ISSN 1552-5279 (Electronic) 1552-5260

(Linking). doi: 10.1016/j.jalz.2015.04.005.

M. W. Weiner, D. P. Veitch, P. S. Aisen, L. A. Beckett, N. J. Cairns, R. C. Green, D. Harvey, C. R. Jack Jr., W. Jagust, J. C. Morris, R. C. Petersen, J. Salazar, A. J. Saykin, L. M. Shaw, A. W. Toga, J. Q. Trojanowski, and Initiative Alzheimer's Disease Neuroimaging. The Alzheimer's Disease Neuroimaging Initiative 3: Continued innovation for clinical trial improvement. *Alzheimers Dement*, 13(5):561--571, May 2017. ISSN 1552-5279 (Electronic) 1552-5260 (Linking). doi: 10.1016/j.jalz.2016.10.006.

Serge Weis, Melitta Kimbacher, Emanuel Wenger, and Andreas Neuhold. Morphometric analysis of the corpus callosum using MR: Correlation of measurements with aging in healthy individuals. *AJNR Am J Neuroradiol*, 14(3):637--645, 1993. ISSN 0195-6108.

R. Westerhausen, F. Kreuder, S. Dos Santos Sequeira, C. Walter, W. Woerner, R. A. Wittling, E. Schweiger, and W. Wittling. Effects of handedness and gender on macro- and microstructure of the corpus callosum and its subregions: A combined high-resolution and diffusion-tensor MRI study. *Brain Res Cogn Brain Res*, 21(3):418--426, November 2004. ISSN 0926-6410 (Print) 0926-6410 (Linking). doi: 10.1016/j.cogbrainres.2004.07.002.

L. T. Westlye, K. B. Walhovd, A. M. Dale, A. Bjørnerud, P. Due-Tønnessen, A. Engvig, H. Grydeland, C. K. Tamnes, Y. Østby, and A. M. Fjell. Life-span changes of the human brain white matter: Diffusion tensor imaging (DTI) and volumetry. *Cereb Cortex*, 20(9):2055--2068, September 2010. ISSN 1460-2199 (Electronic) 1047-3211 (Linking). doi: 10.1093/cercor/bhp280.

Kenneth P Whittall, Alex L. Mackay, Douglas A. Graeb, Robert A. Nugent, David K. B. Li, and Donald W. Paty. In vivo measurement of T2 distributions and water contents in normal human brain. *Magnetic Resonance in Medicine*, 37(1):34--43, January 1997. ISSN 0740-3194. doi: 10.1002/mrm.1910370107.

P. J. Winklewski, A. Sabisz, P. Naumczyk, K. Jodzio, E. Szurowska, and A. Szarmach. Understanding the physiopathology behind axial and radial diffusivity changes - What do we know? *Front Neurol*, 9:92, 2018. ISSN 1664-2295 (Print) 1664-2295 (Linking). doi: 10.3389/fneur.2018.00092.

S. F. Witelson. Hand and sex differences in the isthmus and genu of the human corpus callosum. A postmortem morphological study. *Brain*, 112(3):799--835, June 1989. ISSN 0006-8950 (Print) 0006-8950 (Linking). doi: 10.1093/brain/112.3.799.

Girma Woldehawariat, Pedro E. Martinez, Peter Hauser, David M. Hoover, Wayne W. C. Drevets, and Francis J. McMahon. Corpus Callosum Size Is Highly Heritable in Humans, and May Reflect Distinct Genetic Influences on Ventral and Rostral Regions. *PLoS One*, 9(6):e99980, June 2014. ISSN 1932-6203. doi: 10.1371/journal.pone.0099980.

J. J. Wolff, G. Gerig, J. D. Lewis, T. Soda, M. A. Styner, C. Vachet, K. N. Botteron, J. T. Elison, S. R. Dager, A. M. Estes, H. C. Hazlett, R. T. Schultz, L. Zwaigenbaum, J. Piven, and Ibis Network. Altered corpus callosum morphology associated with autism over the first 2 years of life. *Brain*, 138(Pt 7):2046--2058, July 2015. ISSN 1460-2156 (Electronic) 0006-8950 (Linking). doi: 10.1093/brain/awv118.

M. W. Woolrich, S. Jbabdi, B. Patenaude, M. Chappell, S. Makni, T. Behrens, C. Beckmann, M. Jenkinson, and S. M. Smith. Bayesian analysis of neuroimaging data in FSL. *Neuroimage*, 45(1 Suppl):S173--186, March 2009. ISSN 1095-9572 (Electronic) 1053-8119 (Linking). doi: 10.1016/j.neuroimage.2008.10.055.

H. Yamada, O. Abe, T. Shizukuishi, J. Kikuta, T. Shinozaki, K. Dezawa, A. Nagano, M. Matsuda, H. Haradome, and Y. Imamura. Efficacy of distortion correction on diffusion imaging: Comparison of FSL eddy and eddy_correct using 30 and 60 directions diffusion encoding. *PLoS One*, 9(11): e112411, 2014. ISSN 1932-6203 (Electronic) 1932-6203 (Linking). doi: 10.1371/journal.pone.0112411.

J. D. Yeatman, R. F. Dougherty, N. J. Myall, B. A. Wandell, and H. M. Feldman. Tract profiles of white matter properties: Automating fiber-tract quantification. *PLoS One*, 7(11):e49790, 2012. ISSN 1932-6203 (Electronic) 1932-6203 (Linking). doi: 10.1371/journal.pone.0049790.

C. H. Yeh, B. Schmitt, D. Le Bihan, J. R. Li-Schlittgen, C. P. Lin, and C. Poupon. Diffusion

microscopist simulator: A general Monte Carlo simulation system for diffusion magnetic resonance imaging. *PLoS One*, 8(10):e76626, 2013. ISSN 1932-6203 (Electronic) 1932-6203 (Linking). doi: 10.1371/journal.pone.0076626.

Hyon Ah Yi, Christiane Möller, Nikki Dieleman, Femke H Bouwman, Frederik Barkhof, Philip Scheltens, Wiesje M van der Flier, and Hugo Vrenken. Relation between subcortical grey matter atrophy and conversion from mild cognitive impairment to Alzheimer's disease. *J Neurol Neurosurg Psychiatry*, 87(4):425--432, April 2016. doi: 10.1136/jnnp-2014-309105.

F. Yu, Q. Fan, Q. Tian, C. Ngamsombat, N. Machado, J.D. Bireley, A.W. Russo, A. Nummenmaa, T. Witzel, L.L. Wald, E.C. Klawiter, and S.Y. Huang. Imaging G-Ratio in Multiple Sclerosis Using High-Gradient Diffusion MRI and Macromolecular Tissue Volume. *Am. J. Neuroradiol.*, November 2019. doi: 10.3174/ajnr.A6283.

L. Yu, R. J. Dawe, A. S. Buchman, P. A. Boyle, J. A. Schneider, K. Arfanakis, and D. A. Bennett. Ex vivo MRI transverse relaxation in community based older persons with and without Alzheimer's dementia. *Behav Brain Res*, 322(Pt B):233--240, March 2017. ISSN 1872-7549 (Electronic) 0166-4328 (Linking). doi: 10.1016/j.bbr.2016.09.001.

A. Zavaliangos-Petropulu, T. M. Nir, S. I. Thomopoulos, R. I. Reid, M. A. Bernstein, B. Borowski, C. R. Jack Jr., M. W. Weiner, N. Jahanshad, and P. M. Thompson. Diffusion MRI Indices and Their Relation to Cognitive Impairment in Brain Aging: The Updated Multi-protocol Approach in ADNI3. *Front Neuroinform*, 13:2, 2019. ISSN 1662-5196 (Print) 1662-5196 (Linking). doi: 10.3389/fninf.2019.00002.

H. Zhang, P. L. Hubbard, G. J. Parker, and D. C. Alexander. Axon diameter mapping in the presence of orientation dispersion with diffusion MRI. *Neuroimage*, 56(3):1301--1315, June 2011. ISSN 1095-9572 (Electronic) 1053-8119 (Linking). doi: 10.1016/j.neuroimage.2011.01.084.

H. Zhang, T. Schneider, C. A. Wheeler-Kingshott, and D. C. Alexander. NODDI: Practical in vivo neurite orientation dispersion and density imaging of the human brain. *Neuroimage*, 61 (4):1000--1016, July 2012. ISSN 1095-9572 (Electronic) 1053-8119 (Linking). doi: 10.1016/j.neuroimage.2012.03.072.

Y. Zhang, N. Schuff, G. H. Jahng, W. Bayne, S. Mori, L. Schad, S. Mueller, A. T. Du, J. H. Kramer, K. Yaffe, H. Chui, W. J. Jagust, B. L. Miller, and M. W. Weiner. Diffusion tensor imaging of cingulum fibers in mild cognitive impairment and Alzheimer's disease. *Neurology*, 68(1):13--19, 2007.

Y. Zhang, N. Schuff, A. T. Du, H. J. Rosen, J. H. Kramer, M. L. Gorno-Tempini, B. L. Miller, and M. W. Weiner. White matter damage in frontotemporal dementia and Alzheimer's disease measured by diffusion MRI. *Brain*, 132(Pt 9):2579--2592, September 2009. ISSN 1460-2156 (Electronic) 0006-8950 (Linking). doi: 10.1093/brain/awp071.

Q. F. Zhao, L. Tan, H. F. Wang, T. Jiang, M. S. Tan, L. Tan, W. Xu, J. Q. Li, J. Wang, T. J. Lai, and J. T. Yu. The prevalence of neuropsychiatric symptoms in Alzheimer's disease: Systematic review and meta-analysis. *J Affect Disord*, 190:264--271, January 2016. ISSN 1573-2517 (Electronic) 0165-0327 (Linking). doi: 10.1016/j.jad.2015.09.069.

Minwei Zhu, Wenpeng Gao, Xudong Wang, Chen Shi, and Zhiguo Lin. Progression of Corpus Callosum Atrophy in Early Stage of Alzheimer's Disease: MRI Based Study. *Acad Radiol*, 19(5): 512--517, May 2012. ISSN 1076-6332. doi: 10.1016/j.acra.2012.01.006.

Xiongwei Zhu, Arun K. Raina, George Perry, and Mark A. Smith. Alzheimer's disease: The two-hit hypothesis. *The Lancet Neurology*, 3(4):219--226, 2004. ISSN 14744422. doi: 10.1016/s1474-4422(04)00707-0.

Lin Zhuang, Perminder S. Sachdev, Julian N. Trollor, Nicole A. Kochan, Simone Reppermund, Henry Brodaty, and Wei Wen. Microstructural white matter changes in cognitively normal individuals at risk of amnestic MCI. *Neurology*, 79(8):748--754, August 2012. doi: 10.1212/WNL.0b013e3182661f4d.

Appendix A

Supporting Information

A.1 Software used for processing DTI

A.1.1 FSL (FMRIB's Software Library)

The official web page for FSL has described it as a comprehensive library of analysis tools for MRI, functional MRI (FMRI), and DTI brain imaging data. It is being developed, maintained, and distributed free of charge by researchers at the Oxford Centre for Functional MRI of the Brain (FMRIB), University of Oxford [Jenkinson et al., 2012; Woolrich et al., 2009; Smith et al., 2004]. It supports installation on Unix-based operating systems and may be used from the command line and a graphical user interface (GUI) (figure A.1a).

FMRIB's Diffusion Toolbox (FDT) is a collection of algorithms for processing DTI such as '*eddy_correct*' for elimination of eddy current artefacts, '*bet*' for extraction of the brain by eliminating the skull, '*dtifit*' for estimation of the diffusion tensor, '*probtrackx*' for tractography based analysis, and '*flirt*' and '*fnirt*' for linear and non-linear registration of images respectively. An upgraded version of the tool '*eddy_correct*' called '*eddy*' is now available, but was released after the initial processing of data for this thesis had been completed. Therefore, the command '*eddy_correct*' has been used consistently to eliminate eddy current artefacts from DW-MRI. It removes effects such as image stretching, shearing, and translation induced by eddy currents by an affine registration of diffusion weighted images to the non-diffusion weighted image [Yamada et al., 2014]. However, '*eddy*' has been validated to perform better than '*eddy_correct*' and has been discussed further in section 7.2.1 [Andersson and Sotiropoulos, 2016; Graham et al., 2016].

The command '*dtifit*' fits a diffusion tensor for every voxel in the image. It needs a diffusion weighted image (typically the output from the command

'*eddy_correct*'), a brain mask, a list of b-values (known as the '*bval*' file), and gradient directions (known as the '*bvec*' file) used in acquisition. The tensors are estimated either using the least squares or weighted least squares fit of a linear model depending on the option specified [Basser et al., 1994a]. Diffusion parameters such as FA, MD, RD, and AxD may be estimated from the tensor along with the eigen value and eigen vector maps.

FSL offers a method called tract based spatial statistics (TBSS) that enables group-wise comparison of white matter tracts. To carry out TBSS, diffusion weighted images are initially processed by commands '*eddy_correct*' and '*bet*'. Diffusion tensors are fitted using '*dtifit*' and the FA maps estimated and aligned to a standard space. A mean FA skeleton is generated to represent the centres of tracts common to all subjects. Each subject's FA map is then projected onto this skeleton and voxel-wise statistics between disease groups is carried out. Further details have been given later in this chapter as part of a feasibility study (section 3.7.2). Region-wise analysis of the white matter may be performed using the atlases provided by FSL [Mori et al., 2005; Wakana et al., 2007; Hua et al., 2008]. Binary masks of the ROI may be generated using the atlas labels, with the accuracy of the ROI depending on the accuracy of these labels.

A.1.2 Camino

Camino is an open source software package developed and maintained by the Microstructure Imaging Group at University College London [Cook et al., 2006]. It has a modular design that enables construction of processing pipelines including modules from other software packages. It supports installation on Unix systems with its codes written in Java to support calls from other programming environments such as MATLAB.

Camino provides an option to convert FSL-style '*bval*' and '*bvec*' files to '*scheme*' files supported by its tensor fitting module '*modelfit*'. The tensor may be fitted using linear, weighted linear, or non-linear models based on the user-specified option. The command '*modelfit*' also supports fitting analytic multi-compartment models including two-tensor and three-tensor models to DW-MRI acquired using a Stejskal-Tanner pulse sequence [Panagiotaki et al., 2012].

Advanced techniques such as multi-fibre reconstruction of DW-MRI are available in Camino [Seunarine and Alexander, 2009; Alexander, 2005]. A processing pipeline first classifies voxels into isotropic or anisotropic, Gaussian or non-Gaussian, revealing regions with crossing fibres. Results of voxel classification are used to determine whether a single-tensor or two-tensor model should be fit to the data on a

voxel-by-voxel basis. The ODF for each voxel is then estimated using a specialised algorithm designed to handle multiple fibre directions [Descoteaux et al., 2007]. However, these advanced techniques require that the DW-MRI be acquired using multiple HARDI shells. This requirement has not been satisfied by images in ADNI. Camino also offers a platform to carry out Monte-Carlo simulations to generate synthetic MR data [Hall and Alexander, 2009]. The simulator allows creation of simple to very complex diffusion environments using different substrates such as cylinders and meshes, and several DTI pulse sequences.

A.1.3 ROIEditor (Region of Interest Editing Tools)

ROIEditor is an open-access toolkit developed by the Center for Imaging Science, Johns Hopkins University. It supports installation on Windows operating system. It offers several tools that may be used to define an ROI on DTI and DTI-derived images, as well as obtain summary statistics in the ROI. It is being offered as part of a software suite called MRIStudio (earlier known as DTIStudio) which can perform DTI processing tasks such as tensor estimation and tractography. Segmentation

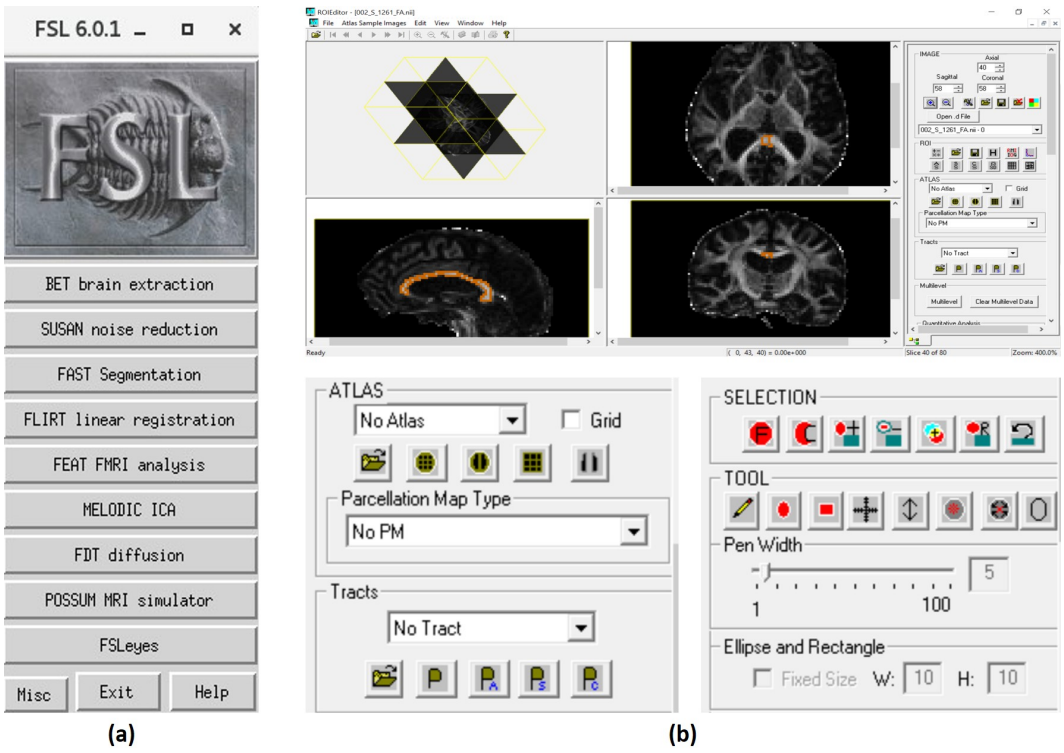

Figure A.1: (a) The FSL GUI (b) Top: ROIEditor GUI. Bottom: The atlas and manual drawing tools used for segmentation in ROIEditor magnified for visibility.

of the ROI may be carried out in ROIEditor either using an atlas or the different drawing tools provided. The software GUI has been shown in figure A.1b.

A.1.4 MATLAB

MATLAB is a widely used commercial software package developed by MathWorks with capability to carry out intensive computations, both imaging-related and otherwise. Custom codes written in MATLAB have been used for data analysis in this thesis. They have been provided in the appendix and referred to in relevant sections.

A.1.5 ImageJ (Image Processing and Analysis in Java)

ImageJ is a generic image processing and editing software developed at the National Institute of Mental Health, Bethesda (figure A.2). Since its first release, the scope and capability of ImageJ has been extended by the inclusion of user-written codes called plugins. Manual segmentation of the ROI may be carried out in ImageJ using freehand, rectangular, elliptical, or other drawing tools.

A.1.6 The R Project for Statistical Computing

R is an open-access environment for statistical computing and graphics, offering linear and non-linear modelling, classification and clustering of data. It also provides tools to visualise data and results of statistical tests. The capability of R can be easily extended using packages, which are often user-written codes available for download.

A.1.7 Other software

TractSeg and Blender are two other software tools that have been used in this thesis. TractSeg offers a tractography algorithm for images that have been acquired with typical clinical scan parameters. Blender, together with add-on software called MCell

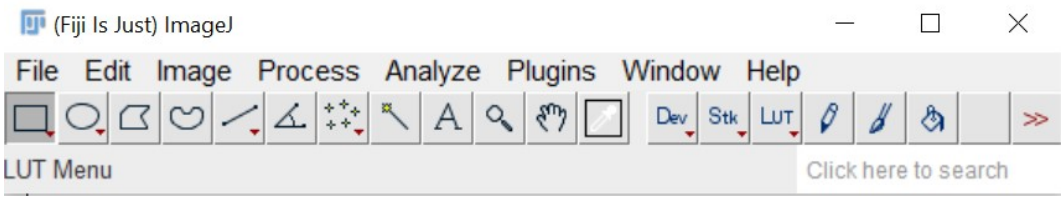

Figure A.2: The ImageJ GUI.

and DIFSIM, offers a means for spatial simulation of white matter models. Details of these software packages and their algorithms have been described in chapters 5 and 6.

A.2 MATLAB code to estimate χ^2_p map from DW-MRI

The code provided by Lauzon et al. at https://www.nitrc.org/projects/masimatlab has been adapted as required and is given below.

```
function [reportFile,state] = ...
    DTI_QA_Pipeline(file_name,output_folder,path_to_QA_DTI)

%%%%%%%%%%%%%%%%%%%%%%%%%%%%%%%%%%%
%CALCULATE CHI_2
%%%%%%%%%%%%%%%%%%%%%%%%%%%%%%%%%%%
% sd contains the fitting error to be plotted

% name_tensor_dt_nii = /filename/of/tensor/image/estimated/by/Camino
% name_md_nii=/filename/of/MD/map
% name_fa_nii=/filename/of/FA/map
% mask_nii_name=/filename/of/brain/mask
% name_reg=/filename/of/input/image/from/which/DTI/was/estimated

T=double(niftiread(name_tensor_dt_nii));
Reg_Im=double(niftiread(name_reg));

ADC=double(niftiread(name_md_nii));
ADC=reshape(ADC,[],1);
FA=double(niftiread(name_fa_nii));
FA=reshape(FA,[],1);

mask_nii=double(niftiread(mask_nii_name));
brain=(mask_nii==1);

mADC=ADC(brain);
mFA=FA(brain);
stdFA=std(FA(brain));
stdADC=std(ADC(brain));

% temp folder to save temporary outputs
tmp=sprintf('%s/temp_folder',output_folder);
mkdir tmp;
```

```
[scan_info_text grad_file bval_vec resolution name_Y_data] = ...
    getNIIinfo(tmp,file_name);

[sd Nz ModelData ...
    Errors]=calDTIrevC_norm(T,grad_file,bval_vec,Reg_Im,mask_nii);

%plot(1:Nz,sd);
%histogram(sd);

%%%%%%%%%%%%%%%%%%%%%%%%%%%%%%%%%%%%%%%%%%%%%%%%%%%%%%%%%%%%%%%%%%%%%%%

function [ss Nz Se ...
    Errors]=calDTIrevC_norm(T,grad_file,bvals,S_measured,mask)
%normalised according to 2003 "A measure of curve fitting error for noise
%filtering diffusion tensor MRI data"

Nx=size(S_measured,1);
Ny=size(S_measured,2);
Nz=size(S_measured,3);
bo=reshape(S_measured(:,:,:,end),1,[]);

D_vec=[];

D_vec(1,:)=reshape(T(:,:,:,1),1,[]); %Dxx
D_vec(2,:)=reshape(T(:,:,:,3),1,[]); %Dyy
D_vec(3,:)=reshape(T(:,:,:,6),1,[]); %Dzz
D_vec(4,:)=reshape(T(:,:,:,2),1,[]); %Dxy
D_vec(5,:)=reshape(T(:,:,:,4),1,[]); %Dxz
D_vec(6,:)=reshape(T(:,:,:,5),1,[]); %Dyz

%create gradient vector
grads=grad_file;
gs=[grads.^2  2*grads(:,1).*grads(:,2) 2*grads(:,1).*grads(:,3) ...
    2*grads(:,3).*grads(:,2)];

S_model=[];
for vol=1:size(grad_file,1)-5
gb(vol,1:6)=bvals(1,vol)*gs(vol,:);
end

Sm=S_measured(:,:,:,1:end-5)./repmat(S_measured(:,:,:,end),[1 1 1 ...
    size(S_measured,4)-5]);
Sm=reshape(Sm,Nx*Ny*Nz,size(gs,1)-5); Sm=permute(Sm,[2 1]);

Se=exp(-gb*D_vec);
Errors=double(Sm)-Se;
```

```
ee=repmat(double(bo),size(gs,1)-5,1).*Se;

S_model=reshape(permute(ee,[2 1]),Nx,Ny,Nz,size(gs,1)-5);
del_S=(S_model-double(S_measured(:,:,:,1:end-5))).^2;
S_fi=S_measured(:,:,:,1:end-5);
normS=sum(S_fi.^2,4);

chi_sq_p=zeros(Nx*Ny*Nz,size(gs,1)-5);
mask=mask(:);
mask=(mask==1);
del_S=reshape(del_S,Nx*Ny*Nz,size(gs,1)-5);
normS=reshape(normS,Nx*Ny*Nz,1);
for vol=1:size(gs,1)-5
chi_sq_p(mask,vol)=del_S(mask,vol)./normS(mask);
end

s=reshape(chi_sq_p,[Nx Ny Nz size(grad_file,1)-5]);
s=sum(s,4);
ss=zeros(1,Nz);
for i=1:Nz
avg=mean(mean(s(:,:,i)));
ss(1,i)=avg;
end
```

A.3 Estimation of mid-sagittal slice

Detection of the mid-sagittal slice of the brain was carried out automatically on an FA image using the method described by Freitas et al. (2011). It makes use of the inter-hemispheric fissure as a landmark of the mid-sagittal slice. The FA map for this slice will contain large areas corresponding to CSF with low FA and white matter structures such as the corpus callosum with high FA. The average FA estimated for this slice will therefore be low. In fact, if slices from image extremities with small cross-sectional area of the brain are discarded, the average FA of the mid-sagittal slice will be the lowest. The method described by Freitas et al. is as follows:

1. Estimate the FA map of the image.
2. Use the brain mask to estimate the cross-sectional area of the brain in each slice. Discard slices with brain area less than 80% of the maximum.
3. For each of the remaining slices, calculate the average FA. Discard values greater than 50% of the maximum FA when estimating the average.

4. Plot the average FA for all slices to visualise the results (figure A.3a).

5. Find the slice with the lowest FA to be the mid-sagittal slice (figure A.3b).

A.4 Power analysis

Power analysis is used to estimate the sample size required to detect an effect size with a given degree of confidence. Conversely, it can be used to determine the probability of detecting an effect size with a given level of confidence under sample size constraints. The following four parameters are involved in power analysis and given any three, the fourth can be determined.

- Sample size.
- Effect size - this is typically an educated guess or derived from pilot studies. Typical values are 0.2 (small), 0.5 (medium) and 0.8 (large).
- Significance level - probability of finding an effect that is not present, i.e., a false positive.
- Power of the test - probability of finding an effect that is present.

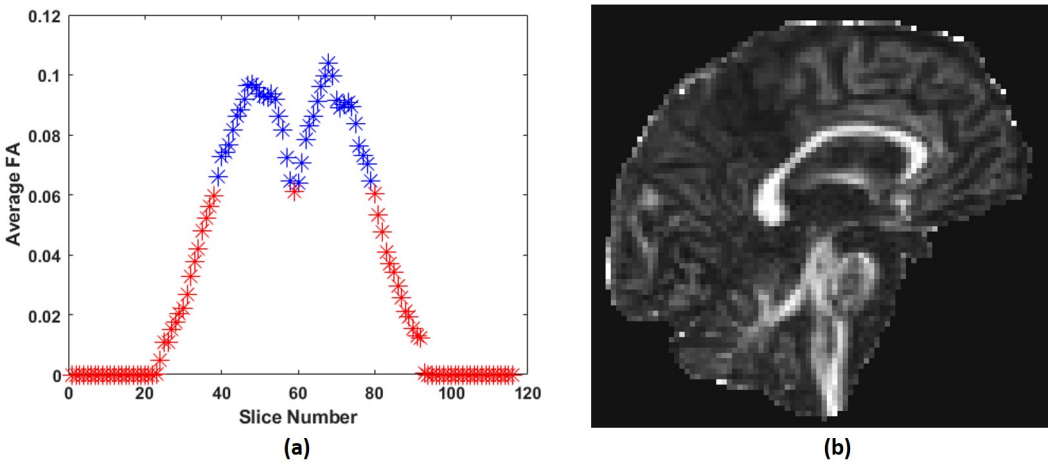

Figure A.3: (a) Plot of average FA versus slice number, with data points in red being below the threshold FA and discarded. After factoring in the brain cross-sectional area, the mid-sagittal slice was estimated to be the slice where FA is the lowest between two peaks (red marker between the blue markers), which was 60 for this image. (b) Slice number 60 from the FA image (brightness and contrast adjusted to increase visibility).

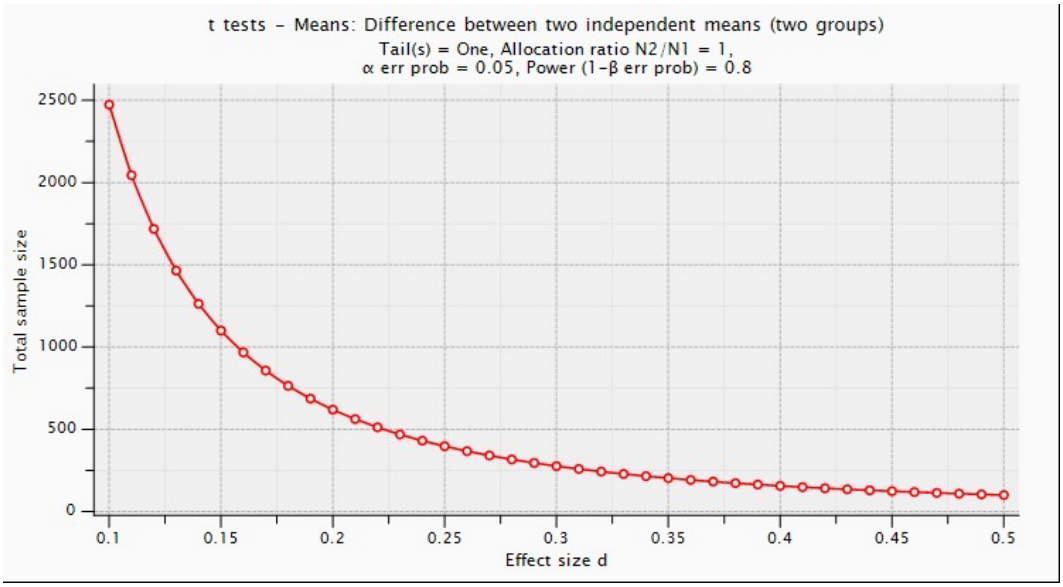

Figure A.4: Plot of effect size against sample size required to conduct a two-sample t test between AD and HC plotted in G*Power.

A liberal statistical power of 0.8 and a significance level of 0.05 were set and sample size required for the feasibility study (section 3.7.2) was estimated in G*Power. As described in section 3.7.1, an effect size of 0.605 was calculated for AD versus HC and 0.503 for MCI versus HC [Sexton et al., 2011]. Plots of effect size against sample size, and details of sample size estimation have been given in figures A.4, A.5, A.6, andA.7.

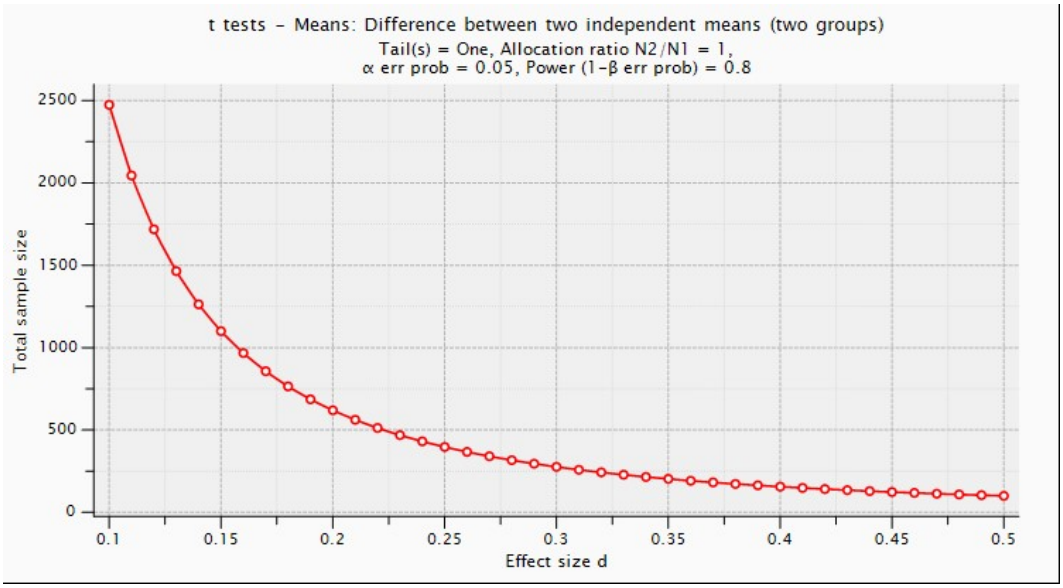

Figure A.5: Plot of effect size against sample size required to conduct a two-sample t test between MCI and HC plotted in G*Power.

A.5 TBSS code

Example of a command script written in Linux CentOS to carry out TBSS on HC and AD images has been given in figure A.8. A similar code was used for comparison between HC and MCI groups with only the file names changed. The instructions

t tests – Means: Difference between two independent means (two groups)

Analysis:	A priori: Compute required sample size		
Input:	Tail(s)	=	One
	Effect size d	=	0.503
	α err prob	=	0.05
	Power (1–β err prob)	=	0.8
	Allocation ratio N2/N1	=	1
Output:	Noncentrality parameter δ	=	2.5150000
	Critical t	=	1.6605512
	Df	=	98
	Sample size group 1	=	50
	Sample size group 2	=	50
	Total sample size	=	100
	Actual power	=	0.8030935

Figure A.6: Details of the a-priori sample size estimation carried out in G*Power for a two-sample t-test between MCI and HC

given in FSL official website (https://fsl.fmrib.ox.ac.uk/fsl/fslwiki/TBSS/UserGuide) to carry out TBSS were followed to generate this command script.

t tests – Means: Difference between two independent means (two groups)

Analysis:	A priori: Compute required sample size		
Input:	Tail(s)	=	One
	Effect size d	=	0.605
	α err prob	=	0.05
	Power (1−β err prob)	=	0.8
	Allocation ratio N2/N1	=	1
Output:	Noncentrality parameter δ	=	2.5308966
	Critical t	=	1.6675723
	Df	=	68
	Sample size group 1	=	35
	Sample size group 2	=	35
	Total sample size	=	70
	Actual power	=	0.8053070

Figure A.7: Details of the a-priori sample size estimation carried out in G*Power for a two-sample t-test between AD and HC

```
# As per TBSS user manual, all FA images are placed in one folder, with files named as HC_1, HC_2, AD_1, AD_2 etc.
# MD, RD and AxD images are placed in subfolders named md, rd and axd respectively.

tbss = "/path/to/FA/images/"
cd $tbss

tbss_1_preproc *.nii.gz
tbss_2_reg -T
tbss_3_postreg -S
tbss_4_prestats 0.3

tbss_non_FA md
tbss_non_FA rd
tbss_non_FA axd

cd stats
design_ttest2 design 10 10
randomise -i all_FA_skeletonised -o tbss -m mean_FA_skeleton_mask -d design.mat -t design.con -n 500 --T2 -o fa
randomise -i all_md_skeletonised -o tbss -m mean_FA_skeleton_mask -d design.mat -t design.con -n 500 --T2 -o md
randomise -i all_rd_skeletonised -o tbss -m mean_FA_skeleton_mask -d design.mat -t design.con -n 500 --T2 -o dr
randomise -i all_axd_skeletonised -o tbss -m mean_FA_skeleton_mask -d design.mat -t design.con -n 500 --T2 -o da
```

Figure A.8: Codes written in FSL to carry out TBSS between AD and HC. Similar codes have been used to compare MCI and HC.

A.6 MATLAB code to estimate median FA, MD, RD and AxD

```
clc;
clear;

folder='/path/to/directory/containing/image/files/';

load('imageID.mat'); %names of folders to be processed

D=dir(folder);
cd(folder);
for i=1:length(imageID)
      file=num2str(imageID(i));
      cd(file);

      FA = importdata('PixelValue_FA.txt');
      MD = importdata('PixelValue_MD.txt');
      RD = importdata('PixelValue_RD.txt');
      AxD = importdata('PixelValue_AxD.txt');

      medianFA = median(FA);
      fprintf('FA = %12f\n',medianFA);
      medianMD = median(MD);
      fprintf('MD = %12f\n',medianMD);
      medianRD = median(RD);
      fprintf('RD = %12f\n',medianRD);
      medianAxD = median(AxD);
      fprintf('AxD = %12f\n',medianAxD);

      cd(folder);
end
```

A.7 White matter modelling

A.7.1 Software

In chapter 6, the following software tools have been used to design and simulate a model of the white matter.

A.7.1.1 Blender

Blender is an open source 3D creation suite capable of modelling, animation, simulation, rendering, and motion tracking. It has been developed as a public project, realised using contributions from studios and individual artists around the world. More information about the software project may be found at www.blender.org. Advanced and customised capabilities of Blender may also be realised using its interface with Python programming language. Supported platforms include Linux, Windows, and Macintosh. Blender has been made available under the GNU General Public Licence which imposes no restrictions on how the software may be used. The geometry of the white matter model was designed in chapter 6 using Blender.

A.7.1.2 MCell and Cellblender

MCell stands for 'Monte Carlo cell'. It is a toolkit that enables particle-based stochastic simulations in 3D geometries, allowing numerical investigations to be carried out in biochemical systems [Kerr et al., 2008; Stiles and Bartol, 2001; Stiles et al., 1996]. It has been developed as a collaborative project by several groups at the University of Pittsburgh and the Salk Institute. A brief introduction to stochastic modelling as well as details of its implementation in MCell have been given below.

A stochastic simulation contains variables that can change their values stochastically or randomly with individual probabilities. A particle-based stochastic simulator is one that can locate and monitor the interactions between different particles in a stochastic system [Blackwell, 2014]. If the average distance travelled by a particle during its lifetime (l_k) is very small compared to the scale of volume of the model, the system may be assumed to be heterogeneous with changes in concentration being localised. Spatial modelling methods such as the particle-based stochastic simulator implemented in MCell may be used in this case to investigate various properties of the system. There are four essential components to an MCell model [Gupta et al., 2018]:

1. Mesh objects: They are surfaces that may be defined directly in MCell or through Blender GUI, that describe the geometry of the model being designed. The objects are triangulated for use in MCell, i.e., each face of an object is divided into triangles. This may be performed in Blender or in MCell's GUI (Cellblender).

2. Molecules: Two types of molecules may be defined, i.e., surface or volume molecules. The diffusion coefficient of each molecule type may be defined

separately. Surface molecules are allowed to diffuse only in a 2D space in the model, while volume molecules may diffuse in a 3D space.

3. Molecule release sites: These are regions or locations where the molecules are placed at the start of or during a simulation. Surface molecules may only be released on a 2D surface, while volume molecules may be released in a 3D volume.

4. Reactions: They define the manner in which molecules in the model interact with each other. They may be unimolecular or bimolecular interactions with specific reaction rates that determine the probability of their occurrence.

Using the above components, there are four processes that may occur at each simulation time step in MCell:

1. Diffusion: The molecules may diffuse with a random step length and direction estimated in MCell as described in later sections.

2. Collision: The molecules may collide with surfaces or other molecules. This can be detected using a collision radius which is checked at every time step to estimate if a collision occurs.

3. Reaction: If a collision occurs, a user-specified reaction may be triggered depending on the reaction rate and its associated probability. A reaction may be between two volume molecules, two surface molecules, or a volume molecule and a surface molecule.

Random walk diffusion

At each time step in a simulation, the motion and trajectory of a molecule is determined by randomly selecting a direction and moving the molecule by one unit in that direction. This is called a random walk diffusion. It has been developed to simulate Brownian motion, where diffusion of a molecule in a medium may be influenced by random collisions with surfaces or other molecules [Codling et al., 2008]. In a 3D volume, the probability of a volume molecule with diffusion coefficient D moving a distance r in time t is given by [Gupta et al., 2018]:

$$p(r,t) = \frac{1}{[4\pi Dt]^{3/2}} e^{-r^2/4Dt} \tag{A.1}$$

The cumulative distribution function (cdf) of $p(r,t)$ is given by:

$$cdf(R,t) = \int_0^R p(r,t) 4\pi r^2 dr \tag{A.2}$$

where R is the magnitude of displacement. The value of $cdf(R,t)$ lies between 0 and 1 and R may be estimated through the inverse of cdf. The value of R is then scaled by $\sqrt{4Dt}$ as explained later. Along with the displacement, MCell also calculates the direction of diffusion in a volume by computing the azimuthal angle ϕ and the polar angle θ. While ϕ is randomly selected from a distribution within $[0, 2\pi)$, θ is randomly chosen from a lookup table containing solutions of θ for the equation $Y = (1 - cos\theta)/2,\ Y \in [0,1]$ [Gupta et al., 2018].

Other implementations of random walk diffusion, such as that in Camino, assign a fixed displacement and a random direction to molecules at each simulation step. This does not truly represent free diffusion and require averaging over several simulation steps to make it so. On the other hand, equation A.1 is used by MCell to initialise a look-up table at the start of the simulation to store a large number of diffusion step lengths and directions with an equal probability of being assigned to a molecule. At each simulation time step, this look-up table is used to randomly select a displacement and direction. The displacement is then scaled by a factor $\sqrt{4Dt}$ and the molecule is moved in the chosen direction by an amount equal to this scaled displacement. By implementing random walk diffusion this way, MCell offers the flexibility to set longer time steps that enables a quicker completion of the simulation.

A.7.1.3 DIFSIM

DIFSIM is a diffusion simulator developed at the Centre for Scientific Computation in Imaging at the University of California San Diego. It provides the capability to simulate a diffusion MRI experiment on a tissue model defined within MCell [Baxter and Frank, 2013; Balls and Frank, 2009]. The acquired output signal may then be used to compute various DTI parameters including FA, MD, RD, and AxD. DIFSIM provides an excellent means to test hypotheses about disease models, e.g., how alterations in tissue structure may impact the widely used DTI parameters.

DIFSIM has integrated MCell within itself as a function that is called during the simulated scan. The phase shift of the molecules in the MCell model is updated in DIFSIM through this function at each simulation time step, and the signal

attenuation E due to phase differences is estimated as [Balls and Frank, 2009]:

$$E = \frac{1}{N_p} \sum_{j=1}^{N_p} e^{i\gamma\theta_j} \tag{A.3}$$

where N_p is the total number of diffusing molecules or spins, i is the imaginary unit $\sqrt{-1}$, γ is the gyromagnetic ratio, and θ_j is the phase of a spin j due to its displacement in the diffusion MRI pulse gradient direction given by

$$\theta_j(t) = \sum_{i=0}^{N_t} G(t_i) \; . \; x_j(t_i) dt \tag{A.4}$$

where '.' represents the dot product between magnetic field gradient $G(t_i)$ and displacement $x_j(t_i)$ at a time step t_i with the time having been discretised into N_t steps each of length dt. Effects of T_1 and T_2 relaxation on the acquired signal may be accounted for by setting their corresponding values for the various compartments simulated in the model. DIFSIM also offers several pulse sequences including spin echo and gradient echo pulses to simulate a DTI scan, with options to set the values of the diffusion time (Δ), pulse duration (δ), gradient strength (G), and the gradient ramp time (t_r). An example of a diffusion encoding pulse has been shown in figure 2.4. Using the parameters of the pulse, the b-value is estimated automatically by DIFSIM. The acquired signal is provided as input to an external program called Analysis of Functional Neuroimages (AFNI) which estimates the diffusion tensor, its eigen values and parameters such as FA and MD [Balls and Frank, 2009].

A.7.2 Test models

Two models, one with a single cylinder and the other with a cylinder enclosed inside a cube, were designed. Variable parameters included cylinder radius (r_{cy}) and length (l), cube side length (r_{cu}), number of molecules inside the cylinder (n_{cy}) and the cube (n_{cu}), their diffusion coefficient (dc), simulation time (t), and the permeability of the cylinder membrane (p) when placed inside the cube. The dependence of FA, MD, RD, and AxD on these factors at b=1000 s/mm^2 were studied.

A.7.2.1 Radius of the cylinder

In the model consisting of just the cylinder without the cube, r_{cy} was varied while keeping the other parameters constant at $l = 15$ μm, $n_{cy} = 100,000$, $dc = 7.5 * 10^{-6}$ cm^2/s, and $t = 40$ ms. The cylinder surface was assumed to be impermeable. A decrease in FA accompanied by increases in MD, RD, and AxD was observed with

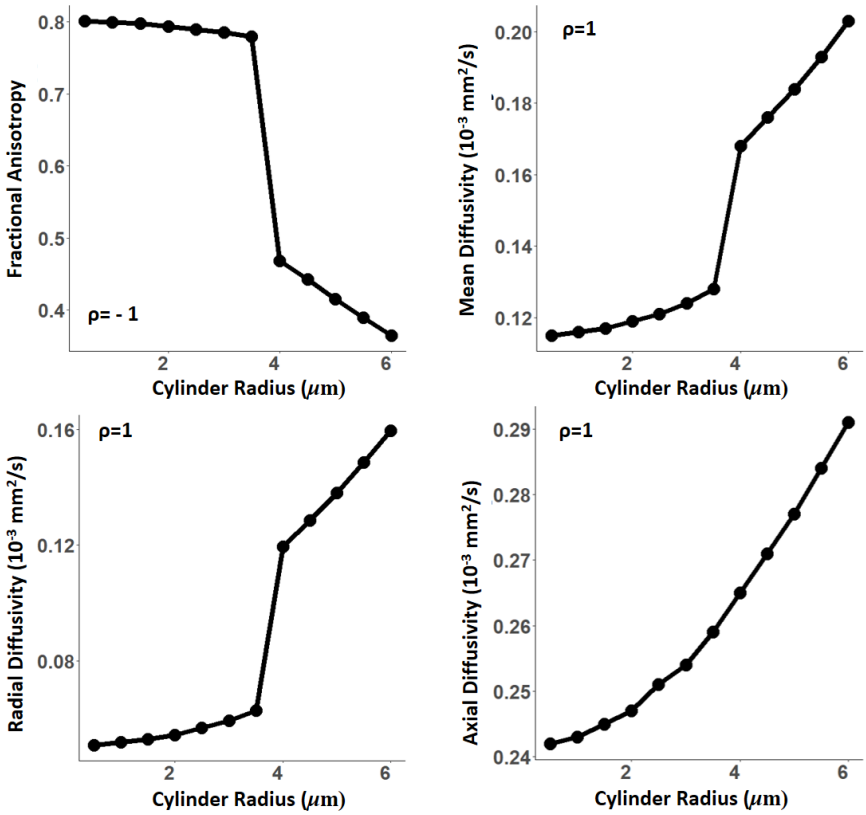

Figure A.9: Variation of measured FA, MD, RD, and AxD of a cylinder with varying radius. Spearman's rank correlation coefficient (ρ) has been estimated for each of the parameters for variation in radius, testing for a monotonic association.

increasing r_{cy} as shown in figure A.9. This may be attributed to an increase in the space available to a molecule for diffusion as the radius was increased. This likely resulted in a reduction in the number of molecular collisions leading to an overall increase in diffusion. Interestingly, increasing the dimensions radially was observed to lead to an increase in diffusion in both radial and axial directions (RD and AxD).

A.7.2.2 Length of the cylinder

The length of the cylinder was varied at three different radii (r_{cy}=1 μm, 3 μm, 6 μm) while keeping the other parameters constant at $n_{cy} = 100,000$, $dc = 7.5 * 10^{-6}$ cm^2/s, and $t = 40$ ms. The cylinder surface was assumed to be impermeable as before. The values of FA, MD, RD, and AxD were observed to stay fairly constant as the cylinder length was varied, although a difference was observed in corresponding values between cylinders of different radii (figure A.10). For given dc and t, increasing l may not impact the space available for molecular diffusion except in locations

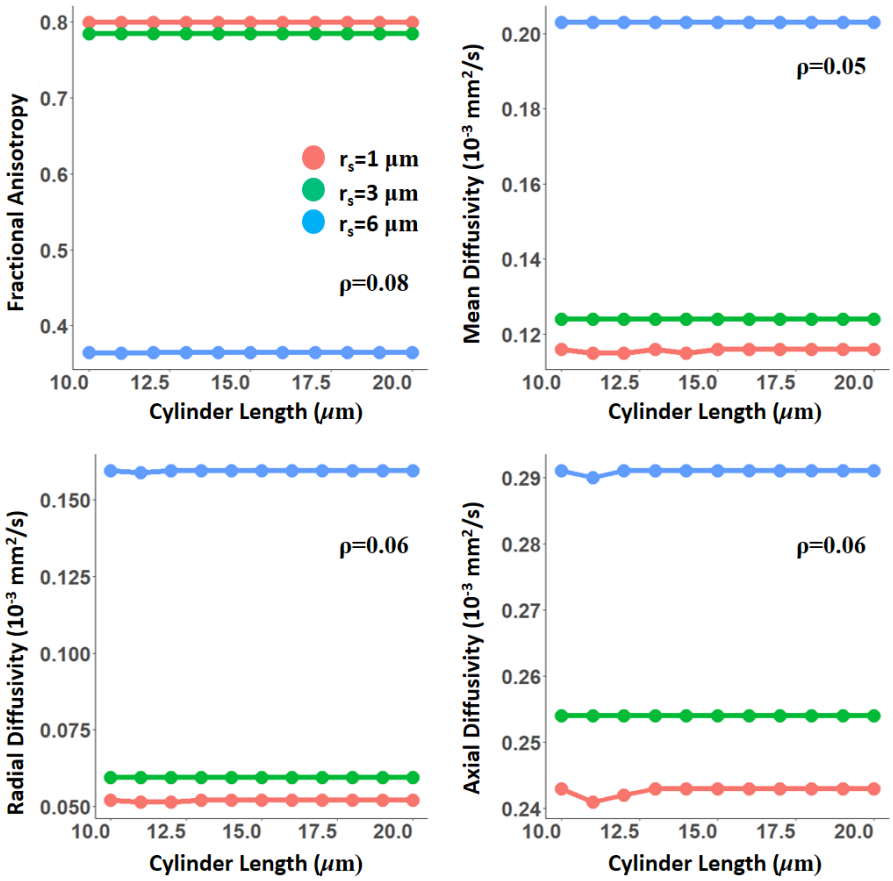

Figure A.10: Variation of measured FA, MD, RD, and AxD of a cylinder with length at different radii. Spearman's rank correlation coefficient (ρ) has been shown on the corresponding plots for monotonic association of each of the DTI parameters with the cylinder length.

towards the cylinder end-regions. This may help explain the patterns seen figure A.10.

A.7.2.3 Number of molecules

Cylinders with r_{cy}=1 μm, 3 μm, and 6 μm were modelled by setting $l = 15$ μm, $dc = 7.5 * 10^{-6}$ cm^2/s, and $t = 40$ ms. The cylinder surface was assumed to be impermeable. The number of molecules simulated was varied on a logarithmic scale as shown in figure A.11 and the corresponding DTI parameters were measured. It was observed that for all three radii, the measurements plateaued as the number of molecules was increased. This indicated that the DTI parameters depended on the number of molecules simulated and a minimum number was required to obtain a

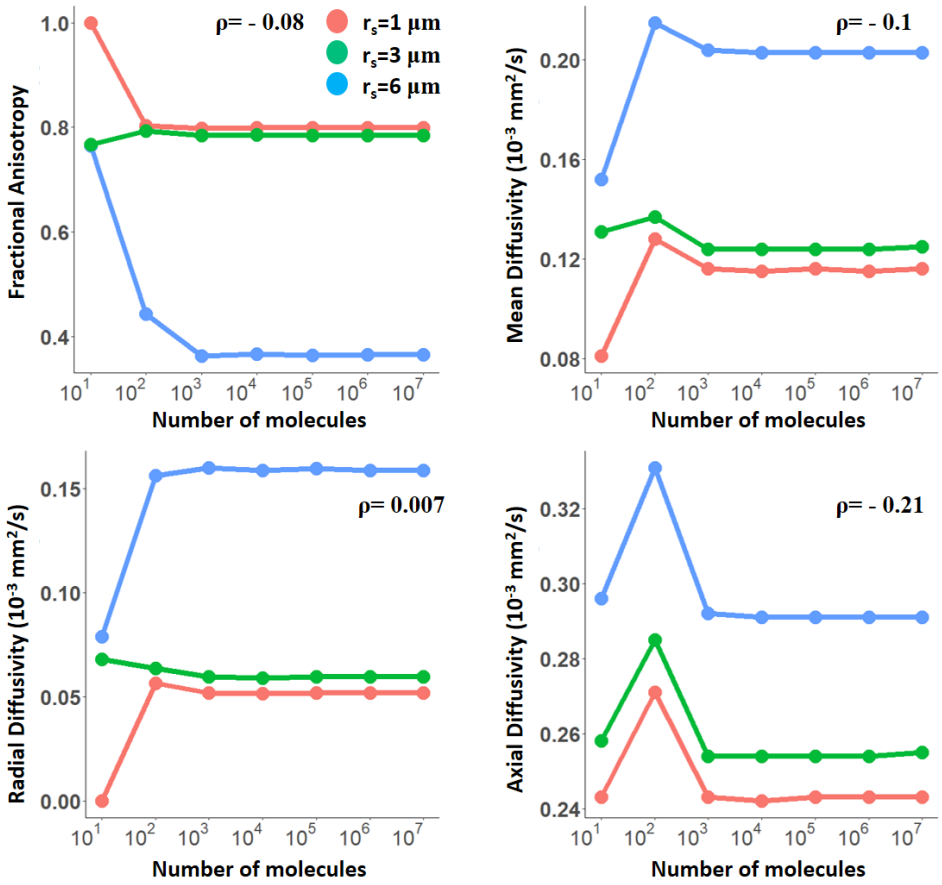

Figure A.11: Variation of measured FA, MD, RD, and AxD of a cylinder with number of molecules simulated at different radii. Spearman's rank correlation coefficient (ρ) has been shown on the corresponding plots for monotonic association of each of the DTI parameters with the number of molecules simulated.

fair estimate.

A.7.2.4 Simulation time

Cylinders with r_{cy}=1 μm, 3 μm, and 6 μm were simulated for varying durations by keeping $l = 15$ μm, $n_{cy} = 100,000$, $dc = 7.5 * 10^{-6}$ cm^2/s and DTI scans were acquired. The cylinder surface was assumed to be impermeable. A decrease in FA accompanied by increases in MD, RD, and AxD was observed as simulation time was increased on a logarithmic scale (figure A.12). This may be attributed to the increasing distance travelled by the molecules with time resulting in an increase in overall diffusion and a subsequent decrease in anisotropy. Interestingly for the cylinder with r_{cy}=6 μm, FA was observed to increase for a brief period of time after

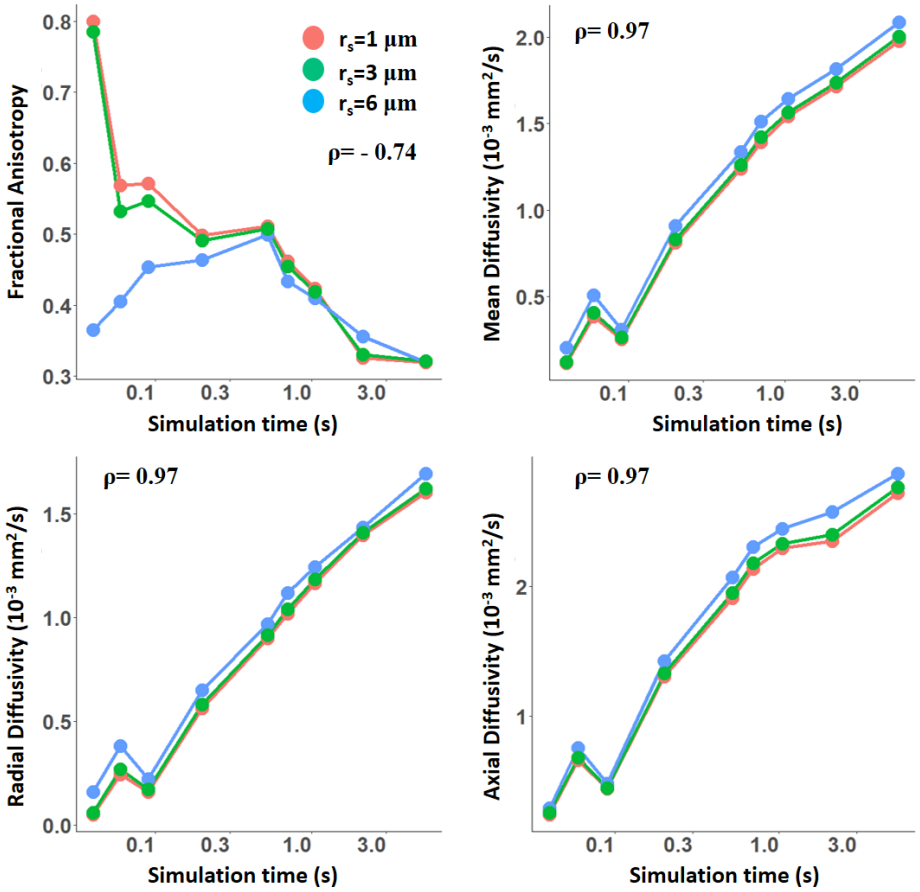

Figure A.12: Variation of measured FA, MD, RD, and AxD of a cylinder with simulation time at different radii. Spearman's rank correlation coefficient (ρ) was estimated for monotonic association of each DTI parameter with the simulation time.

which it started decreasing. The reason behind this pattern was not clear but may perhaps be rising from the larger radius of the cylinder.

A.7.2.5 Diffusion coefficient

Diffusion coefficient *dc* is an estimate of the distance or area covered by a molecule in a given unit of time. Cylinders of radii r_{cy}=1 μm, 3 μm, and 6 μm were used to simulate DTI scans at varying values of *dc* while keeping other parameters constant at $l = 15$ μm, $n_{cy} = 100,000$, and $t = 40$ ms. The cylinder surface was assumed to be impermeable. A decrease in FA accompanied by increases in MD, RD, and AxD was observed with increasing *dc* (figure A.13). This may be attributed to the increased overall diffusion occurring as a result of increased *dc* for a given simulation time,

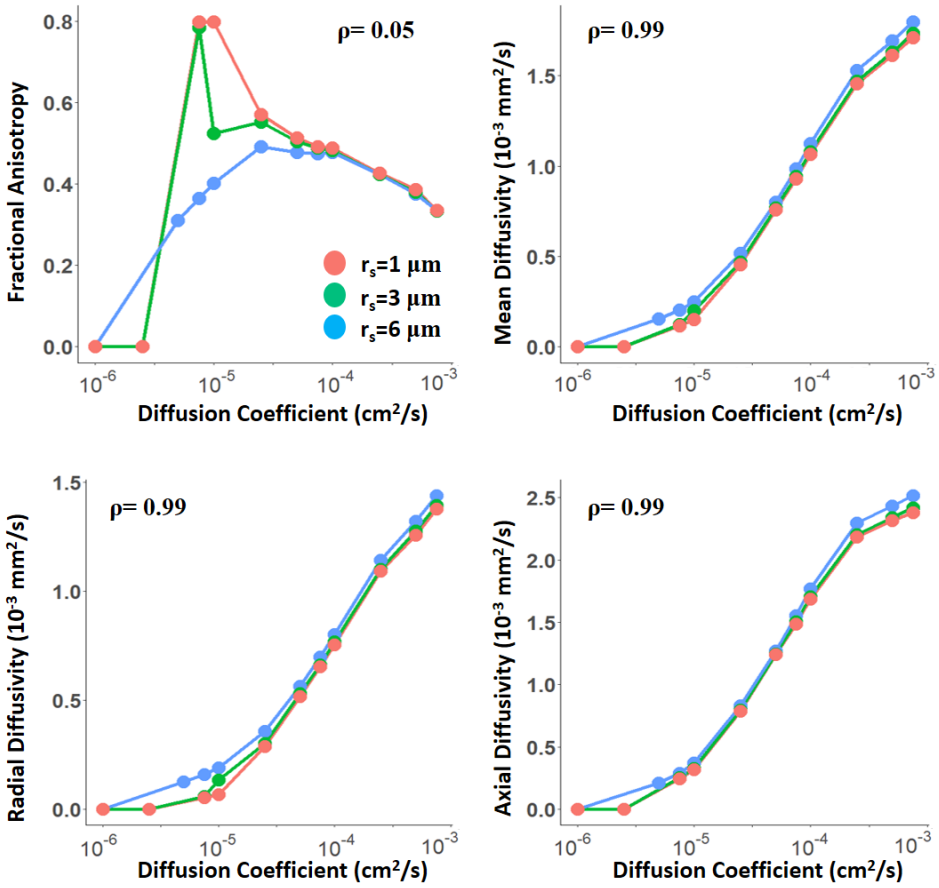

Figure A.13: Variation of measured FA, MD, RD, and AxD of a cylinder with diffusion coefficient of molecules at different radii. Spearman's rank correlation coefficient (ρ) was estimated for monotonic association of each DTI parameter with the molecular diffusion coefficient.

leading to a greater overall diffusivity and a subsequent reduction in FA. However, an initial increase in the values of FA was observed before it started decreasing as shown in figure A.12. This may be related to the similar pattern observed in section A.7.2.4 and may perhaps be arising from the distances travelled by the molecules as the simulation time or diffusion coefficient are varied.

A.7.2.6 Permeability

The parameters described above have been investigated using a model constituting of a single cylinder. In order to investigate the properties of the cylinder in a medium, a second model was designed with a cylinder placed inside a cube. The following values were assigned to the different parameters: r_{cy}=1 μm, 3 μm, and 6 μm, $l = 15$

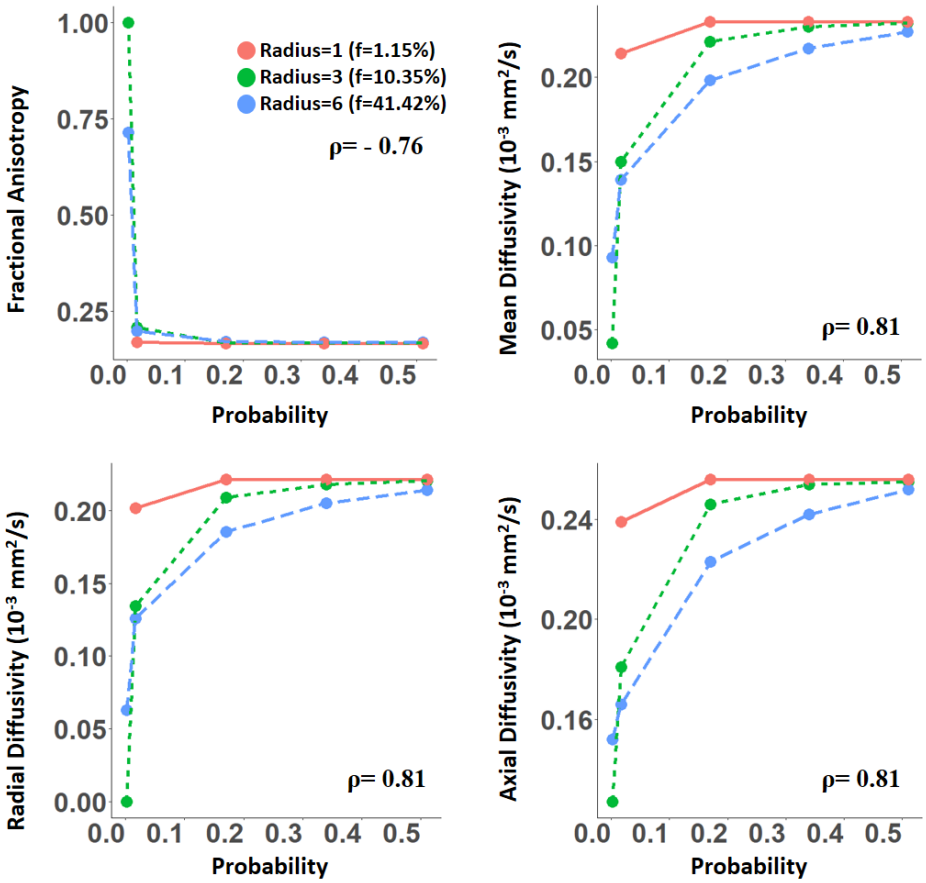

Figure A.14: Variation of measured FA, MD, RD, and AxD of a cylinder with permeability defined as the probability of transition of a molecule from inside the cylinder to outside. The volume fraction of the cylinder inside the cube is denoted as 'f'. Spearman's rank correlation coefficient (ρ) has been shown for monotonic association of each DTI parameter with the probability of transition at the boundary.

μm, r_{cu}=16 μm, $n_{cy} = n_{cu} = 100,000$, $dc = 7.5 * 10^{-6}$ cm^2/s, and $t = 40$ ms. The cylinder surface was assumed to be permeable, with the molecules carrying a probability of transition from inside to outside when it hits the surface. In MCell, this may be controlled by setting the rate of reaction, where the reaction is the transition of the molecule from one side of the boundary to the other. As shown in figure A.14, increasing the permeability of the cylinder surface was observed to lead to an increase in overall diffusion and subsequent increases in MD, RD, and AxD accompanied by a decrease in FA. It was observed that a small increase in permeability led to a drastic reduction in the value of FA. This may be attributed to small changes in radial diffusion (represented by diffusion tensor eigen values λ_2

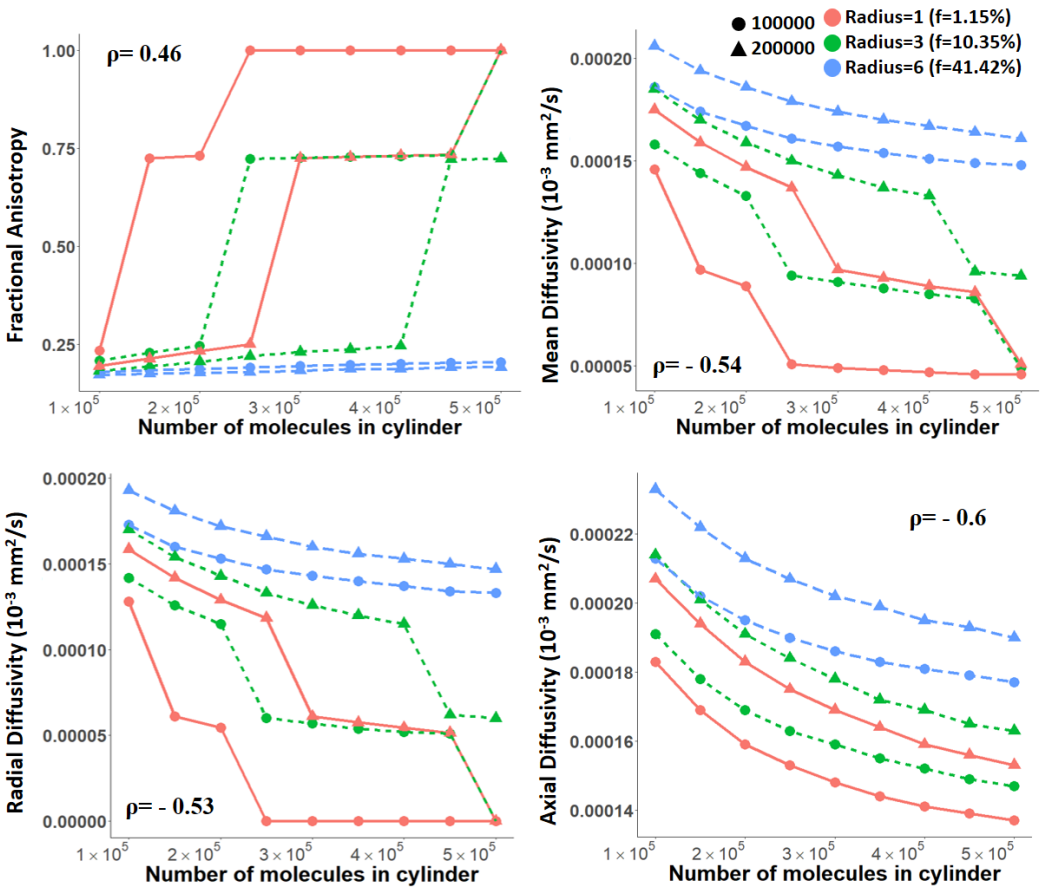

Figure A.15: Variation of measured FA, MD, RD, and AxD of a cylinder with the number of molecules simulated inside the cylinder and cube. The volume fraction of the cylinder inside the cube is denoted as 'f'. Different symbols indicate different values of n_{cu} as shown in the legend. Spearman's rank correlation coefficient (ρ) has been shown on the corresponding plots for monotonic association of each DTI parameter with the number of molecules simulated inside the cylinder.

and λ_3) causing large changes in FA, owing to the non-linear relationship between them (see section 2.2).

A.7.2.7 Permeability and the number of molecules

The impact of the number of molecules simulated inside and outside a permeable cylinder when placed in a cube was investigated. The values of different parameters were set as: r_{cy}=1 μm, 3 μm, and 6 μm, l = 15 μm, r_{cu}=16 μm, $dc = 7.5 * 10^{-6}$ cm^2/s, and t = 40 ms. The value of n_{cy} was varied from 100,000 to 500,000 at two different values of n_{cu} (100,000 and 200,000). An increase in FA accompanied by

decreases in MD, RD, and AxD was observed with increasing n_{cy}. Moreover, at any given value of n_{cy}, the FA measured from the model with n_{cu}=200,000 was less than the FA measured from the model with n_{cu}=100,000. This was reversed for the case of MD, RD, and AxD (figure A.15). This result contrasted with the results in section A.7.2.3 where FA, MD, RD, and AxD plateaued as the number of molecules was increased. Figure A.15 indicated that the number of molecules may have an impact on DTI parameters in models with a permeable cylinder surface.

A.7.3 MATLAB codes

A.7.3.1 Single compartment fitting, with and without T_2 relaxation terms

```
clc; clear; format longG;

global b;
b = 8000;
% change to each seed folder to get results
file_location = ".../seed200/";
bval_filename = sprintf(".../bvals_%d.txt",b);
bvec_filename = ".../bvecs.txt";

b_value = importdata(bval_filename);
b_value = b_value(2:end, :);
g = importdata(bvec_filename);
g = g(2:end, :);
global Gi;
Gi = zeros(30,6);
for i=1:30
    Gi(i,:) = [g(i,1)^2 g(i,2)^2 g(i,3)^2 2*g(i,1)*g(i,2) ...
        2*g(i,1)*g(i,3) 2*g(i,2)*g(i,3)];
end

T2 = 110; %ms
TE = 100; %ms
t2term = exp(-TE/T2);

models = ["1" "2" "3" "69" "70"];  % array carrying all 70 model names

FAresults = zeros(size(models, 2),1);
MDresults = zeros(size(models, 2),1);
RDresults = zeros(size(models, 2),1);
AxDresults = zeros(size(models, 2),1);
L1results = zeros(size(models, 2),1);
L2results = zeros(size(models, 2),1);
L3results = zeros(size(models, 2),1);

% fanDTasia toolbox is used in this code.

fields = {'bt'} ; c = cell(length(fields),1); global xps;  xps = ...
    cell2struct(c,fields);
type = {'dti_nls'}; c=cell(length(type),1); opts = cell2struct(c, type);
```

```
opts.dti_nls.do_plot = 1; opts.dti_nls.lsq_opts=[];
t_guess = [1 1 1 1 1 1];
t_lb    = [0 0 0 0 -9 -9 -9];
t_ub    = [2 9 9 9 +9 +9 +9];

for modelnumber = 1:size(models,2)
    signal_file = sprintf("%s%s/signal_%d.dat", ...
                          file_location, models(1, modelnumber), b);
    signal = importdata(signal_file).data;

    %% signal - 1: total     2: myelin      3: axon      4:ecs
    signal = signal(2:end, :);
    signal_total = signal(:,1);

    %% estimations
    modelfun = fittype(@(Di, x) t2term*(exp(-x*Di)));
    for i=1:30
        Dtemp{i} = ...
            fit(b_value(i,1),signal_total(i,1),modelfun,'StartPoint', ...
            0,'Lower', 0,'Upper', 0.01);
        Di(i,1) = Dtemp{i}.Di;
    end

    R = lsqcurvefit(@DTfun, t_guess, [], Di, opts.dti_nls.lsq_opts);

    % using cholesky factorisation to get positive eigen values
    DT = [R(1)^2 R(1)*R(2) R(1)*R(3);
          R(1)*R(2) R(2)^2+R(4)^2 R(2)*R(3)+R(4)*R(5);
          R(1)*R(3) R(2)*R(3)+R(4)*R(5) R(3)^2+R(5)^2+R(6)^2];
    e = eig(DT);
    e = sort(e, 'descend');
    FA = sqrt(0.5 *  ( (e(1)-e(2))^2 ...
            + (e(1)-e(3))^2 ...
            + (e(2)-e(3))^2) ...
            /(sum(e.*e)));
    MD = (e(1) + e(2) + e(3))/3;
    RD = (e(2) + e(3))/2;
    AxD = e(1);

    L1results(modelnumber,1) = e(1);
    L2results(modelnumber,1) = e(2);
    L3results(modelnumber,1) = e(3);
    FAresults(modelnumber, 1) = FA;
    MDresults(modelnumber, 1) = MD;
    RDresults(modelnumber, 1) = RD;
    AxDresults(modelnumber, 1) = AxD;
```

```
end

function Di = DTfun(t,varargin)
    global xps; global Gi; global b;
    C = [t(1) t(2)  t(3);
        0    t(4)  t(5);
        0      0   t(6)];
    m(1:6) = tm_3x3_to_1x6(C' * C);  % function from fanDTasia toolbox
    dt = zeros(1,6);
    dt(1:6) = m(1:6);
    Di = Gi*dt';
end
```

A.7.3.2 Multi compartment fitting, with T_2 relaxation terms

```
clc; clear; format longG;

b = [1004 4000 8000];
file_location = "../seed200/";
bval_filename = sprintf("../bvals_");
bvec_filename = "../bvecs_all.txt";

f = 0.8;
ra = 0.7;
gratio = 0.65;
De = 2*10^-5*100;

rm = ra/gratio;
L = sqrt((2*pi*rm*rm)/(sqrt(3)*f));
f_a = (2*pi*ra*ra)/(sqrt(3)*L*L);
f_m = (2*pi*((rm*rm)-(ra*ra)))/(sqrt(3)*L*L);
f_e = 1 - f;

TE = 100;   %ms
T1a = 965;  %ms
T1m = 465;  %ms
T1e = 965;  %ms
T2a = 90;  %ms
T2m = 12;  %ms
T2e = 90;  %ms
Da = 2*10^-5*100;
Dm = 0.3*10^-5*100;
```

```
axon = f_a * exp(-TE/T2a);
myelin = f_m * exp(-TE/T2m);
ecs = f_e * exp(-TE/T2e);

%% signal - 1: total     2: myelin      3: axon      4:ecs
g = importdata(bvec_filename);
global Gi;
Gi = zeros(30,6);
for i=1:30
    Gi(i,:) = [g(i,1)^2 g(i,2)^2 g(i,3)^2 2*g(i,1)*g(i,2) ...
        2*g(i,1)*g(i,3) 2*g(i,2)*g(i,3)];
end

models = ["1" "2" "3" "69" "70"]; % array carrying all 70 model names

FAresults = zeros(size(models, 2),1);
MDresults = zeros(size(models, 2),1);
RDresults = zeros(size(models, 2),1);
AxDresults = zeros(size(models, 2),1);
L1results = zeros(size(models, 2),1);
L2results = zeros(size(models, 2),1);
L3results = zeros(size(models, 2),1);

b_value = [];
for i=1:3
    bvalue_file = sprintf("%s%d.txt",bval_filename,b(i));
    bvalue = importdata(bvalue_file);
    bvalue = bvalue(2:end, 1);
    b_value = [b_value; bvalue];
end
xdata = [[60, 1004], [80, 4000], [100, 8000]];

for modelnumber = 1:size(models,2)
    signal_total = [];
    for i=1:3
        signal_file = sprintf("%s%s/signal_%d.dat",file_location, ...
            models(1,modelnumber), b(i));
        signal = importdata(signal_file).data;
        signal = signal(2:end, :);
        T = signal(:,1);
        signal_total = [signal_total; T];
    end

    modelD = fittype(@(Da, Dm, De, x) ...
                        axon * exp(-x*Da) + ...
                        myelin * exp(-x*Dm) +...
```

```
                        ecs * exp(-x*De));
    for i=1:30
        signal_all = [signal_total(i,1) signal_total(i+30, 1) ...
            signal_total(i+60, 1)];
        CompDiff{i} = fit(b',signal_all',modelD,'StartPoint',[Da Dm ...
            De],'Lower',[0 0 0],'Upper',[0.01 0.01 0.01]);
        Dia(i,modelnumber) = CompDiff{i}.Da;
        Dim(i,modelnumber) = CompDiff{i}.Dm;
        Die(i,modelnumber) = CompDiff{i}.De;
    end
end

% fanDTasia toolbox
fields = {'bt'} ; c = cell(length(fields),1); global xps;  xps = ...
    cell2struct(c,fields);
type = {'dti_nls'}; c=cell(length(type),1); opts = cell2struct(c, type);
opts.dti_nls.do_plot = 1; opts.dti_nls.lsq_opts=[]; %xps.bt = Bm;
t_guess = [1 1 1 1 1 1];
t_lb    = [0 0 0 0 -9 -9 -9];
t_ub    = [2 9 9 9 +9 +9 +9];

for modelnumber = 1:size(models, 2)
    %change Die to Dia or Dim to obtain results of other compartments
    R = lsqcurvefit(@DTfun, t_guess, [], Die(:, modelnumber), ...
        opts.dti_nls.lsq_opts);
    %cholesky factorisation to obtain positive eigen values
    DT = [R(1)^2 R(1)*R(2) R(1)*R(3);
          R(1)*R(2) R(2)^2+R(4)^2 R(2)*R(3)+R(4)*R(5);
          R(1)*R(3) R(2)*R(3)+R(4)*R(5) R(3)^2+R(5)^2+R(6)^2];
    e = eig(DT);
    e = sort(e, 'descend');
    FA = sqrt(0.5 *  ( (e(1)-e(2))^2 ...
                + (e(1)-e(3))^2 ...
                + (e(2)-e(3))^2) ...
                /(sum(e.*e)));
    MD = (e(1) + e(2) + e(3))/3;
    RD = (e(2) + e(3))/2;
    AxD = e(1);
    L1results(modelnumber,1) = e(1);
    L2results(modelnumber,1) = e(2);
    L3results(modelnumber,1) = e(3);
    FAresults(modelnumber, 1) = FA;
    MDresults(modelnumber, 1) = MD;
    RDresults(modelnumber, 1) = RD;
    AxDresults(modelnumber, 1) = AxD;
end
```

```
function Di = DTfun(t,varargin)
    global xps; global Gi; global b;
    C = [t(1) t(2)  t(3);
         0    t(4)  t(5);
         0      0   t(6)];
    m(1:6) = tm_3x3_to_1x6(C' * C);  % function from fanDTasia toolbox
    dt = zeros(1,6);
    dt(1:6) = m(1:6);
    Di = Gi*dt';
end
```

A.7.4 White matter model

For the main study in chapter 6, 70 models of the white matter were simulated, with each of them representing one of four scenarios: healthy tissue, acute or chronic demyelination, or neuroinflammation. Each model represented a specific combination of parameters, signifying a specific fibre size and disease state. The parameter values of these models have been given in the table below, along with the table legend.

- Chronic Dem. - Chronic Demyelination
- Acute Dem. - Acute Demyelination
- Inflamm. - Inflammation
- r_a - Axon radius in μm
- g - g-ratio
- r_m - Myelin radius in μm
- L - Fibre spacing in μm
- f - Fibre packing density
- C_m - Myelin water concentration
- C - Base concentration (100 molecules per μm^3)
- D_e - Diffusion coefficient of water in the extra-cellular space in 10^{-5} cm^2/s

Model	r_a	Type	g	r_m	L	f	C_m/C	D_e
1	0.7	Normal	0.65	1.076	2.290	0.80	0.130	2.00
2		Chronic Dem.	0.70	1.000	2.129	0.80	0.118	2.00
3		Chronic Dem.	0.75	0.930	1.980	0.80	0.106	2.00
4		Chronic Dem.	0.80	0.875	1.863	0.80	0.094	2.00
5		Chronic Dem.	0.85	0.823	1.752	0.80	0.082	2.00
6		Acute Dem.	0.70	1.000	2.290	0.69	0.118	2.00
7		Acute Dem.	0.75	0.930	2.290	0.60	0.106	2.00
8		Acute Dem.	0.80	0.875	2.290	0.53	0.094	2.00
9		Acute Dem.	0.85	0.823	2.290	0.47	0.082	2.00
10		Inflamm.	0.65	1.076	2.370	0.75	0.130	1.50
11		Inflamm.	0.65	1.076	2.450	0.70	0.130	1.00
12		Inflamm.	0.65	1.076	2.540	0.65	0.130	0.50
13		Inflamm.	0.65	1.076	2.640	0.60	0.130	0.10
14		Inflamm.	0.65	1.076	2.760	0.55	0.130	0.05
15	1.2	Normal	0.65	1.850	3.940	0.80	0.130	2.00
16		Chronic Dem.	0.70	1.710	3.640	0.80	0.118	2.00
17		Chronic Dem.	0.75	1.600	3.400	0.80	0.106	2.00
18		Chronic Dem.	0.80	1.500	3.190	0.80	0.094	2.00
19		Chronic Dem.	0.85	1.410	3.000	0.80	0.082	2.00
20		Acute Dem.	0.70	1.710	3.940	0.68	0.118	2.00
21		Acute Dem.	0.75	1.600	3.940	0.60	0.106	2.00
22		Acute Dem.	0.80	1.500	3.940	0.53	0.094	2.00
23		Acute Dem.	0.85	1.410	3.940	0.46	0.082	2.00
24		Inflamm.	0.65	1.850	4.060	0.75	0.130	1.50
25		Inflamm.	0.65	1.850	4.210	0.70	0.130	1.00
26		Inflamm.	0.65	1.850	4.370	0.65	0.130	0.50
27		Inflamm.	0.65	1.850	4.540	0.60	0.130	0.10
28		Inflamm.	0.65	1.850	4.750	0.55	0.130	0.05
29	1.75	Normal	0.65	2.700	5.750	0.80	0.130	2.00
30		Chronic Dem.	0.70	2.500	5.320	0.80	0.118	2.00
31		Chronic Dem.	0.75	2.330	4.960	0.80	0.106	2.00
32		Chronic Dem.	0.80	2.180	4.640	0.80	0.094	2.00
33		Chronic Dem.	0.85	2.050	4.360	0.80	0.082	2.00
34		Acute Dem.	0.70	2.500	5.750	0.68	0.118	2.00
35		Acute Dem.	0.75	2.330	5.750	0.60	0.106	2.00
36		Acute Dem.	0.80	2.180	5.750	0.52	0.094	2.00
37		Acute Dem.	0.85	2.050	5.750	0.46	0.082	2.00
38		Inflamm.	0.65	2.700	5.940	0.75	0.130	1.50
39		Inflamm.	0.65	2.700	6.150	0.70	0.130	1.00
40		Inflamm.	0.65	2.700	6.380	0.65	0.130	0.50
41		Inflamm.	0.65	2.700	6.640	0.60	0.130	0.10
42		Inflamm.	0.65	2.700	6.930	0.55	0.130	0.05
43	2.2	Normal	0.65	3.380	7.190	0.80	0.130	2.00
44		Chronic Dem.	0.70	3.140	6.680	0.80	0.118	2.00
45		Chronic Dem.	0.75	2.930	6.240	0.80	0.106	2.00
46		Chronic Dem.	0.80	2.750	5.850	0.80	0.094	2.00
47		Chronic Dem.	0.85	2.600	5.540	0.80	0.082	2.00
48		Acute Dem.	0.70	3.140	7.190	0.69	0.118	2.00
49		Acute Dem.	0.75	2.930	7.190	0.60	0.106	2.00

50	2.2	Acute Dem.	0.80	2.750	7.190	0.53	0.094	2.00
51		Acute Dem.	0.85	2.600	7.190	0.47	0.082	2.00
52		Inflamm.	0.65	3.380	7.430	0.75	0.130	1.50
53		Inflamm.	0.65	3.380	7.700	0.70	0.130	1.00
54		Inflamm.	0.65	3.380	7.980	0.65	0.130	0.50
55		Inflamm.	0.65	3.380	8.300	0.60	0.130	0.10
56		Inflamm.	0.65	3.380	8.680	0.55	0.130	0.05
57	3	Normal	0.65	4.615	9.827	0.80	0.130	2.00
58		Chronic Dem.	0.70	4.280	9.114	0.80	0.118	2.00
59		Chronic Dem.	0.75	4.000	8.517	0.80	0.106	2.00
60		Chronic Dem.	0.80	3.750	7.980	0.80	0.094	2.00
61		Chronic Dem.	0.85	3.530	7.517	0.80	0.082	2.00
62		Acute Dem.	0.70	4.280	9.827	0.69	0.118	2.00
63		Acute Dem.	0.75	4.000	9.827	0.60	0.106	2.00
64		Acute Dem.	0.80	3.750	9.827	0.53	0.094	2.00
65		Acute Dem.	0.85	3.530	9.827	0.47	0.082	2.00
66		Inflamm.	0.65	4.615	10.150	0.75	0.130	1.50
67		Inflamm.	0.65	4.615	10.500	0.70	0.130	1.00
68		Inflamm.	0.65	4.615	10.900	0.65	0.130	0.50
69		Inflamm.	0.65	4.615	11.350	0.60	0.130	0.10
70		Inflamm.	0.65	4.615	11.850	0.55	0.130	0.05

Appendix B

ADNI-2 participant data

The tables given here contain the measurements taken from the corpus callosum ROI described in the feasibility study in chapter 3. Table B.1 contains FA, MD, RD, and AxD values and table B.2 contains volumes of the manually segmented ROI, the brain mask ('Total'), and the normalised volume ('Norm.'). Diffusivities are of unit 10^{-3} mm^2/s and volumes in mm^3.

B.1 DTI parameters

ID	Age	Gender	Group	FA	MD	RD	AxD
003_S_4136	67	M	AD	0.62	0.93	0.54	1.79
003_S_4892	75	F	AD	0.64	0.88	0.48	1.74
007_S_4911	75	M	AD	0.63	0.89	0.5	1.71
007_S_5196	73	F	AD	0.56	0.97	0.61	1.71
016_S_4591	66	F	AD	0.64	0.85	0.49	1.7
016_S_4887	74	M	AD	0.58	0.97	0.6	1.78
016_S_4963	72	F	AD	0.59	0.89	0.55	1.69
016_S_5057	76	M	AD	0.69	0.85	0.44	1.74
094_S_4089	74	M	AD	0.59	0.9	0.55	1.69
094_S_4737	74	F	AD	0.49	1.12	0.77	1.83
003_S_4839	66	M	HC	0.65	0.8	0.44	1.58
007_S_4387	76	F	HC	0.64	0.87	0.49	1.77
007_S_4516	71	M	HC	0.61	0.92	0.53	1.74
007_S_4620	77	M	HC	0.61	0.92	0.56	1.69
007_S_4637	71	F	HC	0.65	0.82	0.45	1.59
016_S_4097	71	F	HC	0.65	0.8	0.44	1.55
094_S_4234	70	M	HC	0.68	0.85	0.44	1.71
094_S_4460	67	F	HC	0.7	0.84	0.43	1.7
094_S_4560	70	F	HC	0.7	0.87	0.44	1.77
131_S_0123	80	M	HC	0.65	0.9	0.5	1.8
007_S_4272	71	M	MCI	0.59	0.88	0.54	1.66
007_S_4611	67	M	MCI	0.74	0.83	0.39	1.71
016_S_2031	73	M	MCI	0.53	1.07	0.69	1.85
016_S_4584	78	F	MCI	0.67	0.88	0.48	1.73
016_S_4601	73	M	MCI	0.68	0.84	0.45	1.72
016_S_5007	72	M	MCI	0.63	0.95	0.56	1.88
027_S_2336	74	F	MCI	0.57	0.96	0.59	1.71
027_S_4729	78	F	MCI	0.63	0.91	0.54	1.76
027_S_4869	77	M	MCI	0.66	0.85	0.47	1.67
094_S_4434	67	M	MCI	0.68	0.79	0.42	1.62

B.2 Volume

ID	Age	Gender	Group	ROI	Total	Norm.
003_S_4136	67	M	AD	3957	2301326.235	1.72E-03
003_S_4892	75	F	AD	2902	1607380.632	1.81E-03
007_S_4911	75	M	AD	3624	2185074.684	1.66E-03
007_S_5196	73	F	AD	3270	2028034.476	1.61E-03
016_S_4591	66	F	AD	3240	1486374.435	2.18E-03
016_S_4887	74	M	AD	3089	2054737.152	1.50E-03
016_S_4963	72	F	AD	3184	1675894.077	1.90E-03
016_S_5057	76	M	AD	3351	2180215.089	1.54E-03
094_S_4089	74	M	AD	3518	2313550.512	1.52E-03
094_S_4737	74	F	AD	3144	1662150.321	1.89E-03
003_S_4839	66	M	HC	3180	1546756.614	2.06E-03
007_S_4387	76	F	HC	3210	1866828.249	1.72E-03
007_S_4516	71	M	HC	3291	1820230.893	1.81E-03
007_S_4620	77	M	HC	3341	1886855.256	1.77E-03
007_S_4637	71	F	HC	2963	1746611.451	1.70E-03
016_S_4097	71	F	HC	3003	1646919.027	1.82E-03
094_S_4234	70	M	HC	2887	1948834.485	1.48E-03
094_S_4460	67	F	HC	2619	1690066.755	1.55E-03
094_S_4560	70	F	HC	2816	1791014.004	1.57E-03
131_S_0123	80	M	HC	2619	1760752.188	1.49E-03
007_S_4272	71	M	MCI	3180	1902291.885	1.67E-03
007_S_4611	67	M	MCI	3159	2131933.986	1.48E-03
016_S_2031	73	M	MCI	3018	3491753.616	8.64E-04
016_S_4584	78	F	MCI	2947	1862119.233	1.58E-03
016_S_4601	73	M	MCI	2958	1941871.347	1.52E-03
016_S_5007	72	M	MCI	2947	2203846.866	1.34E-03
027_S_2336	74	F	MCI	3205	1672896.186	1.92E-03
027_S_4729	78	F	MCI	3200	1755308.529	1.82E-03
027_S_4869	77	M	MCI	2705	2083931.226	1.30E-03
094_S_4434	67	M	MCI	3295	1933694.451	1.70E-03

Appendix C

ADNI-3 participant data

The tables given here contain the measurements taken from the corpus callosum ROI in the studies described in chapters 4 and 5. Table C.1 contains FA, MD, RD, and AxD measured in the whole corpus callosum ROI. Table C.2 contains these measurements in the corpus callosum sub-regions. All diffusivities are of unit 10^{-3} mm^2/s. Tables C.3 and C.4 contain estimates of neurite density (ND) and orientation dispersion index (OD) in the whole corpus callosum and sub-regions.

C.1 DTI parameters

ID	Age	Gender	Group	FA	MD	RD	AxD
002_S_0413	87	F	HC	0.64	0.91	0.51	1.79
002_S_1261	82	F	HC	0.64	0.91	0.52	1.79
002_S_1280	81	F	HC	0.61	0.89	0.51	1.77
002_S_4213	84	F	HC	0.56	0.93	0.64	1.78
002_S_6007	78	F	HC	0.63	0.89	0.5	1.76
002_S_6009	68	M	HC	0.65	0.83	0.46	1.64
002_S_6030	65	F	HC	0.7	0.78	0.4	1.63
002_S_6053	66	M	HC	0.67	0.87	0.46	1.73
002_S_6066	68	F	HC	0.64	0.86	0.5	1.67
002_S_6103	70	F	HC	0.56	0.96	0.61	1.74
002_S_6456	86	M	HC	0.63	0.93	0.52	1.78
003_S_4288	78	F	HC	0.66	0.92	0.5	1.84
003_S_4644	73	F	HC	0.67	0.89	0.47	1.84
003_S_6014	67	M	HC	0.69	0.82	0.42	1.79
003_S_6067	63	F	HC	0.72	0.79	0.38	1.67
003_S_6092	65	F	HC	0.64	0.85	0.48	1.6
003_S_6256	66	F	HC	0.67	0.8	0.44	1.62
003_S_6257	62	M	HC	0.69	0.8	0.41	1.67
003_S_6259	71	M	HC	0.67	0.88	0.47	1.8
003_S_6260	69	M	HC	0.7	0.79	0.39	1.67
003_S_6307	76	M	HC	0.67	0.83	0.46	1.66
011_S_0021	85	F	HC	0.63	0.92	0.54	1.75
011_S_4105	77	F	HC	0.63	0.91	0.51	1.77
011_S_4278	81	M	HC	0.58	1.04	0.63	1.91
011_S_6367	81	F	HC	0.63	0.9	0.51	1.72
011_S_6418	67	M	HC	0.67	0.85	0.45	1.68
020_S_6185	83	M	HC	0.69	0.88	0.46	1.9
020_S_6227	62	F	HC	0.67	0.84	0.45	1.67
020_S_6282	76	M	HC	0.64	0.9	0.5	1.76
020_S_6449	66	F	HC	0.62	0.89	0.51	1.7
020_S_6470	69	M	HC	0.68	0.91	0.46	1.88
020_S_6504	69	M	HC	0.68	0.82	0.43	1.66

020_S_6513	66	F	HC	0.63	0.92	0.52	1.75
024_S_6005	67	F	HC	0.6	0.9	0.53	1.72
024_S_6184	71	F	HC	0.67	0.84	0.45	1.73
024_S_6472	68	F	HC	0.62	0.84	0.48	1.59
032_S_0677	82	M	HC	0.68	0.85	0.44	1.74
032_S_1169	83	F	HC	0.65	0.94	0.52	1.78
032_S_4277	78	F	HC	0.72	0.84	0.4	1.76
032_S_4429	83	M	HC	0.72	0.83	0.39	1.75
032_S_6211	81	M	HC	0.68	0.89	0.47	1.77
032_S_6279	89	M	HC	0.69	0.9	0.46	1.8
032_S_6293	86	F	HC	0.7	0.82	0.41	1.65
032_S_6294	82	M	HC	0.69	0.86	0.45	1.8
035_S_0156	86	M	HC	0.62	1.01	0.59	1.89
035_S_0555	88	M	HC	0.57	0.97	0.6	1.79
035_S_4464	76	M	HC	0.63	0.93	0.53	1.8
035_S_6156	76	M	HC	0.64	0.88	0.49	1.71
035_S_6160	61	M	HC	0.68	0.83	0.45	1.69
037_S_0303	95	M	HC	0.61	1.03	0.62	1.89
037_S_0454	93	F	HC	0.65	0.91	0.5	1.8
037_S_4028	70	F	HC	0.73	0.78	0.36	1.7
037_S_4071	90	M	HC	0.58	1.06	0.66	1.89
037_S_4308	80	M	HC	0.59	1	0.6	1.88
037_S_4410	74	F	HC	0.75	0.79	0.36	1.76
037_S_6031	67	F	HC	0.63	0.88	0.49	1.7
037_S_6032	66	F	HC	0.66	0.85	0.47	1.72
037_S_6046	76	M	HC	0.7	0.85	0.43	1.7
037_S_6115	71	F	HC	0.71	0.82	0.41	1.71
037_S_6144	65	F	HC	0.63	0.89	0.51	1.74
041_S_4037	82	M	HC	0.6	0.91	0.53	1.74
041_S_4200	76	F	HC	0.64	0.89	0.51	1.74
041_S_4427	77	M	HC	0.72	0.81	0.38	1.78
041_S_6136	61	M	HC	0.71	0.79	0.38	1.65
041_S_6159	76	M	HC	0.65	0.84	0.47	1.65
041_S_6192	83	F	HC	0.68	0.87	0.45	1.82
041_S_6226	66	F	HC	0.68	0.82	0.43	1.66

041_S_6292	77	M	HC	0.68	0.9	0.48	1.83
041_S_6314	74	M	HC	0.67	0.9	0.48	1.78
068_S_0127	82	M	HC	0.58	1.01	0.62	1.85
068_S_0210	84	F	HC	0.68	0.84	0.44	1.69
068_S_4340	72	F	HC	0.69	0.86	0.44	1.7
068_S_4424	72	F	HC	0.73	0.78	0.37	1.68
094_S_4649	71	M	HC	0.61	0.87	0.52	1.67
094_S_6250	72	F	HC	0.72	0.83	0.4	1.72
094_S_6269	70	F	HC	0.69	0.84	0.44	1.72
094_S_6419	76	M	HC	0.66	0.85	0.47	1.69
168_S_6049	73	F	HC	0.7	0.81	0.41	1.64
168_S_6051	66	F	HC	0.7	0.88	0.45	1.85
168_S_6059	65	F	HC	0.7	0.83	0.42	1.71
168_S_6062	67	F	HC	0.67	0.83	0.45	1.64
168_S_6064	69	F	HC	0.69	0.91	0.46	1.88
168_S_6065	71	F	HC	0.66	0.84	0.45	1.62
168_S_6085	56	F	HC	0.69	0.8	0.41	1.63
168_S_6086	70	F	HC	0.67	0.87	0.47	1.75
168_S_6098	63	M	HC	0.64	0.88	0.51	1.73
168_S_6107	65	F	HC	0.68	0.78	0.41	1.55
168_S_6108	72	M	HC	0.66	0.83	0.45	1.66
168_S_6121	69	F	HC	0.7	0.87	0.44	1.77
168_S_6128	70	F	HC	0.72	0.81	0.39	1.68
168_S_6131	68	F	HC	0.69	0.85	0.43	1.73
168_S_6151	65	M	HC	0.63	0.86	0.49	1.62
168_S_6233	76	F	HC	0.66	0.84	0.46	1.69
168_S_6281	80	F	HC	0.6	0.89	0.53	1.65
168_S_6285	67	F	HC	0.69	0.78	0.4	1.6
168_S_6318	69	F	HC	0.69	0.84	0.43	1.68
168_S_6320	65	F	HC	0.64	0.83	0.46	1.68
168_S_6321	73	M	HC	0.64	0.94	0.53	1.78
168_S_6492	70	F	HC	0.68	0.81	0.43	1.64
941_S_4100	85	F	HC	0.6	0.98	0.6	1.8
941_S_4292	77	M	HC	0.65	0.82	0.46	1.64
941_S_4365	86	M	HC	0.67	0.91	0.49	1.88

941_S_6044	75	F	HC	0.68	0.75	0.39	1.55
941_S_6054	79	F	HC	0.66	0.88	0.47	1.74
941_S_6058	68	F	HC	0.72	0.77	0.37	1.63
941_S_6080	77	F	HC	0.59	0.97	0.59	1.84
941_S_6094	70	F	HC	0.72	0.83	0.41	1.74
002_S_1155	68.2	M	MCI	0.7	0.85	0.43	1.79
003_S_0908	74	F	MCI	0.73	0.83	0.39	1.72
003_S_1074	95.9	F	MCI	0.68	0.89	0.47	1.74
003_S_1122	87.2	F	MCI	0.71	0.86	0.43	1.83
003_S_6258	79.8	M	MCI	0.69	0.87	0.45	1.81
003_S_6268	69.6	M	MCI	0.67	0.85	0.45	1.67
003_S_6432	67.3	F	MCI	0.76	0.82	0.36	1.76
003_S_6606	73.6	F	MCI	0.68	0.9	0.48	1.83
003_S_6678	76	F	MCI	0.71	0.89	0.44	1.83
011_S_6618	84.8	M	MCI	0.69	0.95	0.49	1.97
012_S_6073	63	M	MCI	0.7	0.88	0.44	1.78
024_S_6033	58.4	F	MCI	0.73	0.77	0.36	1.69
032_S_6055	75.2	M	MCI	0.69	0.82	0.42	1.66
037_S_6083	72.2	M	MCI	0.7	0.84	0.42	1.72
037_S_6125	71	F	MCI	0.7	0.85	0.43	1.79
037_S_6141	60.2	F	MCI	0.67	0.86	0.46	1.73
041_S_0679	74	M	MCI	0.74	0.77	0.36	1.63
041_S_1418	91.6	M	MCI	0.65	0.94	0.51	1.83
068_S_0802	91.8	F	MCI	0.68	0.88	0.46	1.75
168_S_6180	86.8	M	MCI	0.74	0.8	0.36	1.69
168_S_6426	79.5	F	MCI	0.73	0.8	0.38	1.68
168_S_6467	71.3	F	MCI	0.72	0.83	0.4	1.71
168_S_6591	76.7	F	MCI	0.59	1.02	0.61	1.84
168_S_6619	71.9	M	MCI	0.71	0.86	0.42	1.75
168_S_6634	80.3	F	MCI	0.76	0.82	0.36	1.81
941_S_6017	76.7	M	MCI	0.7	0.91	0.47	1.83
941_S_6052	88.2	F	MCI	0.6	0.99	0.6	1.85
941_S_6068	75.8	M	MCI	0.73	0.85	0.4	1.82
003_S_6264	55.3	M	AD	0.72	0.82	0.4	1.7
011_S_4827	76.2	M	AD	0.66	0.95	0.51	1.83

011_S_6303	70.4	M	AD	0.68	0.88	0.46	1.75
032_S_6600	71.3	F	AD	0.73	0.8	0.39	1.67
168_S_6142	86.1	F	AD	0.66	0.89	0.49	1.73

C.2 DTI parameters by region

ID	Age	Gender	Group	Region	FA	MD	RD	AxD
002_S_0413	87	F	HC	1	0.69	0.84	0.44	1.7
002_S_1261	82	F	HC	1	0.77	0.82	0.34	1.71
002_S_1280	81	F	HC	1	0.65	0.95	0.58	1.78
002_S_4213	84	F	HC	1	0.6	0.87	0.54	1.53
002_S_6007	78	F	HC	1	0.75	0.82	0.36	1.66
002_S_6009	68	M	HC	1	0.79	0.76	0.31	1.64
002_S_6030	65	F	HC	1	0.79	0.75	0.29	1.65
002_S_6053	66	M	HC	1	0.74	0.79	0.37	1.74
002_S_6066	68	F	HC	1	0.72	0.81	0.39	1.66
002_S_6103	70	F	HC	1	0.65	0.79	0.45	1.55
002_S_6456	86	M	HC	1	0.69	0.84	0.42	1.84
003_S_4288	78	F	HC	1	0.75	0.8	0.37	1.72
003_S_4644	73	F	HC	1	0.75	0.83	0.38	1.76
003_S_6014	67	M	HC	1	0.81	0.8	0.3	1.79
003_S_6067	63	F	HC	1	0.83	0.76	0.26	1.7
003_S_6092	65	F	HC	1	0.65	0.84	0.46	1.61
003_S_6256	66	F	HC	1	0.75	0.77	0.36	1.66
003_S_6257	62	M	HC	1	0.75	0.78	0.34	1.69
003_S_6259	71	M	HC	1	0.59	0.91	0.54	1.61
003_S_6260	69	M	HC	1	0.74	0.78	0.36	1.65
003_S_6307	76	M	HC	1	0.65	0.78	0.44	1.51
011_S_0021	85	F	HC	1	0.68	0.91	0.58	1.78
011_S_4105	77	F	HC	1	0.76	0.78	0.34	1.63
011_S_4278	81	M	HC	1	0.57	1.04	0.57	1.95
011_S_6367	81	F	HC	1	0.74	0.82	0.37	1.7
011_S_6418	67	M	HC	1	0.7	0.83	0.41	1.65
020_S_6185	83	M	HC	1	0.75	0.81	0.39	1.79
020_S_6227	62	F	HC	1	0.74	0.83	0.37	1.72
020_S_6282	76	M	HC	1	0.66	0.9	0.47	1.73
020_S_6449	66	F	HC	1	0.69	0.83	0.42	1.64
020_S_6470	69	M	HC	1	0.79	0.77	0.31	1.71
020_S_6504	69	M	HC	1	0.72	0.84	0.41	1.72

020_S_6513	66	F	HC	1	0.74	0.82	0.39	1.74
024_S_6005	67	F	HC	1	0.72	0.82	0.41	1.65
024_S_6184	71	F	HC	1	0.7	0.83	0.41	1.84
024_S_6472	68	F	HC	1	0.68	0.78	0.39	1.57
032_S_0677	82	M	HC	1	0.71	0.85	0.41	1.71
032_S_1169	83	F	HC	1	0.64	0.92	0.5	1.75
032_S_4277	78	F	HC	1	0.74	0.81	0.37	1.67
032_S_4429	83	M	HC	1	0.76	0.81	0.35	1.71
032_S_6211	81	M	HC	1	0.73	0.87	0.41	1.79
032_S_6279	89	M	HC	1	0.65	0.95	0.52	1.88
032_S_6293	86	F	HC	1	0.68	0.84	0.42	1.62
032_S_6294	82	M	HC	1	0.76	0.81	0.36	1.81
035_S_0156	86	M	HC	1	0.52	1.15	0.79	2.03
035_S_0555	88	M	HC	1	0.72	0.81	0.4	1.67
035_S_4464	76	M	HC	1	0.61	0.92	0.54	1.72
035_S_6156	76	M	HC	1	0.7	0.87	0.47	1.77
035_S_6160	61	M	HC	1	0.72	0.83	0.4	1.75
037_S_0303	95	M	HC	1	0.59	1.09	0.65	1.9
037_S_0454	93	F	HC	1	0.73	0.87	0.41	1.77
037_S_4028	70	F	HC	1	0.73	0.74	0.33	1.6
037_S_4071	90	M	HC	1	0.59	1.06	0.65	1.91
037_S_4308	80	M	HC	1	0.73	0.91	0.42	1.9
037_S_4410	74	F	HC	1	0.8	0.76	0.29	1.66
037_S_6031	67	F	HC	1	0.72	0.85	0.42	1.74
037_S_6032	66	F	HC	1	0.69	0.8	0.42	1.72
037_S_6046	76	M	HC	1	0.71	0.8	0.4	1.67
037_S_6115	71	F	HC	1	0.78	0.8	0.37	1.75
037_S_6144	65	F	HC	1	0.66	0.85	0.45	1.72
041_S_4037	82	M	HC	1	0.7	0.86	0.45	1.83
041_S_4200	76	F	HC	1	0.68	0.91	0.52	1.8
041_S_4427	77	M	HC	1	0.82	0.74	0.26	1.7
041_S_6136	61	M	HC	1	0.77	0.74	0.31	1.57
041_S_6159	76	M	HC	1	0.69	0.82	0.43	1.66
041_S_6192	83	F	HC	1	0.83	0.78	0.29	1.78
041_S_6226	66	F	HC	1	0.79	0.77	0.3	1.7

041_S_6292	77	M	HC	1	0.74	0.89	0.4	1.84
041_S_6314	74	M	HC	1	0.69	0.88	0.44	1.71
068_S_0127	82	M	HC	1	0.6	0.98	0.57	1.85
068_S_0210	84	F	HC	1	0.65	0.82	0.47	1.67
068_S_4340	72	F	HC	1	0.72	0.84	0.41	1.72
068_S_4424	72	F	HC	1	0.77	0.7	0.3	1.5
094_S_4649	71	M	HC	1	0.63	0.84	0.5	1.57
094_S_6250	72	F	HC	1	0.73	0.74	0.35	1.58
094_S_6269	70	F	HC	1	0.69	0.76	0.4	1.57
094_S_6419	76	M	HC	1	0.73	0.82	0.39	1.72
168_S_6049	73	F	HC	1	0.74	0.74	0.36	1.57
168_S_6051	66	F	HC	1	0.77	0.84	0.36	1.79
168_S_6059	65	F	HC	1	0.76	0.79	0.33	1.74
168_S_6062	67	F	HC	1	0.69	0.8	0.42	1.57
168_S_6064	69	F	HC	1	0.76	0.85	0.39	1.8
168_S_6065	71	F	HC	1	0.7	0.79	0.42	1.57
168_S_6085	56	F	HC	1	0.77	0.76	0.32	1.64
168_S_6086	70	F	HC	1	0.73	0.78	0.37	1.62
168_S_6098	63	M	HC	1	0.65	0.84	0.47	1.61
168_S_6107	65	F	HC	1	0.75	0.75	0.33	1.58
168_S_6108	72	M	HC	1	0.7	0.81	0.42	1.65
168_S_6121	69	F	HC	1	0.73	0.87	0.4	1.76
168_S_6128	70	F	HC	1	0.73	0.81	0.36	1.66
168_S_6131	68	F	HC	1	0.67	0.79	0.42	1.65
168_S_6151	65	M	HC	1	0.64	0.85	0.46	1.65
168_S_6233	76	F	HC	1	0.7	0.87	0.46	1.71
168_S_6281	80	F	HC	1	0.71	0.82	0.4	1.7
168_S_6285	67	F	HC	1	0.76	0.77	0.33	1.67
168_S_6318	69	F	HC	1	0.72	0.8	0.36	1.74
168_S_6320	65	F	HC	1	0.7	0.79	0.41	1.65
168_S_6321	73	M	HC	1	0.69	0.9	0.49	1.82
168_S_6492	70	F	HC	1	0.73	0.8	0.38	1.64
941_S_4100	85	F	HC	1	0.58	1.05	0.68	1.96
941_S_4292	77	M	HC	1	0.73	0.82	0.39	1.66
941_S_4365	86	M	HC	1	0.68	0.84	0.43	1.65

941_S_6044	75	F	HC	1	0.76	0.75	0.33	1.57
941_S_6054	79	F	HC	1	0.74	0.82	0.38	1.69
941_S_6058	68	F	HC	1	0.72	0.74	0.37	1.53
941_S_6080	77	F	HC	1	0.65	0.91	0.51	1.77
941_S_6094	70	F	HC	1	0.75	0.8	0.36	1.69
002_S_0413	87	F	HC	2	0.63	0.97	0.52	1.82
002_S_1261	82	F	HC	2	0.73	0.91	0.44	1.89
002_S_1280	81	F	HC	2	0.61	0.85	0.48	1.7
002_S_4213	84	F	HC	2	0.65	0.89	0.49	1.73
002_S_6007	78	F	HC	2	0.64	0.8	0.45	1.54
002_S_6009	68	M	HC	2	0.73	0.81	0.37	1.66
002_S_6030	65	F	HC	2	0.71	0.79	0.38	1.63
002_S_6053	66	M	HC	2	0.65	0.8	0.45	1.46
002_S_6066	68	F	HC	2	0.68	0.93	0.49	1.84
002_S_6103	70	F	HC	2	0.54	0.88	0.59	1.52
002_S_6456	86	M	HC	2	0.67	0.97	0.52	1.83
003_S_4288	78	F	HC	2	0.62	1.06	0.61	1.91
003_S_4644	73	F	HC	2	0.71	0.92	0.45	1.82
003_S_6014	67	M	HC	2	0.8	0.79	0.32	1.84
003_S_6067	63	F	HC	2	0.73	0.78	0.37	1.64
003_S_6092	65	F	HC	2	0.59	0.82	0.51	1.43
003_S_6256	66	F	HC	2	0.67	0.9	0.48	1.75
003_S_6257	62	M	HC	2	0.66	0.83	0.44	1.7
003_S_6259	71	M	HC	2	0.65	0.86	0.45	1.71
003_S_6260	69	M	HC	2	0.73	0.86	0.41	1.76
003_S_6307	76	M	HC	2	0.59	0.89	0.58	1.51
011_S_0021	85	F	HC	2	0.52	1.01	0.69	1.66
011_S_4105	77	F	HC	2	0.71	0.8	0.4	1.61
011_S_4278	81	M	HC	2	0.55	1.14	0.72	1.98
011_S_6367	81	F	HC	2	0.64	0.77	0.42	1.42
011_S_6418	67	M	HC	2	0.67	0.93	0.52	1.74
020_S_6185	83	M	HC	2	0.72	0.86	0.39	1.84
020_S_6227	62	F	HC	2	0.64	0.81	0.45	1.49
020_S_6282	76	M	HC	2	0.59	0.84	0.54	1.55
020_S_6449	66	F	HC	2	0.61	0.94	0.56	1.7

020_S_6470	69	M	HC	2	0.77	0.85	0.35	1.88
020_S_6504	69	M	HC	2	0.72	0.84	0.39	1.75
020_S_6513	66	F	HC	2	0.58	0.88	0.54	1.48
024_S_6005	67	F	HC	2	0.58	0.83	0.52	1.48
024_S_6184	71	F	HC	2	0.73	0.79	0.38	1.66
024_S_6472	68	F	HC	2	0.6	0.88	0.51	1.62
032_S_0677	82	M	HC	2	0.65	0.8	0.45	1.57
032_S_1169	83	F	HC	2	0.6	1.03	0.62	1.83
032_S_4277	78	F	HC	2	0.71	0.82	0.4	1.62
032_S_4429	83	M	HC	2	0.71	0.87	0.42	1.79
032_S_6211	81	M	HC	2	0.67	0.97	0.51	1.87
032_S_6279	89	M	HC	2	0.57	1.04	0.67	1.74
032_S_6293	86	F	HC	2	0.64	0.83	0.47	1.53
032_S_6294	82	M	HC	2	0.67	0.92	0.51	1.8
035_S_0156	86	M	HC	2	0.58	1.09	0.7	1.9
035_S_0555	88	M	HC	2	0.51	0.96	0.63	1.62
035_S_4464	76	M	HC	2	0.63	0.89	0.47	1.65
035_S_6156	76	M	HC	2	0.67	0.91	0.48	1.75
035_S_6160	61	M	HC	2	0.61	0.88	0.52	1.62
037_S_0303	95	M	HC	2	0.55	1.12	0.76	1.81
037_S_0454	93	F	HC	2	0.75	0.85	0.39	1.83
037_S_4028	70	F	HC	2	0.7	0.79	0.39	1.6
037_S_4071	90	M	HC	2	0.48	1.25	0.93	1.99
037_S_4308	80	M	HC	2	0.54	1.1	0.74	1.87
037_S_4410	74	F	HC	2	0.76	0.84	0.39	1.81
037_S_6031	67	F	HC	2	0.67	0.9	0.47	1.85
037_S_6032	66	F	HC	2	0.62	0.84	0.47	1.52
037_S_6046	76	M	HC	2	0.61	0.97	0.63	1.75
037_S_6115	71	F	HC	2	0.61	0.81	0.5	1.55
037_S_6144	65	F	HC	2	0.6	0.84	0.52	1.51
041_S_4037	82	M	HC	2	0.6	0.99	0.64	1.76
041_S_4200	76	F	HC	2	0.55	0.95	0.61	1.64
041_S_4427	77	M	HC	2	0.78	0.81	0.33	1.86
041_S_6136	61	M	HC	2	0.73	0.76	0.37	1.58
041_S_6159	76	M	HC	2	0.63	0.87	0.5	1.61

041_S_6192	83	F	HC	2	0.81	0.83	0.33	1.87
041_S_6226	66	F	HC	2	0.75	0.79	0.36	1.68
041_S_6292	77	M	HC	2	0.76	0.88	0.38	1.88
041_S_6314	74	M	HC	2	0.57	0.99	0.62	1.71
068_S_0127	82	M	HC	2	0.53	1.23	0.81	2.03
068_S_0210	84	F	HC	2	0.63	0.91	0.51	1.69
068_S_4340	72	F	HC	2	0.73	0.88	0.41	1.81
068_S_4424	72	F	HC	2	0.73	0.71	0.34	1.48
094_S_4649	71	M	HC	2	0.57	0.89	0.56	1.57
094_S_6250	72	F	HC	2	0.7	0.76	0.39	1.55
094_S_6269	70	F	HC	2	0.65	0.82	0.45	1.53
094_S_6419	76	M	HC	2	0.65	0.86	0.47	1.62
168_S_6049	73	F	HC	2	0.67	0.79	0.42	1.48
168_S_6051	66	F	HC	2	0.67	0.95	0.52	1.89
168_S_6059	65	F	HC	2	0.68	0.79	0.42	1.58
168_S_6062	67	F	HC	2	0.61	0.81	0.48	1.48
168_S_6064	69	F	HC	2	0.75	0.95	0.43	1.98
168_S_6065	71	F	HC	2	0.66	0.79	0.42	1.5
168_S_6085	56	F	HC	2	0.69	0.78	0.4	1.57
168_S_6086	70	F	HC	2	0.77	0.85	0.38	1.8
168_S_6098	63	M	HC	2	0.53	0.91	0.6	1.58
168_S_6107	65	F	HC	2	0.57	0.77	0.49	1.38
168_S_6108	72	M	HC	2	0.61	0.89	0.5	1.59
168_S_6121	69	F	HC	2	0.63	0.9	0.54	1.64
168_S_6128	70	F	HC	2	0.66	0.82	0.43	1.57
168_S_6131	68	F	HC	2	0.64	0.8	0.47	1.51
168_S_6151	65	M	HC	2	0.57	0.84	0.55	1.5
168_S_6233	76	F	HC	2	0.56	0.84	0.56	1.52
168_S_6281	80	F	HC	2	0.55	0.87	0.52	1.5
168_S_6285	67	F	HC	2	0.72	0.81	0.39	1.62
168_S_6318	69	F	HC	2	0.57	0.84	0.55	1.49
168_S_6320	65	F	HC	2	0.55	0.78	0.51	1.37
168_S_6321	73	M	HC	2	0.55	0.98	0.65	1.59
168_S_6492	70	F	HC	2	0.75	0.78	0.39	1.62
941_S_4100	85	F	HC	2	0.54	0.97	0.65	1.67

941_S_4292	77	M	HC	2	0.62	0.88	0.51	1.61
941_S_4365	86	M	HC	2	0.71	0.82	0.42	1.74
941_S_6044	75	F	HC	2	0.72	0.77	0.38	1.56
941_S_6054	79	F	HC	2	0.66	0.88	0.55	1.56
941_S_6058	68	F	HC	2	0.7	0.73	0.37	1.49
941_S_6080	77	F	HC	2	0.57	1	0.61	1.81
941_S_6094	70	F	HC	2	0.73	0.87	0.41	1.84
002_S_0413	87	F	HC	3	0.71	0.93	0.51	1.86
002_S_1261	82	F	HC	3	0.77	0.88	0.38	1.85
002_S_1280	81	F	HC	3	0.69	0.89	0.4	1.93
002_S_4213	84	F	HC	3	0.69	0.79	0.4	1.71
002_S_6007	78	F	HC	3	0.6	0.91	0.54	1.58
002_S_6009	68	M	HC	3	0.6	0.85	0.53	1.55
002_S_6030	65	F	HC	3	0.65	1	0.58	1.82
002_S_6053	66	M	HC	3	0.53	0.87	0.59	1.46
002_S_6066	68	F	HC	3	0.68	0.95	0.54	1.87
002_S_6103	70	F	HC	3	0.61	0.85	0.54	1.56
002_S_6456	86	M	HC	3	0.7	1.02	0.5	2.03
003_S_4288	78	F	HC	3	0.66	0.92	0.48	1.98
003_S_4644	73	F	HC	3	0.72	0.86	0.42	1.81
003_S_6014	67	M	HC	3	0.83	0.82	0.28	1.9
003_S_6067	63	F	HC	3	0.74	0.75	0.34	1.58
003_S_6092	65	F	HC	3	0.62	0.79	0.46	1.43
003_S_6256	66	F	HC	3	0.52	1.38	0.97	2.22
003_S_6257	62	M	HC	3	0.74	0.84	0.39	1.74
003_S_6259	71	M	HC	3	0.79	0.94	0.4	2.03
003_S_6260	69	M	HC	3	0.77	0.83	0.35	1.79
003_S_6307	76	M	HC	3	0.52	0.9	0.66	1.57
011_S_0021	85	F	HC	3	0.58	0.94	0.61	1.68
011_S_4105	77	F	HC	3	0.76	0.79	0.35	1.67
011_S_4278	81	M	HC	3	0.68	0.95	0.45	1.95
011_S_6367	81	F	HC	3	0.63	0.78	0.44	1.49
011_S_6418	67	M	HC	3	0.69	0.86	0.42	1.75
020_S_6185	83	M	HC	3	0.77	0.84	0.36	1.89
020_S_6227	62	F	HC	3	0.67	0.8	0.43	1.5

020_S_6282	76	M	HC	3	0.56	0.86	0.56	1.54
020_S_6449	66	F	HC	3	0.6	0.92	0.56	1.64
020_S_6470	69	M	HC	3	0.78	0.89	0.33	2.08
020_S_6504	69	M	HC	3	0.66	0.92	0.5	1.78
020_S_6513	66	F	HC	3	0.58	0.87	0.54	1.53
024_S_6005	67	F	HC	3	0.63	0.77	0.45	1.54
024_S_6184	71	F	HC	3	0.66	0.87	0.46	1.77
024_S_6472	68	F	HC	3	0.65	0.89	0.5	1.62
032_S_0677	82	M	HC	3	0.68	0.79	0.42	1.54
032_S_1169	83	F	HC	3	0.65	0.97	0.57	1.81
032_S_4277	78	F	HC	3	0.77	0.79	0.35	1.73
032_S_4429	83	M	HC	3	0.77	0.8	0.31	1.79
032_S_6211	81	M	HC	3	0.71	0.89	0.44	1.78
032_S_6279	89	M	HC	3	0.67	0.85	0.45	1.59
032_S_6293	86	F	HC	3	0.55	0.88	0.55	1.52
032_S_6294	82	M	HC	3	0.64	0.94	0.53	1.81
035_S_0156	86	M	HC	3	0.7	1	0.51	1.98
035_S_0555	88	M	HC	3	0.61	0.94	0.56	1.7
035_S_4464	76	M	HC	3	0.62	0.85	0.5	1.58
035_S_6156	76	M	HC	3	0.71	0.89	0.44	1.75
035_S_6160	61	M	HC	3	0.72	0.82	0.41	1.66
037_S_0303	95	M	HC	3	0.52	0.97	0.62	1.68
037_S_0454	93	F	HC	3	0.71	0.87	0.44	1.78
037_S_4028	70	F	HC	3	0.78	0.82	0.34	1.79
037_S_4071	90	M	HC	3	0.55	1.13	0.73	1.89
037_S_4308	80	M	HC	3	0.56	1.16	0.77	1.93
037_S_4410	74	F	HC	3	0.82	0.82	0.29	1.91
037_S_6031	67	F	HC	3	0.76	0.87	0.38	1.89
037_S_6032	66	F	HC	3	0.7	0.84	0.42	1.64
037_S_6046	76	M	HC	3	0.65	0.84	0.45	1.6
037_S_6115	71	F	HC	3	0.64	0.81	0.49	1.57
037_S_6144	65	F	HC	3	0.59	0.83	0.52	1.47
041_S_4037	82	M	HC	3	0.46	1.12	0.82	1.67
041_S_4200	76	F	HC	3	0.54	0.91	0.63	1.48
041_S_4427	77	M	HC	3	0.75	0.81	0.35	1.91

041_S_6136	61	M	HC	3	0.73	0.73	0.35	1.49
041_S_6159	76	M	HC	3	0.73	0.83	0.38	1.7
041_S_6192	83	F	HC	3	0.81	0.84	0.31	1.91
041_S_6226	66	F	HC	3	0.75	0.79	0.35	1.66
041_S_6292	77	M	HC	3	0.8	0.84	0.33	1.95
041_S_6314	74	M	HC	3	0.69	0.87	0.44	1.7
068_S_0127	82	M	HC	3	0.54	1.15	0.76	2
068_S_0210	84	F	HC	3	0.59	0.82	0.48	1.54
068_S_4340	72	F	HC	3	0.75	0.81	0.38	1.71
068_S_4424	72	F	HC	3	0.72	0.73	0.35	1.5
094_S_4649	71	M	HC	3	0.65	0.92	0.52	1.66
094_S_6250	72	F	HC	3	0.73	0.72	0.35	1.47
094_S_6269	70	F	HC	3	0.71	0.83	0.43	1.7
094_S_6419	76	M	HC	3	0.56	0.84	0.53	1.51
168_S_6049	73	F	HC	3	0.65	0.92	0.52	1.7
168_S_6051	66	F	HC	3	0.75	0.82	0.36	1.85
168_S_6059	65	F	HC	3	0.71	0.79	0.39	1.62
168_S_6062	67	F	HC	3	0.6	0.89	0.56	1.55
168_S_6064	69	F	HC	3	0.77	0.92	0.41	2.05
168_S_6065	71	F	HC	3	0.66	0.8	0.42	1.53
168_S_6085	56	F	HC	3	0.7	0.76	0.4	1.48
168_S_6086	70	F	HC	3	0.78	0.86	0.36	1.83
168_S_6098	63	M	HC	3	0.65	0.87	0.49	1.65
168_S_6107	65	F	HC	3	0.65	0.79	0.45	1.52
168_S_6108	72	M	HC	3	0.64	0.8	0.46	1.49
168_S_6121	69	F	HC	3	0.59	0.95	0.59	1.68
168_S_6128	70	F	HC	3	0.72	0.74	0.36	1.49
168_S_6131	68	F	HC	3	0.65	0.8	0.45	1.51
168_S_6151	65	M	HC	3	0.53	0.83	0.55	1.41
168_S_6233	76	F	HC	3	0.64	0.86	0.5	1.67
168_S_6281	80	F	HC	3	0.53	0.83	0.56	1.33
168_S_6285	67	F	HC	3	0.71	0.74	0.36	1.49
168_S_6318	69	F	HC	3	0.55	0.86	0.61	1.47
168_S_6320	65	F	HC	3	0.61	0.79	0.49	1.39
168_S_6321	73	M	HC	3	0.58	0.86	0.61	1.44

168_S_6492	70	F	HC	3	0.77	0.76	0.35	1.58
941_S_4100	85	F	HC	3	0.51	1.16	0.82	1.8
941_S_4292	77	M	HC	3	0.62	0.8	0.45	1.51
941_S_4365	86	M	HC	3	0.75	0.87	0.37	1.93
941_S_6044	75	F	HC	3	0.71	0.79	0.4	1.54
941_S_6054	79	F	HC	3	0.73	0.84	0.44	1.73
941_S_6058	68	F	HC	3	0.72	0.76	0.36	1.59
941_S_6080	77	F	HC	3	0.63	1.22	0.78	2.1
941_S_6094	70	F	HC	3	0.79	0.82	0.33	1.81
002_S_0413	87	F	HC	4	0.65	1.06	0.63	1.98
002_S_1261	82	F	HC	4	0.67	0.93	0.52	1.94
002_S_1280	81	F	HC	4	0.71	1	0.5	2.01
002_S_4213	84	F	HC	4	0.72	0.86	0.36	1.87
002_S_6007	78	F	HC	4	0.53	0.92	0.62	1.57
002_S_6009	68	M	HC	4	0.52	0.85	0.55	1.45
002_S_6030	65	F	HC	4	0.59	1.04	0.64	1.77
002_S_6053	66	M	HC	4	0.55	0.9	0.62	1.42
002_S_6066	68	F	HC	4	0.65	0.92	0.53	1.71
002_S_6103	70	F	HC	4	0.57	1.03	0.68	1.74
002_S_6456	86	M	HC	4	0.6	1.11	0.63	2.07
003_S_4288	78	F	HC	4	0.68	0.89	0.43	1.87
003_S_4644	73	F	HC	4	0.68	0.96	0.51	1.96
003_S_6014	67	M	HC	4	0.79	0.82	0.31	1.93
003_S_6067	63	F	HC	4	0.68	0.85	0.45	1.59
003_S_6092	65	F	HC	4	0.61	0.86	0.51	1.54
003_S_6256	66	F	HC	4	0.55	0.96	0.59	1.91
003_S_6257	62	M	HC	4	0.65	1.01	0.57	1.78
003_S_6259	71	M	HC	4	0.65	1.13	0.69	2.03
003_S_6260	69	M	HC	4	0.66	0.99	0.52	1.94
003_S_6307	76	M	HC	4	0.46	1.19	0.9	1.75
011_S_0021	85	F	HC	4	0.44	1.22	0.96	1.75
011_S_4105	77	F	HC	4	0.68	0.87	0.45	1.74
011_S_4278	81	M	HC	4	0.47	1.27	0.93	2.14
011_S_6367	81	F	HC	4	0.66	0.89	0.47	1.73
011_S_6418	67	M	HC	4	0.72	0.9	0.45	1.79

020_S_6185	83	M	HC	4	0.68	1.04	0.52	2.1
020_S_6227	62	F	HC	4	0.67	0.81	0.42	1.61
020_S_6282	76	M	HC	4	0.55	1.06	0.73	1.68
020_S_6449	66	F	HC	4	0.55	1.1	0.73	1.8
020_S_6470	69	M	HC	4	0.66	1.1	0.58	2.15
020_S_6504	69	M	HC	4	0.57	1.08	0.66	1.93
020_S_6513	66	F	HC	4	0.49	0.94	0.65	1.53
024_S_6005	67	F	HC	4	0.53	0.94	0.63	1.55
024_S_6184	71	F	HC	4	0.57	1.18	0.8	2.06
024_S_6472	68	F	HC	4	0.63	0.9	0.51	1.67
032_S_0677	82	M	HC	4	0.47	0.89	0.63	1.41
032_S_1169	83	F	HC	4	0.61	1.04	0.63	1.83
032_S_4277	78	F	HC	4	0.8	0.83	0.35	1.95
032_S_4429	83	M	HC	4	0.72	0.9	0.44	1.85
032_S_6211	81	M	HC	4	0.71	0.9	0.46	1.79
032_S_6279	89	M	HC	4	0.63	0.95	0.58	1.72
032_S_6293	86	F	HC	4	0.48	0.85	0.6	1.47
032_S_6294	82	M	HC	4	0.55	1	0.67	1.75
035_S_0156	86	M	HC	4	0.56	1.32	0.87	2.12
035_S_0555	88	M	HC	4	0.57	1.08	0.68	1.85
035_S_4464	76	M	HC	4	0.59	0.83	0.51	1.56
035_S_6156	76	M	HC	4	0.67	0.89	0.48	1.8
035_S_6160	61	M	HC	4	0.7	0.78	0.39	1.67
037_S_0303	95	M	HC	4	0.43	1.07	0.82	1.6
037_S_0454	93	F	HC	4	0.72	0.86	0.44	1.73
037_S_4028	70	F	HC	4	0.8	0.83	0.32	1.84
037_S_4071	90	M	HC	4	0.4	1.19	0.88	1.81
037_S_4308	80	M	HC	4	0.45	1.2	0.88	1.84
037_S_4410	74	F	HC	4	0.81	0.8	0.35	1.89
037_S_6031	67	F	HC	4	0.74	0.92	0.41	1.95
037_S_6032	66	F	HC	4	0.77	0.78	0.33	1.65
037_S_6046	76	M	HC	4	0.56	0.96	0.65	1.56
037_S_6115	71	F	HC	4	0.61	0.87	0.56	1.59
037_S_6144	65	F	HC	4	0.56	0.98	0.66	1.7
041_S_4037	82	M	HC	4	0.38	1.09	0.86	1.53

041_S_4200	76	F	HC	4	0.44	1.04	0.74	1.69
041_S_4427	77	M	HC	4	0.54	1.15	0.8	1.96
041_S_6136	61	M	HC	4	0.73	0.78	0.38	1.55
041_S_6159	76	M	HC	4	0.62	0.98	0.59	1.77
041_S_6192	83	F	HC	4	0.71	0.95	0.5	1.95
041_S_6226	66	F	HC	4	0.78	0.75	0.31	1.58
041_S_6292	77	M	HC	4	0.81	0.88	0.33	1.98
041_S_6314	74	M	HC	4	0.6	1.05	0.68	1.8
068_S_0127	82	M	HC	4	0.41	1.24	0.94	1.91
068_S_0210	84	F	HC	4	0.53	0.94	0.64	1.67
068_S_4340	72	F	HC	4	0.64	0.91	0.53	1.73
068_S_4424	72	F	HC	4	0.61	0.84	0.5	1.56
094_S_4649	71	M	HC	4	0.52	1.02	0.68	1.7
094_S_6250	72	F	HC	4	0.73	0.79	0.38	1.62
094_S_6269	70	F	HC	4	0.65	0.94	0.53	1.78
094_S_6419	76	M	HC	4	0.4	0.99	0.77	1.43
168_S_6049	73	F	HC	4	0.61	0.97	0.61	1.71
168_S_6051	66	F	HC	4	0.74	0.93	0.49	1.97
168_S_6059	65	F	HC	4	0.52	1.2	0.88	1.94
168_S_6062	67	F	HC	4	0.41	0.97	0.73	1.44
168_S_6064	69	F	HC	4	0.72	0.94	0.48	1.98
168_S_6065	71	F	HC	4	0.68	0.82	0.43	1.59
168_S_6085	56	F	HC	4	0.59	0.8	0.5	1.39
168_S_6086	70	F	HC	4	0.75	0.93	0.42	1.92
168_S_6098	63	M	HC	4	0.68	0.86	0.47	1.66
168_S_6107	65	F	HC	4	0.67	0.79	0.44	1.5
168_S_6108	72	M	HC	4	0.59	0.95	0.59	1.63
168_S_6121	69	F	HC	4	0.59	0.98	0.59	1.76
168_S_6128	70	F	HC	4	0.66	0.79	0.43	1.52
168_S_6131	68	F	HC	4	0.61	0.88	0.53	1.65
168_S_6151	65	M	HC	4	0.49	0.93	0.63	1.46
168_S_6233	76	F	HC	4	0.65	0.91	0.52	1.7
168_S_6281	80	F	HC	4	0.27	1.17	1.02	1.49
168_S_6285	67	F	HC	4	0.69	0.83	0.45	1.61
168_S_6318	69	F	HC	4	0.44	0.98	0.75	1.49

168_S_6320	65	F	HC	4	0.5	0.95	0.67	1.49
168_S_6321	73	M	HC	4	0.42	1.07	0.74	1.54
168_S_6492	70	F	HC	4	0.7	0.92	0.57	1.66
941_S_4100	85	F	HC	4	0.45	1.13	0.84	1.7
941_S_4292	77	M	HC	4	0.52	0.83	0.53	1.48
941_S_4365	86	M	HC	4	0.79	0.91	0.37	1.98
941_S_6044	75	F	HC	4	0.58	0.95	0.62	1.61
941_S_6054	79	F	HC	4	0.66	1.07	0.72	1.81
941_S_6058	68	F	HC	4	0.71	0.82	0.4	1.62
941_S_6080	77	F	HC	4	0.58	1.01	0.63	1.77
941_S_6094	70	F	HC	4	0.81	0.8	0.31	1.89
002_S_0413	87	F	HC	5	0.79	0.76	0.32	1.7
002_S_1261	82	F	HC	5	0.75	0.78	0.36	1.68
002_S_1280	81	F	HC	5	0.8	0.74	0.29	1.63
002_S_4213	84	F	HC	5	0.68	0.84	0.43	1.75
002_S_6007	78	F	HC	5	0.8	0.74	0.28	1.67
002_S_6009	68	M	HC	5	0.77	0.75	0.34	1.62
002_S_6030	65	F	HC	5	0.78	0.75	0.31	1.67
002_S_6053	66	M	HC	5	0.79	0.78	0.32	1.75
002_S_6066	68	F	HC	5	0.74	0.78	0.36	1.68
002_S_6103	70	F	HC	5	0.79	0.83	0.35	1.8
002_S_6456	86	M	HC	5	0.72	0.81	0.4	1.73
003_S_4288	78	F	HC	5	0.76	0.83	0.36	1.79
003_S_4644	73	F	HC	5	0.8	0.84	0.33	1.82
003_S_6014	67	M	HC	5	0.85	0.69	0.22	1.66
003_S_6067	63	F	HC	5	0.78	0.72	0.3	1.56
003_S_6092	65	F	HC	5	0.7	0.86	0.43	1.68
003_S_6256	66	F	HC	5	0.77	0.7	0.29	1.53
003_S_6257	62	M	HC	5	0.72	0.77	0.37	1.7
003_S_6259	71	M	HC	5	0.78	0.75	0.29	1.69
003_S_6260	69	M	HC	5	0.74	0.71	0.31	1.42
003_S_6307	76	M	HC	5	0.77	0.78	0.33	1.7
011_S_0021	85	F	HC	5	0.71	0.81	0.39	1.67
011_S_4105	77	F	HC	5	0.78	0.75	0.33	1.69
011_S_4278	81	M	HC	5	0.73	0.91	0.42	1.81

011_S_6367	81	F	HC	5	0.71	0.78	0.38	1.68
011_S_6418	67	M	HC	5	0.71	0.79	0.4	1.56
020_S_6185	83	M	HC	5	0.83	0.81	0.27	1.84
020_S_6227	62	F	HC	5	0.76	0.81	0.36	1.7
020_S_6282	76	M	HC	5	0.67	0.83	0.46	1.59
020_S_6449	66	F	HC	5	0.69	0.81	0.4	1.65
020_S_6470	69	M	HC	5	0.78	0.8	0.33	1.78
020_S_6504	69	M	HC	5	0.73	0.75	0.37	1.59
020_S_6513	66	F	HC	5	0.73	0.8	0.37	1.7
024_S_6005	67	F	HC	5	0.79	0.83	0.34	1.75
024_S_6184	71	F	HC	5	0.7	0.84	0.42	1.71
024_S_6472	68	F	HC	5	0.77	0.73	0.32	1.68
032_S_0677	82	M	HC	5	0.66	0.79	0.43	1.6
032_S_1169	83	F	HC	5	0.73	0.78	0.37	1.67
032_S_4277	78	F	HC	5	0.81	0.79	0.29	1.72
032_S_4429	83	M	HC	5	0.81	0.77	0.29	1.77
032_S_6211	81	M	HC	5	0.72	0.83	0.4	1.72
032_S_6279	89	M	HC	5	0.79	0.82	0.32	1.82
032_S_6293	86	F	HC	5	0.73	0.76	0.36	1.53
032_S_6294	82	M	HC	5	0.72	0.76	0.37	1.56
035_S_0156	86	M	HC	5	0.72	0.93	0.47	1.76
035_S_0555	88	M	HC	5	0.67	0.96	0.53	1.69
035_S_4464	76	M	HC	5	0.74	0.85	0.38	1.82
035_S_6156	76	M	HC	5	0.69	0.84	0.44	1.67
035_S_6160	61	M	HC	5	0.75	0.77	0.35	1.65
037_S_0303	95	M	HC	5	0.67	0.98	0.55	1.9
037_S_0454	93	F	HC	5	0.78	0.83	0.34	1.83
037_S_4028	70	F	HC	5	0.79	0.71	0.3	1.57
037_S_4071	90	M	HC	5	0.67	0.94	0.51	1.72
037_S_4308	80	M	HC	5	0.74	0.89	0.4	1.89
037_S_4410	74	F	HC	5	0.85	0.77	0.24	1.8
037_S_6031	67	F	HC	5	0.72	0.77	0.37	1.6
037_S_6032	66	F	HC	5	0.8	0.79	0.3	1.76
037_S_6046	76	M	HC	5	0.77	0.74	0.32	1.62
037_S_6115	71	F	HC	5	0.78	0.76	0.31	1.63

037_S_6144	65	F	HC	5	0.73	0.82	0.36	1.79
041_S_4037	82	M	HC	5	0.66	0.83	0.45	1.59
041_S_4200	76	F	HC	5	0.75	0.81	0.34	1.69
041_S_4427	77	M	HC	5	0.78	0.77	0.32	1.63
041_S_6136	61	M	HC	5	0.87	0.79	0.23	1.9
041_S_6159	76	M	HC	5	0.71	0.79	0.41	1.58
041_S_6192	83	F	HC	5	0.78	0.74	0.32	1.6
041_S_6226	66	F	HC	5	0.81	0.75	0.28	1.71
041_S_6292	77	M	HC	5	0.79	0.77	0.3	1.75
041_S_6314	74	M	HC	5	0.7	0.86	0.44	1.77
068_S_0127	82	M	HC	5	0.66	0.9	0.45	1.8
068_S_0210	84	F	HC	5	0.8	0.81	0.3	1.77
068_S_4340	72	F	HC	5	0.68	0.82	0.44	1.58
068_S_4424	72	F	HC	5	0.81	0.76	0.28	1.78
094_S_4649	71	M	HC	5	0.65	0.81	0.44	1.54
094_S_6250	72	F	HC	5	0.84	0.8	0.27	1.85
094_S_6269	70	F	HC	5	0.74	0.71	0.34	1.48
094_S_6419	76	M	HC	5	0.7	0.78	0.4	1.56
168_S_6049	73	F	HC	5	0.78	0.81	0.33	1.83
168_S_6051	66	F	HC	5	0.82	0.78	0.29	1.78
168_S_6059	65	F	HC	5	0.76	0.74	0.32	1.56
168_S_6062	67	F	HC	5	0.7	0.76	0.39	1.51
168_S_6064	69	F	HC	5	0.83	0.76	0.28	1.76
168_S_6065	71	F	HC	5	0.72	0.77	0.37	1.59
168_S_6085	56	F	HC	5	0.82	0.75	0.28	1.68
168_S_6086	70	F	HC	5	0.74	0.74	0.34	1.55
168_S_6098	63	M	HC	5	0.74	0.83	0.39	1.73
168_S_6107	65	F	HC	5	0.81	0.72	0.27	1.6
168_S_6108	72	M	HC	5	0.78	0.77	0.31	1.7
168_S_6121	69	F	HC	5	0.79	0.85	0.34	1.89
168_S_6128	70	F	HC	5	0.77	0.77	0.34	1.67
168_S_6131	68	F	HC	5	0.77	0.79	0.33	1.76
168_S_6151	65	M	HC	5	0.7	0.81	0.41	1.61
168_S_6233	76	F	HC	5	0.74	0.8	0.37	1.67
168_S_6281	80	F	HC	5	0.69	0.83	0.41	1.65

168_S_6285	67	F	HC	5	0.71	0.75	0.37	1.53
168_S_6318	69	F	HC	5	0.74	0.71	0.33	1.48
168_S_6320	65	F	HC	5	0.72	0.83	0.46	1.71
168_S_6321	73	M	HC	5	0.77	0.78	0.33	1.67
168_S_6492	70	F	HC	5	0.78	0.77	0.32	1.68
941_S_4100	85	F	HC	5	0.74	0.9	0.41	1.79
941_S_4292	77	M	HC	5	0.7	0.76	0.38	1.51
941_S_4365	86	M	HC	5	0.82	0.76	0.26	1.73
941_S_6044	75	F	HC	5	0.73	0.73	0.34	1.51
941_S_6054	79	F	HC	5	0.75	0.78	0.37	1.63
941_S_6058	68	F	HC	5	0.77	0.76	0.34	1.64
941_S_6080	77	F	HC	5	0.72	0.83	0.38	1.68
941_S_6094	70	F	HC	5	0.83	0.77	0.27	1.74
002_S_1155	68	M	MCI	1	0.71	0.87	0.44	1.82
003_S_0908	74	F	MCI	1	0.75	0.82	0.36	1.7
003_S_1074	96	F	MCI	1	0.68	0.89	0.48	1.75
003_S_1122	87	F	MCI	1	0.75	0.82	0.37	1.72
003_S_6258	80	M	MCI	1	0.75	0.83	0.4	1.75
003_S_6268	70	M	MCI	1	0.69	0.84	0.44	1.69
003_S_6432	67	F	MCI	1	0.74	0.89	0.41	1.8
003_S_6606	74	F	MCI	1	0.72	0.86	0.39	1.86
003_S_6678	76	F	MCI	1	0.76	0.8	0.37	1.76
011_S_6618	85	M	MCI	1	0.75	0.91	0.43	1.85
012_S_6073	63	M	MCI	1	0.7	0.87	0.46	1.76
024_S_6033	58	F	MCI	1	0.76	0.71	0.32	1.54
032_S_6055	75	M	MCI	1	0.67	0.82	0.46	1.61
037_S_6083	72	M	MCI	1	0.73	0.86	0.4	1.73
037_S_6125	71	F	MCI	1	0.8	0.83	0.35	1.77
037_S_6141	60	F	MCI	1	0.7	0.83	0.41	1.7
041_S_0679	74	M	MCI	1	0.74	0.74	0.35	1.57
041_S_1418	92	M	MCI	1	0.66	0.98	0.54	1.85
068_S_0802	92	F	MCI	1	0.67	0.86	0.48	1.71
168_S_6180	87	M	MCI	1	0.75	0.81	0.37	1.68
168_S_6426	80	F	MCI	1	0.67	0.76	0.41	1.45
168_S_6467	71	F	MCI	1	0.71	0.79	0.39	1.61

168_S_6591	77	F	MCI	1	0.57	1.03	0.64	1.89
168_S_6619	72	M	MCI	1	0.66	0.83	0.45	1.61
168_S_6634	80	F	MCI	1	0.7	0.84	0.44	1.82
941_S_6017	77	M	MCI	1	0.73	0.92	0.47	1.88
941_S_6052	88	F	MCI	1	0.6	0.98	0.56	1.73
941_S_6068	76	M	MCI	1	0.72	0.83	0.4	1.72
002_S_1155	68	M	MCI	2	0.69	0.91	0.46	1.88
003_S_0908	74	F	MCI	2	0.67	0.88	0.49	1.7
003_S_1074	96	F	MCI	2	0.63	0.91	0.54	1.65
003_S_1122	87	F	MCI	2	0.77	0.82	0.35	1.84
003_S_6258	80	M	MCI	2	0.62	0.99	0.56	1.87
003_S_6268	70	M	MCI	2	0.62	0.89	0.53	1.62
003_S_6432	67	F	MCI	2	0.63	1.01	0.59	1.86
003_S_6606	74	F	MCI	2	0.64	0.99	0.55	1.87
003_S_6678	76	F	MCI	2	0.74	0.92	0.43	1.97
011_S_6618	85	M	MCI	2	0.66	1.15	0.6	2.16
012_S_6073	63	M	MCI	2	0.65	1.01	0.56	1.88
024_S_6033	58	F	MCI	2	0.79	0.78	0.32	1.78
032_S_6055	75	M	MCI	2	0.57	0.79	0.5	1.43
037_S_6083	72	M	MCI	2	0.66	0.92	0.5	1.73
037_S_6125	71	F	MCI	2	0.69	0.91	0.52	1.8
037_S_6141	60	F	MCI	2	0.6	0.83	0.51	1.48
041_S_0679	74	M	MCI	2	0.65	0.78	0.42	1.49
041_S_1418	92	M	MCI	2	0.51	1.2	0.83	1.86
068_S_0802	92	F	MCI	2	0.59	0.95	0.62	1.65
168_S_6180	87	M	MCI	2	0.72	0.9	0.44	1.85
168_S_6426	80	F	MCI	2	0.64	0.87	0.49	1.55
168_S_6467	71	F	MCI	2	0.68	0.82	0.42	1.6
168_S_6591	77	F	MCI	2	0.45	1.39	1.04	2.1
168_S_6619	72	M	MCI	2	0.61	0.92	0.54	1.67
168_S_6634	80	F	MCI	2	0.62	0.87	0.56	1.63
941_S_6017	77	M	MCI	2	0.66	0.98	0.54	1.85
941_S_6052	88	F	MCI	2	0.49	1.27	0.92	1.93
941_S_6068	76	M	MCI	2	0.74	0.85	0.4	1.86
002_S_1155	68	M	MCI	3	0.71	0.91	0.43	1.9

003_S_0908	74	F	MCI	3	0.68	0.87	0.48	1.69
003_S_1074	96	F	MCI	3	0.59	0.93	0.58	1.62
003_S_1122	87	F	MCI	3	0.84	0.77	0.27	1.83
003_S_6258	80	M	MCI	3	0.66	0.88	0.46	1.92
003_S_6268	70	M	MCI	3	0.54	0.88	0.56	1.54
003_S_6432	67	F	MCI	3	0.74	0.89	0.42	1.88
003_S_6606	74	F	MCI	3	0.67	1.02	0.52	2.02
003_S_6678	76	F	MCI	3	0.72	1.03	0.51	2.07
011_S_6618	85	M	MCI	3	0.7	1.03	0.48	2.06
012_S_6073	63	M	MCI	3	0.67	0.96	0.53	1.85
024_S_6033	58	F	MCI	3	0.8	0.82	0.31	1.91
032_S_6055	75	M	MCI	3	0.63	0.74	0.42	1.39
037_S_6083	72	M	MCI	3	0.8	0.84	0.34	1.81
037_S_6125	71	F	MCI	3	0.72	1.19	0.82	1.95
037_S_6141	60	F	MCI	3	0.62	0.82	0.49	1.56
041_S_0679	74	M	MCI	3	0.71	0.8	0.41	1.56
041_S_1418	92	M	MCI	3	0.52	1.05	0.73	1.72
068_S_0802	92	F	MCI	3	0.7	0.82	0.41	1.64
168_S_6180	87	M	MCI	3	0.79	0.86	0.37	1.83
168_S_6426	80	F	MCI	3	0.71	0.84	0.43	1.66
168_S_6467	71	F	MCI	3	0.68	0.81	0.42	1.55
168_S_6591	77	F	MCI	3	0.5	1.01	0.69	1.66
168_S_6619	72	M	MCI	3	0.65	0.99	0.57	1.73
168_S_6634	80	F	MCI	3	0.7	0.82	0.41	1.7
941_S_6017	77	M	MCI	3	0.67	0.92	0.5	1.82
941_S_6052	88	F	MCI	3	0.57	1.1	0.71	1.93
941_S_6068	76	M	MCI	3	0.77	0.84	0.35	1.89
002_S_1155	68	M	MCI	4	0.76	0.89	0.4	1.92
003_S_0908	74	F	MCI	4	0.72	0.8	0.39	1.68
003_S_1074	96	F	MCI	4	0.52	1.11	0.79	1.81
003_S_1122	87	F	MCI	4	0.74	0.98	0.47	1.9
003_S_6258	80	M	MCI	4	0.71	0.83	0.4	1.81
003_S_6268	70	M	MCI	4	0.53	0.86	0.57	1.45
003_S_6432	67	F	MCI	4	0.62	1.13	0.66	2.08
003_S_6606	74	F	MCI	4	0.55	1.24	0.8	2.13

003_S_6678	76	F	MCI	4	0.54	1.23	0.85	1.99
011_S_6618	85	M	MCI	4	0.52	1.18	0.77	1.93
012_S_6073	63	M	MCI	4	0.66	1.01	0.57	1.88
024_S_6033	58	F	MCI	4	0.78	0.77	0.35	1.85
032_S_6055	75	M	MCI	4	0.52	0.86	0.57	1.43
037_S_6083	72	M	MCI	4	0.64	1.03	0.63	1.92
037_S_6125	71	F	MCI	4	0.58	1.29	0.96	1.95
037_S_6141	60	F	MCI	4	0.63	0.88	0.51	1.59
041_S_0679	74	M	MCI	4	0.68	0.79	0.42	1.55
041_S_1418	92	M	MCI	4	0.64	0.86	0.48	1.63
068_S_0802	92	F	MCI	4	0.67	0.93	0.52	1.81
168_S_6180	87	M	MCI	4	0.76	0.79	0.37	1.67
168_S_6426	80	F	MCI	4	0.71	0.91	0.45	1.82
168_S_6467	71	F	MCI	4	0.66	0.88	0.5	1.65
168_S_6591	77	F	MCI	4	0.52	1.05	0.73	1.69
168_S_6619	72	M	MCI	4	0.62	0.92	0.54	1.64
168_S_6634	80	F	MCI	4	0.72	0.82	0.4	1.72
941_S_6017	77	M	MCI	4	0.71	0.87	0.44	1.74
941_S_6052	88	F	MCI	4	0.49	1.21	0.77	2.15
941_S_6068	76	M	MCI	4	0.74	0.84	0.39	1.89
002_S_1155	68	M	MCI	5	0.78	0.8	0.34	1.79
003_S_0908	74	F	MCI	5	0.74	0.85	0.4	1.72
003_S_1074	96	F	MCI	5	0.72	0.78	0.39	1.58
003_S_1122	87	F	MCI	5	0.81	0.76	0.29	1.73
003_S_6258	80	M	MCI	5	0.76	0.77	0.34	1.67
003_S_6268	70	M	MCI	5	0.67	0.82	0.43	1.58
003_S_6432	67	F	MCI	5	0.81	0.77	0.29	1.7
003_S_6606	74	F	MCI	5	0.73	0.8	0.37	1.71
003_S_6678	76	F	MCI	5	0.76	0.83	0.37	1.77
011_S_6618	85	M	MCI	5	0.72	0.86	0.43	1.73
012_S_6073	63	M	MCI	5	0.75	0.83	0.39	1.74
024_S_6033	58	F	MCI	5	0.74	0.69	0.33	1.46
032_S_6055	75	M	MCI	5	0.75	0.82	0.36	1.73
037_S_6083	72	M	MCI	5	0.7	0.78	0.41	1.54
037_S_6125	71	F	MCI	5	0.81	0.81	0.45	1.78

037_S_6141	60	F	MCI	5	0.76	0.82	0.37	1.72
041_S_0679	74	M	MCI	5	0.77	0.75	0.32	1.66
041_S_1418	92	M	MCI	5	0.75	0.84	0.38	1.78
068_S_0802	92	F	MCI	5	0.71	0.89	0.47	1.75
168_S_6180	87	M	MCI	5	0.75	0.75	0.35	1.55
168_S_6426	80	F	MCI	5	0.8	0.77	0.29	1.75
168_S_6467	71	F	MCI	5	0.82	0.78	0.28	1.76
168_S_6591	77	F	MCI	5	0.67	0.88	0.46	1.73
168_S_6619	72	M	MCI	5	0.71	0.85	0.45	1.65
168_S_6634	80	F	MCI	5	0.85	0.78	0.24	1.78
941_S_6017	77	M	MCI	5	0.75	0.85	0.4	1.8
941_S_6052	88	F	MCI	5	0.73	0.85	0.42	1.81
941_S_6068	76	M	MCI	5	0.71	0.74	0.37	1.5
003_S_6264	55	M	AD	1	0.71	0.81	0.42	1.7
011_S_4827	76	M	AD	1	0.65	0.91	0.52	1.8
011_S_6303	70	M	AD	1	0.72	0.9	0.44	1.85
032_S_6600	71	F	AD	1	0.72	0.81	0.4	1.65
168_S_6142	86	F	AD	1	0.67	0.87	0.47	1.71
003_S_6264	55	M	AD	2	0.58	0.9	0.58	1.59
011_S_4827	76	M	AD	2	0.55	0.98	0.64	1.78
011_S_6303	70	M	AD	2	0.59	1.07	0.67	1.91
032_S_6600	71	F	AD	2	0.72	0.89	0.44	1.81
168_S_6142	86	F	AD	2	0.57	0.94	0.59	1.61
003_S_6264	55	M	AD	3	0.64	0.82	0.47	1.51
011_S_4827	76	M	AD	3	0.54	0.95	0.61	1.53
011_S_6303	70	M	AD	3	0.64	0.94	0.54	1.74
032_S_6600	71	F	AD	3	0.72	0.86	0.42	1.72
168_S_6142	86	F	AD	3	0.57	0.88	0.58	1.58
003_S_6264	55	M	AD	4	0.6	0.77	0.47	1.38
011_S_4827	76	M	AD	4	0.42	0.98	0.76	1.56
011_S_6303	70	M	AD	4	0.63	0.92	0.55	1.63
032_S_6600	71	F	AD	4	0.56	0.91	0.58	1.56
168_S_6142	86	F	AD	4	0.48	1.05	0.74	1.72
003_S_6264	55	M	AD	5	0.74	0.77	0.36	1.57
011_S_4827	76	M	AD	5	0.71	0.92	0.47	1.79

011_S_6303	70	M	AD	5	0.7	0.85	0.45	1.69
032_S_6600	71	F	AD	5	0.8	0.75	0.31	1.69
168_S_6142	86	F	AD	5	0.75	0.8	0.38	1.67

C.3 ND and OD

ID	Age	Gender	Group	ND	OD
002_S_0413	87	F	HC	0.33	1
002_S_1261	82	F	HC	0.34	1
002_S_1280	81	F	HC	0.35	1
002_S_4213	84	F	HC	0.32	1
002_S_6007	78	F	HC	0.35	1
002_S_6009	68	M	HC	0.41	0.95
002_S_6030	65	F	HC	0.45	0.95
002_S_6053	66	M	HC	0.37	1
002_S_6066	68	F	HC	0.38	0.98
002_S_6103	70	F	HC	0.29	1
002_S_6456	86	M	HC	0.32	1
003_S_4288	78	F	HC	0.32	1
003_S_4644	73	F	HC	0.35	1
003_S_6014	67	M	HC	0.41	1
003_S_6067	63	F	HC	0.45	0.98
003_S_6092	65	F	HC	0.39	0.92
003_S_6256	66	F	HC	0.43	0.93
003_S_6257	62	M	HC	0.43	0.97
003_S_6259	71	M	HC	0.36	1
003_S_6260	69	M	HC	0.44	0.97
003_S_6307	76	M	HC	0.4	0.97
011_S_0021	85	F	HC	0.32	1
011_S_4105	77	F	HC	0.33	1
011_S_4278	81	M	HC	0.23	1
011_S_6367	81	F	HC	0.35	1
011_S_6418	67	M	HC	0.39	0.99
020_S_6185	83	M	HC	0.35	1
020_S_6227	62	F	HC	0.39	0.98
020_S_6282	76	M	HC	0.34	1
020_S_6449	66	F	HC	0.36	1
020_S_6470	69	M	HC	0.33	1
020_S_6504	69	M	HC	0.41	0.96

020_S_6513	66	F	HC	0.33	1
024_S_6005	67	F	HC	0.34	1
024_S_6184	71	F	HC	0.39	1
024_S_6472	68	F	HC	0.4	0.92
032_S_0677	82	M	HC	0.39	1
032_S_1169	83	F	HC	0.31	1
032_S_4277	78	F	HC	0.4	1
032_S_4429	83	M	HC	0.4	1
032_S_6211	81	M	HC	0.35	1
032_S_6279	89	M	HC	0.34	1
032_S_6293	86	F	HC	0.42	0.96
032_S_6294	82	M	HC	0.37	1
035_S_0156	86	M	HC	0.25	1
035_S_0555	88	M	HC	0.28	1
035_S_4464	76	M	HC	0.31	1
035_S_6156	76	M	HC	0.36	1
035_S_6160	61	M	HC	0.4	0.99
037_S_0303	95	M	HC	0.24	1
037_S_0454	93	F	HC	0.33	1
037_S_4028	70	F	HC	0.45	0.99
037_S_4071	90	M	HC	0.22	1
037_S_4308	80	M	HC	0.26	1
037_S_4410	74	F	HC	0.43	1
037_S_6031	67	F	HC	0.36	0.99
037_S_6032	66	F	HC	0.38	1
037_S_6046	76	M	HC	0.39	0.99
037_S_6115	71	F	HC	0.42	1
037_S_6144	65	F	HC	0.34	1
041_S_4037	82	M	HC	0.33	0.98
041_S_4200	76	F	HC	0.35	1
041_S_4427	77	M	HC	0.42	1
041_S_6136	61	M	HC	0.44	0.96
041_S_6159	76	M	HC	0.4	0.95
041_S_6192	83	F	HC	0.36	1
041_S_6226	66	F	HC	0.42	0.97

041_S_6292	77	M	HC	0.34	1
041_S_6314	74	M	HC	0.34	1
068_S_0127	82	M	HC	0.25	1
068_S_0210	84	F	HC	0.4	1
068_S_4340	72	F	HC	0.38	1
068_S_4424	72	F	HC	0.45	0.98
094_S_4649	71	M	HC	0.37	0.97
094_S_6250	72	F	HC	0.41	1
094_S_6269	70	F	HC	0.4	1
094_S_6419	76	M	HC	0.38	0.99
168_S_6049	73	F	HC	0.42	0.95
168_S_6051	66	F	HC	0.36	1
168_S_6059	65	F	HC	0.41	1
168_S_6062	67	F	HC	0.41	0.95
168_S_6064	69	F	HC	0.33	1
168_S_6065	71	F	HC	0.4	0.94
168_S_6085	56	F	HC	0.43	0.95
168_S_6086	70	F	HC	0.37	1
168_S_6098	63	M	HC	0.36	1
168_S_6107	65	F	HC	0.46	0.9
168_S_6108	72	M	HC	0.41	0.96
168_S_6121	69	F	HC	0.36	1
168_S_6128	70	F	HC	0.42	0.99
168_S_6131	68	F	HC	0.39	1
168_S_6151	65	M	HC	0.39	0.93
168_S_6233	76	F	HC	0.39	0.99
168_S_6281	80	F	HC	0.36	0.96
168_S_6285	67	F	HC	0.45	0.93
168_S_6318	69	F	HC	0.39	0.97
168_S_6320	65	F	HC	0.41	0.97
168_S_6321	73	M	HC	0.3	1
168_S_6492	70	F	HC	0.42	0.95
941_S_4100	85	F	HC	0.27	1
941_S_4292	77	M	HC	0.41	0.94
941_S_4365	86	M	HC	0.33	1

941_S_6044	75	F	HC	0.48	0.89
941_S_6054	79	F	HC	0.36	1
941_S_6058	68	F	HC	0.46	0.95
941_S_6080	77	F	HC	0.28	1
941_S_6094	70	F	HC	0.4	1

C.4 ND and OD by region

ID	Age	Gender	Group	Region	ND	OD
002_S_0413	87	F	HC	1	0.36	0.97
002_S_1261	82	F	HC	1	0.39	1
002_S_1280	81	F	HC	1	0.28	0.98
002_S_4213	84	F	HC	1	0.37	0.87
002_S_6007	78	F	HC	1	0.38	0.97
002_S_6009	68	M	HC	1	0.44	0.97
002_S_6030	65	F	HC	1	0.45	0.97
002_S_6053	66	M	HC	1	0.4	1
002_S_6066	68	F	HC	1	0.38	0.97
002_S_6103	70	F	HC	1	0.43	0.9
002_S_6456	86	M	HC	1	0.37	1
003_S_4288	78	F	HC	1	0.4	0.98
003_S_4644	73	F	HC	1	0.38	1
003_S_6014	67	M	HC	1	0.41	1
003_S_6067	63	F	HC	1	0.44	1
003_S_6092	65	F	HC	1	0.36	0.94
003_S_6256	66	F	HC	1	0.42	0.97
003_S_6257	62	M	HC	1	0.42	0.94
003_S_6259	71	M	HC	1	0.31	0.9
003_S_6260	69	M	HC	1	0.41	0.95
003_S_6307	76	M	HC	1	0.43	0.87
011_S_0021	85	F	HC	1	0.33	1
011_S_4105	77	F	HC	1	0.43	0.95
011_S_4278	81	M	HC	1	0.24	1
011_S_6367	81	F	HC	1	0.4	1
011_S_6418	67	M	HC	1	0.37	0.94
020_S_6185	83	M	HC	1	0.39	1
020_S_6227	62	F	HC	1	0.37	1
020_S_6282	76	M	HC	1	0.32	0.95
020_S_6449	66	F	HC	1	0.37	0.96
020_S_6470	69	M	HC	1	0.43	1
020_S_6504	69	M	HC	1	0.37	0.98

020_S_6513	66	F	HC	1	0.38	1
024_S_6005	67	F	HC	1	0.38	0.97
024_S_6184	71	F	HC	1	0.41	0.95
024_S_6472	68	F	HC	1	0.42	0.85
032_S_0677	82	M	HC	1	0.36	1
032_S_1169	83	F	HC	1	0.3	0.95
032_S_4277	78	F	HC	1	0.39	0.97
032_S_4429	83	M	HC	1	0.39	0.99
032_S_6211	81	M	HC	1	0.34	1
032_S_6279	89	M	HC	1	0.28	1
032_S_6293	86	F	HC	1	0.37	0.93
032_S_6294	82	M	HC	1	0.4	1
035_S_0156	86	M	HC	1	0.22	1
035_S_0555	88	M	HC	1	0.39	0.98
035_S_4464	76	M	HC	1	0.31	0.96
035_S_6156	76	M	HC	1	0.34	1
035_S_6160	61	M	HC	1	0.38	1
037_S_0303	95	M	HC	1	0.24	1
037_S_0454	93	F	HC	1	0.34	1
037_S_4028	70	F	HC	1	0.45	0.93
037_S_4071	90	M	HC	1	0.24	1
037_S_4308	80	M	HC	1	0.32	1
037_S_4410	74	F	HC	1	0.44	0.97
037_S_6031	67	F	HC	1	0.35	1
037_S_6032	66	F	HC	1	0.4	1
037_S_6046	76	M	HC	1	0.4	0.96
037_S_6115	71	F	HC	1	0.39	1
037_S_6144	65	F	HC	1	0.36	0.95
041_S_4037	82	M	HC	1	0.35	1
041_S_4200	76	F	HC	1	0.31	0.98
041_S_4427	77	M	HC	1	0.47	0.99
041_S_6136	61	M	HC	1	0.45	0.91
041_S_6159	76	M	HC	1	0.38	0.94
041_S_6192	83	F	HC	1	0.42	1
041_S_6226	66	F	HC	1	0.43	0.99

041_S_6292	77	M	HC	1	0.33	1
041_S_6314	74	M	HC	1	0.34	1
068_S_0127	82	M	HC	1	0.27	1
068_S_0210	84	F	HC	1	0.37	0.93
068_S_4340	72	F	HC	1	0.36	1
068_S_4424	72	F	HC	1	0.56	0.86
094_S_4649	71	M	HC	1	0.37	0.92
094_S_6250	72	F	HC	1	0.47	0.92
094_S_6269	70	F	HC	1	0.43	0.9
094_S_6419	76	M	HC	1	0.38	1
168_S_6049	73	F	HC	1	0.46	0.88
168_S_6051	66	F	HC	1	0.38	1
168_S_6059	65	F	HC	1	0.41	1
168_S_6062	67	F	HC	1	0.41	0.91
168_S_6064	69	F	HC	1	0.36	1
168_S_6065	71	F	HC	1	0.43	0.91
168_S_6085	56	F	HC	1	0.43	0.96
168_S_6086	70	F	HC	1	0.42	0.94
168_S_6098	63	M	HC	1	0.36	0.89
168_S_6107	65	F	HC	1	0.44	0.91
168_S_6108	72	M	HC	1	0.4	0.96
168_S_6121	69	F	HC	1	0.34	1
168_S_6128	70	F	HC	1	0.42	0.99
168_S_6131	68	F	HC	1	0.4	0.92
168_S_6151	65	M	HC	1	0.36	0.95
168_S_6233	76	F	HC	1	0.34	1
168_S_6281	80	F	HC	1	0.38	1
168_S_6285	67	F	HC	1	0.42	0.98
168_S_6318	69	F	HC	1	0.4	0.99
168_S_6320	65	F	HC	1	0.41	0.94
168_S_6321	73	M	HC	1	0.32	1
168_S_6492	70	F	HC	1	0.4	0.95
941_S_4100	85	F	HC	1	0.23	1
941_S_4292	77	M	HC	1	0.39	0.97
941_S_4365	86	M	HC	1	0.36	0.97

941_S_6044	75	F	HC	1	0.45	0.91
941_S_6054	79	F	HC	1	0.39	0.97
941_S_6058	68	F	HC	1	0.48	0.88
941_S_6080	77	F	HC	1	0.3	1
941_S_6094	70	F	HC	1	0.41	0.99
002_S_0413	87	F	HC	2	0.26	1
002_S_1261	82	F	HC	2	0.32	1
002_S_1280	81	F	HC	2	0.36	0.97
002_S_4213	84	F	HC	2	0.32	0.98
002_S_6007	78	F	HC	2	0.43	0.88
002_S_6009	68	M	HC	2	0.4	0.9
002_S_6030	65	F	HC	2	0.4	0.95
002_S_6053	66	M	HC	2	0.4	0.83
002_S_6066	68	F	HC	2	0.29	1
002_S_6103	70	F	HC	2	0.34	0.87
002_S_6456	86	M	HC	2	0.26	1
003_S_4288	78	F	HC	2	0.25	1
003_S_4644	73	F	HC	2	0.3	1
003_S_6014	67	M	HC	2	0.42	1
003_S_6067	63	F	HC	2	0.42	0.95
003_S_6092	65	F	HC	2	0.46	0.8
003_S_6256	66	F	HC	2	0.32	1
003_S_6257	62	M	HC	2	0.38	0.91
003_S_6259	71	M	HC	2	0.35	1
003_S_6260	69	M	HC	2	0.36	1
003_S_6307	76	M	HC	2	0.37	0.85
011_S_0021	85	F	HC	2	0.24	0.95
011_S_4105	77	F	HC	2	0.4	0.94
011_S_4278	81	M	HC	2	0.24	0.98
011_S_6367	81	F	HC	2	0.47	0.79
011_S_6418	67	M	HC	2	0.3	1
020_S_6185	83	M	HC	2	0.36	1
020_S_6227	62	F	HC	2	0.44	0.84
020_S_6282	76	M	HC	2	0.37	0.88
020_S_6449	66	F	HC	2	0.28	1

020_S_6470	69	M	HC	2	0.36	1
020_S_6504	69	M	HC	2	0.37	1
020_S_6513	66	F	HC	2	0.4	0.83
024_S_6005	67	F	HC	2	0.44	0.84
024_S_6184	71	F	HC	2	0.34	1
024_S_6472	68	F	HC	2	0.33	0.91
032_S_0677	82	M	HC	2	0.41	0.87
032_S_1169	83	F	HC	2	0.24	1
032_S_4277	78	F	HC	2	0.38	0.94
032_S_4429	83	M	HC	2	0.34	1
032_S_6211	81	M	HC	2	0.28	1
032_S_6279	89	M	HC	2	0.23	0.97
032_S_6293	86	F	HC	2	0.37	0.89
032_S_6294	82	M	HC	2	0.3	1
035_S_0156	86	M	HC	2	0.23	1
035_S_0555	88	M	HC	2	0.28	0.84
035_S_4464	76	M	HC	2	0.33	0.96
035_S_6156	76	M	HC	2	0.31	1
035_S_6160	61	M	HC	2	0.32	0.92
037_S_0303	95	M	HC	2	0.23	0.99
037_S_0454	93	F	HC	2	0.34	1
037_S_4028	70	F	HC	2	0.4	0.93
037_S_4071	90	M	HC	2	0.2	0.94
037_S_4308	80	M	HC	2	0.22	1
037_S_4410	74	F	HC	2	0.36	1
037_S_6031	67	F	HC	2	0.32	1
037_S_6032	66	F	HC	2	0.39	0.87
037_S_6046	76	M	HC	2	0.26	0.99
037_S_6115	71	F	HC	2	0.39	0.87
037_S_6144	65	F	HC	2	0.37	0.86
041_S_4037	82	M	HC	2	0.24	0.93
041_S_4200	76	F	HC	2	0.27	0.91
041_S_4427	77	M	HC	2	0.39	1
041_S_6136	61	M	HC	2	0.42	0.92
041_S_6159	76	M	HC	2	0.34	0.93

041_S_6192	83	F	HC	2	0.38	1
041_S_6226	66	F	HC	2	0.4	0.99
041_S_6292	77	M	HC	2	0.34	1
041_S_6314	74	M	HC	2	0.24	0.94
068_S_0127	82	M	HC	2	0.21	1
068_S_0210	84	F	HC	2	0.3	0.96
068_S_4340	72	F	HC	2	0.34	1
068_S_4424	72	F	HC	2	0.57	0.85
094_S_4649	71	M	HC	2	0.34	0.89
094_S_6250	72	F	HC	2	0.45	0.9
094_S_6269	70	F	HC	2	0.38	0.87
094_S_6419	76	M	HC	2	0.36	0.94
168_S_6049	73	F	HC	2	0.49	0.87
168_S_6051	66	F	HC	2	0.29	1
168_S_6059	65	F	HC	2	0.4	0.91
168_S_6062	67	F	HC	2	0.47	0.84
168_S_6064	69	F	HC	2	0.29	1
168_S_6065	71	F	HC	2	0.44	0.86
168_S_6085	56	F	HC	2	0.42	0.9
168_S_6086	70	F	HC	2	0.36	1
168_S_6098	63	M	HC	2	0.3	0.89
168_S_6107	65	F	HC	2	0.5	0.78
168_S_6108	72	M	HC	2	0.33	0.9
168_S_6121	69	F	HC	2	0.31	0.95
168_S_6128	70	F	HC	2	0.38	0.9
168_S_6131	68	F	HC	2	0.4	0.88
168_S_6151	65	M	HC	2	0.39	0.84
168_S_6233	76	F	HC	2	0.4	0.87
168_S_6281	80	F	HC	2	0.37	0.84
168_S_6285	67	F	HC	2	0.38	0.94
168_S_6318	69	F	HC	2	0.4	0.81
168_S_6320	65	F	HC	2	0.49	0.75
168_S_6321	73	M	HC	2	0.27	0.93
168_S_6492	70	F	HC	2	0.42	0.95
941_S_4100	85	F	HC	2	0.25	0.91

941_S_4292	77	M	HC	2	0.33	0.94
941_S_4365	86	M	HC	2	0.37	1
941_S_6044	75	F	HC	2	0.42	0.91
941_S_6054	79	F	HC	2	0.35	0.97
941_S_6058	68	F	HC	2	0.56	0.86
941_S_6080	77	F	HC	2	0.25	1
941_S_6094	70	F	HC	2	0.34	1
002_S_0413	87	F	HC	3	0.29	1
002_S_1261	82	F	HC	3	0.34	1
002_S_1280	81	F	HC	3	0.33	1
002_S_4213	84	F	HC	3	0.41	0.97
002_S_6007	78	F	HC	3	0.3	0.87
002_S_6009	68	M	HC	3	0.35	0.9
002_S_6030	65	F	HC	3	0.24	1
002_S_6053	66	M	HC	3	0.4	0.83
002_S_6066	68	F	HC	3	0.28	1
002_S_6103	70	F	HC	3	0.37	0.88
002_S_6456	86	M	HC	3	0.25	1
003_S_4288	78	F	HC	3	0.31	1
003_S_4644	73	F	HC	3	0.34	1
003_S_6014	67	M	HC	3	0.39	1
003_S_6067	63	F	HC	3	0.44	0.91
003_S_6092	65	F	HC	3	0.49	0.8
003_S_6256	66	F	HC	3	0.12	1
003_S_6257	62	M	HC	3	0.38	0.94
003_S_6259	71	M	HC	3	0.3	1
003_S_6260	69	M	HC	3	0.38	1
003_S_6307	76	M	HC	3	0.38	0.83
011_S_0021	85	F	HC	3	0.28	0.98
011_S_4105	77	F	HC	3	0.41	0.98
011_S_4278	81	M	HC	3	0.29	1
011_S_6367	81	F	HC	3	0.48	0.83
011_S_6418	67	M	HC	3	0.35	1
020_S_6185	83	M	HC	3	0.37	1
020_S_6227	62	F	HC	3	0.43	0.86

020_S_6282	76	M	HC	3	0.33	0.86
020_S_6449	66	F	HC	3	0.29	0.93
020_S_6470	69	M	HC	3	0.34	1
020_S_6504	69	M	HC	3	0.29	1
020_S_6513	66	F	HC	3	0.36	0.85
024_S_6005	67	F	HC	3	0.48	0.89
024_S_6184	71	F	HC	3	0.38	1
024_S_6472	68	F	HC	3	0.32	0.96
032_S_0677	82	M	HC	3	0.41	0.9
032_S_1169	83	F	HC	3	0.26	1
032_S_4277	78	F	HC	3	0.41	1
032_S_4429	83	M	HC	3	0.4	1
032_S_6211	81	M	HC	3	0.33	1
032_S_6279	89	M	HC	3	0.35	0.91
032_S_6293	86	F	HC	3	0.34	0.86
032_S_6294	82	M	HC	3	0.29	1
035_S_0156	86	M	HC	3	0.26	1
035_S_0555	88	M	HC	3	0.29	0.96
035_S_4464	76	M	HC	3	0.39	0.84
035_S_6156	76	M	HC	3	0.33	1
035_S_6160	61	M	HC	3	0.38	0.98
037_S_0303	95	M	HC	3	0.25	0.93
037_S_0454	93	F	HC	3	0.35	1
037_S_4028	70	F	HC	3	0.38	1
037_S_4071	90	M	HC	3	0.23	1
037_S_4308	80	M	HC	3	0.22	1
037_S_4410	74	F	HC	3	0.39	1
037_S_6031	67	F	HC	3	0.35	1
037_S_6032	66	F	HC	3	0.36	0.95
037_S_6046	76	M	HC	3	0.41	0.9
037_S_6115	71	F	HC	3	0.39	0.88
037_S_6144	65	F	HC	3	0.43	0.84
041_S_4037	82	M	HC	3	0.21	0.85
041_S_4200	76	F	HC	3	0.37	0.85
041_S_4427	77	M	HC	3	0.39	1

041_S_6136	61	M	HC	3	0.47	0.86
041_S_6159	76	M	HC	3	0.37	1
041_S_6192	83	F	HC	3	0.38	1
041_S_6226	66	F	HC	3	0.41	0.97
041_S_6292	77	M	HC	3	0.37	1
041_S_6314	74	M	HC	3	0.34	1
068_S_0127	82	M	HC	3	0.23	1
068_S_0210	84	F	HC	3	0.41	0.9
068_S_4340	72	F	HC	3	0.39	1
068_S_4424	72	F	HC	3	0.49	0.86
094_S_4649	71	M	HC	3	0.3	0.94
094_S_6250	72	F	HC	3	0.56	0.85
094_S_6269	70	F	HC	3	0.37	1
094_S_6419	76	M	HC	3	0.38	0.85
168_S_6049	73	F	HC	3	0.3	1
168_S_6051	66	F	HC	3	0.38	1
168_S_6059	65	F	HC	3	0.4	0.95
168_S_6062	67	F	HC	3	0.32	0.89
168_S_6064	69	F	HC	3	0.32	1
168_S_6065	71	F	HC	3	0.4	0.88
168_S_6085	56	F	HC	3	0.52	0.84
168_S_6086	70	F	HC	3	0.36	1
168_S_6098	63	M	HC	3	0.34	0.89
168_S_6107	65	F	HC	3	0.43	0.87
168_S_6108	72	M	HC	3	0.41	0.85
168_S_6121	69	F	HC	3	0.28	0.98
168_S_6128	70	F	HC	3	0.48	0.85
168_S_6131	68	F	HC	3	0.41	0.88
168_S_6151	65	M	HC	3	0.45	0.78
168_S_6233	76	F	HC	3	0.34	0.98
168_S_6281	80	F	HC	3	0.43	0.73
168_S_6285	67	F	HC	3	0.5	0.85
168_S_6318	69	F	HC	3	0.37	0.82
168_S_6320	65	F	HC	3	0.48	0.77
168_S_6321	73	M	HC	3	0.4	0.83

168_S_6492	70	F	HC	3	0.44	0.95
941_S_4100	85	F	HC	3	0.21	0.94
941_S_4292	77	M	HC	3	0.44	0.86
941_S_4365	86	M	HC	3	0.36	1
941_S_6044	75	F	HC	3	0.45	0.89
941_S_6054	79	F	HC	3	0.37	1
941_S_6058	68	F	HC	3	0.43	0.92
941_S_6080	77	F	HC	3	0.22	1
941_S_6094	70	F	HC	3	0.39	1
002_S_0413	87	F	HC	4	0.24	1
002_S_1261	82	F	HC	4	0.29	1
002_S_1280	81	F	HC	4	0.25	1
002_S_4213	84	F	HC	4	0.36	1
002_S_6007	78	F	HC	4	0.29	0.9
002_S_6009	68	M	HC	4	0.43	0.82
002_S_6030	65	F	HC	4	0.24	1
002_S_6053	66	M	HC	4	0.38	0.8
002_S_6066	68	F	HC	4	0.3	1
002_S_6103	70	F	HC	4	0.23	0.98
002_S_6456	86	M	HC	4	0.24	1
003_S_4288	78	F	HC	4	0.34	1
003_S_4644	73	F	HC	4	0.27	1
003_S_6014	67	M	HC	4	0.39	1
003_S_6067	63	F	HC	4	0.35	0.92
003_S_6092	65	F	HC	4	0.34	0.88
003_S_6256	66	F	HC	4	0.27	0.97
003_S_6257	62	M	HC	4	0.25	1
003_S_6259	71	M	HC	4	0.23	1
003_S_6260	69	M	HC	4	0.26	1
003_S_6307	76	M	HC	4	0.2	0.89
011_S_0021	85	F	HC	4	0.21	0.89
011_S_4105	77	F	HC	4	0.34	1
011_S_4278	81	M	HC	4	0.19	0.98
011_S_6367	81	F	HC	4	0.32	0.96
011_S_6418	67	M	HC	4	0.33	1

020_S_6185	83	M	HC	4	0.25	1
020_S_6227	62	F	HC	4	0.39	0.9
020_S_6282	76	M	HC	4	0.24	0.86
020_S_6449	66	F	HC	4	0.23	1
020_S_6470	69	M	HC	4	0.25	1
020_S_6504	69	M	HC	4	0.23	1
020_S_6513	66	F	HC	4	0.28	0.87
024_S_6005	67	F	HC	4	0.31	0.83
024_S_6184	71	F	HC	4	0.22	1
024_S_6472	68	F	HC	4	0.31	0.97
032_S_0677	82	M	HC	4	0.35	0.76
032_S_1169	83	F	HC	4	0.24	1
032_S_4277	78	F	HC	4	0.37	1
032_S_4429	83	M	HC	4	0.32	1
032_S_6211	81	M	HC	4	0.32	1
032_S_6279	89	M	HC	4	0.28	0.99
032_S_6293	86	F	HC	4	0.42	0.78
032_S_6294	82	M	HC	4	0.23	1
035_S_0156	86	M	HC	4	0.21	1
035_S_0555	88	M	HC	4	0.24	0.99
035_S_4464	76	M	HC	4	0.38	0.91
035_S_6156	76	M	HC	4	0.32	1
035_S_6160	61	M	HC	4	0.41	0.97
037_S_0303	95	M	HC	4	0.21	0.84
037_S_0454	93	F	HC	4	0.35	1
037_S_4028	70	F	HC	4	0.38	1
037_S_4071	90	M	HC	4	0.21	0.88
037_S_4308	80	M	HC	4	0.21	0.86
037_S_4410	74	F	HC	4	0.4	1
037_S_6031	67	F	HC	4	0.31	1
037_S_6032	66	F	HC	4	0.42	0.96
037_S_6046	76	M	HC	4	0.26	0.96
037_S_6115	71	F	HC	4	0.34	0.82
037_S_6144	65	F	HC	4	0.25	1
041_S_4037	82	M	HC	4	0.25	0.78

041_S_4200	76	F	HC	4	0.22	0.89
041_S_4427	77	M	HC	4	0.23	1
041_S_6136	61	M	HC	4	0.42	0.9
041_S_6159	76	M	HC	4	0.26	1
041_S_6192	83	F	HC	4	0.28	1
041_S_6226	66	F	HC	4	0.45	0.92
041_S_6292	77	M	HC	4	0.35	1
041_S_6314	74	M	HC	4	0.25	1
068_S_0127	82	M	HC	4	0.2	0.91
068_S_0210	84	F	HC	4	0.27	0.93
068_S_4340	72	F	HC	4	0.3	1
068_S_4424	72	F	HC	4	0.35	0.88
094_S_4649	71	M	HC	4	0.23	0.97
094_S_6250	72	F	HC	4	0.4	0.94
094_S_6269	70	F	HC	4	0.28	1
094_S_6419	76	M	HC	4	0.31	0.78
168_S_6049	73	F	HC	4	0.26	1
168_S_6051	66	F	HC	4	0.3	1
168_S_6059	65	F	HC	4	0.22	0.96
168_S_6062	67	F	HC	4	0.33	0.79
168_S_6064	69	F	HC	4	0.29	1
168_S_6065	71	F	HC	4	0.37	0.92
168_S_6085	56	F	HC	4	0.48	0.77
168_S_6086	70	F	HC	4	0.31	1
168_S_6098	63	M	HC	4	0.34	0.95
168_S_6107	65	F	HC	4	0.45	0.86
168_S_6108	72	M	HC	4	0.28	0.93
168_S_6121	69	F	HC	4	0.25	0.99
168_S_6128	70	F	HC	4	0.44	0.88
168_S_6131	68	F	HC	4	0.31	0.96
168_S_6151	65	M	HC	4	0.32	0.82
168_S_6233	76	F	HC	4	0.3	1
168_S_6281	80	F	HC	4	0.27	0.64
168_S_6285	67	F	HC	4	0.37	0.92
168_S_6318	69	F	HC	4	0.24	0.83

168_S_6320	65	F	HC	4	0.35	0.81
168_S_6321	73	M	HC	4	0.22	0.77
168_S_6492	70	F	HC	4	0.3	1
941_S_4100	85	F	HC	4	0.21	0.86
941_S_4292	77	M	HC	4	0.45	0.83
941_S_4365	86	M	HC	4	0.32	1
941_S_6044	75	F	HC	4	0.27	0.98
941_S_6054	79	F	HC	4	0.25	1
941_S_6058	68	F	HC	4	0.38	0.94
941_S_6080	77	F	HC	4	0.28	0.94
941_S_6094	70	F	HC	4	0.4	1
002_S_0413	87	F	HC	5	0.45	0.99
002_S_1261	82	F	HC	5	0.41	0.98
002_S_1280	81	F	HC	5	0.46	0.96
002_S_4213	84	F	HC	5	0.37	1
002_S_6007	78	F	HC	5	0.46	0.97
002_S_6009	68	M	HC	5	0.46	0.92
002_S_6030	65	F	HC	5	0.44	0.97
002_S_6053	66	M	HC	5	0.43	1
002_S_6066	68	F	HC	5	0.42	0.98
002_S_6103	70	F	HC	5	0.38	1
002_S_6456	86	M	HC	5	0.39	1
003_S_4288	78	F	HC	5	0.36	1
003_S_4644	73	F	HC	5	0.37	1
003_S_6014	67	M	HC	5	0.51	0.98
003_S_6067	63	F	HC	5	0.48	0.91
003_S_6092	65	F	HC	5	0.36	0.97
003_S_6256	66	F	HC	5	0.5	0.9
003_S_6257	62	M	HC	5	0.44	0.96
003_S_6259	71	M	HC	5	0.44	0.96
003_S_6260	69	M	HC	5	0.53	0.82
003_S_6307	76	M	HC	5	0.42	0.99
011_S_0021	85	F	HC	5	0.39	0.95
011_S_4105	77	F	HC	5	0.46	0.98
011_S_4278	81	M	HC	5	0.31	1

011_S_6367	81	F	HC	5	0.43	0.95
011_S_6418	67	M	HC	5	0.41	0.9
020_S_6185	83	M	HC	5	0.41	1
020_S_6227	62	F	HC	5	0.39	1
020_S_6282	76	M	HC	5	0.37	0.92
020_S_6449	66	F	HC	5	0.41	0.94
020_S_6470	69	M	HC	5	0.4	1
020_S_6504	69	M	HC	5	0.45	0.91
020_S_6513	66	F	HC	5	0.41	0.99
024_S_6005	67	F	HC	5	0.38	1
024_S_6184	71	F	HC	5	0.39	0.98
024_S_6472	68	F	HC	5	0.48	0.93
032_S_0677	82	M	HC	5	0.44	0.91
032_S_1169	83	F	HC	5	0.41	0.96
032_S_4277	78	F	HC	5	0.41	1
032_S_4429	83	M	HC	5	0.43	1
032_S_6211	81	M	HC	5	0.37	1
032_S_6279	89	M	HC	5	0.39	1
032_S_6293	86	F	HC	5	0.44	0.89
032_S_6294	82	M	HC	5	0.46	0.89
035_S_0156	86	M	HC	5	0.29	0.99
035_S_0555	88	M	HC	5	0.28	0.94
035_S_4464	76	M	HC	5	0.36	1
035_S_6156	76	M	HC	5	0.37	0.97
035_S_6160	61	M	HC	5	0.42	0.95
037_S_0303	95	M	HC	5	0.25	1
037_S_0454	93	F	HC	5	0.38	1
037_S_4028	70	F	HC	5	0.49	0.92
037_S_4071	90	M	HC	5	0.29	0.99
037_S_4308	80	M	HC	5	0.33	1
037_S_4410	74	F	HC	5	0.43	1
037_S_6031	67	F	HC	5	0.44	0.93
037_S_6032	66	F	HC	5	0.41	1
037_S_6046	76	M	HC	5	0.46	0.95
037_S_6115	71	F	HC	5	0.44	0.94

037_S_6144	65	F	HC	5	0.39	1
041_S_4037	82	M	HC	5	0.38	0.91
041_S_4200	76	F	HC	5	0.4	0.96
041_S_4427	77	M	HC	5	0.43	0.95
041_S_6136	61	M	HC	5	0.42	1
041_S_6159	76	M	HC	5	0.41	0.9
041_S_6192	83	F	HC	5	0.47	0.92
041_S_6226	66	F	HC	5	0.45	1
041_S_6292	77	M	HC	5	0.43	1
041_S_6314	74	M	HC	5	0.37	1
068_S_0127	82	M	HC	5	0.32	0.94
068_S_0210	84	F	HC	5	0.4	1
068_S_4340	72	F	HC	5	0.37	0.9
068_S_4424	72	F	HC	5	0.45	1
094_S_4649	71	M	HC	5	0.4	0.88
094_S_6250	72	F	HC	5	0.41	1
094_S_6269	70	F	HC	5	0.57	0.85
094_S_6419	76	M	HC	5	0.43	0.9
168_S_6049	73	F	HC	5	0.4	1
168_S_6051	66	F	HC	5	0.43	1
168_S_6059	65	F	HC	5	0.45	0.91
168_S_6062	67	F	HC	5	0.46	0.86
168_S_6064	69	F	HC	5	0.44	1
168_S_6065	71	F	HC	5	0.43	0.92
168_S_6085	56	F	HC	5	0.47	0.98
168_S_6086	70	F	HC	5	0.47	0.9
168_S_6098	63	M	HC	5	0.37	0.98
168_S_6107	65	F	HC	5	0.47	0.93
168_S_6108	72	M	HC	5	0.43	1
168_S_6121	69	F	HC	5	0.36	1
168_S_6128	70	F	HC	5	0.43	0.96
168_S_6131	68	F	HC	5	0.41	1
168_S_6151	65	M	HC	5	0.39	0.93
168_S_6233	76	F	HC	5	0.4	0.98
168_S_6281	80	F	HC	5	0.38	0.95

168_S_6285	67	F	HC	5	0.45	0.88
168_S_6318	69	F	HC	5	0.55	0.84
168_S_6320	65	F	HC	5	0.37	0.98
168_S_6321	73	M	HC	5	0.42	0.96
168_S_6492	70	F	HC	5	0.42	0.97
941_S_4100	85	F	HC	5	0.32	1
941_S_4292	77	M	HC	5	0.46	0.87
941_S_4365	86	M	HC	5	0.44	1
941_S_6044	75	F	HC	5	0.48	0.87
941_S_6054	79	F	HC	5	0.42	0.99
941_S_6058	68	F	HC	5	0.43	0.95
941_S_6080	77	F	HC	5	0.39	0.97
941_S_6094	70	F	HC	5	0.44	1

Appendix D

Conferences and publications

D.1 Alzheimer's and Parkinson's Diseases Congress 2019

254 - DIFFUSION TENSOR IMAGING CHARACTERISATION OF THE NORMALLY AGEING CORPUS CALLOSUM VERSUS INDIVIDUALS WITH MILD COGNITIVE IMPAIRMENT AND ALZHEIMER'S DISEASE

View Session Detail to add to Schedule

254 - DIFFUSION TENSOR IMAGING CHARACTERISATION OF THE NORMALLY AGEING CORPUS CALLOSUM VERSUS INDIVIDUALS WITH MILD COGNITIVE IMPAIRMENT AND ALZHEIMER'S DISEASE

S. Rajan [1]
[1]*University of Warwick, School of Engineering, Coventry, United Kingdom*
J. Brettschneider [2]
[2]*University of Warwick, Department of Statistics, Coventry, United Kingdom*
J.F. Collingwood [3]
[3]*University of Warwick, School of Engineering, Coventry, United Kingdom*

Abstract body

Objectives: Degeneration of the corpus callosum is suspected in the early stages of Alzheimer's disease. To differentiate changes occurring in corpus callosum with age from disease, characterisation of detectable changes in normal ageing is necessary.

Methods: Analysis was performed on diffusion weighted MRI scans of healthy controls (HC, n=277) and the available population of age-matched Alzheimer's disease (AD, n=39) and mild cognitive impairment (MCI, n=39) patients from the Alzheimer's Disease Neuroimaging Initiative. For every subject, four maps (fractional anisotropy, mean, radial and axial diffusivities) were calculated, and the corpus callosum manually segmented. Regression trends of healthy controls were analysed with ageing and compared with AD and MCI groups.

Results: Preliminary box plot analysis reveals significant differences at $p<0.05$ between groups. Weak regression trends with age are observed for HC, consistent with the literature. This is due to an established wide range of values for these parameters in the normal adult population. Grouped regression plots show differences in trends indicating a different path of progression for AD and MCI compared to HC.

Figure 1: (a) Manual segmentation of corpus callosum (b) box plot illustrating the fractional anisotropy distribution for the HC, MCI and AD corpus callosum

Conclusions: The data are consistent with evidence that degeneration in corpus callosum occurs with age but is greater in AD and MCI. Longitudinal tracking of the diffusion tensor metrics, at the level of the individual developing MCI, may support clinical bio-marker development for the early stages of AD.

D.2 Alzheimer's Research UK 2019

segmentation algorithms to 'ground-truth' measures. The open-source algorithms were Lesion Growth Algorithm (LGA) and Lesion Probability Algorithm (LPA) provided by the Lesion Segmentation Toolbox. Our 'ground-truth' measures were lesion volume derived from manual lesion maps in one dataset (n = 39), and total Scheltens score in a larger dataset (n = 277). Comparisons included spatial and volumetric comparisons, as well as comparisons of volume with lesion burden score.

Results We aimed to identify an optimal algorithm through comparisons with manually delineated lesion maps, and then aimed to determine whether the selected algorithm still performed best when compared with a commonly used visual rating method.We found LGA performed better than LPA in volumetric comparisons with lesion volume derived from manually-drawn lesion maps. LPA performed better than LGA in spatial comparison with manually-drawn lesion maps, although this may be due to an overestimation of lesion volume by LPA. Both LGA and LPA correlated strongly with the visual rating scale, with LGA performing best.

Conclusions Our results indicate that automated lesion segmentation is a suitable alternative to visual rating scales and is an efficient method of analysing WMH lesion burden in large datasets.

P8.11 Investigation of the corpus callosum in ageing and Alzheimer's Disease using Diffusion Weighted Magnetic Resonance Imaging

Rajan S.

Authors Rajan S[1], Brettschneider J[2], Collingwood J[1]

Affiliations [1]School of Engineering, University of Warwick, [2]Department of Statistics, University of Warwick

Introduction Degeneration of the corpus callosum is suspected in the early stages of Alzheimer's disease (AD); however it also occurs with ageing. To differentiate changes due to ageing from those due to AD, characterisation of detectable changes in normal ageing is necessary.

Methods and Materials Diffusion weighted images of 107 healthy controls (56 – 95 years) from the Alzheimer's Disease Neuroimaging Initiative (ADNI) were analysed to calculate anisotropy and diffusivity measures, intra-cellular volume fraction and orientation dispersion in the manually segmented corpus callosum. Regression analysis was conducted to characterise variation of these parameters with ageing. This was used as a reference against which the available population of age-matched AD and mild cognitive impairment (MCI) patients can be compared. A subset of HC, AD and MCI images were also used to manually segment the genu and splenium and compare regional differences in variation of the diffusion parameters.

Results Analysis of diffusion weighted images of the HC group reveals statistically significant linear trends with ageing in all parameters measured. Box plot analysis of the preliminary data indicates differences between AD, HC and MCI, as well as regional differences between genu and splenium.

Conclusions The preliminary data are consistent with evidence that degeneration in corpus callosum occurs with age and provide a means to quantify these changes within the corpus callosum. This approach offers a standard of reference against which changes due to diseases such as AD can be compared. Evidence suggests that variation in diffusion parameters due to AD occurs in a different pattern than that due to ageing. Therefore, longitudinal tracking of diffusion parameters, at the level of the individual developing MCI, may support clinical biomarker development for the early stages of AD.

P8.12 Exploring the effect of Type II Diabetes on brain structure and cerebral perfusion in patients with early Alzheimer's disease

Dhananjay Dake M.

Authors Dhananjay Dake M[1], De Marco M[1], Wilkinson I[2], Teh K[2], Mitolo M[3], Remes A[4], Liu Y[4], Pikkarainen M[4], Soininen H[4], Venneri A[1]

Affiliations [1]Department of Neuroscience, The University of Sheffield, 2Department of Infection, Immunity & Cardiovascular Disease , The University of Sheffield, [3]Functional MR Unit, Policlinico S.Orsola-Malpighi, [4]Department of Neurology, Kuopio University Hospital, University of East Finland, [5]Department of Clinical Radiology, Kuopio University Hospital, University of East Finland

Introduction Past research has shown that Alzheimer's Disease (AD) can have a significant detrimental effect on the cerebrovascular system.

D.3 Publication 2019: Journal of Neuroscience Methods

Journal of Neuroscience Methods 319 (2019) 28–39

Contents lists available at ScienceDirect

Journal of Neuroscience Methods

journal homepage: www.elsevier.com/locate/jneumeth

Research Article

Synchrotron XRF imaging of Alzheimer's disease basal ganglia reveals linear dependence of high-field magnetic resonance microscopy on tissue iron concentration

Mary E. Finnegan[a,b], Naomi P. Visanji[c], Isolda Romero-Canelon[d], Emily House[e], Surya Rajan[f], J. Frederick W. Mosselmans[g], Lili-Naz Hazrati[h], Jon Dobson[i], Joanna F. Collingwood[f,j,*]

[a] Department of Imaging, Imperial College Healthcare NHS Trust, London, UK
[b] Department of Bioengineering, Imperial College London, London, UK
[c] The Edmond J Safra Program in Parkinson's Disease and the Morton & Gloria Shulman Movement Disorders Clinic, Toronto Western Hospital, Toronto, Ontario, M5T 2S8, Canada
[d] School of Pharmacy, Institute of Clinical Sciences, University of Birmingham, Birmingham B15 2TT, UK
[e] Lancaster Environment Centre, Lancaster University, Lancaster, LA1 4YQ, UK
[f] School of Engineering, University of Warwick, Coventry, CV4 7AL, UK
[g] Diamond Light Source, Didcot, Oxfordshire OX11 0DE, UK
[h] The Hospital for Sick Children, Toronto, Ontario, Canada
[i] J. Crayton Pruitt Family Department of Biomedical Engineering, University of Florida, Gainesville, FL 32611, USA
[j] Department of Materials Science and Engineering, University of Florida, Gainesville, FL 32611, USA

GRAPHICAL ABSTRACT

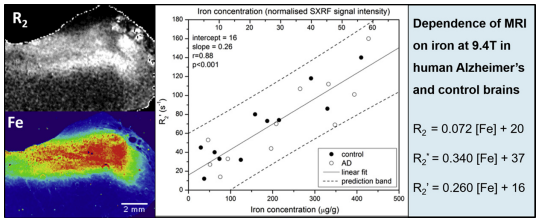

ARTICLE INFO

Keywords:
Alzheimer's
Imaging
Iron
MRI
Relaxometry
Synchrotron
X-ray fluorescence

ABSTRACT

Background: Chemical imaging of the human brain has great potential for diagnostic and monitoring purposes. The heterogeneity of human brain iron distribution, and alterations to this distribution in Alzheimer's disease, indicate iron as a potential endogenous marker. The influence of iron on certain magnetic resonance imaging (MRI) parameters increases with magnetic field, but is under-explored in human brain tissues above 7 T.
New Method: Magnetic resonance microscopy at 9.4 T is used to calculate parametric images of chemically-unfixed post-mortem tissue from Alzheimer's cases (n = 3) and healthy controls (n = 2). Iron-rich regions including caudate nucleus, putamen, globus pallidus and substantia nigra are analysed prior to imaging of total iron distribution with synchrotron X-ray fluorescence mapping. Iron fluorescence calibration is achieved with adjacent tissue blocks, analysed by inductively coupled plasma mass spectrometry or graphite furnace atomic

* Corresponding author at: School of Engineering, University of Warwick, Coventry, CV4 7AL, UK.
E-mail address: J.F.Collingwood@warwick.ac.uk (J.F. Collingwood).

https://doi.org/10.1016/j.jneumeth.2019.03.002
Received 4 October 2018; Received in revised form 2 March 2019; Accepted 2 March 2019
Available online 06 March 2019

absorption spectroscopy.
Results: Correlated MR images and fluorescence maps indicate linear dependence of R_2, R_2* and R_2' on iron at 9.4 T, for both disease and control, as follows: $[R_2(s^{-1}) = 0.072[Fe] + 20]$; $[R_2*(s^{-1}) = 0.34[Fe] + 37]$; $[R_2'(s^{-1}) = 0.26[Fe] + 16]$ for Fe in μg/g tissue (wet weight).
Comparison with Existing Methods: This method permits simultaneous non-destructive imaging of most bioavailable elements. Iron is the focus of the present study as it offers strong scope for clinical evaluation; the approach may be used more widely to evaluate the impact of chemical elements on clinical imaging parameters.
Conclusion: The results at 9.4 T are in excellent quantitative agreement with predictions from experiments performed at lower magnetic fields.

1. Introduction

1.1. The need for biomarkers of Alzheimer's disease

Despite recent improvement in the proportion of individuals with dementia receiving a diagnosis, confirmation of a diagnosis of Alzheimer's disease is generally dependent on *post mortem* examination of the underlying disease pathology. Developments in imaging, including PET (positron emission tomography) imaging of amyloid deposition, volumetric MRI (magnetic resonance imaging) of brain atrophy and measurement of amyloid in the cerebral spinal fluid (CSF) have led to a series of proposals and recommendations to update AD diagnostic criteria e.g. (Dubois et al., 2010; McKhann et al., 2011; Dubois et al., 2016; Morris et al., 2014; Jack et al., 2013). The identification and monitoring of markers, and characterising marker profiles as a function of disease progression, remain major challenges in Alzheimer's research.

MRI is a particularly attractive diagnostic tool as it is non-invasive and does not require exposure to ionising radiation. Studies of volumetric changes in the brain have shown greater atrophy in AD subjects, but also a significant overlap with normal aging (Laakso et al., 1995; Doan et al., 2017; Habes et al., 2016; Pini et al., 2016; Wisse et al., 2014). Furthermore, atrophy indicates significant cell death has already occurred. For this reason, it is a priority to identify changes that are a precursor to irreversible atrophy, including those changes that may be detected by chemical imaging, to enable earlier diagnosis and possible future protective intervention.

1.2. Brain iron in Alzheimer's disease

Over a century ago, developments in histological methods allowed demonstration of iron in mammalian tissues, underpinning the subsequent investigation of iron and other transition metals in the human brain in health and disease (Perls, 1867). The descriptions of metal distributions throughout the cellular architecture of the brain are accompanied by quantitative post-mortem measurements of metal concentrations, such as the study of iron levels in the healthy human brain as a function of age by Hallgren and Sourander in 1958 (Hallgren and Sourander, 1958). The concentration and distribution of transition metals, including iron, are of particular interest in the context of neurodegenerative diseases. In certain rare disorders, iron dysregulation is a primary cause of mortality (Kumar et al., 2016), but in other neurodegenerative disorders the impact of observed iron dysregulation is less clear. Many studies have shown altered non-haem brain iron in specific regions of the AD brain (Samudralwar et al., 1995; Cornett et al., 1998; Loeffler et al., 1995; House et al., 2008; Thompson et al., 1988; Dedman et al., 1992; Connor et al., 1992; Deibel et al., 1996; Tao et al., 2014; Pankhurst et al., 2008; House et al., 2007; Akatsu et al., 2012; Graham et al., 2014; Hare et al., 2016; van Duijn et al., 2017), also in Parkinson's disease (Dexter et al., 1991; Oakley et al., 2007; Wang et al., 2016) and Wilson's disease (Dusek et al., 2017) amongst others. Conflicting results in the literature may be at least in part due to variability in sample archiving conditions and analytical methods, but there is undoubtedly a spectrum of 'normal' regional brain iron concentrations even taking into account variables such as health and age. The disparity is likely not fully captured in the current literature, given that studies where no significant differences between populations are observed may be unpublished or less frequently cited. In an analysis of the literature only the putamen was found to have significantly elevated iron in AD (Schrag et al., 2011). A subsequent meta-analysis by Tao and coworkers (Tao et al., 2014) evidenced elevated iron concentration in eight regions of the AD brain compared with healthy controls, specifically: frontal lobe, parietal lobe, temporal lobe, amygdala, putamen, globus pallidus, cingulate cortex, and caudate nucleus.

1.3. MRI evaluation of brain iron in Alzheimer's disease

Since the contribution of iron to MRI contrast was recognised and explored in the 1980s (Drayer et al., 1986), a number of different techniques have been developed to calculate tissue iron content in organs, including liver and heart, so that this can be used in the evaluation of patients, especially those with iron-overload disorders (St Pierre et al., 2004; Wood, 2011). Changes in non-haem iron have the potential to act as a marker of AD, because of the impact of brain tissue iron on MRI, affecting tissue susceptibility and relaxation parameters (Haacke et al., 2005). This has been demonstrated in various systems ranging from phantoms and animal models (Vymazal et al., 1992; Yang et al., 2013; Tan et al., 2014; Gossuin et al., 2004) to human post mortem tissue (House et al., 2008; Langkammer et al., 2010; Bulk et al., 2018; Antharam et al., 2012; Langkammer et al., 2012).

MR relaxometry techniques allow the quantitative mapping of the relaxation rates R_1, R_2, R_2*and related parameters (e.g. R_2'). As the transverse relaxation rate R_2, and to a lesser extent the longitudinal relaxation rate R_1, have been shown to be linearly proportional to the iron concentration at field strengths up to 7 T (Gossuin et al., 2004), MR relaxometry can provide a tool for investigating brain iron in vivo (Langkammer et al., 2014; Ghadery et al., 2015; Tang et al., 2018). A linear correlation has also been shown between R_2* and iron concentration at fields of 1.5 T – 7 T (Yao et al., 2009), with a steeper gradient (and therefore greater sensitivity) than R_2 at 3 T, the field typically used in clinical neuroimaging (Langkammer et al., 2010). As alternative and more sophisticated MRI measures of iron are developed, the well-established clinically-accessible R_2 and R_2* sequences that have been validated post-mortem retain value for the determination of iron, and offer potential to detect changes in brain iron distribution and concentration as a function of AD in critical regions such as the hippocampus and amygdala (Langkammer et al., 2014; Tang et al., 2018).

The field dependent R_2 increase (FDRI) is the degree to which the value of R_2 depends on the external magnetic field. Bartzokis and coworkers used this property to develop a means of examining iron content in R_2 MRI scans (Bartzokis et al., 1993). R_2 was obtained from dual echo sequences measured at two different field strengths; the difference calculated determined the FDRI. They showed that FDRI of the frontal white matter, caudate nucleus, putamen, and globus pallidus correlated strongly with published iron concentration values in healthy adults and with phantoms of ferritin containing agarose gels (Bartzokis et al., 1993). FDRI has since been used to study ferritin iron concentration in AD compared to control (Bartzokis et al., 1994) and also

in other neurodegenerative diseases such as Parkinson's disease and Huntington's disease (Bartzokis et al., 2004; Bartzokis and Tishler, 2000). The obvious disadvantage of FDRI is that it requires MRI mapping with two different instruments, increasing the cost and time of the imaging. It also requires careful matching of anatomical features across the two data sets. A recent publication compared FDRI obtained at 1.5 T and 4.7 T to predicted iron content from a single T_2* measurement at 4.7 T and concluded that FDRI offered few advantages over measurements at a single field (Uddin et al, 2016). Similarly, in R_2 measurements that used four single-echo acquisitions in a study of 10 healthy adults, we found that the quality of the linear relationship between R_2 and predicted iron values was only slightly more robust for FDRI using 3 T and 1.5 T, than for just the R_2 data obtained at 3 T (Collingwood et al., 2014).

Tissue degeneration, which occurs in AD, causes increased water concentration in the tissue and reduces R_2 (Bondareff et al., 1988; Bartzokis et al., 1994) in opposition to the effect of increased iron concentration. R_2' is the portion of R_2* that is caused by the dephasing of spins due to inhomogeneity of the local field, and is independent of water concentration (Yablonskiy and Haacke, 1994; Jensen and Chandra, 2000). Ordidge and co-workers developed a method for mapping R_2' that reduces the influence of background field variations and used this technique to measure an increase in iron in the SN of Parkinson's disease patients that agrees with post mortem studies, but that had not been observed in R_2 mapping (Ordidge et al., 1994). Susceptibility weighted imaging (SWI) uses a mask of phase information to enhance the contrast in an MR image. The mask can be chosen to highlight particular phases (features), so that the combined magnitude and phase information can be used, for example, to enhance contrast between grey and white matter (Haacke et al., 2004), resolve structures not observable with T_2 or T_1 weighted imaging (Manova et al., 2009) and examine the iron concentration distribution of brain tissue (Yao et al., 2009). SWI alone does not allow for quantification of the magnetic susceptibility of the tissue, and suffers from blooming artefacts (Kim et al., 2017), and developments in post-acquisition processing are enabling quantitative susceptibility mapping (QSM) to become established as a method with excellent sensitivity to iron distribution in tissue in vivo, including for the evaluation of brain iron in AD at clinically-routine field strengths (Langkammer et al., 2012; Kim et al., 2017).

The past decade has seen a significant shift from 1.5 T to 3 T MRI in clinical neuroimaging, and the ongoing move to higher field strengths brings access to increased tissue iron contrast. Early work in primate brain at fields up to 4.7 T suggested that the increased contrast would reach a threshold where the magnetisation of ferritin-bound iron became saturated (Bizzi et al., 1990). Subsequent studies in post-mortem human tissue reported a strong linear relationship was sustained between iron and R_2 at 4.7 T (House et al., 2007), and between iron and R_2* at 7 T post-mortem and *in-vivo* (Yao et al., 2009). More recent post-mortem human tissue analysis supports the use of QSM and R_2* for iron quantification in tissue at 7 T (Hametner et al., 2018; Betts et al., 2016).

We found evidence of a linear dependence of R_2 and R_2* on normalized iron concentration in post-mortem human hippocampus imaged at 14 T (Antharam et al., 2012), using synchrotron XRF (SXRF) maps to evaluate the relationship between iron distribution and these MRI parameters. As relative (rather than absolute) iron concentration was obtained, the magnitude of the field-dependent increase in R_2 and R_2* could not be tested at 14 T to determine if the effect was saturating. The present study, utilizing adjacent tissue blocks to calibrate SXRF iron maps, demonstrates one route to overcome this constraint. In the following sections, we discuss approaches to validate the relationship between clinical imaging parameters (typically MRI) and iron content in tissue.

1.4. Validating iron contrast in MRI data

Reported values for regional brain iron concentrations vary considerably, as evidenced in the landmark review by Haacke and coworkers (Haacke et al., 2005). This likely reflects a combination of natural heterogeneity in the population, and differences attributable to experimental method and study design. The field continues to be constrained by an absence of iron concentration data from large well-described cohorts. When validating MRI methods for sensitivity to iron in the brain, many studies (Bartzokis et al., 2000; Gelman et al., 1999; Persson et al., 2015; Liu et al., 2015; Gao et al., 2017; Collingwood et al., 2014) have used the data published by Hallgren and Sourander in 1958 (Hallgren and Sourander, 1958) as the definitive source of information on regional iron concentration as a function of age in the normal human brain. Comparatively few studies have quantified iron in post-mortem tissue to validate directly the relationship with the MRI parameters. To date, this has been done for R_2 and/or R_2* in studies including post-mortem human brain at fields from < 1 T up to 7 T (Vymazal et al., 1996; House et al., 2008, 2007; Langkammer et al., 2010; Yao et al., 2009; Hametner et al., 2018; Bulk et al., 2018). These studies are critical, as they do not rely on the assumption that the average iron concentration quoted in the literature accurately represents the iron in the individual(s) they are studying. However, post-mortem sample archiving and processing presents additional challenges. It is extremely rare to be in a position to work rapidly and safely with fresh human brain tissue at body temperature, and the majority of samples are either fresh-frozen and archived at −80 °C or stored in an appropriately buffered solution containing a chemical fixative such as formalin to prevent tissue deterioration. Both freezing and chemical fixation impact absolute relaxation parameters in MRI (Vymazal et al., 1996; Thelwall et al., 2006; Antharam et al., 2012), and a further complication of chemical fixation is that it can result in unpredictable levels of mineral transformation and/or metal leaching from the samples (Gellein et al., 2008; Dobson and Grassi, 1996). Some have sought to quantify the impact of iron loss in this context: Hametner and coworkers report 20% loss from in white matter, and 27% loss from putamen, after 24 days in fixative (Hametner et al., 2018). In the present study only fresh-frozen tissues were used, by following previously established protocols to enable sequential imaging analysis by MRI and SXRF (Antharam et al., 2012).

1.4.1. Validation by synchrotron X-ray fluorescence mapping

Synchrotron X-ray fluorescence mapping of biological tissues can be used to produce highly sensitive and specific maps of elemental distributions in tissue at high spatial resolution (Collingwood et al., 2005; Ugarte et al., 2012; Gallagher et al., 2012). The method offers significant advantages over histochemical staining with sensitivity to trace concentrations, specificity for the chemical elements present (e.g. unambiguous distinction between copper and zinc), and no requirement for any labelling or contrast agent. Simultaneous acquisition of the elemental spectra within a pixel, enabling a full analysis of the chemical elements present within the energy range of the instrument used, can be performed for a single tissue section (Collingwood and Adams, 2017). A number of studies have now sought to correlate MRI maps (either contrast-weighted or parametric) with post-mortem tissue sections (either chemically-fixed or fresh-frozen) analysed by SXRF, for example (Hopp et al., 2010; Antharam et al., 2012; House et al., 2014). This has enabled direct comparison of the spatial distribution of iron with MRI data. One approach is to use rapid scanning SXRF, where this is calibrated with metal foils to compare iron distribution with SWI obtained at clinical spatial resolutions at 1.5 T, evidencing a linear relationship between SWI and iron concentration in 1 mm thick fixed brain tissue (McCrea et al., 2008; Hopp et al., 2010). This approach offers the advantage of being able to cover a spatial area encompassing multiple regions of the human brain (which is not normally viable with the micro-focussed SXRF beam). However, it requires chemically fixed

samples or a cryo-environment that can accommodate large area rastering of a frozen tissue sample, and the calibration with metal foils is constrained by matrix differences between the foils and the tissues.

In the present study we incorporate a method previously developed by our group to obtain MRI and SXRF data from fresh-frozen human hippocampus at high spatial resolution (60 μm in-plane) at 14 T (Antharam et al., 2012). Here, equivalent measurements are performed for a series of brain regions from AD and healthy control cases, with the MRI analysis performed at 9.4 T. The additional step of calibrating the iron SXRF signal intensity using high precision bulk analysis of representative adjacent tissue samples permits determination of the dependence of R_2, R_2* and R_2' as a function of iron concentration, and to test the dependence of these relationships at a field exceeding 7 T.

2. Materials and methods

2.1. Samples

All tissues used in this study were from donated human brain provided by the Canadian Brain Tissue Bank and studied under ethical approval 07/MRE08/12. Tissue samples from two control (males, aged 76 and 78) and three confirmed AD cases (male, aged 73, females, aged 75 and 95) were investigated with samples taken from regions of the basal ganglia: primarily the caudate nucleus (CN), putamen (Pu), globus pallidus (GP) and substantia nigra (SN). Based on prior meta-analyses, the Pu is most likely to show increased iron concentration in AD. Where additional adjacent structures were included in MRI samples, such as the anterior limb of the internal capsule which is adjacent to the caudate nucleus, these have been segmented and included in the analysis. Case details and the samples measured for each case are given in Table 1; all samples had been stored at −80 °C. Each SXRF map took upwards of 6 h to collect, and as synchrotron beam time is limited only one section was imaged for each region per individual.

The experimental strategy was to cut pairs of blocks (adjacent tissue) from within each anatomical structure. Examples of the frozen blocks, prior to dissection, are given in Fig. 1. The first block (A) was used for MRI quantitative relaxometry and SXRF mapping, and was cut to fit inside a 20 mm diameter NMR tube. Dissection included tissue from surrounding structures to aid anatomical orientation. Block B, for iron quantification in this study by ICP-MS (where GFAAS might be used as an alternative), was selected to include only the target structure. The quantitative iron information from block B was used to calibrate the iron distribution maps from block A. As the SN anatomy is difficult to define with precision in unstained tissue, the cerebral crus was included in both samples. Where available sample volume or asymmetry prevented block B from being representative of block A (in the present study this was the case for the GP samples), the relationship between absolute iron content and SXRF signal was used to calibrate the GP images as described in section 3.1.

Before dissection, samples were warmed from archive conditions at −80 °C to a few degrees below 0 °C. They were then dissected in the temperature-controlled environment of a cryomicrotome. All sample handling was performed using acid-washed non-ferrous surfaces and tools, including ceramic blades for dissection to avoid metal particulate contamination.

2.2. Bulk iron quantification

There are several methods by which the concentration of a chemical element may be determined with great accuracy. Here we include data from two example methods that are suitable for iron determination in brain tissue. The first is inductively coupled plasma mass spectrometry (ICP-MS), here used to determine iron concentration in block B for the CN and Pu samples, and the second is graphite furnace atomic absorption spectroscopy (GFAAS) used for the equivalent blocks of SN tissue. Each method presents its own challenges, and is described in detail in the supporting references. The SN block B samples were analysed by GFAAS (instead of ICP-MS) as they were measured in the context of a study parallel to the main MRI-SXRF investigation (Visanji et al., 2013; Finnegan, 2013). Ideally the same technique and instrument would have been used to measure all the bulk iron concentrations, but the sensitivity and accuracy of these methods were sufficient (as discussed in Section 3.3.1 Method Assumptions), that here it was appropriate to pool the data for the purpose of the regression analysis.

2.2.1. Inductively coupled plasma mass spectrometry (ICP-MS)

Iron concentration was determined for the individual tissue blocks by ICP-MS, using the ICP-MS Agilent technologies 7500 series as previously described (Finnegan, 2013). Briefly, the samples were freeze dried and transferred into acid washed 3 ml capacity glass Wheaton v-vials for digestion in 72% double distilled nitric acid. A total of 1.5 ml of nitric acid was added to the vials in aliquots of 0.5 ml and then the samples were dissolved in a 55 °C oven for approximately 20 h. Each sample was diluted to 1:100 using Milli-Q® grade water (18.2 MΩ). Blanks consisting of a 1:100 dilution of the 72% nitric acid used for digestion were run after every 4 samples and consistently produced an iron concentration below the detection limit of the spectrometer.

2.2.2. Graphite furnace atomic absorption spectroscopy (GFAAS)

GFAAS was used to measure the iron concentration of the substantia nigra samples as previously described (Visanji et al., 2013). Briefly, a Mars Xpress microwave was used to digest the tissue samples in 1 ml HNO_3 and 1 ml H_2O_2 using a CEM-provided Tissue Xpress program. Ultrapure water (3 ml) was added and the digest volume corrected for venting. The iron concentration was determined from 800-fold dilutions using a hollow-cathode lamp at 30 mA and atomic absorption measured at 248.3 nm.

2.3. MRI relaxometry

MRI was performed using a Bruker micro-imaging MicWB40 probe and a 400 MHz vertical wide bore Bruker spectrometer. Each tissue sample, initially frozen, was suspended in Fluorinert in a standard glass NMR tube (Antharam et al., 2012; Finnegan, 2013). Samples were warmed to and maintained at 2 °C throughout the image acquisition, and re-frozen directly afterwards.

Before imaging, the probe was tuned and matched to the ^{1}H channel. TopSpin was used to manually shim the gradients and achieve a smooth free induction decay (FID) of maximum size, and a symmetrical, as narrow as possible water peak with a full-width-half-maximum (FWHM) of < 60 Hz. The Bruker relaxometry scans from Paravision 4.0 were used: a multi-spin, multi-echo (MSME) sequence to map T_2 and a multi-gradient echo sequence (MGE) to map T_2*. The number of averages, slice thickness and echo times were optimised to

Table 1
Case details for the samples used in this project. The sex and age of each individual at death is given. For the control cases the cause of death is stated. For the Alzheimer's Disease (AD) cases the Braak stage of the disease pathology is given (Braak and Braak, 1991). The Case References are not linked with the original numbers issued by the brain bank, they are the identifiers corresponding to the supporting analytical information for this study (Finnegan, 2013).

Case Reference	Brain regions	Sex	Age	Pathology
C2	Caudate nucleus Substantia nigra	M	78	Lung cancer
C3	Putamen Globus pallidus	M	76	Cardiac infarction
AD1	Caudate nucleus	M	73	Braak vi
AD2	Globus pallidus Substantia nigra	F	75	Braak vi
AD3	Putamen	F	98	Braak v

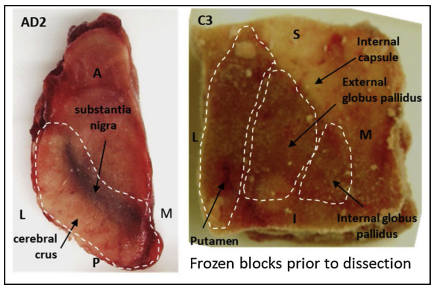

Fig. 1. Examples of the tissue blocks from the Canadian Brain Tissue Bank prior to dissection for imaging and bulk analysis, with anatomical orientations indicated (A/P: anterior/posterior; L/M: lateral/medial; S/I: superior/inferior).

give a good signal to noise ratio for even the rapid decays shown in tissue with a high iron content. The scan parameters are summarized in Table 2. Careful shimming was required to ensure optimum signal from the region of interest.

Scan geometry and workflow was similar to that described previously (Collingwood et al., 2008; Antharam et al., 2012). Low resolution scans were used first to measure the majority of the tissue sample volume. Data from these scans were then used to choose the part of the tissue to image at high resolution in order to obtain the best representation of the brain region of interest. Low resolution data were collected by three sets of scans with interleaving geometry. Two sets of interleaved high resolution scans were used to map a 7 mm thick volume of tissue.

The decays were fitted to create T_2 and T_2* maps using the open source software Image *J* with the plugins 'Bruker Opener' and 'MRI Processor'. The MRI Processor plugin was used to fit the T_2 and T_2* decays for the voxels in each respective dataset to mono-exponential Equation 1 using a Levenberg-Marquardt algorithm.

$$y = A + Ce^{\left(-\frac{t}{T_2}\right)} \quad (1)$$

where the constant A takes into account a finite background. The reciprocal of the T_2 and T_2*images provided the R_2 and R_2* images respectively.

2.4. Histology

The tissue blocks that had been initially imaged by MRI microscopy were subsequently mounted to permit cryosectioning in the same plane as the virtual slices in the MRI acquisition. Sectioning was performed in a Leica cryomicrotome (Jung CM3000) at an angle of 10 ° and a nominal thickness of 30 µm. Sections were cut with an acid-washed sapphire blade to avoid metal particulate contamination from the stainless steel blades used in routine sectioning. Serial sectioning was performed, with sections for SXRF analysis mounted on spectroscopically clean quartz slides, and adjacent sections mounted on glass histology slides and stained with a standard haematoxylin and Congo red protocol (Finnegan, 2013). Only haematoxylin staining was used for the quartz sections after SXRF imaging, and initial fixation required in ice-cold ethanol (Gallagher et al., 2012), as extended imaging can render the organic material in the tissue section very fragile. This, combined with the absence of an adherent coating on the slides (to avoid a potential source of contamination) resulted in development of a staining protocol using a liquid blocking PAP pen so that sections could be individually stained with the slide maintained in a horizontal position (Finnegan, 2013).

2.5. Synchrotron X-ray fluorescence microfocus imaging

SXRF mapping of elemental metal ion distributions was performed at the microfocus beamline I18 at Diamond Light Source, following previously described protocols (Antharam et al., 2012; Gallagher et al., 2012). Briefly, a 10 keV primary beam was used to excite fluorescence from the unstained tissue section, with the incident flux I_0 limited to avoid saturation of the nine element Ge detector. The quartz-mounted sections were protected during measurement under an X-ray transparent Kapton film, and mounted with the imaging plane at 45° to I_0 and the detector at 90° to I_0. The quartz has a spatially uniform fluorescence signal making it straightforward to subtract it as a contribution to background noise in the acquired spectrum. It is also very rigid which is an advantage during SXRF measurement, and tolerates exposure typically required for supporting histological analysis. However, as it blocks transmission of much of the hard X-ray beam, it is helpful to use a transparent support film for samples where analyte concentrations approaches the detection limits at the beamline. This permits a pair of detectors to be positioned, each at 90° to I_0, to maximise the solid angle over which fluorescence from the sample is acquired (Mosselmans et al., 2009; Collingwood and Adams, 2017).

To enable correlation with the MRI R_2 and R_2* maps, tissue sections corresponding to the higher resolution MRI images were mapped over the full slice area of interest, and the adjacent (glass-mounted) section which had been histochemically stained was used to confirm the area required. Rastering in the focused X-ray beam provided in-plane 60 × 60 µm pixels where the X-ray beam sampled the full depth of the tissue section; the acquisition rate corresponded to a 1 s dwell per point in the image matrix. A full SXRF spectrum was acquired for each pixel, and these spectra were processed using the open source software PyMCA (Solé et al., 2007), which was used to fit all detectable elements within the accessible energy range and compute the signal intensity from the primary fluorescence peak for each element. The spectrum in each pixel was normalised to the corresponding I_0 value to remove the effect of changing incident flux over the period of measurement, and the signal from a blank area on each quartz slide was used to correct for any difference in sample-detector distance. The resulting spectra were processed to produce precise maps of the normalized concentration distribution of the primary transition metals present in each tissue section (Finnegan, 2013).

2.6. Correlating SXRF and MRI images

The SXRF iron maps acquired from the 30 µm thick sections were correlated with the MRI microscopy data obtained with slightly lower (86 × 86 µm) in-plane spatial resolution and 150 µm thick virtual slices. By taking thinner sections for SXRF, this ensured that several serial cryosections could be well-matched to each virtual MRI slice. Image J was used to rotate the images from the different modalities to achieve a common orientation, and this was achieved by comparing

Table 2
Scan parameters for MRI relaxometry at 9.4 T for the low-spatial-resolution and high-spatial-resolution imaging of the tissue blocks. MSME = multi-slice multi-echo; MGE = multi-gradient-echo. T_R = repetition time. T_E = echo spacing.

Measurement: Parameter:	T_2 (low res)	T_2 (high res)	T_2* (low res)	T_2* (high res)
Resolution (µm)	195 × 195	86 × 86	195 × 195	86 × 86
Slice thickness (µm)	250	150	250	150
Scan sequence	MSME	MSME	MGE	MGE
Attenuators: A0, A1	16, 3	16, 3	22.5, -	22.5, -
T_R (ms)	7000	7000	3500	4000
T_E [T first echo] (ms)	7.248	9.783	6.0 [3.08]	6.0 [3.90]
No. of echoes	16	16	16	16
No. of averages	2	4	2	4
Scan time	22m24s	1h29m36s	11m12s	51m12s

anatomical features in the SXRF and MRI images, and microscope camera images of the stained and unstained SXRF section and the adjacent histochemically stained tissue sections. Factors that occasionally compromised correlation of the images included any misalignment of the block for sectioning, slight deformation of the tissue by the Fluorinert during MRI analysis, or sectioning artefacts such as cracks or folds in the unembedded tissue. This approach, in combination with the careful preservation of tissue architecture, made manual correlation viable at the level of individual brain regions.

2.7. Statistical analysis

SSPS Statistics Version 21 was used to carry out linear regression analysis, creating simple linear regression models to describe the relationship between the measured MRI parameters (dependent variables: R_2, R_2*, R_2') and the predictor (independent variable: iron). The correlation coefficient, r, described the linear relationship, and the goodness of fit was reported as r-squared. SSPS was used to calculate a p-value for the predictor in each case, testing for violation of the null hypothesis, that there was no dependence of each measured MRI parameter (R_2, R_2*, R_2') on iron, at a significance level of $p < 0.05$.

3. Results and discussion

Examples of matched SXRF and R_2 images, showing the approximate boundaries for segmentation, are given in Fig. 2, and the structures segmented for analysis are detailed in Table 3; those structures adjacent to the main regions of interest were segmented where possible. The correspondence between the SXRF and MRI images permitted determination of the relationship between the MR relaxation values and the associated iron concentration in each region. One section included elevated iron directly associated with a major blood vessel; the affected region was excluded from the analysis.

3.1. Calibration of SXRF maps

The iron concentration represented by one unit of normalised SXRF signal intensity was calculated for each sample by dividing the mean SXRF signal for that region by the mean bulk iron concentration measured in the adjacent tissue block. The mean and standard deviation for each sample was calculated and then averaged for all samples giving a mean of 7.3 ± 12% μg Fe / g hydrated tissue for every unit of normalised SXRF intensity.

3.2. The dependence of R_2, R_2*, and R_2' on iron concentration

Fig. 3 shows the mean iron concentration versus R_2 and R_2* for each of the main segmented regions from the correlated SXRF and MRI image data, for the pooled data, and separately for the grey matter (GM) and white matter (WM). The prediction bands show the range within which 95% of any new measurements would be expected to fall.

The linear regression analysis described in Fig. 3, and the results of this analysis set out in Table 4, produced the following equations relating R_2 and R_2* (s^{-1}) to iron concentration ([Fe] in μg/g, with an

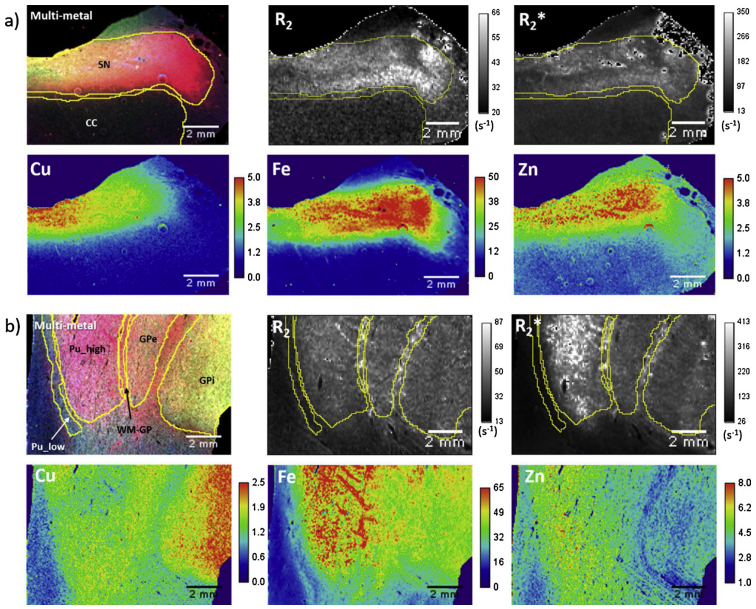

Fig. 2. Matched and segmented SXRF transition metal maps and MRI R_2 and R_2* maps from a) the substantia nigra and b) the globus pallidus regions in case AD2. During segmentation the intensity maps for the high abundance elements as well as the individual transition metals, were used to aid boundary identification. Here, RBG images are shown to illustrate how there are distinct distributions of Fe, Zn, and Cu at this level of structural organisation. In the multi-metal maps these are represented as Fe (red), Cu (green), Zn (blue). The accompanying scale bars show the computed R_2 and R_2* values for the MRI maps, and the temperature scale bars for the transition metal maps show the normalized fluorescence intensity. Labels for the segmented regions are defined in Table 3.

Table 3
Summary of the regions segmented in the SXRF and MRI R_2 maps.

Region	Main Structures	Additional Structures
Caudate Nucleus	caudate nucleus (CN); anterior limb of the internal capsule (AIC-CN); white matter medial to the caudate nucleus (WM-CN)	n/a
Putamen	putamen with high iron concentration (Pu_high); putamen with low iron concentration (Pu_low); white matter lateral to the putamen (Pu-WM)	Control sample only: anterior limb of the internal capsule (AIC-Pu)
Globus Pallidus	external globus pallidus (GPe); putamen with high iron concentration (Pu_high-GP); lamina of white matter separating the external globus pallidus and putamen (WM-GP)	Control sample only: internal capsule (IC); internal globus pallidus (GPi) AD sample only: putamen with low iron concentration (Pu_low-GP)
Substantia Nigra	substantia nigra (SN); cerebral crus (CC)	n/a

estimated experimental uncertainty of ± 12%:

$$R_2 = 0.072\,[Fe] + 20 \quad (2)$$

$$R_2^* = 0.34\,[Fe] + 37 \quad (3)$$

The linear relationship proved robust, regardless of whether the data were grouped by disease, or tissue type (grey or white matter). Furthermore, the slope and intercept of the fitted lines agree within error for each model for both R_2 and R_2*. In a prior study of the hippocampus (Antharam et al., 2012), we previously demonstrated that areas of increased iron concentration corresponded to increased R_2 and R_2* in matched MRI and SXRF maps at 14.1 T, but here the relationship was not quantified. Although a strong linear relationship has previously been shown between iron and R_2* at lower fields (between 1.5 T and 7 T (Yao et al., 2009)), this present study provides, to the best of our knowledge, the first demonstration of the linear relationship between iron concentration and R_2 and R_2* in human brain tissue at 9.4 T and the first demonstration, with quantified iron values, above 7 T.

In clinical MRI imaging the different relaxation rates of grey and white matter tissues provide contrast in the image and this is attributed to their differing fat and water content in addition to iron content. However, in this study the agreement of the linear relationship between iron and R_2 and R_2* for both grey and white matter suggests that at 9.4 T, iron is the most significant factor in determining the value of R_2 and R_2*. The r-squared values obtained in the regression analysis indicate that > 65% of variation in the data is accounted for by this linear relationship. The evidence for this has not always previously been apparent in studies including white matter (House et al., 2008), and here the inclusion of white matter regions with higher iron levels than typically observed in cortical regions may be a factor. The linear relationship we report at 9.4 T is not observed below a threshold of 100 μg/g, and this observation is in keeping with prior work at 4.7 T reporting a threshold of 55 μg/g for R_2 (House et al., 2007). We consider the relationship between R_2, iron, and field strength in the following section.

The effect of iron on R_2 increases linearly with field strength (B, Tesla), as formerly described empirically by Vymazal and co-workers (Eq. (4)). They derived this from iron and R_2 data measured at multiple field strengths (0.05 to 1.5 T) at 37 °C in primate brain tissue (Vymazal et al., 1996).

$$\text{slope} = 14.1 + 6.2B\ s^{-1}/mg/g \quad (4)$$

When Eq. (4) is solved for an imaging field of 9.4 T (400 MHz), it gives a slope of 0.0724 s^{-1}/μg/g. This compares extremely well with the gradient of Eq. (2) above, 0.072 ± 0.008 s^{-1}/μg/g, with no evidence of saturation of the field dependent R_2 increase at 9.4 T.

House and co-workers also compared their observations at 4.7 T to Vymazal's prediction and noted good agreement after accounting for differences in experiment design (House et al., 2007). Therefore, while the agreement we observe between our findings for R_2 and Vymazal's prediction is excellent, it is important to note differences in experiment design that may contribute experimental uncertainty in addition to ± 12% arising from calibration of the iron images with the SXRF data:

1 R_2 may be increased in tissue which has been frozen and defrosted (Vymazal et al., 1996), and the samples used to determine Eq. (4) were fresh compared with the defrosted post-mortem human brain used in the present study.
2 R_2 has been shown to decrease with temperature (Kamman et al., 1988) and Eq. (4) is for tissue at 37 °C compared for the present study performed at 2 °C.
3 The inter-echo time used in the sequence to obtain R_2 may influence the effect of iron content on R_2 (Vymazal et al., 1996).

The susceptibility related relaxation rate R_2* is generally understood to represent the combination of the transverse relaxation rate R_2 and the field inhomogeneity induced R_2'. R_2* is reportedly more sensitive to changes in tissue iron concentration than R_2 (Langkammer et al., 2010), and this is reflected in the present results (Fig. 3, Eq. (3)). The approximate mean R_2' was subsequently calculated for each segmented region, using Eq. (5):

$$R_2' = R_2^* - R_2 \quad (5)$$

and plotted against iron concentration as shown in Fig. 4 with the results of linear regression analysis for the combined and separated control and AD data, confirming a strong linear dependence of R_2', consistent with the earlier results for R_2 and R_2*. We note that the gradient for this relationship for R_2' is 3.75 times larger than the gradient for R_2 (Fig. 3, Eq. (2)). These gradients have been reported approximately equivalent at 3 T (Gelman et al., 1999), so these new data at 9.4 T indicate that not only is there a B-field-dependent contribution to the relationship between of R_2 with iron (Vymazal et al., 1996); there is also a field-dependent contribution arising from the dependence of R_2' on iron concentration. It is reasonable to assume a linear relationship between the magnitude of the field B and R_2', as this has previously been shown for the field-dependence of R_2* (Yao et al., 2009). The present result obtained at 9.4 T and the prior result from Gelman and co-workers at 3 T can then be used to compute the gradient (slope) for the dependence of R_2' on iron concentration at a particular imaging field B as follows:

$$\text{slope} = -51.1 + 34.4B\ s^{-1}/mg/g \quad (6)$$

It is long-postulated that MRI-detectable changes in iron concentration may aid diagnosis of neurodegenerative disorders, including AD (Antharam et al., 2012; Haacke et al., 2005; Langkammer et al., 2014; Bartzokis et al., 1994). In the present study, despite the strong linear relationships established with a very small sample size, the

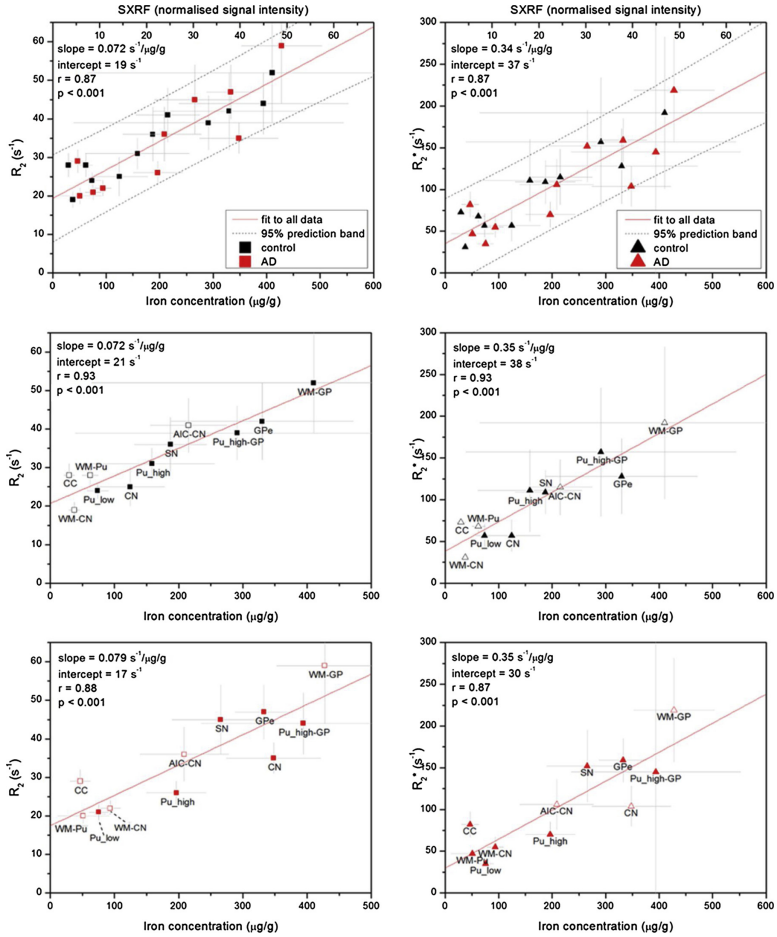

Fig. 3. Iron concentration versus R_2 and R_2* at 9.4 T. Results from linear regression analysis are shown in graphs a) and b) for the dependence of R_2 and R_2* respectively on iron concentration in the pooled control and AD data. The light grey error bars represent the standard deviation within each the segmented region, and are primarily a measure of signal heterogeneity rather than experimental uncertainty. The upper x-axis shows normalised SXRF iron signal intensity and the lower x-axis shows the calibrated iron concentration. The prediction bands show the region in which 95% of any new measurements would be predicted to fall. Graphs c) and d) show the dependence of R_2 and R_2* respectively on iron for control GM (filled symbol) and WM (open symbol) samples; e) and f) show the equivalent data from the AD cases. The results support a linear relationship, with $r > 0.85$ in all examples.

indications are that a substantial increase in tissue iron would be required to be reliably detected as a deviation from normal levels observed in cross-sectional studies, even at the highest clinically-available fields. The evaluation of multiple regions, and of more than one marker of iron status, offers scope to discriminate between disease states even in small cohorts (Visanji et al., 2013). Given the heterogeneity in normal regional iron concentration, it is likely that longitudinal imaging to track change in individuals may provide the greatest sensitivity and specificity to detect changes in the chemistry of the brain.

3.3. Method assumptions

3.3.1. ICP-MS and GFAAS determination of iron concentration are equivalent

As noted in Section 2.2, practical constraints in the present study resulted in most of the bulk analyses being performed using ICP-MS,

Table 4
Results of linear regression analysis of iron versus R_2 or R_2*. a) The linear relationship between iron and R_2. b) The linear relationship between iron and R_2*. The relationship is examined for the control and AD data separately and with both sets of data pooled. Data from grey and white matter regions is also examined separately. In all cases there a statistically significant, strong linear relationship. The r-squared values show that at least 67% of the variation in the data is explained by the linear relationship. All R_2 models show a slope and intercept which agree within error. The same is true for all of the fits to the R_2* data. *p < 0.05; **p < 0.01; ***p < 0.001.

a) Iron vs. R_2

Tissue regions	Disease	n	Slope (s^{-1}/(μg/g))	Intercept (s^{-1})	r	r^2	p
All	pooled	22	0.072 ± 0.008	19 ± 2	0.87	0.75	***
	Control	11	0.072 ± 0.009	21 ± 2	0.93	0.87	***
	AD	11	0.079 ± 0.012	17 ± 4	0.88	0.77	***
GM	Control	6	0.072 ± 0.011	19 ± 2	0.96	0.92	**
	AD	6	0.076 ± 0.027	16 ± 8	0.82	0.67	*
WM	Control	5	0.076 ± 0.013	22 ± 3	0.96	0.91	*
	AD	5	0.094 ± 0.016	18 ± 3	0.96	0.92	**

b) Iron vs. R_2*

Tissue regions	Disease	n	Slope (s^{-1}/(μg/g))	Intercept (s^{-1})	r	r^2	p
All	pooled	22	0.34 ± 0.04	37 ± 9	0.87	0.75	***
	Control	11	0.35 ± 0.05	38 ± 10	0.93	0.87	***
	AD	11	0.35 ± 0.07	30 ± 17	0.87	0.75	***
GM	Control	6	0.35 ± 0.10	35 ± 21	0.87	0.76	*
	AD	6	0.35 ± 0.12	16 ± 35	0.82	0.7	*
WM	Control	5	0.36 ± 0.06	41 ± 120	0.97	0.93	**
	AD	5	0.42 ± 0.07	33 ± 150	0.96	0.92	**

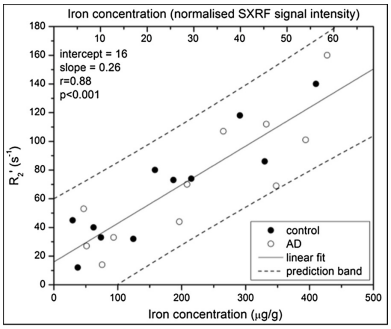

Disease	n	Slope (s^{-1}/(μg/g))	Intercept (s^{-1})	r	r^2	P
pooled	22	0.27 ± 0.03	16 ± 7	0.88	0.77	***
Control	11	0.28 ± 0.04	18 ± 9	0.92	0.84	***
AD	11	0.27 ± 0.05	12 ± 14	0.86	0.74	**

Fig. 4. Iron concentration versus approximate R_2'. The x-axis at the top of the graphs shows the normalised iron SXRF signal intensity and the lower axis shows the calibrated iron concentration. Simple linear regression analysis shows a strong (r > 0.85) linear relationship between iron concentration and R_2'. The prediction bands show where 95% of any new measurements are predicted to fall. The slope and the intercept of the fit agree within error for both the pooled and separated control and AD data, representing 22 samples from two control and three Alzheimer's disease cases, encompassing the regions detailed in Table 3. **p < 0.01; ***p < 0.001.

with the exception of the SN blocks which were analysed by GFAAS. In order for the equivalence of these measures to be a justified assumption, careful calibration and quantification were performed for both methods (Finnegan, 2013; Visanji et al., 2013). In each case, signal is obtained from the analyte following dissolution of the complete tissue block, rather than selectively sampling within a volume of interest, and there is no reason to expect any deviation in accuracy given that both processes included careful calibration. An extensive review of post-mortem iron quantification by Haacke and colleagues (Haacke et al., 2005), which is summarized in Table 3.2 in (Finnegan, 2013), includes reported values for these same regions of the brain obtained by both ICP-MS and atomic absorption spectroscopy (AAS). There is no systematic difference in the reported values as a function of analytical technique: in some cases AAS returns higher concentrations, in other cases ICP-MS is higher. We suggest that the greatest source of experimental uncertainty will be in the method of dissection, and that having a single team perform all the dissections in a consistent manner (as was the case for the present study) is a critical factor in minimising experimental uncertainty.

3.3.2. Adjacent tissue blocks for bulk and SXRF analysis have equivalent iron concentrations

The method of calibrating the SXRF maps assumes that the tissue samples measured with ICP-MS or GFAAS and the corresponding ROIs mapped by SXRF have an equal concentration of iron. The dissection of each block was carefully planned in order to best achieve this, for example, the substantia nigra shown in Fig. 1 (AD2) was bisected parallel to the plane of the image to obtain SNpc and SNpr in both blocks. Tissue samples were approximately 1 cm thick, with the centre of adjacent samples (for bulk iron concentration and SXRF) approximately 0.5–1 cm apart. The validity of the assumption of equivalent iron concentrations was tested for relative levels, not absolute concentrations, by calculating the ratio of AD to control iron concentration for the bulk tissue iron measurements and the mean relative iron concentration measured by SXRF mapping. The ratios were in good agreement [CN: bulk tissue iron 3.04 versus SXRF 2.80 (8% difference); Pu: bulk tissue iron 1.28 versus SXRF 1.24 (3% difference); SN: bulk tissue 1.50 versus SXRF 1.41 (6% difference)]. Agreement of these ratios within 10% indicates that the relative iron concentrations are well-preserved across the tissue volumes sampled.

3.3.3. SXRF and MRI slices can be correlated despite different thicknesses

The difference in SXRF (30 μm) and MRI (150 μm) slice thicknesses, despite similar in-plane resolution, means that the SXRF maps account for iron signal from approximately 20% of the corresponding MRI slice volume. The properties of the tissue precluded cutting significantly thicker sections for SXRF, and the signal recovery in the MRI would have been compromised if thinner slices had been obtained. Cutting up to five sections for SXRF from within each MRI slice accommodated minor misalignment of the tissue block, and provided one or more adjacent sections for staining to confirm tissue architecture. Although this means the matching between the SXRF and MRI is imperfect, the method did allow examination of the relationship between iron, R_2 and R_2^* in unfixed samples at higher spatial resolution than in most prior work, with the anatomical structures of interest substantially unaltered over the 150 μm length-scale. The spatial resolution made it viable to explore contrast variation within anatomically defined regions, reducing the need to attempt bulk dissection within subfields. Indeed the difficulty in precisely excising brain structures has been commented on in the literature (House et al., 2007). The scope for pixel-by-pixel correlation in the ROIs was explored for these datasets, incorporating a protocol to rescale the MRI data relative to the SXRF data to bring them into a shared matrix using Matlab. In practice this approach did not provide such a robust outcome as the method applied in the current study, which takes the average signal intensity value from segmented ROIs where each sampled area includes thousands of pixels. This approach is more robust and pragmatic in studies where sections are imperfectly matched, as it is less prone to distortions arising from the experimental uncertainties.

3.3.4. Approaches to quantifying tissue iron distribution

Evaluation of total iron concentration in adjacent tissue blocks was used here as a pragmatic method to estimate brain iron concentration distribution in the SXRF iron maps. This was successful, with an experimental uncertainty ± 12% that is equivalent to or is better than the accuracy typically achieved with SXRF reference foils for tissue samples due to issues with matrix matching (Collingwood and Davidson, 2014). It is technically possible to achieve fully quantitative SXRF mapping of elemental distributions where the phase contrast information can be measured to perform the necessary mass correction (Kosior et al., 2012), but this is not yet routinely available at SXRF beamlines. The rationale for using SXRF here is that it is non-destructive, has a sensitivity that increases with spatial resolution as it is a flux- (rather than mass-) limited technique, and permits simultaneous acquisition of a rich multi-element spectral image (Collingwood and Adams, 2017). There are several excellent alternative beam methods (which by contrast to SXRF are destructive), including laser ablation ICP-MS imaging and others reviewed elsewhere (Collingwood and Adams, 2017); for these alternatives the concentration detection limit decreases as the spatial resolution of the imaging is increased.

We observed distinct variations in iron distribution both between and within the primary regions studied. This marked heterogeneity of iron distribution within the sub-fields of the brain may in part account for wide variations in the experimental reports of healthy adult brain levels (Haacke et al., 2005), along with variations due to the analytical approach used.

In the study from Frisoni and co-workers: *'Imaging markers for Alzheimer disease: Which vs how'*, a large number of candidate imaging markers for AD were evaluated, including volumetric MRI. They concluded that the way in which an imaging marker is measured is at least as important to its success as the marker itself (Frisoni et al., 2013). This would certainly apply to the measurement of tissue iron concentration by MRI.

4. Conclusion

A linear dependence of R_2, R_2* and R_2' on iron concentration was observed at 9.4 T, independent of disease state or tissue type. The gradient of the relationship between iron and R_2 agrees with the predicted relationship at 9.4 T, with no indication of saturation of the field dependent R_2 increase. Iron is the focus of the present study as it offers strong scope for clinical evaluation, but the approach may be used more widely to evaluate other elements in Alzheimer's and related disorders, and to test their relative impact on candidate imaging parameters including quantitative susceptibility mapping and other clinically applicable modalities.

Declarations of interest

None.

Ethical considerations

The work described involving human tissue has been carried out in accordance with The Code of Ethics of the World Medical Association (Declaration of Helsinki). The work in this project was done under multi regional ethics committee (MREC) approval for the project 'Metal-ion accumulation in neurodegenerative disease' (REC ref: 07/MRE08/12, Collingwood).

Data sharing

The source information for the data is available at http://wrap.warwick.ac.uk/60293/

Acknowledgements

This study received support from the Alzheimer's Society (PhD studentship: MEF, JFC, JD), and the EPSRC (grants EP/K035193/1 and EP/M028186/1). This work was carried out with the support of Diamond Light Source, under allocations SP1125 and SP7453. Our thanks to Drs Paul Quinn and Kalotina Geraki for assistance at I18. The development work for the MRI scans was performed in the McKnight Brain Institute at the National High Magnetic Field Laboratory's AMRIS Facility, which is supported by National Science Foundation Cooperative Agreement No. DMR-1157490 and the State of Florida. The MRI probe used in this research was obtained through the Birmingham Science City Translational Medicine: Experimental Medicine Network of Excellence project, with support from Advantage West Midlands (AWM).

References

Akatsu, H., Hori, A., Yamamoto, T., Yoshida, M., Mimuro, M., Hashizume, Y., Tooyama, I., Yezdimer, E.M., 2012. 'Transition metal abnormalities in progressive dementias. Biometals 25, 337–350.

Antharam, V., Collingwood, J.F., Bullivant, J.P., Davidson, M.R., Chandra, S., Mikhaylova, A., Finnegan, M.E., Batich, C., Forder, J.R., Dobson, J., 2012. High field magnetic resonance microscopy of the human hippocampus in Alzheimer's disease: quantitative imaging and correlation with iron. Neuroimage 59, 1249–1260.

Bartzokis, G., Tishler, T.A., 2000. MRI evaluation of basal ganglia ferritin iron and neurotoxicity in Alzheimer's and Huntingon's disease. Cell. Mol. Biol. (Noisy-le-grand) 46, 821–833.

Bartzokis, G., Aravagiri, M., Oldendorf, W.H., Mintz, J., Marder, S.R., 1993. Field-Dependent transverse relaxation rate increase may be a specific measure of tissue iron stores. Magn. Reson. Med. 29, 459–464.

Bartzokis, G., Sultzer, D., Mintz, J., Holt, L.E., Marx, P., Phelan, C.K., Marder, S.R., 1994. In vivo evaluation of brain iron in Alzheimer's disease and normal subjects using MRI. Biol. Psychiatry 35, 480–487.

Bartzokis, George, Sultzer, David, Cummings, Jeffrey, Holt, Lori E., Hance, DarwoodB., Henderson, Victor W., Mintz, Jim, 2000. In vivo evaluation of brain iron in alzheimer disease using magnetic resonance imaging. Achiv. Gen. Psychiatry 57, 47–53.

Bartzokis, G., Tishler, T.A., Shin, I.S., Lu, P.H., Cummings, J.L., 2004. Brain ferritin iron as a risk factor for age at onset in neurodegenerative diseases. Redox-Active Metals Neurol. Disord. 1012, 224–236.

Betts, M.J., Acosta-Cabronero, J., Cardenas-Blanco, A., Nestor, P.J., Duzel, E., 2016. High-resolution characterisation of the aging brain using simultaneous quantitative susceptibility mapping (QSM) and R2* measurements at 7T. Neuroimage 138, 43–63.

Bizzi, A., Brooks, R.A., Brunetti, A., Hill, J.M., Alger, J.R., Miletich, R.S., Francavilla, T.L., Di Chiro, G., 1990. Role of iron and ferritin in MR imaging of the brain: a study in primates at different field strengths. Radiology 177, 59–65.
Bondareff, W., Raval, J., Colletti, P.M., Hauser, D.L., 1988. Quantitative magnetic resonance imaging and the severity of dementia in Alzheimer's disease. Am. J. Psychiatry 145, 853–856.
Braak, H., Braak, E., 1991. Neuropathological stageing of Alzheimer-related changes. Acta Neuropathol. 82, 239–259.
Bulk, M., Abdelmoula, W.M., Nabuurs, R.J.A., van der Graaf, L.M., Mulders, C.W.H., Mulder, A.A., Jost, C.R., Koster, A.J., van Buchem, M.A., Natte, R., Dijkstra, J., van der Weerd, L., 2018. Postmortem MRI and histology demonstrate differential iron accumulation and cortical myelin organization in early- and late-onset Alzheimer's disease. Neurobiol. Aging 62, 231–242.
Collingwood, Joanna F., Adams, Freddy, 2017. Chemical imaging analysis of the brain with X-ray methods. Spectrochim. Acta Part B At. Spectrosc. 130, 101–118.
Collingwood, J.F., Davidson, M.R., 2014. The role of iron in neurodegenerative disorders: insights and opportunities with synchrotron light. Front. Pharmacol. 5, 191.
Collingwood, J.F., Mikhaylova, A., Davidson, M., Batich, C., Steirt, W.J., Terry, J., Dobson, J., 2005. *In situ* characterisation and mapping of iron compounds in Alzheimer's disease tissue. J. Alzheimer's Dis. 7, 267–272.
Collingwood, J.F., Chandra, S., Davidson, M., Mikhaylova, A., Eksin, T., Dobson, J., Forder, J., Batich, C., 2008. High-resolution magnetic resonance imaging to quantify relaxation parameters in Alzheimer's brain tissue. Alzheimers Dementia 4.
Collingwood, J.F., Finnegan, M.E., Arya, Z., Hagen, J.P., Chen, S., Chowdhury, A., Wayte, S., Ngandwe, E., Visanji, N.P., Dobson, J., Gowland, P.A., Hazrati, L.N., Hutchinson, C.E., 2014. MRI evaluation of the relationship between R2, R2*, and tissue iron in the human basal ganglia. In: ISMRM (Ed.), Joint Annual Meeting ISMRM-ESMRMB. International Society for Magnetic Resonance in Medicine, Madrid, Italy.
Connor, J.R., Snyder, B.S., Beard, J.L., Fine, R.E., Mufson, E.J., 1992. Regional distribution of iron and iron-regulatory proteins in the brain in aging and Alzheimers-disease. J. Neurosci. Res. 31, 327–335.
Cornett, C.R., Markesbery, W.R., Ehmann, W.D., 1998. Imbalances of trace elements related to oxidative damage in Alzheimer's disease brain. Neurotoxicology 19, 339–345.
Dedman, D.J., Treffry, A., Candy, J.M., Taylor, G.A.A., Morris, C.M., Bloxham, C.A., Perry, R.H., Edwardson, J.A., Harrison, P.M., 1992. Iron and aluminum in relation to brain ferritin in normal individuals and Alzheimers-disease and chronic renal-dialysis patients. Biochem. J. 287, 509–514.
Deibel, M.A., Ehmann, W.D., Markesbery, W.R., 1996. Copper, iron, and zinc imbalances in severely degenerated brain regions in Alzheimer's disease: possible relation to oxidative stress. J. Neurol. Sci. 143, 137–142.
Dexter, D.T., Carayon, A., Javoy-Agid, F., Agid, Y., Wells, F.R., Daniel, S.E., Lees, A.J., Jenner, P., Marsden, C.D., 1991. Alterations in the levels of iron, ferritin and other trace metals in Parkinson's disease and other neurodegenerative diseases affecting the basal ganglia. Brain 114 (Pt 4), 1953–1975.
Doan, N.T., Engvig, A., Zaske, K., Persson, K., Lund, M.J., Kaufmann, T., Cordova-Palomera, A., Alnaes, D., Moberget, T., Braekhus, A., Barca, M.L., Nordvik, J.E., Engedal, K., Agartz, I., Selbaek, G., Andreassen, O.A., Westlye, L.T., Initiative Alzheimer's Disease Neuroimaging, 2017. Distinguishing early and late brain aging from the Alzheimer's disease spectrum: consistent morphological patterns across independent samples. Neuroimage 158, 282–295.
Dobson, J., Grassi, P., 1996. Magnetic properties of human hippocampal tissue–evaluation of artefact and contamination sources. Brain Res. Bull. 39, 255–259.
Drayer, B., Burger, P., Darwin, R., Riederer, S., Herfkens, R., Johnson, G.A., 1986. MRI of brain iron. AJR Am. J. Roentgenol. 147, 103–110.
Dubois, Bruno, Feldman, Howard H., Jacova, Claudia, Cummings, Jeffrey L., DeKosky, Steven T., Barberger-Gateau, Pascale, Delacourte, André, Frisoni, Giovanni, Fox, Nick C., Galasko, Douglas, Gauthier, Serge, Hampel, Harald, Jicha, Gregory A., Meguro, Kenichi, O'Brien, John, Pasquier, Florence, Robert, Philippe, Rossor, Martin, Salloway, Steven, Sarazin, Marie, de Souza, Leonardo C., Stern, Yaakov, Visser, Pieter J., Scheltens, Philip, 2010. Revising the definition of Alzheimer's disease: a new lexicon. Lancet Neurol. 9, 1118–1127.
Dubois, B., Hampel, H., Feldman, H.H., Scheltens, P., Aisen, P., Andrieu, S., Bakardjian, H., Benali, H., Bertram, L., Blennow, K., Broich, K., Cavedo, E., Crutch, S., Dartigues, J.F., Duyckaerts, C., Epelbaum, S., Frisoni, G.B., Gauthier, S., Genthon, R., Gouw, A.A., Habert, M.O., Holtzman, D.M., Kivipelto, M., Lista, S., Molinuevo, J.L., O'Bryant, S.E., Rabinovici, G.D., Rowe, C., Salloway, S., Schneider, L.S., Sperling, R., Teichmann, M., Carrillo, M.C., Cummings, J., Jack Jr., C.R., Group Proceedings of the Meeting of the International Working, A. D, the American Alzheimer's Association on "The Preclinical State of, July, and U. S. A. Washington Dc, 2016. Preclinical Alzheimer's disease: definition, natural history, and diagnostic criteria. Alzheimers Dement. 12, 292–323.
Dusek, P., Bahn, E., Litwin, T., Jablonka-Salach, K., Luciuk, A., Huelnhagen, T., Madai, V.I., Dieringer, M.A., Bulska, E., Knauth, M., Niendorf, T., Sobesky, J., Paul, F., Schneider, S.A., Czlonkowska, A., Bruck, W., Wegner, C., Wuerfel, J., 2017. Brain iron accumulation in Wilson disease: a post mortem 7 Tesla MRI - histopathological study. Neuropathol. Appl. Neurobiol. 43, 514–532.
Finnegan, M.E., 2013. Investigation of the relationship between iron and high field MRI in healthy and Alzheimer's disease tissue. Ph.D. thesis. University of Warwick.
Frisoni, G.B., Bocchetta, M., Chetelat, G., Rabinovici, G.D., de Leon, M.J., Kaye, J., Reiman, E.M., Scheltens, P., Barkhof, F., Black, S.E., Brooks, D.J., Carrillo, M.C., Fox, N.C., Herholz, K., Nordberg, A., Jack Jr., C.R., Jagust, W.J., Johnson, K.A., Rowe, C.C., Sperling, R.A., Thies, W., Wahlund, L.O., Weiner, M.W., Pasqualetti, P., Decarli, C., 2013. Imaging markers for Alzheimer disease: which vs how. Neurology 81, 487–500.
Gallagher, J.J., Finnegan, M.E., Grehan, B., Dobson, J., Collingwood, J.F., Lynch, M.A., 2012. Modest amyloid deposition is associated with iron dysregulation, microglial activation, and oxidative stress. J. Alzheimer Dis. 28, 147–161.
Gao, L., Jiang, Z., Cai, Z., Cai, M., Zhang, Q., Ma, Y., Li, G., Zhao, F., Ma, Q., 2017. Brain iron deposition analysis using susceptibility weighted imaging and its association with body iron level in patients with mild cognitive impairment. Mol. Med. Rep. 16, 8209–8215.
Gellein, K., Flaten, T.P., Erikson, K.M., Aschner, M., Syversen, T., 2008. Leaching of trace elements from biological tissue by formalin fixation. Biol. Trace Elem. Res. 121, 221–225.
Gelman, N., Gorell, J.M., Barker, P.B., Savage, R.M., Spickler, E.M., Windham, J.P., Knight, R.A., 1999. MR imaging of human brain at 3.0 T: preliminary report on transverse relaxation rates and relation to estimated iron content. Radiology 210, 759–767.
Ghadery, C., Pirpamer, L., Hofer, E., Langkammer, C., Petrovic, K., Loitfelder, M., Schwingenschuh, P., Seiler, S., Duering, M., Jouvent, E., Schmidt, H., Fazekas, F., Mangin, J.F., Chabriat, H., Dichgans, M., Ropele, S., Schmidt, R., 2015. R2* mapping for brain iron: associations with cognition in normal aging. Neurobiol. Aging 36, 925–932.
Gossuin, Y., Burtea, C., Monseux, A., Toubeau, G., Roch, A., Muller, R.N., Gillis, P., 2004. Ferritin-induced relaxation in tissues: an in vitro study. J. Magn. Reson. Imaging 20, 690–696.
Graham, S.F., Nasaruddin, M.B., Carey, M., Holscher, C., McGuinness, B., Kehoe, P.G., Love, S., Passmore, P., Elliott, C.T., Meharg, A.A., Green, B.D., 2014. Age-associated changes of brain copper, iron, and zinc in Alzheimer's disease and dementia with Lewy bodies. J. Alzheimers Dis. 42, 1407–1413.
Haacke, E.M., Xu, Y.B., Cheng, Y.C.N., Reichenbach, J.R., 2004. Susceptibility weighted imaging (SWI). Magn. Reson. Med. 52, 612–618.
Haacke, E.M., Cheng, Y.C.N., House, M.J., Liu, Q., Neelavlli, J., Ogg, R.J., Khan, A., Ayaz, M., Kirsch, W., Obernaus, A., 2005. Imaging iron stores in the brain using magnetic resonance imaging. Magn. Reson. Imaging 23, 1–25.
Habes, M., Janowitz, D., Erus, G., Toledo, J.B., Resnick, S.M., Doshi, J., Van der Auwera, S., Wittfeld, K., Hegenscheid, K., Hosten, N., Biffar, R., Homuth, G., Volzke, H., Grabe, H.J., Hoffmann, W., Davatzikos, C., 2016. Advanced brain aging: relationship with epidemiologic and genetic risk factors, and overlap with Alzheimer disease atrophy patterns. Transl. Psychiatry 6, e775.
Hallgren, B., Sourander, P., 1958. The effect of age on the non-haemin iron in the human brain. J. Neurochem. 3, 41–51.
Hametner, S., Endmayr, V., Deistung, A., Palmrich, P., Prihoda, M., Haimburger, E., Menard, C., Feng, X., Haider, T., Leisser, M., Kock, U., Kaider, A., Hoftberger, R., Robinson, S., Reichenbach, J.R., Lassmann, H., Traxler, H., Trattnig, S., Grabner, G., 2018. The influence of brain iron and myelin on magnetic susceptibility and effective transverse relaxation - A biochemical and histological validation study. Neuroimage 179, 117–133.
Hare, D.J., Raven, E.P., Roberts, B.R., Bogeski, M., Portbury, S.D., McLean, C.A., Masters, C.L., Connor, J.R., Bush, A.I., Crouch, P.J., Doble, P.A., 2016. Laser ablation-inductively coupled plasma-mass spectrometry imaging of white and gray matter iron distribution in Alzheimer's disease frontal cortex. Neuroimage 137, 124–131.
Hopp, K., Popescu, B.F., McCrea, R.P., Harder, S.L., Robinson, C.A., Haacke, M.E., Rajput, A.H., Rajput, A., Nichol, H., 2010. Brain iron detected by SWI high pass filtered phase calibrated with synchrotron X-ray fluorescence. J. Magn. Reson. Imaging 31, 1346–1354.
House, M.J., St Pierre, T.G., Kowdley, K.V., Montine, T., Connor, J., Beard, J., Berger, J., Siddaiah, N., Shankland, E., Jin, L.W., 2007. Correlation of proton transverse relaxation rates (R2) with iron concentrations in postmortem brain tissue from Alzheimer's disease patients. Magn. Reson. Med. 57, 172–180.
House, M.J., Pierre, T.G.S., McLean, C., 2008. 1.4T study of proton magnetic relaxation rates, iron concentrations, and plaque burden in Alzheimer's disease and control postmortem brain tissue. Magn. Reson. Med. 60, 41–52.
House, M.J., Fleming, A.J., de Jonge, M.D., Paterson, D., Howard, D.L., Carpenter, J.P., Pennell, D.J., St Pierre, T.G., 2014. MApping iron in human heart tissue with synchrotron x-ray fluorescence microscopy and cardiovascular magnetic resonance. J. Cardiovasc. Magn. Reson. 16, 80.
Jack, Clifford R., Knopman, David S., Jagust, William J., Petersen, Ronald C., Weiner, Michael W., Aisen, Paul S., Shaw, Leslie M., Vemuri, Prashanthi, Wiste, Heather J., Weigand, Stephen D., Lesnick, Timothy G., Pankratz, Vernon S., Donohue, Michael C., Trojanowski, John Q., 2013. Tracking pathophysiological processes in Alzheimer's disease: an updated hypothetical model of dynamic biomarkers. Lancet Neurol. 12, 207–216.
Jensen, J.H., Chandra, R., 2000. Strong field behavior of the NMR signal from magnetically heterogeneous tissues. Magn. Reson. Med. 43, 226–236.
Kamman, R.L., Go, K.G., Brouwer, W., Berendsen, H.J.C., 1988. Nuclear magnetic resonance relaxation in experimental brain edema: effects of water concentration, protein concentration, and temperature. Magn. Reson. Med. 6, 265–274.
Kim, H.G., Park, S., Rhee, H.Y., Lee, K.M., Ryu, C.W., Rhee, S.J., Lee, S.Y., Wang, Y., Jahng, G.H., 2017. Quantitative susceptibility mapping to evaluate the early stage of Alzheimer's disease. Neuroimage Clin. 16, 429–438.
Kosior, E., Bohic, S., Suhonen, H., Ortega, R., Deves, G., Carmona, A., Marchi, F., Guillet, J.F., Cloetens, P., 2012. Combined use of hard X-ray phase contrast imaging and X-ray fluorescence microscopy for sub-cellular metal quantification. J. Struct. Biol. 177, 239–247.
Kumar, N., Rizek, P., Jog, M., 2016. Neuroferritinopathy: Pathophysiology, Presentation, Differential Diagnoses and Management. Tremor Other Hyperkinet. Mov. (N Y) 6, 355.
Laakso, M.P., Partanen, K., Lehtovirta, M., Hallikainen, M., Hanninen, T., Vainio, P., Riekkinen, P., Soininen, H., 1995. MRI of amygdala fails to diagnose early Alzheimer's disease. Neuroreport 6, 2414–2418.

Langkammer, C., Krebs, N., Goessler, W., Scheurer, E., Ebner, F., Yen, K., Fazekas, F., Ropele, S., 2010. Quantitative MR imaging of brain iron: a postmortem validation study. Radiology 257, 455–462.
Langkammer, C., Schweser, F., Krebs, N., Deistung, A., Goessler, W., Scheurer, E., Sommer, K., Reishofer, G., Yen, K., Fazekas, F., Ropele, S., Reichenbach, J.R., 2012. Quantitative susceptibility mapping (QSM) as a means to measure brain iron? A post mortem validation study. Neuroimage 62, 1593–1599.
Langkammer, C., Ropele, S., Pirpamer, L., Fazekas, F., Schmidt, R., 2014. MRI for iron mapping in Alzheimer's disease. Neurodegener. Dis. 13, 189–191.
Liu, C., Li, C., Yang, J., Gui, L., Zhao, L., Evans, A.C., Yin, X., Wang, J., 2015. Characterizing brain iron deposition in subcortical ischemic vascular dementia using susceptibility-weighted imaging: An in vivo MR study. Behav. Brain Res. 288, 33–38.
Loeffler, D.A., Connor, J.R., Juneau, P.L., Snyder, B.S., Kanaley, L., Demaggio, A.J., Nguyen, H., Brickman, C.M., Lewitt, P.A., 1995. Transferrin and iron in normal, Alzheimers-disease, and Parkinsons-disease brain-regions. J. Neurochem. 65, 710–716.
Manova, E.S., Habib, C.A., Boikov, A.S., Ayaz, M., Khan, A., Kirsch, W.M., Kido, D.K., Haacke, E.M., 2009. Characterizing the mesencephalon using susceptibility-weighted imaging. AJNR Am. J. Neuroradiol. 30, 569–574.
McCrea, R.P.E., Harder, S.L., Martin, M., Buist, R., Nichol, H., 2008. A comparison of rapid-scanning X-ray fluorescence mapping and magnetic resonance imaging to localize brain iron distribution. Eur. J. Radiol. 68 S109-S13.
McKhann, Guy M., Knopman, David S., Chertkow, Howard, Hyman, Bradley T., Jack Jr., Clifford R., Kawas, Claudia H., Klunk, William E., Koroshetz, Walter J., Manly, Jennifer J., Mayeux, Richard, Mohs, Richard C., Morris, John C., Rossor, Martin N., Scheltens, Philip, Carrillo, Maria C., Thies, Bill, Weintraub, Sandra, Phelps, Creighton H., 2011. The diagnosis of dementia due to Alzheimer's disease: recommendations from the National Institute on Aging-Alzheimer's Association workgroups on diagnostic guidelines for Alzheimer's disease. Alzheimers Dementia 7, 263–269.
Morris, J.C., Blennow, K., Froelich, L., Nordberg, A., Soininen, H., Waldemar, G., Wahlund, L.O., Dubois, B., 2014. Harmonized diagnostic criteria for Alzheimer's disease: recommendations. J. Intern. Med. 275, 204–213.
Mosselmans, J.F., Quinn, P.D., Dent, A.J., Cavill, S.A., Moreno, S.D., Peach, A., Leicester, P.J., Keylock, S.J., Gregory, S.R., Atkinson, K.D., Rosell, J.R., 2009. I18—the microfocus spectroscopy beamline at the Diamond Light Source. J. Synchrotron Radiat. 16, 818–824.
Oakley, A.E., Collingwood, J.F., Dobson, J., Love, G., Perrott, H.R., Edwardson, J.A., Elstner, M., Morris, C.M., 2007. Individual dopaminergic neurons show raised iron levels in Parkinson disease. Neurology 68, 1820–1825.
Ordidge, R.J., Gorell, J.M., Deniau, J.C., Knight, R.A., Helpern, J.A., 1994. Assessment of relative brain iron concentrations using T2-weighted and T2*-weighted MRI at 3 Tesla. Magn. Reson. Med. 32, 335–341.
Pankhurst, Q., Hautot, D., Khan, N., Dobson, J., 2008. Increased levels of magnetic iron compounds in Alzheimer's disease. J. Alzheimers Dis. 13, 49–52.
Perls, M., 1867. Nachweis von Eisenoxyd in gewissen Pigmenten. Archiv für Pathologische Anatomie und Physiologie und für Klinische Medicin 39, 42–48.
Persson, N., Wu, J., Zhang, Q., Liu, T., Shen, J., Bao, R., Ni, M., Liu, T., Wang, Y., Spincemaille, P., 2015. Age and sex related differences in subcortical brain iron concentrations among healthy adults. Neuroimage 122, 385–398.
Pini, L., Pievani, M., Bocchetta, M., Altomare, D., Bosco, P., Cavedo, E., Galluzzi, S., Marizzoni, M., Frisoni, G.B., 2016. Brain atrophy in Alzheimer's Disease and aging. Ageing Res. Rev. 30, 25–48.
Samudralwar, D.L., Diprete, C.C., Ni, B.F., Ehmann, W.D., Markesbery, W.R., 1995. Elemental imbalances in the olfactory pathway in Alzheimer's disease. J. Neurol. Sci. 130, 139–145.
Schrag, Matthew, Mueller, Claudius, Oyoyo, Udochukwu, Smith, Mark A., Kirsch, Wolff M., 2011. Iron, zinc and copper in the Alzheimer's disease brain: A quantitative meta-analysis. Some insight on the influence of citation bias on scientific opinion. Prog. Neurobiol. 94, 296–306.
Solé, V.A., Papillon, E., Cotte, M., Walter, Ph, Susini, J., 2007. A multiplatform code for the analysis of energy-dispersive X-ray fluorescence spectra. Spectrochim. Acta Part B At. Spectrosc. 62, 63–68.
St Pierre, T.G., Clark, P.R., Chua-anusorn, W., 2004. Single spin-echo proton transverse relaxometry of iron-loaded liver. NMR Biomed. 17, 446–458.
Tan, H., Liu, T., Wu, Y., Thacker, J., Shenkar, R., Mikati, A.G., Shi, C., Dykstra, C., Wang, Y., Prasad, P.V., Edelman, R.R., Awad, I.A., 2014. Evaluation of iron content in human cerebral cavernous malformation using quantitative susceptibility mapping. Invest. Radiol. 49, 498–504.
Tang, X., Cai, F., Ding, D.X., Zhang, L.L., Cai, X.Y., Fang, Q., 2018. Magnetic resonance imaging relaxation time in Alzheimer's disease. Brain Res. Bull. 140, 176–189.
Tao, Y., Wang, Y., Rogers, J.T., Wang, F., 2014. Perturbed Iron Distribution in Alzheimer's Disease Serum, Cerebrospinal Fluid, and Selected Brain Regions: A Systematic Review and Meta-Analysis. J. Alzheimers Dis.
Thelwall, P.E., Shepherd, T.M., Stanisz, G.J., Blackband, S.J., 2006. Effects of temperature and aldehyde fixation on tissue water diffusion properties, studied in an erythrocyte ghost tissue model. Magn. Reson. Med. 56, 282–289.
Thompson, C.M., Markesbery, W.R., Ehmann, W.D., Mao, Y.X., Vance, D.E., 1988. Regional brain trace-element studies in Alzheimers-disease. Neurotoxicology 9, 1–8.
Ugarte, M., Grime, G.W., Lord, G., Geraki, K., Collingwood, J.F., Finnegan, M.E., Farnfield, H., Merchant, M., Bailey, M.J., Ward, N.I., Foster, P.J., Bishop, P.N., Osborne, N.N., 2012. Concentration of various trace elements in the rat retina and their distribution in different structures. Metallomics 4, 1245–1254.
van Duijn, S., Bulk, M., van Duinen, S.G., Nabuurs, R.J.A., van Buchem, M.A., van der Weerd, L., Natte, R., 2017. Cortical iron reflects severity of Alzheimer's disease. J. Alzheimers Dis. 60, 1533–1545.
Visanji, N.P., Collingwood, J.F., Finnegan, M.E., Tandon, A., House, E., Hazrati, L.N., 2013. Iron deficiency in parkinsonism: region-specific iron dysregulation in Parkinson's disease and multiple system atrophy. J. Parkinsons Dis. 3, 523–537.
Vymazal, J., Brooks, R.A., Zak, O., McRill, C., Shen, C., Dichiro, G., 1992. T1 and T2 of ferritin at different field strengths: effect on MRI. Magn. Reson. Med. 27, 368–374.
Vymazal, J., Brooks, R.A., Baumgarner, C., Tran, V., Katz, D., Bulte, J.W.M., Bauminger, E.R., DiChiro, G., 1996. The relation between brain iron and NMR relaxation times: an in vitro study. Magn. Reson. Med. 35, 56–61.
Wang, J.Y., Zhuang, Q.Q., Zhu, L.B., Zhu, H., Li, T., Li, R., Chen, S.F., Huang, C.P., Zhang, X., Zhu, J.H., 2016. Meta-analysis of brain iron levels of Parkinson's disease patients determined by postmortem and MRI measurements. Sci. Rep. 6, 36669.
Wisse, L.E., Biessels, G.J., Heringa, S.M., Kuijf, H.J., Koek, D.H., Luijten, P.R., Geerlings, M.I., Group Utrecht Vascular Cognitive Impairment Study, 2014. Hippocampal subfield volumes at 7T in early Alzheimer's disease and normal aging. Neurobiol. Aging 35, 2039–2045.
Wood, J.C., 2011. Impact of iron assessment by MRI. Hematology Am. Soc. Hematol. Educ. Program 2011, 443–450.
Yablonskiy, D.A., Haacke, E.M., 1994. Theory of NMR signal behavior in magnetically inhomogeneous tissues: the static dephasing regime. Magn. Reson. Med. 32, 749–763.
Yang, Ching-Hui, Hong, San-He, Jao, Jo-Chi, Tsai, Shu-Neng, Shiao, Chia-Chi, Yeung, Kwok-Wan, Chen, Po-Chou, 2013. Correlation between SPGR MR signal intensity and iron concentration: Phantom study. Biomark. Genom. Med. 5, 39–43.
Yao, B., Li, T.Q., Gelderen, P., Shmueli, K., de Zwart, J.A., Duyn, J.H., 2009. Susceptibility contrast in high field MRI of human brain as a function of tissue iron content. Neuroimage 44, 1259–1266.

D.4 Publication 2020: Journal of Neuroscience Methods

Journal of Neuroscience Methods 345 (2020) 108870

Contents lists available at ScienceDirect

Journal of Neuroscience Methods

journal homepage: www.elsevier.com/locate/jneumeth

Regional segmentation strategy for DTI analysis of human corpus callosum indicates motor function deficit in mild cognitive impairment

Surya Rajan[a], Julia Brettschneider[b], Joanna F. Collingwood[a,*], for the Alzheimer's Disease Neuroimaging Initiative[1]

[a] School of Engineering, University of Warwick, Coventry, UK
[b] Department of Statistics, University of Warwick, Coventry, UK

GRAPHICAL ABSTRACT

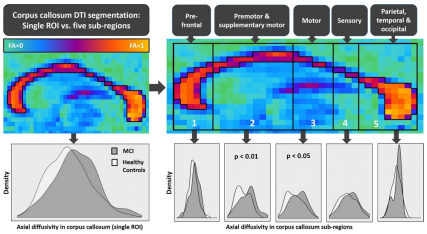

ARTICLE INFO

Keywords:
Corpus callosum
Diffusion tensor imaging
Ageing
Mild cognitive impairment
Motor impairment

ABSTRACT

Background: The corpus callosum is the largest white matter tract in the human brain, involved in inter-hemispheric transfer and integration of lateralised visual, sensory-motor, language, and cognitive information. Microstructural alterations are implicated in ageing as well as various neurological conditions.
New method: Cross-sectional diffusion-weighted images of 107 healthy adults were used to create a linear regression model of the ageing corpus callosum and its sub-regions to evaluate the impact of analysis by sub-region, and to test for deviations from healthy ageing parameters in 28 subjects with mild cognitive impairment (MCI). Alterations in diffusion properties including fractional anisotropy, mean, radial and axial diffusivities were investigated as a function of age.
Results: Changes in DTI parameters showed age-dependent regional differences, likely arising from axonal diameter variation across cross-sectional regions of interest in the corpus callosum. Patterns suggestive of degeneration with healthy ageing were observed in all regions. Diffusion parameters in sub-regions projecting to pre-motor, primary, and supplementary motor areas of the brain differed for MCI versus healthy controls, and MCI subjects were more likely than healthy controls to experience a reduction in motor skills.
Comparison with existing methods: : Statistical analyses of the corpus callosum by five manually-defined sub-regions, instead of a single manually-defined region of interest, revealed region-specific changes in

* Corresponding author at: School of Engineering, University of Warwick, Coventry, CV4 7AL, UK.
E-mail address: J.F.Collingwood@warwick.ac.uk (J.F. Collingwood).

[1] Data used in preparation of this article were obtained from the Alzheimer's Disease Neuroimaging Initiative (ADNI) database (adni.loni.usc.edu). As such, the investigators within the ADNI contributed to the design and implementation of ADNI and/or provided data but did not participate in analysis or writing of this report. A complete listing of ADNI investigators can be found at: http://adni.loni.usc.edu/wpcontent/uploads/how_to_apply/ADNI_Acknowledgement_List.pdf

https://doi.org/10.1016/j.jneumeth.2020.108870
Received 29 April 2020; Received in revised form 15 July 2020; Accepted 16 July 2020
Available online 17 July 2020

microstructure in healthy ageing and MCI, and accounted for clinically-evaluated differences in motor skills between cohorts.
Conclusion: : This method will support future studies of corpus callosum, enabling identification and measurement of white matter changes that are undetectable with the single ROI approach.

1. Introduction

The topology of the human brain is constantly changing from birth, plateauing in adulthood and degenerating in later life. Both grey matter and white matter tissues in the brain are susceptible to ageing, with observations in post-mortem studies of healthy human brains of more severe age-related changes in white matter than in grey matter (Marner et al., 2003; Piguet et al., 2009). The corpus callosum is the largest white matter tract in the human brain, with more than 300 million fibres interconnecting the two cerebral hemispheres. Recent technological advances have found fibres of the corpus callosum projecting into prefrontal, pre-motor, supplementary and primary motor, and sensory areas of the brain (Hofer and Frahm, 2006), and involved in interhemispheric transfer and integration of lateralised visual, sensorymotor, language and cognitive information (van der Knaap and van der Ham, 2011). Corpus callosum anatomy has been divided into sub-regions based on geometry (Clarke and Zaidel, 1994; Witelson, 1989), connectivity (Hofer and Frahm, 2006), and statistically derived cohesiveness (Denenberg et al., 1991; Peters et al., 2002). Studies on effects of age, sex and handedness in the healthy brain have reported differences in these properties in the corpus callosum by sub-region (Peters et al., 2002; Prendergast et al., 2015; Reuter-Lorenz and Stanczak, 2000; Sullivan et al., 2001a, 2001b; Witelson, 1989).

Post-mortem studies have linked altered properties of the corpus callosum to normal ageing (Hou and Pakkenberg, 2012) as well as neurological disorders including schizophrenia (Woodruff et al., 1995), multiple sclerosis (Evangelou et al., 2000), Huntington's disease and progressive supranuclear palsy (Mann et al., 1993). Recent magnetic resonance imaging (MRI) studies have strengthened these conclusions with evidence of atrophy (Goldman et al., 2017; Granberg et al., 2015; Lee et al., 2016; Wang et al., 2015a), morphological changes (Ardekani et al., 2014; Pardoe et al., 2015; Wolff et al., 2015), and demyelination in the human corpus callosum (Decker et al., 2018; Køster et al., 2018) and mouse models (Xiu et al., 2015). Diffusion tensor magnetic resonance imaging (DT-MRI or DTI) has also been applied to study the corpus callosum. DTI is an advanced technique that is used to image the diffusion properties of water molecules in tissue, providing a means to interpret the presence or absence of barriers to this diffusion (Le Bihan et al., 2001). DTI has been previously used to study the microstructural properties of the corpus callosum in healthy ageing and various neurological disorders (Hasan et al., 2005; Shahab et al., 2018; Sullivan and Pfefferbaum, 2003).

The corpus callosum is reportedly the white matter structure most affected by age (Sala et al., 2012), with some studies also revealing differences in the extent to which its sub-regions are affected (Ota et al., 2006). These variations between the sub-regions have been suggested as indicative of the differing effects of age in the corresponding parts of the brain they project to (Lebel et al., 2010; Ota et al., 2006). However, there are conflicting study results in the literature with some indicating a larger effect of age in the anterior corpus callosum than in the posterior (Hasan et al., 2005; Lebel et al., 2010; Ota et al., 2006; Sullivan et al., 2001a, 2001b), and a few suggesting the opposite (Bennett et al., 2017). MRI and DTI studies of the corpus callosum have also been carried out for various neurological disorders including mild cognitive impairment (MCI) and Alzheimer's disease (AD) (Ardekani et al., 2014; Lee et al., 2016; Wang et al., 2015b). Results of these studies indicate degeneration of the corpus callosum in disease that exceeds changes arising from healthy ageing.

The corpus callosum incorporates a heterogeneous bundle of fibres connecting the hemispheres of the brain. Different segments of this fibre bundle have been observed to be of different sizes or diameters, likely depending on the region of the brain they project to (Aboitiz et al., 1992). This may have an impact on the quantitative parameters measured *in vivo*, particularly in DTI. In previous DTI investigations of the corpus callosum in healthy ageing and disease, it has been treated as a single region of interest (ROI), and/or by sub-region (Ma et al., 2009; Bennett et al., 2017; Feng et al., 2018; Ota et al., 2006, Lebel et al., 2010). While a single ROI approach is easier to implement, the heterogeneity of the corpus callosum may be better represented through a region-wise analysis. This, in turn, may be influenced by the choice of scheme used to define the sub-regions. Here, we investigated DTI properties of the corpus callosum as a function of age and tested for cohort differences between ageing healthy controls (HC) and individuals with MCI, examining how this is influenced by segmenting the corpus callosum as a single ROI and by sub-region. Strategies for segmentation of the corpus callosum were explored. The data available to this study were acquired in the axial plane, but the corpus callosum is better delineated in the sagittal plane, so at the outset comparisons were made between atlas-based and manual delineation of the corpus callosum to determine the most appropriate strategy for this study. Having selected a manual delineation approach, the Hofer and Frahm scheme (segmenting in the sagittal plane to create pre-defined fractions), was used to divide the corpus callosum into five sub-regions for analysis (Hofer and Frahm, 2006).

2. Materials and methods

Data used in this study were obtained from the Alzheimer's Disease Neuroimaging Initiative (ADNI) database (http://adni.loni.usc.edu). ADNI was launched in 2003 as a public-private partnership, led by Principal Investigator Michael W. Weiner, MD. The primary goal of ADNI has been to test whether serial MRI, positron emission tomography, other biological markers, and clinical and neuropsychological assessments can be combined to measure the progression of MCI and early AD. ADNI consists of a series of multi-site data acquisition studies, with ADNI-1, ADNI-2, and ADNI-GO completed to date; ADNI-3 is ongoing. This study used data from ADNI-3, in order to utilize DTI data acquired at higher spatial resolution than in the previous ADNI studies. The primary inclusion criterion was that the image data were acquired with a set of fully-matched scan parameters. Prior studies confirm the importance of ensuring a consistent set of acquisition scan parameters to avoid introducing experimental uncertainty into the quantitative results, where their selection reportedly affects diffusion tensor estimation in DTI (Landman et al., 2007; Zavaliangos-Petropulu et al., 2019; Zhu et al., 2009). Application of this criterion to the full cohort in ADNI-3 produced a choice of three study cohorts (Siemens, GE, or Philips), and the largest of these at the time of analysis (Siemens) was selected, providing 140 subjects (107 HC, 28 MCI, 5 AD). All these HC and MCI subjects were included in the present study. Although the sample sizes for HC and MCI differed, this was carefully considered and accommodated for in the choice of statistical methods for comparison between the groups. The 5 AD cases were excluded because power calculations to determine study group size, based on prior-published ADNI-2 data, indicated that the AD group was too small to include for comparison with the HC and MCI.

The scan sequence details of images included in this study are: field strength = 3 T, echo time (TE) =56 ms, repetition time (TR) =7200 ms, b = 0, 1000s/mm^2, number of diffusion weighted images = 48,

number of non-diffusion weighted images = 7, voxel size = 2 mm x 2 mm x 2 mm and approximate scan time = 7 min 30 s.

The ADNI-3 subject images selected for use in this study were collected at the baseline visit for each participant. Ideally, longitudinal data from individuals would be used to analyse changes in DTI parameters as a function of age. In practice, a preliminary analysis (using the lower-spatial-resolution longitudinal data sets from ADNI-2 (Supplementary Figure S1) confirmed an insufficient number of participants in the ADNI-3 study cohort to support a longitudinal analysis. Instead, a cross-sectional analysis of the data from ADNI-3 was performed; this had the advantage of enabling inclusion of all HC and MCI subjects imaged using Siemens scanners during ADNI-3.

Gender has been reported to be a significant risk factor for MCI and AD, with the longitudinal rate of cognitive decline in MCI observed to be greater in women than in men (Laws et al., 2018; Lin et al., 2015). Gender-dependence of the patterns of change in DTI parameters of the white matter have also been observed (Kanaan et al., 2012); however, this finding is contradicted by others where no gender differences were observed (Inano et al., 2011). This apparent difference may be accounted for by factors other than gender dominating the white matter changes (de Schotten et al., 2011). For this reason, differences in DTI parameters as a function of gender were specifically tested for in the ADNI-3 cohorts studied here.

To understand if gender influenced DTI parameters with ageing, HC_{sub} (74 age- and gender-matched healthy subjects (37 F; 37 M)) was created as a subset of the main HC study group. Subject demographics are summarised in Table 1. The rationale for creating HC_{sub} was to test, using multiple regression, whether the DTI parameters were influenced by gender, and thereby to determine whether the main cohort HC or the subset HC_{sub} was most appropriate for use in the study of the relationship between DTI parameters and ageing.

DTI scans were processed in the subject space using FSL (FMRIB Software Library, University of Oxford) which is a comprehensive library of tools for brain imaging data analysis (Smith et al., 2004). Eddy-current-induced artefacts in the scans were corrected using the '*eddy_correct*' command (Jenkinson et al., 2002). The skull was removed, and the brain extracted from the artefact-corrected image using the '*bet*' tool of FSL and visually verifying the output. Weighted fitting of the diffusion tensor on the brain was achieved using the '*dtifit*' command (Jenkinson et al., 2012) and four scalar maps – fractional anisotropy (FA), mean diffusivity (MD), radial diffusivity (RD) and axial diffusivity (AxD) – were computed from the Eigen values of the tensor.

2.1. Selection of corpus callosum segmentation strategy

The ADNI DTI data were acquired in the axial plane, so ROI delineation to segment the corpus callosum would ideally be performed in the same plane to obtain the most accurate measurements. However, the corpus callosum is not easily visualised in the axial plane, and in previous studies it has been segmented in the sagittal plane (Ardekani et al., 2014; Ota et al., 2006; Westerhausen et al., 2004). To address this constraint, we tested several strategies to segment the corpus callosum, comparing the results for atlas-based and manual segmentation in the sagittal plane with the data obtained from the axial acquisition plane (considered ground truth). A small group of ten subjects was sampled from the cohort for this purpose, to enable comparisons between strategies at an individual level. The result from this process was used to select the strategy for use with the full cohort.

Step 1: Measurement in the axial (acquisition) plane using circular ROIs on axial FA image: The corpus callosum was identified on axial FA maps using anatomical landmarks such as the ventricles. Segmenting the whole structure in the axial plane was not attempted, because poor boundary definition had strong potential to increase experimental uncertainty in the results. Instead, using the method illustrated in prior studies (Bartzokis et al., 2010; Li et al., 2009), FA values were sampled with circular ROIs of varying radii (to avoid partial volume effects), placed throughout all axial slices where the corpus callosum was clearly identifiable (Fig. 1a, inset). Although previous studies have used the mean value from these ROIs, the heterogeneous distribution does not necessarily follow a normal distribution. Although mean and median values were very similar, checks on the individual distributions for the 10 subjects sampled for this step supported our use of the median to accommodate non-normal distributions of pixel FA values.

Step 2: Measurement using atlas-based delineation of ROI: The ICBM-DTI-81 atlas (Mori et al., 2008) provided with FSL, was used to obtain a mask of the corpus callosum using the labelled regions corresponding to the genu, the body and the splenium. Each subject's FA map was registered to the Montreal Neurological Institute (MNI) coordinate system (Fig. 1b), and the mean and median values of FA were measured in the ROI using the mask.

Step 3: Measurement using manual delineation in the sagittal plane: In the manual segmentation approach, the FA image was first reconstructed in the sagittal plane, and the mid-sagittal slice of the brain was estimated using the method developed by Freitas et al., 2011. Two slices each on either side of the mid-sagittal slice were segmented along with it to yield a volume of the corpus callosum consisting of five mid-sagittal slices (Fig. 1c). The mean and the median of the FA values of the pixels in this ROI were estimated.

Fractional anisotropy (FA) values measured using the strategies of manual segmentation in the sagittal plane, and atlas-based segmentation, were compared to determine which gave values in best agreement with those obtained manually from the axial plane (which, as the plane of data acquisition, was treated as ground truth for the purpose of these comparisons).

For subsequent region-wise analysis, the corpus callosum was segmented into sub-regions in ImageJ, using the pre-defined fractions for the sagittal plane indicated in the Hofer and Frahm scheme (Hofer and Frahm, 2006) (Fig. 1d). It is noted that while the corpus callosum is a bundle of fibres connecting the left and right hemispheres of the brain (Fig. 1a), analysis using segmentation performed in the sagittal plane parsed this bundle of fibres cross-sectionally from anterior to posterior (Fig. 1c), sampling its properties within a window of five sagittal slices.

Manual segmentation was performed in ROIEditor (Region of Interest Editing Tools v. 1.8). Statistical tests, including linear regression and ANCOVA for the variation in FA, MD, RD, and AxD with age, were conducted using software package R using other relevant factors such as gender and disease group as covariates. For region-wise

Table 1
Age and gender distribution of subjects in the main healthy control (HC) and mild cognitive impairment (MCI) cohorts, and the gender- and age-matched HC subgroup (HC_{sub}) as a subset of the HC cohort; M: male, F: female.

Age range (years)	Healthy controls			Mild cognitive impairment	
	Cohort	M	F	M	F
55 – 60	HC	–	1	–	2
	HC_{sub}	–	–		
61 – 65	HC	5	8	1	–
	HC_{sub}	5	5		
66 – 70	HC	7	24	2	1
	HC_{sub}	7	7		
71 – 75	HC	5	10	4	4
	HC_{sub}	5	5		
76 – 80	HC	11	9	3	4
	HC_{sub}	9	9		
81 – 85	HC	8	9	1	–
	HC_{sub}	8	8		
86 – 90	HC	6	2	1	2
	HC_{sub}	2	2		
90 – 96	HC	1	1	1	2
	HC_{sub}	1	1		
Total	**HC**	**43**	**64**	**13**	**15**
	HC_{sub}	**37**	**37**		

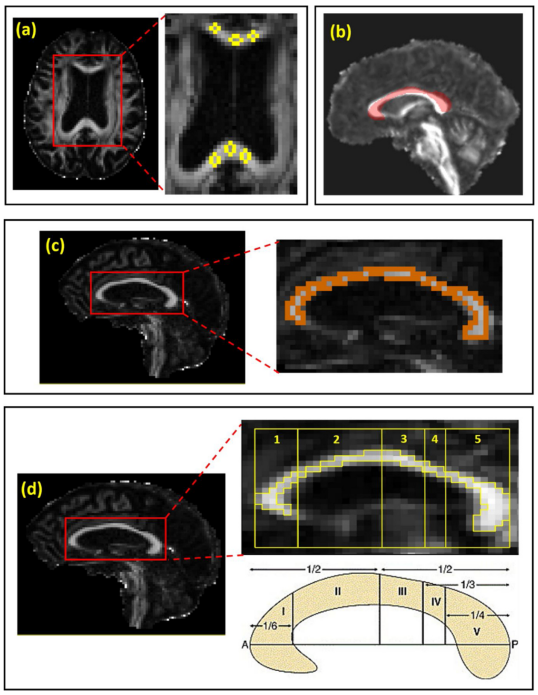

Fig. 1. (a) Segmentation in the axial acquisition plane: circular ROIs (see inset) placed in the corpus callosum in the axial plane to sample median FA values to be used as ground truth; (b) Strategy using atlas-based mask of corpus callosum (ICBM-DTI-81 atlas) to estimate mean and median of pixel-wise values; (c) Strategy using manual segmentation of the corpus callosum on FA image reconstructed in the sagittal plane to estimate mean and median of pixel-wise values; (d) Extended manual segmentation of the corpus callosum in the sagittal plane into five pre-determined regions based on the Hofer and Frahm scheme (schematic adapted with permission from Hofer and Frahm (2006)).

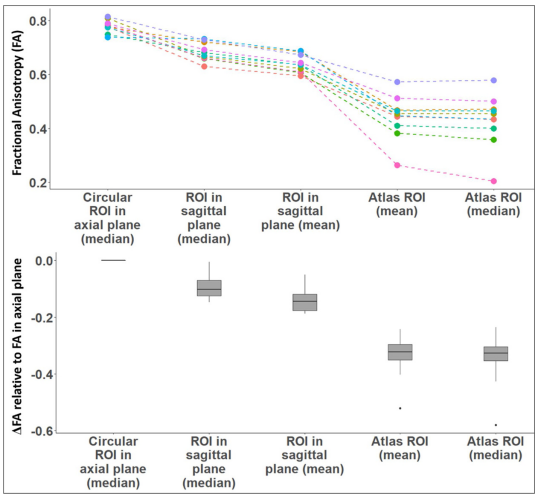

Fig. 2. Measured values of FA in 10 subjects, using different segmentation schemes. Median of pixel-wise FA from multiple circular ROIs placed in the axial corpus callosum (Fig. 1a) are considered ground truth. Corresponding box plots for each strategy show the distribution of offsets from ground truth for the 10 subjects. The experimental uncertainty in the data that can arise in subject comparisons from differences in scan sequence parameters (Zhu et al., 2009) has been avoided by only using images acquired using fully matched parameters; experimental uncertainty from other sources such as eddy current artefacts have been reduced by post-processing. In regions with high FA such as the corpus callosum, the reported experimental uncertainty in FA has been very small (Zhu et al., 2009).

analysis, measurements from each sub-region were tested separately. Measured parameter values and codes written in R to carry out the analyses are available at http://wrap.warwick.ac.uk/138931.

3. Results and discussion

3.1. Effects of gender on age-related changes not found significant in the cohort studied

To test for the effects of gender, multiple linear regression analyses of FA, MD, RD and AxD were carried out on cohort HC_{sub}. Age, gender, and the effect of their interaction were considered as factors. All four parameters exhibited linear trends with age in the age range analysed, in agreement with previously reported observations in the literature (Lebel et al., 2010; Ota et al., 2006). A consistent difference was observed between male and female patterns of changes with age, in regression plots of MD, RD and AxD, although this was not statistically significant. Such an offset was not observed for FA. The corresponding figures and regression equations are given in Figure S2 and Table S1 in Supplementary Materials. Since analysis of the HC_{sub} cohort did not indicate that gender was a statistically significant factor for DTI parameters as a function of age, subsequent analyses were conducted on the larger cohort HC using methods appropriate for application to differently sized study groups.

3.2. Comparison of corpus callosum segmentation methods

The results from the comparison of strategies for segmentation of the corpus callosum are shown in Fig. 2. The primary constraint of the atlas-based ROI approach is evident in Fig. 1b, where the mask of the corpus callosum is misaligned with the target structure evident in the image contrast. The mean and median of the FA in this ROI (Fig. 2: Atlas ROI (mean) and Atlas ROI (median)) were estimated and compared with the manually-segmented axial data (ground truth) and manually-segmented regions in the reconstructed sagittal plane. Atlas-based measurements resulted in a significant reduction in the estimated

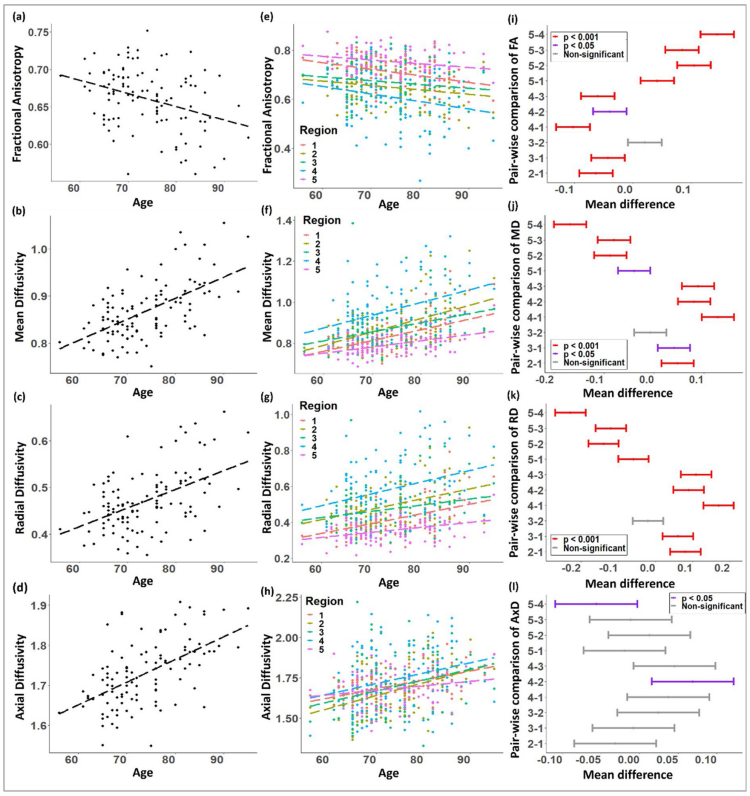

Fig. 3. Scatter plots of DTI parameters versus age with linear regression lines: (a) fractional anisotropy, (b) mean diffusivity, (c) radial diffusivity, and (d) axial diffusivity in the whole corpus callosum. Figures (e)-(h) are the same type of scatter plots but stratified by corpus callosum sub-region. The significance of age as a contributing factor to the observed trends, and the r-squared values, have been given in the Supplementary Tables S2 and S3. Figures (i)-(l) show the results of Tukey's multiple comparison tests between regions, with colours indicating corresponding significance levels. Values of MD, RD, and AxD are in 10^{-3} mm^2/s.

mean and median FA, likely due to partial volume effects. Potential issues with accuracy in the ICBM-DTI-81 atlas are addressed in a prior study (Rohlfing, 2013).

By contrast, as shown in Fig. 2, median values from the manually segmented ROI in the sagittal plane were closest to ground truth for the 10 sampled subjects. The slight offset of the FA values obtained manually in the sagittal plane compared to those from the axial plane may have arisen from i) the constrained sampling in the axial plane (reinforcing the need for ROI delineation in the sagittal plane), and/or from ii) interpolation errors arising from the sagittal reconstruction process. However, the similarity of the values, and the consistency of their distribution, indicated that this slight offset in the measured FA value would not affect the cohort-level relationships observed in subsequent regression analysis, and manual segmentation in the sagittal plane was subsequently used to obtain MD, RD, and AxD for the full cohort study.

3.3. Linear regression analysis of HC reveals age-related changes that vary between sub-regions, with evidence that axon diameters are a factor

Plots of linear regression analysis of FA, MD, RD and AxD on cohort HC, are shown in Fig. 3. For all four diffusion parameters, age was a significant factor contributing to the changes observed ($p < 0.001$). Similar analyses were performed to investigate whether patterns of change with age were different in the sub-regions of corpus callosum (Fig. 3e-h). (See Supplementary Materials for the corresponding regression equations.) Analysis of covariance (ANCOVA) revealed that the measured values of FA, MD, and RD differed significantly ($p < 0.001$) between the sub-regions when controlling for age (Table 2). Tukey's tests were performed for pairwise comparisons between the sub-regions for significantly differing values of the measured parameters (Figs. 3 i–l). Estimates of the effect size of region on the distribution of FA, MD, RD, and AxD are shown in Table 2. Partial omega-squared (ω^2), being a bias-corrected effect size estimator, has been used to describe the effect sizes in this study. When the effect or the sample size is small, ω^2 may carry negative values resulting from the bias correction (Okada, 2016).

A post-mortem study (Aboitiz et al., 1992) has shown that when parsing the corpus callosum cross-sectionally, the anterior region has the highest density of thin fibres. This starts decreasing towards the posterior regions and reaches a minimum before increasing again towards the posterior end. An opposite trend is observed for the density of fibres with a larger diameter. This density distribution of axonal diameter has been visualised in Fig. 4a, in an ROI that provides a cross-sectional view of the corpus callosum. Another study (Barazany et al., 2009) has reported a positive correlation between RD and axon diameter in the corpus callosum of rat brain, potentially due to larger diameters leading to lower packing density and a subsequent increase in perpendicular diffusion. This relationship has been found to hold true in our study in the human corpus callosum as visualised in Fig. 4b, even though we followed a different scheme of sub-division. The regional variations observed in DTI parameters in the cross-sectional corpus callosum ROI (Table 2) could likely be due to the varying density of axons with larger and smaller diameters that connect different regions of the two brain hemispheres (Fig. 4a). An interesting finding here was that regional variations did not affect AxD values of the corpus callosum; this may be due to the relatively simpler and unidirectional nature of axons in the regions analysed. Our analysis suggests that variations in DTI properties between sub-regions in the corpus callosum are significant. Therefore, studies investigating the diffusion properties of corpus callosum in ageing or disease may be better served by analysing each sub-region separately. This has scope to reduce the variance observed in measured data, since our analysis indicates that at least 25 % of variance can be explained by region-wise differences in the case of the parameters FA, MD, and RD (Table 2).

3.4. Comparison between MCI and healthy ageing: data indicating motor-related impairment in MCI reveal merits of corpus callosum analysis by sub-region

The effects of MCI on the corpus callosum and its sub-regions were investigated using data from cohorts HC and MCI (Fig. 5). Initial tests were carried out on the whole corpus callosum ROI using ANCOVA (Fig. 5a); they revealed subtle but significant differences between HC and MCI groups in FA, RD, and AxD, after controlling for the effects of age (Supplementary Table S4). Opposing changes in the magnitudes of RD and AxD (decrease and increase respectively), for patients with MCI compared to HC, may have masked any changes in MD (Supplementary Material Figure S3).

It is worth noting that the measured values for FA in MCI were higher than those for HC, and that the values for MD and RD were lower in MCI than for HC. This contradicts previous reports which showed trends of lower FA and higher diffusivities in degeneration (Amlien et al., 2013; Liu et al., 2013; Nowrangi et al., 2013; Wang et al., 2013), but seems to suggest a role for inflammation in MCI as indicated by increasing FA and decreasing diffusivities (Gupta et al., 2008; Nath et al., 2007; Renoux et al., 2006). This reportedly suggests either intracellular inflammation with inflow of extracellular water in the axons or decreased extracellular space due to cellular infiltration by inflammatory cells (Renoux et al., 2006). Neuroinflammation in MCI and Alzheimer's disease has not been extensively studied in this context. Advanced diffusion models of the brain such as those quantifying extracellular free-water volume are emerging markers being used to study neuro-inflammation (Pasternak et al., 2016, 2012), but are outside the scope of this study.

Investigation of region-specific measurements provided a better insight into differences between HC and MCI subjects (Fig. 5b). Supplementary Table S5 summarises the results of analysis using ANCOVA, controlling for the effects of age. Values of MD, RD, and AxD differed significantly ($p < 0.05$) between HC and MCI in region 2, and that of AxD differed significantly ($p < 0.05$) in region 3. This indicates that degenerative changes observed in MCI are dominant in regions 2 and 3 of the corpus callosum; and that they may be more extensive in region 2 than in region 3. It must be noted that although the effect sizes of MCI in regions 2 and 3 for the significantly different DTI parameters (Supplementary Table S5) were higher than in other regions, their values were still small. This might be accounted for by subtle differences between HC and MCI during the early stages of cognitive impairment.

Physiological interpretations for RD have included demyelination, and that for AxD have included axonal degeneration (Song et al., 2002, 2003). They suggest that the corpus callosum integrity is likely to be diminished in MCI, potentially playing a role in progression to Alzheimer's disease. In a prior study with data from ADNI-2 participants, DTI properties in several white matter structures were compared for patients with MCI, Alzheimer's disease patients, and healthy controls (Nir et al., 2013). They found widespread anisotropy and diffusivity alterations in elderly patients with Alzheimer's disease. They also reported that diffusivity measures were more sensitive to microstructural alterations than FA and could detect subtle differences in patients with MCI compared to controls. This was supported by the results from the analysis of corpus callosum sub-regions in the present study that

Table 2
Results of ANCOVA between regions 1 – 5 in HC, testing for the effects of regional differences after controlling for the effects of age.

Parameter	Cumulative p-value (ANCOVA)	ω^2
FA	< 0.001	0.295
MD	< 0.001	0.291
RD	< 0.001	0.330
AxD	0.006	0.019

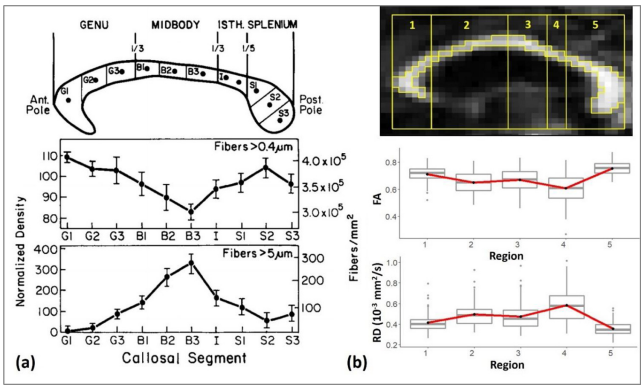

Fig. 4. (a) Density distribution of small and large diameter axons in the corpus callosum; picture adapted with permission (Aboitiz et al., 1992). (b) Distribution of FA and RD values in the corpus callosum sub-regions were observed to follow a similar trajectory. Although the sub-division scheme used in this study is different to that used in (a), it can be observed that the minimum and maximum density for smaller and larger diameter fibres occur in region B3 (isthmus) which is approximately the same as region 4 in the Hofer scheme; where the minimum and maximum for FA and RD distributions have respectively been observed.

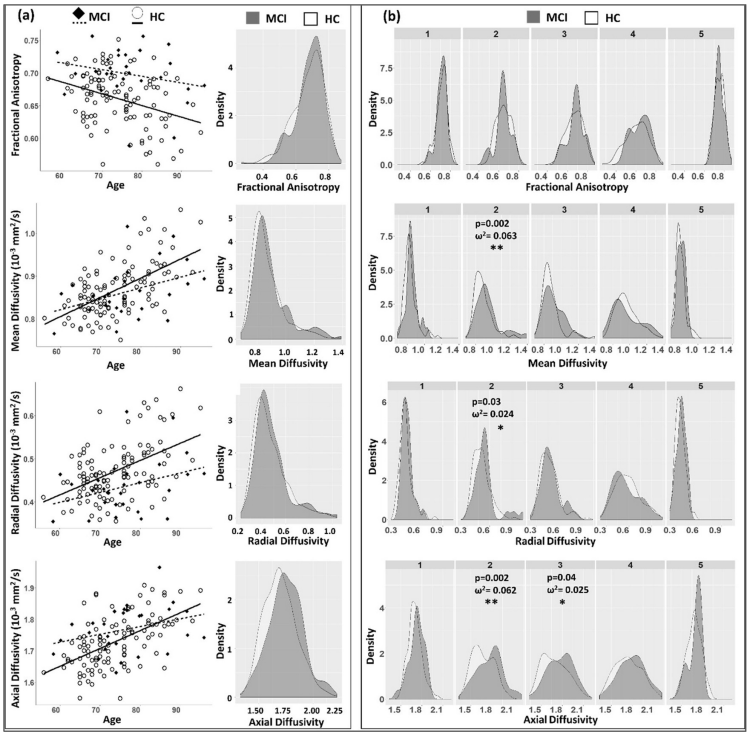

Fig. 5. (a) Linear trends of FA, MD, RD and AxD, for HC and MCI groups, in the whole corpus callosum, with corresponding density plots (smoothed histograms) (b) Density plots of FA, MD, RD and AxD visualised separately in the corpus callosum sub-regions. Values of ω^2 and their p-values for differences in measurements between HC and MCI are shown on the plots where they were observed to be statistically significant. * denotes $p < 0.05$ and ** denotes $p < 0.01$. ω^2 and their p-values for the remaining figures have been given in Supplementary Tables S4 and S5. Values of MD, RD, and AxD are in 10^{-3} mm^2/s.

Table 3
Summary of neurophysiological examinations of ADNI subjects, showing the percentage of subjects with abnormal results. The data shows an increase in motor-related abnormalities in MCI, compared to other functions tested.

Examination	HC % affected	MCI % affected
Visual impairment	5.6	3.6
Auditory impairment	6.5	7.1
Presence of tremors	8.4	21.4
Abnormal tendon reflexes	7.5	10.7
Abnormal plantar reflexes	0.9	3.6
Abnormal gait	8.4	21.4

revealed alterations in MD, RD, and AxD between MCI and HC.

Region 2 of the corpus callosum projects to pre-motor and supplementary motor areas, and region 3 to primary motor areas of the brain (Hofer and Frahm, 2006). An effect of MCI, indicated by significantly different diffusivity measurements in regions 2 and 3 as reported in this study, may help explain motor impairments seen in MCI and pre-clinical Alzheimer's disease (Buchman and Bennett, 2011; de Paula et al., 2016; Förstl and Kurz, 1999; Wirths and Bayer, 2008). Neurophysiological examination data, accompanying individual ADNI-3 participant scans, was used to test this hypothesis. These data were collected as part of the screening process and provide preliminary information about a range of functional networks including motor, visual and auditory systems. They are summarised in Table 3 and show that a higher proportion of MCI subjects than HC were reported to show tremors, abnormal reflexes and impaired gait. It is interesting to note that this pattern was observed only in motor-related functions, and not in the results of visual or auditory examinations. This suggests that an impairment in motor skills is observed for MCI, supporting our results that indicate alterations in the corpus callosum regions projecting to motor areas of the brain.

The results of our study agree with data from previous studies (Snir et al., 2019; de Laat et al., 2011; Bhadelia et al., 2009) that show significant correlations between altered FA in the genu of the corpus callosum and abnormal gait function. It must be noted that our study found an increase in FA in these regions of interest whereas these studies report a decrease in FA. Due to the non-specific nature of DTI, it is difficult to establish the exact nature of pathological changes that may be occurring in the corpus callosum in MCI. A decrease in diffusivity values in regions 2 and 3 of the corpus callosum may indicate demyelination or axonal degeneration (Song et al., 2002, 2003), in the commissural tracts in the anterior parts of the corpus callosum, resulting in diminished processing of information in the pre-motor, supplementary motor and primary motor areas of the brain.

4. Conclusions

Analysis of FA, MD, RD and AxD revealed that the properties of the corpus callosum are better characterised when segmented as five subregions, as opposed to as a single structure. Using this approach revealed changes in corpus callosum regions 2 and 3 of MCI subjects compared to HC, changes which were undetectable using the single ROI approach. The significance of the MCI-associated change is that regions 2 and 3 project to pre-motor, supplementary motor and motor areas of the brain. The DTI alterations in these regions were supported with evidence from ADNI-documented neurophysiological exams of these subjects, confirming that patients with MCI were more likely than HC to experience motor-related deficits, compared to other impairments. A limitation to the interpretation of the neuroscience findings, enabled by the method adopted for this study, is the lack of detailed information about motor functions in the ADNI neurophysiological exams conducted as part of screening. The ADNI evaluations only indicate the presence or absence of abnormalities. Availability of detailed test results in the future may help estimate the correlation between DTI parameters, tremors, reflexes and gait, providing insight into the extent of the role of corpus callosum in motor impairment as observed in MCI and potentially, pre-clinical Alzheimer's disease.

In summary, we anticipate that the method demonstrated in this study will advance the detection in a clinical setting of alterations to the structure of the corpus callosum, and corresponding impacts on brain function, using this comparatively simple method to obtain the ROIs and supporting statistical analysis.

Acknowledgements

Data collection and sharing for this project was funded by the Alzheimer's Disease Neuroimaging Initiative (ADNI) (National Institutes of Health Grant U01 AG024904) and DOD ADNI (Department of Defense award number W81XWH-12-2-0012). ADNI is funded by the National Institute on Aging, the National Institute of Biomedical Imaging and Bioengineering, and through generous contributions from the following: AbbVie, Alzheimer's Association; Alzheimer's Drug Discovery Foundation; Araclon Biotech; BioClinica, Inc.; Biogen; Bristol-Myers Squibb Company; CereSpir, Inc.; Cogstate; Eisai Inc.; Elan Pharmaceuticals, Inc.; Eli Lilly and Company; EuroImmun; F. Hoffmann-La Roche Ltd and its affiliated company Genentech, Inc.; Fujirebio; GE Healthcare; IXICO Ltd.; Janssen Alzheimer Immunotherapy Research & Development, LLC.; Johnson & Johnson Pharmaceutical Research & Development LLC.; Lumosity; Lundbeck; Merck & Co., Inc.; Meso Scale Diagnostics, LLC.; NeuroRx Research; Neurotrack Technologies; Novartis Pharmaceuticals Corporation; Pfizer Inc.; Piramal Imaging; Servier; Takeda Pharmaceutical Company; and Transition Therapeutics. The Canadian Institutes of Health Research is providing funds to support ADNI clinical sites in Canada. Private sector contributions are facilitated by the Foundation for the National Institutes of Health (www.fnih.org). The grantee organization is the Northern California Institute for Research and Education, and the study is coordinated by the Alzheimer's Therapeutic Research Institute at the University of Southern California. ADNI data are disseminated by the Laboratory for Neuro Imaging at the University of Southern California.

Computing facilities were provided by the Scientific Computing Research Technology Platform of the University of Warwick. The authors thank the University of Warwick, including the School of Engineering, for funding this research (SR). We also thank Jierong Luo, School of Engineering, University of Warwick, and Prof Keith D. White, Brain Rehabilitation Research Centre, University of Florida, for input to this study.

Appendix A. Supplementary data

Supplementary material related to this article can be found, in the online version, at doi:https://doi.org/10.1016/j.jneumeth.2020.108870.

References

Aboitiz, F., Scheibel, A.B., Fisher, R.S., Zaidel, E., 1992. Fiber composition of the human corpus callosum. Brain Res. 598, 143–153.
Amlien, I.K., Fjell, A.M., Walhovd, K.B., Selnes, P., Stenset, V., Grambaite, R., Bjornerud, A., Due-Tonnessen, P., Skinningsrud, A., Gjerstad, L., Reinvang, I., Fladby, T., 2013. Mild cognitive impairment: cerebrospinal fluid tau biomarker pathologic levels and longitudinal changes in white matter integrity. Radiology 266, 295–303.
Ardekani, B.A., Bachman, A.H., Figarsky, K., Sidtis, J.J., 2014. Corpus callosum shape changes in early Alzheimer's disease: an MRI study using the OASIS brain database. Brain Struct. Funct. 219, 343–352.
Barazany, D., Basser, P.J., Assaf, Y., 2009. In vivo measurement of axon diameter distribution in the corpus callosum of rat brain. Brain 132, 1210–1220.
Bartzokis, G., Lu, P.H., Tingus, K., Mendez, M.F., Richard, A., Peters, D.G., Oluwadara, B., Barrall, K.A., Finn, J.P., Villablanca, P., Thompson, P.M., Mintz, J., 2010. Lifespan trajectory of myelin integrity and maximum motor speed. Neurobiol. Aging 31, 1554–1562.
Bennett, I.J., Greenia, D.E., Maillard, P., Sajjadi, S.A., DeCarli, C., Corrada, M.M., Kawas, C.H., 2017. Age-related white matter integrity differences in oldest-old without dementia. Neurobiol. Aging 56, 108–114.

Bhadelia, R.A., Price, L.L., Tedesco, K.L., Scott, T., Qiu, W.Q., Patz, S., Folstein, M., Rosenberg, I., Caplan, L.R., Bergethon, P., 2009. Diffusion tensor imaging, white matter lesions, the corpus callosum, and gait in the elderly. Stroke 40, 3816–3820.
Buchman, A.S., Bennett, D.A., 2011. Loss of motor function in preclinical Alzheimer's disease. Expert Rev. Neurother. 11, 665–676.
Clarke, J.M., Zaidel, E., 1994. Anatomical-behavioral relationships: corpus callosum morphometry and hemispheric specialization. Behav. Brain Res. 64, 185–202.
de Laat, K.F., Tuladhar, A.M., van Norden, A.G., Norris, D.G., Zwiers, M.P., de Leeuw, F.E., 2011. Loss of white matter integrity is associated with gait disorders in cerebral small vessel disease. Brain 134, 73–83.
de Paula, J.J., Albuquerque, M.R., Lage, G.M., Bicalho, M.A., Romano-Silva, M.A., Malloy-Diniz, L.F., 2016. Impairment of fine motor dexterity in mild cognitive impairment and Alzheimer's disease dementia: association with activities of daily living. Brazilian Journal of Psychiatry 38, 235–238.
de Schotten, M.T., Bizzi, A., Dell'Acqua, F., Allin, M., Walshe, M., Murray, R., Williams, S.C., Murphy, D.G., Catani, M., 2011. Atlasing location, asymmetry and inter-subject variability of white matter tracts in the human brain with MR diffusion tractography. Neuroimage 54 (1), 49–59.
Decker, B.M., Guitar, B., Solomon, A., 2018. Corpus callosum demyelination associated with acquired stuttering. BMJ Case Rep. 2018.
Denenberg, V.H., Kertesz, A., Cowell, P.E., 1991. A factor analysis of the human's corpus callosum. Brain Res. 548, 126–132.
Evangelou, N., Konz, D., Esiri, M.M., Smith, S., Palace, J., Matthews, P.M., 2000. Regional axonal loss in the corpus callosum correlates with cerebral white matter lesion volume and distribution in multiple sclerosis. Brain 123 (9), 1845–1849.
Feng, Q., Liao, Z., Jiang, H., Mao, D., Wang, M., Yu, E., Ding, Z., 2018. Corpus callosum radiomics-based classification model in Alzheimer's disease: a case-control study. Front. Neurol. 9, 618.
Förstl, H., Kurz, A., 1999. Clinical features of Alzheimer's disease. Eur. Arch. Psychiatry Clin. Neurosci. 249, 288–290.
Freitas, P., Rittner, L., Appenzeller, S., Lotufo, R., 2011. Watershed-based segmentation of the midsagittal section of the corpus callosum in diffusion MRI. In: 2011 24th SIBGRAPI Conference on Graphics, Patterns and Images. IEEE. pp. 274–280.
Goldman, J.G., Bledsoe, I.O., Merkitch, D., Dinh, V., Bernard, B., Stebbins, G.T., 2017. Corpus callosal atrophy and associations with cognitive impairment in Parkinson disease. Neurology 88 (13), 1265–1272.
Granberg, T., Martola, J., Bergendal, G., Shams, S., Damangir, S., Aspelin, P., Fredrikson, S., Kristoffersen-Wiberg, M., 2015. Corpus callosum atrophy is strongly associated with cognitive impairment in multiple sclerosis: Results of a 17-year longitudinal study. Multiple Sclerosis Journal 21, 1151–1158.
Gupta, R.K., Nath, K., Prasad, A., Prasad, K.N., Husain, M., Rathore, R.K., Husain, N., Srivastava, C., Khetan, P., Trivedi, R., Narayana, P.A., 2008. In vivo demonstration of neuroinflammatory molecule expression in brain abscess with diffusion tensor imaging. Am. J. Neuroradiol. 29, 326–332.
Hasan, K.M., Gupta, R.K., Santos, R.M., Wolinsky, J.S., Narayana, P.A., 2005. Diffusion tensor fractional anisotropy of the normal-appearing seven segments of the corpus callosum in healthy adults and relapsing-remitting multiple sclerosis patients. J. Magn. Reson. Imaging 21, 735–743.
Hofer, S., Frahm, J., 2006. Topography of the human corpus callosum revisited–comprehensive fiber tractography using diffusion tensor magnetic resonance imaging. NeuroImage 32, 989–994.
Hou, J., Pakkenberg, B., 2012. Age-related degeneration of corpus callosum in the 90+ years measured with stereology. Neurobiol. Aging 33 1009-e1.
Jenkinson, M., Bannister, P., Brady, M., Smith, S., 2002. Improved optimization for the robust and accurate linear registration and motion correction of brain images. NeuroImage 17, 825–841.
Jenkinson, M., Beckmann, C.F., Behrens, T.E., Woolrich, M.W., Smith, S.M., 2012. Fsl. NeuroImage 62, 782–790.
Kanaan, R.A., Allin, M., Picchioni, M., Barker, G.J., Daly, E., Shergill, S.S., Woolley, J., McGuire, P.K., 2012. Gender differences in white matter microstructure. PLoS One 7 (6).
Køster, R.N., Jesper, R., Bente, P., 2018. The total number of myelinated nerve fibers is reduced in corpus callosum in brains from patients with Alzheimer's disease. Neurobiol. Aging 69, 58–64.
Landman, B.A., Farrell, J.A., Jones, C.K., Smith, S.A., Prince, J.L., Mori, S., 2007. Effects of diffusion weighting schemes on the reproducibility of DTI-derived fractional anisotropy, mean diffusivity, and principal eigenvector measurements at 1.5 T. NeuroImage 36, 1123–1138.
Laws, K.R., Irvine, K., Gale, T.M., 2018. Sex differences in Alzheimer's disease. Curr. Opin. Psychiatry 31 (2), 133–139.
Le Bihan, D., Mangin, J.F., Poupon, C., Clark, C.A., Pappata, S., Molko, N., Chabriat, H., 2001. Diffusion tensor imaging: concepts and applications. J. Magn. Reson. Imaging 13, 534–546.
Lebel, C., Caverhill-Godkewitsch, S., Beaulieu, C., 2010. Age-related regional variations of the corpus callosum identified by diffusion tensor tractography. NeuroImage 52, 20–31.
Lee, S.H., Bachman, A.H., Yu, D., Lim, J., Ardekani, B.A., 2016. Predicting progression from mild cognitive impairment to Alzheimer's disease using longitudinal callosal atrophy. Alzheimer's & Dementia 2, 68–74.
Li, T.Q., Yao, B., van Gelderen, P., Merkle, H., Dodd, S., Talagala, L., Koretsky, A.P., Duyn, J., 2009. Characterization of T2* heterogeneity in human brain white matter. Magn. Reson. Med. 62, 1652–1657.
Lin, K.A., Choudhury, K.R., Rathakrishnan, B.G., Marks, D.M., Petrella, J.R., Doraiswamy, P.M., Alzheimer's Disease Neuroimaging Initiative, 2015. Marked gender differences in progression of mild cognitive impairment over 8 years. Alzheimer's & dementia: translational research & clinical interventions 1 (2), 103–110.
Liu, J., Yin, C., Xia, S., Jia, L., Guo, Y., Zhao, Z., Li, X., Han, Y., Jia, J., 2013. White matter changes in patients with amnestic mild cognitive impairment detected by diffusion tensor imaging. PLoS One 8 (3), e59440.
Ma, L., Hasan, K.M., Steinberg, J.L., Narayana, P.A., Lane, S.D., Zuniga, E.A., Kramer, L.A., Moeller, F.G., 2009. Diffusion tensor imaging in cocaine dependence: regional effects of cocaine on corpus callosum and effect of cocaine administration route. Drug Alcohol Depend. 104, 262–267.
Mann, D.M., Oliver, R., Snowden, J.S., 1993. The topographic distribution of brain atrophy in Huntington's disease and progressive supranuclear palsy. Acta Neuropathol. 85, 553–559.
Marner, L., Nyengaard, J.R., Tang, Y., Pakkenberg, B., 2003. Marked loss of myelinated nerve fibers in the human brain with age. J. Comp. Neurol. 462, 144–152.
Mori, S., Oishi, K., Jiang, H., Jiang, L., Li, X., Akhter, K., Hua, K., Faria, A.V., Mahmood, A., Woods, R., et al., 2008. Stereotaxic white matter atlas based on diffusion tensor imaging in an ICBM template. NeuroImage 40, 570–582.
Nath, K., Husain, M., Trivedi, R., Kumar, R., Prasad, K.N., Rathore, R.K., Gupta, R.K., 2007. Clinical implications of increased fractional anisotropy in meningitis associated with brain abscess. J. Comput. Assist. Tomogr. 31, 888–893.
Nir, T.M., Jahanshad, N., Villalon-Reina, J.E., Toga, A.W., Jack Jr., C.R., Weiner, M.W., Thompson, P.M., Alzheimer's Disease Neuroimaging Initiative, 2013. Effectiveness of regional DTI measures in distinguishing Alzheimer's disease, MCI, and normal aging. Neuroimage Clin. 3, 180–195.
Nowrangi, M.A., Lyketsos, C.G., Leoutsakos, J.M., Oishi, K., Albert, M., Mori, S., Mielke, M.M., 2013. Longitudinal, region-specific course of diffusion tensor imaging measures in mild cognitive impairment and Alzheimer's disease. Alzheimer's & Dementia 9, 519–528.
Okada, K., 2016. Negative estimate of variance-accounted-for effect size: how often it is obtained, and what happens if it is treated as zero. Behav. Res. Methods 49, 979–987.
Ota, M., Obata, T., Akine, Y., Ito, H., Ikehira, H., Asada, T., Suhara, T., 2006. Age-related degeneration of corpus callosum measured with diffusion tensor imaging. NeuroImage 31, 1445–1452.
Pardoe, H.R., Mandelstam, S.A., Hiess, R.K., Kuzniecky, R.I., Jackson, G.D., Alzheimer's Disease Neuroimaging Initiative, Epilepsy Phenome/Genome Project Investigators, 2015. Quantitative assessment of corpus callosum morphology in periventricular nodular heterotopia. Epilepsy Res. 109, 40–47.
Pasternak, O., Westin, C.F., Bouix, S., Seidman, L.J., Goldstein, J.M., Woo, T.U., Petryshen, T.L., Mesholam-Gately, R.I., McCarley, R.W., Kikinis, R., Shenton, M.E., Kubicki, M., 2012. Excessive extracellular volume reveals a neurodegenerative pattern in schizophrenia onset. J. Neurosci. 32, 17365–17372.
Pasternak, O., Kubicki, M., Shenton, M.E., 2016. In vivo imaging of neuroinflammation in schizophrenia. Schizophr. Res. 173, 200–212.
Peters, M., Oeltze, S., Seminowicz, D., Steinmetz, H., Koeneke, S., Jancke, L., 2002. Division of the corpus callosum into subregions. Brain Cogn. 50, 62–72.
Piguet, O., Double, K.L., Kril, J.J., Harasty, J., Macdonald, V., McRitchie, D.A., Halliday, G.M., 2009. White matter loss in healthy ageing: a postmortem analysis. Neurobiol. Aging 30, 1288–1295.
Prendergast, D.M., Ardekani, B., Ikuta, T., John, M., Peters, B., DeRosse, P., Wellington, R., Malhotra, A.K., Szeszko, P.R., 2015. Age and sex effects on corpus callosum morphology across the lifespan. Hum. Brain Mapp. 36, 2691–2702.
Renoux, J., Facon, D., Fillard, P., Huynh, I., Lasjaunias, P., Ducreux, D., 2006. MR diffusion tensor imaging and fiber tracking in inflammatory diseases of the spinal cord. Am. J. Neuroradiol. 27, 1947–1951.
Reuter-Lorenz, P.A., Stanczak, L., 2000. Differential effects of aging on the functions of the corpus callosum. Dev. Neuropsychol. 18, 113–137.
Rohlfing, T., 2013. Incorrect ICBM-DTI-81 atlas orientation and white matter labels. Front. Neurosci. 7.
Sala, S., Agosta, F., Pagani, E., Copetti, M., Comi, G., Filippi, M., 2012. Microstructural changes and atrophy in brain white matter tracts with aging. Neurobiol. Aging 33, 488–498.
Shahab, S., Stefanik, L., Foussias, G., Lai, M.C., Anderson, K.K., Voineskos, A.N., 2018. Sex and diffusion tensor imaging of white matter in schizophrenia: A systematic review plus meta-analysis of the corpus callosum. Schizophrenia Bulletin 44, 203–221.
Smith, S.M., Jenkinson, M., Woolrich, M.W., Beckmann, C.F., Behrens, T.E., Johansen-Berg, H., Bannister, P.R., De Luca, M., Drobnjak, I., Flitney, D.E., Niazy, R.K., Saunders, J., Vickers, J., Zhang, Y., De Stefano, N., Brady, J.M., Matthews, P.M., 2004. Advances in functional and structural MR image analysis and implementation as FSL. NeuroImage 23 (Suppl 1), S208–19.
Snir, J.A., Bartha, R., Montero-Odasso, M., 2019. White matter integrity is associated with gait impairment and falls in mild cognitive impairment. Results from the gait and brain study. NeuroImage: Clinical 29.
Song, S.K., Sun, S.W., Ramsbottom, M.J., Chang, C., Russell, J., Cross, A.H., 2002. Dysmyelination revealed through MRI as increased radial (but unchanged axial) diffusion of water. NeuroImage 17, 1429–1436.
Song, S.K., Sun, S.W., Ju, W.K., Lin, S.J., Cross, A.H., Neufeld, A.H., 2003. Diffusion tensor imaging detects and differentiates axon and myelin degeneration in mouse optic nerve after retinal ischemia. NeuroImage 20, 1714–1722.
Sullivan, E.V., Pfefferbaum, A., 2003. Diffusion tensor imaging in normal aging and neuropsychiatric disorders. Eur. J. Radiol. 45, 244–255.
Sullivan, E.V., Adalsteinsson, E., Hedehus, M., Ju, C., Moseley, M., Lim, K.O., Pfefferbaum, A., 2001a. Equivalent disruption of regional white matter microstructure in ageing healthy men and women. Neuroreport 12, 99–104.
Sullivan, E.V., Rosenbloom, M.J., Desmond, J.E., Pfefferbaum, A., 2001b. Sex differences in corpus callosum size: relationship to age and intracranial size. Neurobiol. Aging 22, 603–611.
van der Knaap, L.J., van der Ham, I.J., 2011. How does the corpus callosum mediate interhemispheric transfer? A review. Behav. Brain Res. 223, 211–221.

Wang, J.H., Lv, P.Y., Wang, H.B., Li, Z.L., Li, N., Sun, Z.Y., Zhao, B.H., Huang, Y., 2013. Diffusion tensor imaging measures of normal appearing white matter in patients who are aging, or have amnestic mild cognitive impairment, or Alzheimer's disease. J. Clin. Neurosci. 20, 1089–1094.
Wang, X.D., Ren, M., Zhu, M.W., Gao, W.P., Zhang, J., Shen, H., Lin, Z.G., Feng, H.L., Zhao, C.J., Gao, K., 2015a. Corpus callosum atrophy associated with the degree of cognitive decline in patients with Alzheimer's dementia or mild cognitive impairment: a meta-analysis of the region of interest structural imaging studies. J. Psychiatr. Res. 63, 10–19.
Wang, Z., Wang, J., Zhang, H., Mchugh, R., Sun, X., Li, K., Yang, Q.X., 2015b. Interhemispheric functional and structural disconnection in Alzheimer's disease: a combined resting-state FMRI and DTI study. PLoS One 10 e0126310.
Westerhausen, R., Kreuder, F., Sequeira, S.S., Walter, C., Woerner, W., Wittling, R.A., Schweiger, E., Wittling, W., 2004. Effects of handedness and gender on macro-and microstructure of the corpus callosum and its subregions: a combined high-resolution and diffusion-tensor MRI study. Cogn. Brain Res. 21 (3), 418–426.
Wirths, O., Bayer, T.A., 2008. Motor impairment in Alzheimer's disease and transgenic Alzheimer's disease mouse models. Genes Brain Behav. 7 (Suppl 1), 1–5.
Witelson, S.F., 1989. Hand and sex differences in the isthmus and genu of the human corpus callosum: a postmortem morphological study. Brain 112 (3), 799–835.
Wolff, J.J., Gerig, G., Lewis, J.D., Soda, T., Styner, M.A., Vachet, C., Botteron, K.N., Elison, J.T., Dager, S.R., Estes, A.M., Hazlett, H.C., Schultz, R.T., Zwaigenbaum, L., Piven, J., Network, I., 2015. Altered corpus callosum morphology associated with autism over the first 2 years of life. Brain 138, 2046–2058.
Woodruff, P.W., McManus, I.C., David, A.S., 1995. Meta-analysis of corpus callosum size in schizophrenia. J. Neurol. Neurosurg. Psychiatr. 58, 457–461.
Xiu, Y., Kong, X.R., Zhang, L., Qiu, X., Gao, Y., Huang, C.X., Chao, F.L., Wang, S.R., Tang, Y., 2015. The myelinated fiber loss in the corpus callosum of mouse model of schizophrenia induced by MK-801. J. Psychiatr. Res. 63, 132–140.
Zavaliangos-Petropulu, A., Nir, T.M., Thomopoulos, S.I., Reid, R.I., Bernstein, M.A., Borowski, B., Jack Jr., C.R., Weiner, M.W., Jahanshad, N., Thompson, P.M., 2019. Diffusion MRI indices and their relation to cognitive impairment in brain aging: the updated multi-protocol approach in ADNI3. Front. Neuroinform. 13.
Zhu, T., Liu, X., Gaugh, M.D., Connelly, P.R., Ni, H., Ekholm, S., et al., 2009. Evaluation of measurement uncertainties in human diffusion tensor imaging (DTI)-derived parameters and optimization of clinical DTI protocols with a wild bootstrap analysis. J. Magn. Reson. Imaging 29, 422–435.

Appendix E

Licences and permissions

- Figure 1.2 adapted from 'Cover, G. S., Herrera, W. G., Bento, M. P., Appenzeller, S., and Rittner, L., Computational methods for corpus callosum segmentation on MRI: A systematic literature review. Computer methods and programs in biomedicine, 154:25-35, 2018', with permission from Elsevier.
- Figure 1.3 reproduced from 'Jack Jr, C. R., Knopman, D. S., Jagust, W. J., Petersen, R. C., Weiner, M. W., Aisen, P. S., Shaw, L. M., Vemuri, P., Wiste, H. J., Weigand, S. D. and Lesnick, T. G., Tracking pathophysiological processes in Alzheimer's disease: an updated hypothetical model of dynamic biomarkers. The Lancet Neurology, 12(2):207-216, 2013', with permission from Elsevier.
- Figure 3.4 adapted from 'Hofer, S., and Frahm, J., Topography of the human corpus callosum revisited - comprehensive fiber tractography using diffusion tensor magnetic resonance imaging. Neuroimage, 32(3): 989-994, 2006', with permission from Elsevier